UNIVERSITÉ DE NEUCHÂTEL

CENTRE OF HYDROGEOLOGY

Relations between retreating alpine glaciers and karst aquifer dynamics. Tsanfleuron-Sanetsch experimental test site, Swiss Alps

PhD thesis presented to the Faculty of Sciences of the University of Neuchâtel
to satisfy the requirements of the degree of Doctor of Philosophy in Science

by

Vivian Gremaud

Thesis defence date: 14. January 2011

PhD thesis evaluation committee:

Prof. Nico Goldscheider, Technical University of Munich, Germany, *Thesis Director*

Prof. Francois Zwahlen, University of Neuchâtel, Switzerland, *Thesis Co-Director*

Dr. Bryn Hubbard, Aberystwyth University, Great Britain, *Jury Member*

Prof. Jacques Mudry, University of Franche-Comte, France, *Jury Member*

Prof. Martin Funk, Swiss Federal Institute of Technology Zürich, Switzerland, *Jury Member*

Université de Neuchâtel

FACULTE DES SCIENCES
Secrétariat-Décanat de la faculté
Rue Emile-Argand 11
CH-2000 Neuchâtel

IMPRIMATUR POUR LA THESE

Relations between retreating alpine glaciers and karst aquifer dynamics. Tsanfleuron-Sanetsch experimental test site, Swiss Alps

Vivian GREMAUD

UNIVERSITE DE NEUCHATEL

FACULTE DES SCIENCES

La Faculté des sciences de l'Université de Neuchâtel,
sur le rapport des membres du jury

MM. F. Zwahlen (directeur de thèse),
N. Goldscheider (co-directeur de thèse, Münich),
B. Hubbard (Aberystwyth, UK),
J. Mudry (Besançon) et M. Funk (ETH Zürich)

autorise l'impression de la présente thèse.

Neuchâtel, le 8 février 2011

Le doyen :
P. Kropf

Téléphone : +41 32 718 21 00 E-mail : secretariat.sciences@unine.ch www.unine.ch/sciences

第七十八章

天下莫柔弱于水，而攻堅強者莫之能勝，以其無以易之。
弱之勝強，柔之勝剛，天下莫不知，莫能行。
是以聖人云：
「受國之垢，是謂社稷主；受國不祥，是爲天下王。」
正言若反。

Rien n'est plus souple et faible au monde que l'eau.
Pourtant pour attaquer ce qui est dur et fort
rien ne la surpasse et personne ne pourrait l'égaler.
Que le faible surpasse la force
que le souple surpasse le dur,
chacun le sait
mais personne ne met ce savoir en pratique.

Nothing in the world is as soft and yielding as water,
Yet nothing can better overcome the hard and strong,
For they can neither control nor do away with it.
The soft overcomes the hard,
The yielding overcomes the strong;
Every person knows this,
But no one can practice it.

Lao Tseu

This research project was funded by the Swiss National Science Foundation (grants 200020-121726). It was carried out at the Centre of Hydrogeology (CHYN) of the University of Neuchâtel (Switzerland).

Abstract

Karst aquifers are of major importance for groundwater resources world-wide. Especially in high moutain catchment areas, where different types of recharge occur, karst systems represent one of the first water supplies for human activities. However, the current available volume of water is highly dependent on surface water storage during the winter season. Snow fields and glaciers in high mountain areas store considerable amounts of freshwater contributing to groundwater recharge in warmer periods. But the precise relations between these volumes of frozen water which overly such systems and aquifer dynamics have rarely been studied in detail. As a consequence of climate change, these frozen areas are rapidly shrinking, decreasing the amount of water available to recharge the karst aquifers. With a general increase in temperature and a slight diminution of precipitations prognosed for the next 50 years, alpine water resources during dry periods are expected to reduce in the coming decades.

The Tsanfleuron area, located in the South western Swiss Alps, was found to be an ideal experimental test site for research on alpine aquifers, glaciers, snowpacks, freshwater resources and climate variations. The rapidly retreating Tsanfleuron glacier, corresponding to an area of $2.8 \cdot 10^6$ m^2 for an ice volume of $100 \cdot 10^6$ m^3 in 2008, overlies a large regional karrenfield of $13.7 \cdot 10^6$ m^2. Its meltwater ($92 \cdot 10^6$ m^3 of water is stored in the glacier) directly recharges the karst aquifer. Relations between stratigraphic and tectonic settings, recharge processes and underground drainage were validated by the means of 22 tracer experiments. Large parts of the karrenfield area are drained by the Glarey spring (mean annual discharge of $1.8 \cdot 10^7$ m^3), which is used as a drinking water source, while marginal parts belong to the catchments of other border springs. Groundwater flow towards the Glarey spring occurs in the superficial aquifer, parallel to stratification, while flow towards another spring crosses the entire stratigraphic sequence, consisting of about 800m of marl and limestone, along deep faults that were probably enlarged by mass movements. The diurnal variability of glacial meltwater production during the warm season influences the shape of tracer breakthrough curves and, consequently, flow and transport in the aquifer.

The Tsanfleuron glacier currently loses an estimated thickness of about 1.4 m per year according to field observations and water balance calculations. Flow measurements and glacial tracer tests allowed characterisation of meltwater drainage and aquifer recharge. Three pathways have been identified. The main glacial stream sinks into the aquifer via swallow holes 3 km downstream of the glacier mouth. Shortly below the front of the glacier numerous small meltwater streams sink underground. Subglacial meltwaters and supraglacial streams sink into the glacier via moulins and contribute to aquifer recharge through fractures and swallow holes beneath the glacier.

Recharge and spring discharge display strong diurnal and seasonal variability, with a general high-flow period during snow and glacier melt from spring to autumn. Annual meteorological variations in the Tsanfleuron area were well defined by a snow cover, a snow melt and an ice melt season. Snow, ice or rain volumes were characterized through water stable isotopes in order to estimate the different recharge contributions to the available volume at the main output. About 65% of available water at Glarey spring comes from glacier or rainfall during the ice melt season, with no significant differences

between sunny and rainy days. Even during the snow cover season, snow melt contributes to 15% of the measured discharge at Glarey spring. Finally the snow melt season produces 55% of the total output water volume. As expected, the glacier has a great influence on the groundwater quantity and moreover drives the diurnal variations of many physical parameters. A time shift of about 10 hours between the lowest electrical conductivity (ice meltwater signature) and the equivalent isotopic ratio was observed. It indicates that specific refrozen ice layers in the glacier (with heavier isotopic ratios) melt first, followed by zones with a more usual isotopic value. The dynamic of the glacier is therefore highly influenced by daily temperature variations, which are able to melt and refreeze deep or basal ice layers, and illustrating its vulnerability to climate change.

Calculated water balance, without applying uncertainties, presents an input of $1.77 \cdot 10^7\ m^3$ for an output of $1.82 \cdot 10^7\ m^3$. The system is close to equilibrium without considering the glacier melt. By modifiying measured values by uncertainties, balances vary from a deficit of 18% to an excess of 61%. Therefore worst prediction of the future availability of spring water after disappearance of the glacier suggests that the discharge may decrease by 22%, with only 18% of this loss resulting from progonosed precipitation decrease in future. More than half of the annual water volume currently available at Glarey spring is snow meltwater. In this scenario, if the glacier vanishes, about two thirds of the annual amount of water will have flown out of the system by the end of June. Therefore nearly all of the loss will occur in summer and autumn, presumably resulting in temporary water shortage. Best cases are on contrary sufficient excess balance, where glacier disappearance would not have any incidence on water availability. For equilibrium scenarios glacier currently completes any deficit, but this completion will vanish in future and decreases the output volume at Glarey spring.

Keywords: Glacierized karst, Retreating glacier, Multi-tracer test, Climate change, Swiss Alps, Groundwater recharge, Ice thickness mapping, Geophysics, Radiomagnetotellurics

Acknowledgements

First of all I want to thank *Pr. Dr. Nico Goldscheider*, who initiated and supervised this research. I appreciate our discussions, your suggestions and advices about my work, your disponibility and your patience during this last four years.

Many thanks also to *Pr. Dr. François Zwahlen*, co-director of this thesis, for the final corrections and all the help provided during my work time at the Centre of Hydrogeology of Neuchâtel.

For their tracer experiments on Tsanfleuron test site, our discussions and their speleological informations, I thank *Gérald Favre* and *Dr. Ludovic Savoy*. Without our collaborations this thesis would have not be the same.

Many thanks to *Roberto Costa* and *François Bourret* for their knowledge and installation of continuous monitoring systems during the fieldwork, and their important contributions, advices and helps when building and installing instruments in the field. I am also very grateful to *Pierre-André Schnegg* and *Marie-Ève Winiger* for their advices about respectively field fluorimeters and chemical sampling and analysis.

Thanks to my friend *James Ingram* for reading and correcting my english before I submit my thesis.

I want also to thank *Dr. Bryn Hubbard* from the Centre of Glaciology at the University of Aberystwyth (UK) for his advices and informations about Tsanfleuron glacier and for his presence in my thesis committee. Thanks to *Pr. Jacques Mudry* from the University of Franche-Comté (F) and *Pr. Dr. Martin Funk* from the Swiss Federal Institute of Technology at Zürich, who also accepted to belong to my thesis committee.

I thank the community of Conthey, especially *Christian Dessimoz* for lending me the key of Glarey spring during four years, sharing discharge data of the years 2004 to 2007 and financial help. I also thank *Lars Theiler* from Glacier3000 company for his obervations about glacier melt and *Edmée Léger* for hosting me many times at the Prarochet Hut.

For his corrections on cross sections and maps, I want to thank *Pr. Dr. Henri Masson*. Many advices about geological details in the geometry of the aquifers were discussed at the beginning of this work.

I also thank all my collegues at the Centre of Hydrogeology for the good and pleasant working environment, but especially for their helps and advices, essential for finishing this thesis. I want here to thank *Pierik Falco* for its help about Latex but also for the great discussions and jokes that we share in the same office. Thank to *Pascale Ducommun* and *Xenia Boutsiadou* for sharing a previous office together but also for their advices about chemical devices and analysis. Thank also to *Dr. Michiel Pronk* and *Dr. François Gainon* for their good advices about fieldwork during the first year of my thesis. A great thank to *Mathieu Beck* for the RMT campaign on the glacier and all the help about

geophysic methods. Thank to *Andrea Borghi* for supporting me during scientific meetings but also for his great karst models. Finally thanks also to all the others PhD students that shared knowledge and discussions with me during these last four years: *Alessandro Communian, Dr. Romain Ducommun, Antoine Bailleux, Paul Bailleux, Domagoj Babič, Dr. Guillaume Bertrand, Simon Jeannottat* and *Florian Breider*.

I want to cite also master students that worked on Tsanfleuron test site with me: *Sébastien Deyres* (2007), *Lena Tobler* (2008) and *Susanna Ramu* (2009). Thank for your help during field campaign and for the good work you produced for your respective master thesis.

Finally many huge thanks to my wife *Lenka* for her essential support and interesting. Also to my son Arthur. Thank also to my parents for giving me the opportunity of doing such long studies and for supporting me during these last ten years.

Contents

List of Figures

List of Tables

Chapter 1

Introduction

1.1 Background

Mountains represent about 22% of the planet's continental areas, and host 720 million inhabitants (12% of the planet's population). They indirectly provide life to over half of the world's population (Beniston et al., 1997). They are of major importance to the hydrological cycle, containing springs of many of the world's major rivers, linked to high altitude aquifers, glaciers and snowfields. In the Alps, stored water runs into the Rhône, Rhine, Pô and Danube rivers, which supply millions of Europeans with irrigation, drinking and industrial water, but also contributes to considering the Alps as "water towers of Europe".

Karst aquifers are present in large parts of Alpine mountain areas (Fig. 1.1) and mainly developed in mesozoic limestone or dolomite, but also in palaeozoic or tertiary formations with rocks such as marble, calcareous sandstone, gypsum, anhydrite or salt (Goldscheider, 2002). Such lithologies are present in a wide variety of landscapes through very different altitudes and climates. Summits can be made of carbonate rocks (Eiger, 3870 m, Switzerland) but erosion created also large karrenfield with gentle topography (Désert de Platé, France; Tsanfleuron karrenfield, Switzerland). With the superposition of strata during the formation of the Alps, some these karstifiable layers may be buried under a stratigraphy of many millions of years. Globally, carbonate rocks represent a substantial part of the external alpine lithologies and most of them are karstified and contain important groundwater resources (Goldscheider, 2002). These alpine aquifers are very interesting from scientific point of view (Zoetl, 1974), because their dynamics are mainly influenced by stratigraphy (lithology, thickness and neighbourhood of the considered strata), tectonic parameters (folds, fractures and faults), geomorphology (glaciations, rockfalls or erosive processes) or recharge parameters (snowfields, glaciers and permafrost). Karst aquifers are indeed very important for human activities in alpine catchments but also in the rest of the world, where carbonate rocks represent nearly 10% of the planet's surface and about 25% of the world population's drinking water supply (Ford and Williams, 2007). In Europe, 35% of land is covered by carbonate terrains, which is a significant portion of Europe's water re-

sources. In some European alpine countries (i.e. Slovenia or Austria) karst aquifers contribute to as much as 50% of the total drinking water supply. Several cities (i.e. Vienna or Innsbruck) are mainly supplied with water from karst aquifers. In Switzerland, karst aquifers also represent 50% of the current groundwater resources. Their contribution to water supply is very important but also strongly dependant on climatic conditions. With their specific hydrological and hydrogeological features, water storage and transit times are reduced in comparison to other types of aquifers. Variations of recharge therefore have a rapid impact on the availability and quality of water resources.

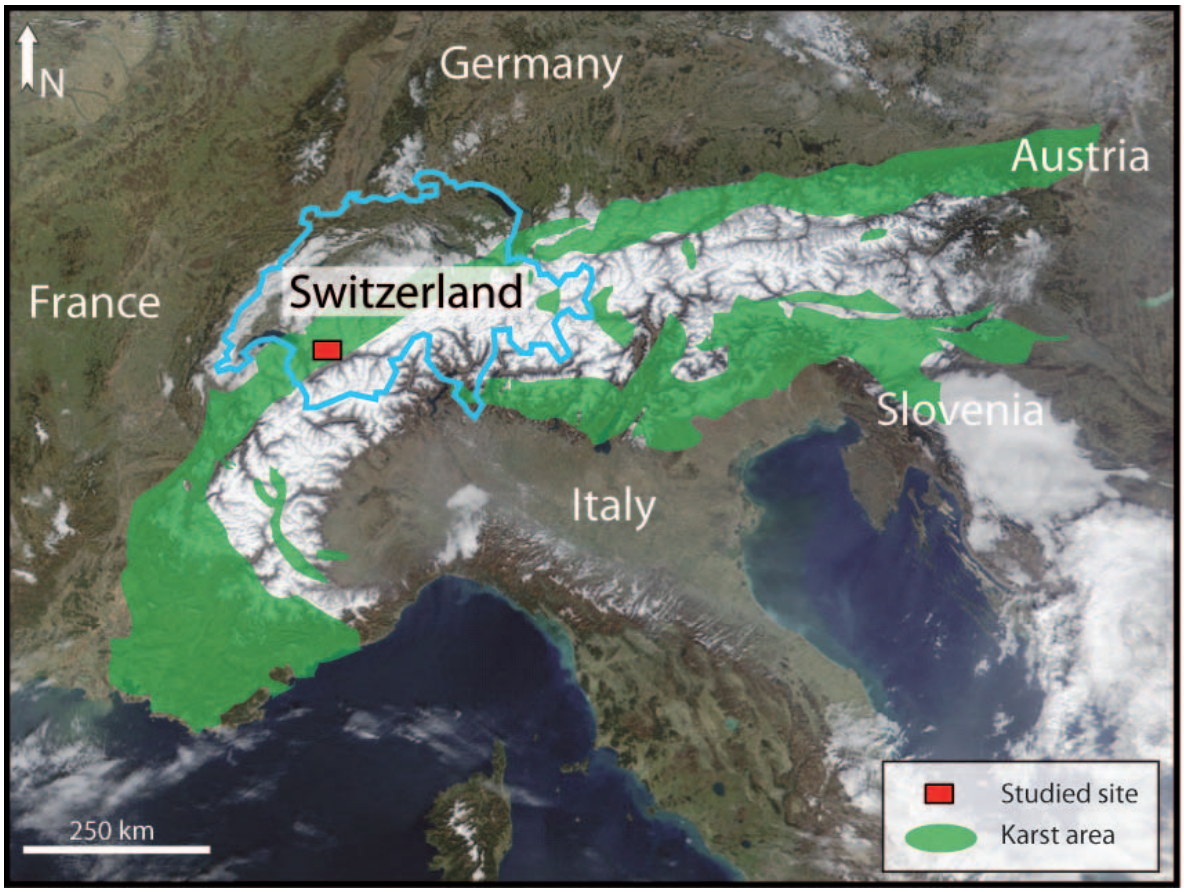

Figure 1.1: Localization of the karst areas in the Alps. The studied site is in the southwest of Switzerland. More details are available in Fig. 1.4. Modified from literature (Goldscheider, 2002) and Google Earth picture (2010).

1.2 Swiss Alps climate change

Climate is extremely variable in mountain regions and precipitations are substantially higher than in surrounding lowlands, creating large volumes of easily available fresh water. Annual precipitation varies from 600 mm to more than 4000 mm per year (Goldscheider, 2002) and is separated into snow or rain, depending on temperature, altitude and exposition parameters. A large part of the snowfall is easily retained in perrenial snowfields and glaciers, frequent in high altitude catchments, and is then slowly released during warmer periods (Viviroli and Weingartner, 2004). Thus climate changes

are clearly visible in high altitude regions. Rapidly retreating glaciers and decreasing permanent snowfields are obvious expressions of changing climate (Greene et al. 1999; Paul et al. 2004). Current summer runoff is therefore already inflated compared to equilibrium states, due to an increased melt rate of high elevation frozen water (Lambrecht and Mayer, 2009). In the worst climatic cases, about 75% of the glaciers in the swiss Alps are expected to disappear by 2050 (Zemp et al., 2006). In the best cases, less than a half of the current volume of swiss glaciers (Fig. 1.2) will remain in 2050 (Haeberli et al., 2007). But glaciers are not the only structure to suffer from climate change. Permafrost surfaces will also decrease, slower than glaciers, but with negative consequences for slope stability (Gruber and Haeberli, 2007). If substantial changes in the mountain snow pack is directly linked to glacier and permafrost retreat, they also have a significant impact on the flow of large scale river basins and concrete consequences for local aquifers or catchments. Such differences in the amount and timing of snow runoff in the future will also create potential for enhanced flooding, erosion, and associated natural hazards (Beniston et al., 2003).

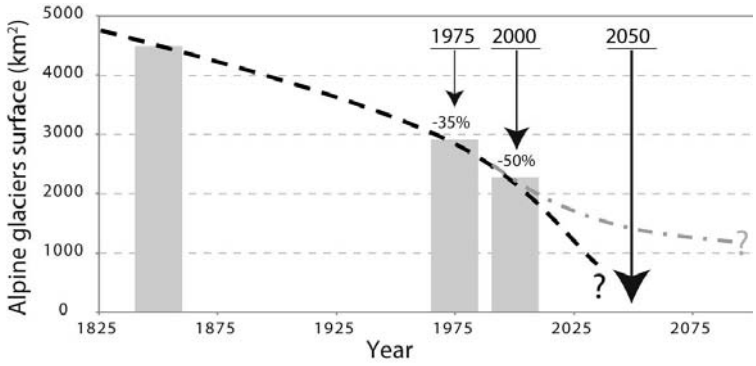

Figure 1.2: Scenario of the evolution of alpine glacier volumes in the next decades. The worst case scenario prognoses (black line) a complete disappearance of glaciers in the Alps, whereas the best case scenario leaves less than the half of the year 2000 volume (grey line). Modified from literature (OcCC, 2008)

Globally alpine landscapes will change, white surface from snowfields and glacier will be replaced by rocks or moraine deposits. In a second period water volumes that could be released during hot seasons disappear with these typical alpine structures. Albedo variations also maximize these changes. These processes are directly linked with last available climate change (OcCC, 2008) suggesting that, during winter, warmer temperatures and more precipitation in the form of rain instead of snow are likely to result in more available freshwater, while less rain in summer (Fig. 1.3), along with the shrinking or disappearance of glaciers, may result in local, temporary water shortage, particularly during warm seasons (Kleinn et al., 2005; Schaefli et al., 2007; Seidel et al., 1998).

1.3 Objectives and structure of the thesis

Karst systems recharged with glacier or snowfield are therefore directly influenced by climate variations and induce new questions about water resource availability or management. The vulnerability of alpine karst systems to new climatic constrains is important to predict water availability and quality in close future. But relatively little research has been done on the current and future impacts of climate change on alpine karst systems. Therefore, this research project was set up to study alpine glaciers and karst aquifer systems, by keeping in mind the water resources availability. Few available studies focus on glacier-groundwater interactions, mostly numerical modelling of large-scale flow beneath recent ice shields (Flowers et al., 2003) or Pleistocene ice shields (Boulton et al., 1993), as well

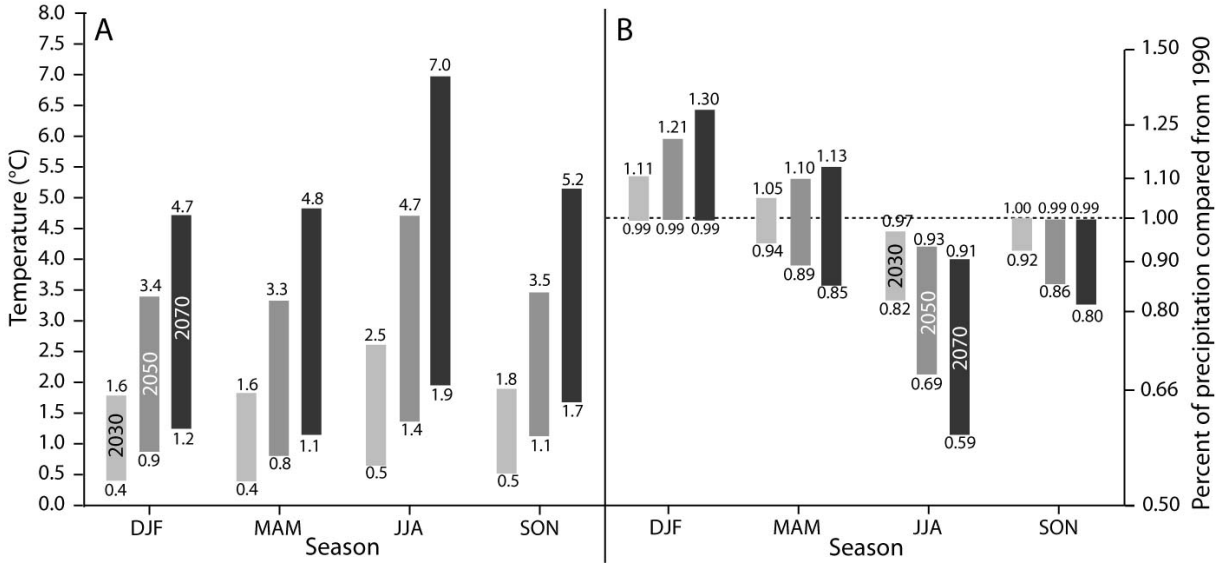

Figure 1.3: Temperature (A) and rainfall (B) prognoses for 2030, 2050 and 2070. Modified from literature (OcCC, 2008)

as long-term simulations evaluating the role of infiltrating meltwaters for the cooling of alpine massifs (Marechal et al., 1999). Only very few researchers have studied the relations between alpine glaciers and directly connected karst aquifers (Smart, 1996) and not with the aim of the characterization of water resources. Therefore the main objective of this research work is to study an alpine karst aquifer and its complexe recharge characterized by the dynamics of annual glacier meltwater production and precipitation variability; to estimate the availability of water, and to compare current and future hydrographs. In association, a description of karst-glacier interactions in relation with the folded geological structure of the aquifer is discussed, with a focus on how and when glacier meltwater infiltrates the karst aquifer and the consequences for the main discharge output.

The body of this thesis is built on six chapters without considering this introduction. Three of them are based on articles that have been or will be published in peer-reviewed journals. The two remaining chapters are an unpublished part of the fieldwork and an exhaustive description of methods used for this work.

- Chapter 2: **Basic concepts and first measurements: a brief overview of test site characteristics** introduces theory and some field applications of the different methods used for this work. Sampling protocol and analysis of water stable isotopes, of tracer tests, parameters and physical properties of RMT methods and different physical and chemical probes parameters are precisely developed in order to characterize uncertainties and limits of the measurements. Basic but important glaciological concepts are also explained.
- Chapter 3: **From geological structure and tracer experiments to a conceptual flow model of the Tsanfleuron karst aquifer** investigates the geology and structure of the Tsanfleuron-Sanetsch site, tracer test descriptions and transit time distributions. A delimitation of spring catchments is also discussed, with characterization of water pathways in the

stratigraphy.

- Chapter 4: **Geometry and drainage of Tsanfleuron glacier recharging the karst aquifer** presents tracer tests and geophysical campaigns on the glacier. The volume of ice available to recharge the aquifer, an estimated meltwater quantity and the different pathways of the dyes first in the ice and then in the aquifer are discussed.

- Chapter 5: **Use of stable isotope to characterize the relationship between glacier melt and alpine karst aquifer dynamics** proposes a methodology to distinguish the different recharge processes, considering snow, rain, glacier or aquifer baseflow. Seasonal dynamics are also explained with conceptual models for each season and relationships between each input and output parameters.

- Chapter 6: **Consequences of the retreat and disappearance of a small alpine glacier for the future quality and availability of water** focuses on the future prognosis if considering that the Tsanfleuron glacier will disappear, based on climate change estimations for the next twenty years. It also deals with the flow dynamic in the karst aquifer, especially the influence of daily glacier melt and of precipitation. A water balance is also built on the precipitation and discharge measurements.

- Chapter 7: **Conclusions, summary and perspectives** provides a general discussion based on the conclusions of all the chapters in order to summarize the specificities and characteristics of the aquifer, its relation with the Tsanfleuron glacier and to discuss the impact of climate change on water resources based on the general results and observations of this study. Some perspectives and limitations for each method are also discussed.

1.4 Research area

1.4.1 Locality

There are few places in the Alps where the interrelations between climate change, retreating glaciers, groundwater resources and freshwater supply are so immediate as in the Tsanfleuron-Sanetsch region in Western Switzerland. A rapidly retreating glacier (Tsanfleuron glacier) directly overlies and recharges the upper part of a large regional karst aquifer, which is drained at its lowest point by a spring (Glarey spring) used for the drinking water supply of a community (Conthey), as well as for irrigation purposes. This experimental site is located in the southwestern Swiss Alps in the Wallis region. The Tsanfleuron karrenfield, karst aquifer and associated glacier rise from an altitude of 1500 m at the main studied spring to 3000 m at the top the glacierized area. The last 400 m are covered by the Tsanfleuron glacier. The complete hydrogeological basin is around 21.5 km^2: 12 km^2 with a gently inclined karrenfield morphology in which 2.8 km^2 are covered by ice. The other 9.5 km^2 are made of other morphologies: to the south the Lizerne Valley is separated from the karrenfield by a 1000 meter rock wall, to the north mountains overlook the Tsanfleuron karrenfield, to the west the Diablerets summit at 3200 m, and to the east the Morge Valley and the Sanetsch pass. The area is constricted in the Swiss coordinates [581'000 132'000] and [591'000 125'000] (see Fig.1.4 and Fig. 1.7).

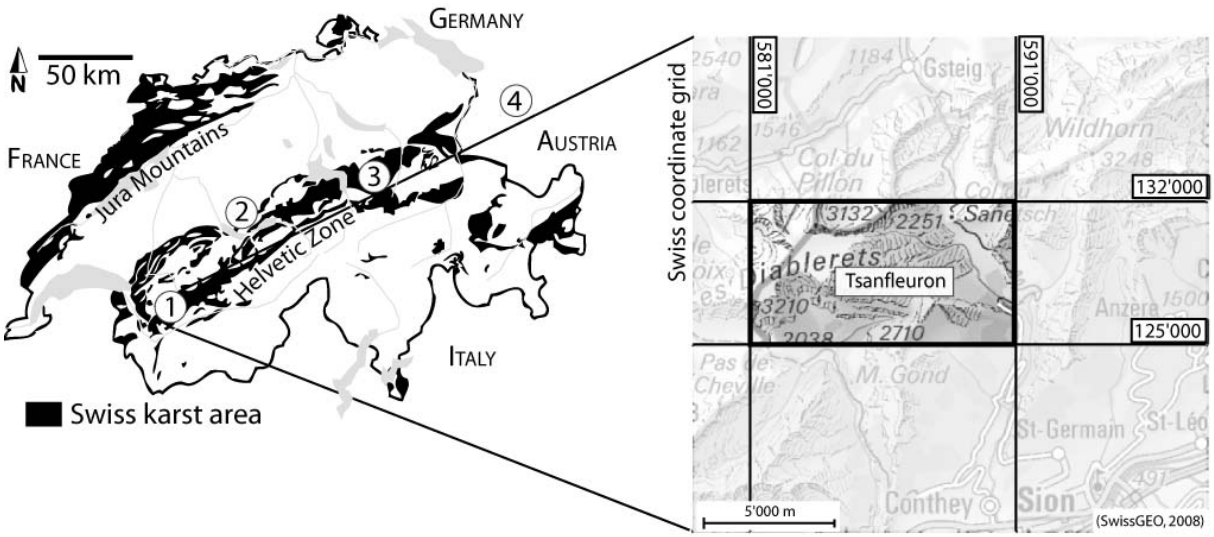

Figure 1.4: The Tsanfleuron karrenfield is located in southwestern Switzerland, near the city of Sion (SwissGEO, 2008), in the Helvetic tetonic area. The Helvetic zone crosses Switzerland from France in the Southwest to Germany and Austria in the Northeast. Tsanfleuron karrenfield is mainly built by the late cretaceous limestone (1). Three well studied karst areas that also belong to Helvetic zone are (2) Sienbenhegste-Hohgant karst; (3) Hoelloch in the Muotathal and (4) Hochifen-Gottesacker zone.

1.4.2 Geology

The Tsanfleuron area belongs to a long chain of karst aquifer systems developed in the Helvetic zone of the Alps (appendix B.1). This geological structure of about 25 km wide starts in the French Alps and ends in Germany from the Southwest to the Northeast of Switzerland. Its stratigraphy goes from triasic formations to paleocene lithologies. In this major tectonic unit, well known karst networks are mostly present in a Cretaceous limestone formation known as Schrattenkalk (German) or Urgonian (French).

Well-studied examples (Fig. 1.4) include the Muotathal area, which encompasses the Hölloch - the longest cave in the Alps (Jeannin, 2001); the Siebenhengste-Hohgant area with the second longest cave in the Alps (Huselmann et al., 2003); and the Hochifen-Gottesacker area, a prime example of a karst system where fold structures were demonstrated to have a major influence upon the underground drainage pattern (Goldscheider, 2005). The Tsanfleuron area does not present such important caves, but the aquifer is mainly constrained by folds and fractures. The overlying glacier, that recharge the aquifer is the major difference compared to the three other systems. Currently, the Tsanfleuron area has received little attention from geologists and hydrogeologists, while glaciologists and glacial sedimentologists have studied the glacier and its forefield for many years (Fairchild et al., 1999; Hubbard et al., 2003; Hubbard, 2002; Hubbard et al., 2000).

1.4.3 Precipitations and recharge

The Tsanfleuron area belongs to an alpine mountain range, which acts like a cloud fence and accumulates rainfall coming from western Switzerland. This geometry preserves the Rhône Valley of many precipitation events but locally increases mean annual precipitations (Fig. 1.5). Annual precipitation also depends on the elevation considered. It ranges between 1240 mm and 1540 mm at the elevation of 1840 m (OldenAlp totalisator) and between 1510 mm and 2200 mm at 2820 m (Sex Rouge totalisator). Some very big differences occur, depending of the localization of each station. A daily measurement was done by the Swiss Meteorological Survey at the elevation of 2966 m that was reported in a monthly time step (Fig. 1.6).

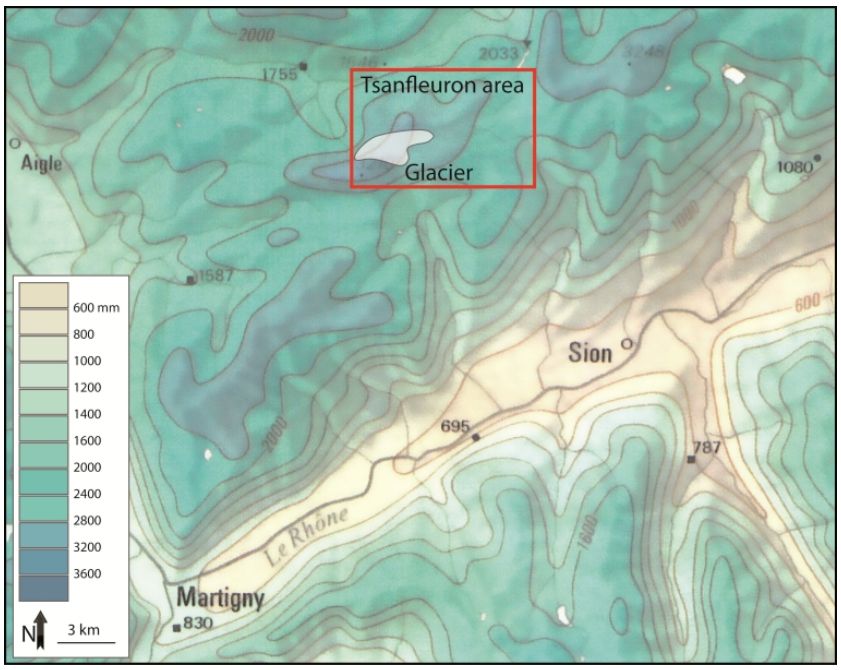

Figure 1.5: Map of annual precipitations in the region of Tsanfleuron area. This map shows that rain gauges in the experimental site suffer from rain loss, minimizing the calculated volume of recharge water (data from the Hydrologic atlas of Switzerland; 2003).

The hydrological regime of the study area is mainly controlled by snow and glacier melt. To characterize the surface and ground water dynamics, it was necessary to separate the annual precipitation in three typical seasons. The snow cover season, between mid October and the end of February, when the glacier has mainly stopped melting and the whole area is covered by 1 to 3 meters of snow. Precipitation occur in the form of snowfall with some rain events. From March to the end of June (snow melt season), snow melts and a large part of the melt water diffusely infiltrates the karst aquifer directly under the snow cover, but the glacier does not yet begin to melt. All surface streams and swallow holes are covered by snow with reduced activities. The system is in stand-by and the recharge of the aquifer is supposed to be minimal. Snowmelt may therefore occur occasionally and creates some observed discharge signals at the springs. These are witnesses of activities under the snow cover. In July, the snow front reaches to the glacier front, and the ice melts. In some years (2003 to 2005 and 2007 to 2009) the entire glacier surface loses its snow cover before the end of September. In mid October the glacier is free of snow and melts. Precipitation only occur as rain and snowfall events are considered to melt very fast. This is the ice melt season (Fig. 1.6).

During the snow melt season, streams and swallow holes contribute to evacuate the meltwater.

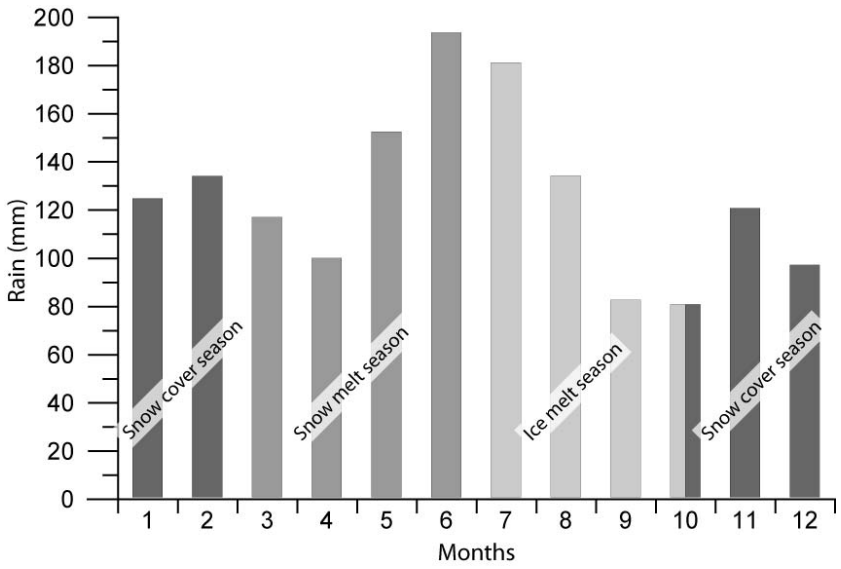

Figure 1.6: Mean precipitation per month at the top of the Tsanfleuron glacier (2966m) between 2005 and 2009. No distinction is made between snow and liquid at this station. Three characteristic seasons are illustrated: Snow cover season, where ice and snow melt are minimal; Snow melt season, where glacier has not started to melt; Ice melt season, where glacier has a high melt rate.

The recharge of the aquifer is maximum during three months. The major part of these structures are only active during this period and during high precipitation events in the ice melt season.

Diffuse infiltration of rain and snowmelt occurs regularly on the whole surface of the karrenfield in summer season.

1.4.4 Streams

The glacier is the main recharge of the aquifer during the dry periods of the ice melt season. It creates small sinking streams beside the glacier front (after 20 to 30 meters on the limestone's surface) and a more important main glacial stream Lachon, which may cross moraines and a large part of the karrenfield, depending on water level conditions. At high water levels, for example during important storm events or snow melt, Lachon stream completely crosses the karrenfield, reaching the main outflow in the Morge valley with minimal underground pathways. During low water conditions, Lachon stream is directly dependant on its discharge. The more discharge, the longer Lachon stream flows on the karrenfield before sinking into the aquifer. One swallow hole zone is important enough (see "main swallow hole" on fig. 1.7) to keep infiltrating the stream during daily discharge increases, but when discharge reaches 120 L/s, Lachon stream continues to flow in its stream bed (appendix A.6). Many small allogenic streams also infiltrate the karst in the Eastern part of the studied area.

1.4.5 Springs

Many springs were observed around the test site, but only five are important enough to drain the Tsanfleuron karst aquifer system. They are distributed on a half-circle around the karst geological border from the Northeast to the South of the karrenfield (Fig. 1.7). Spring characterisations for tracer tests will be developed in chapter 3. Here localization and a brief description is given. When available, chemical and physical parameters are also developed.

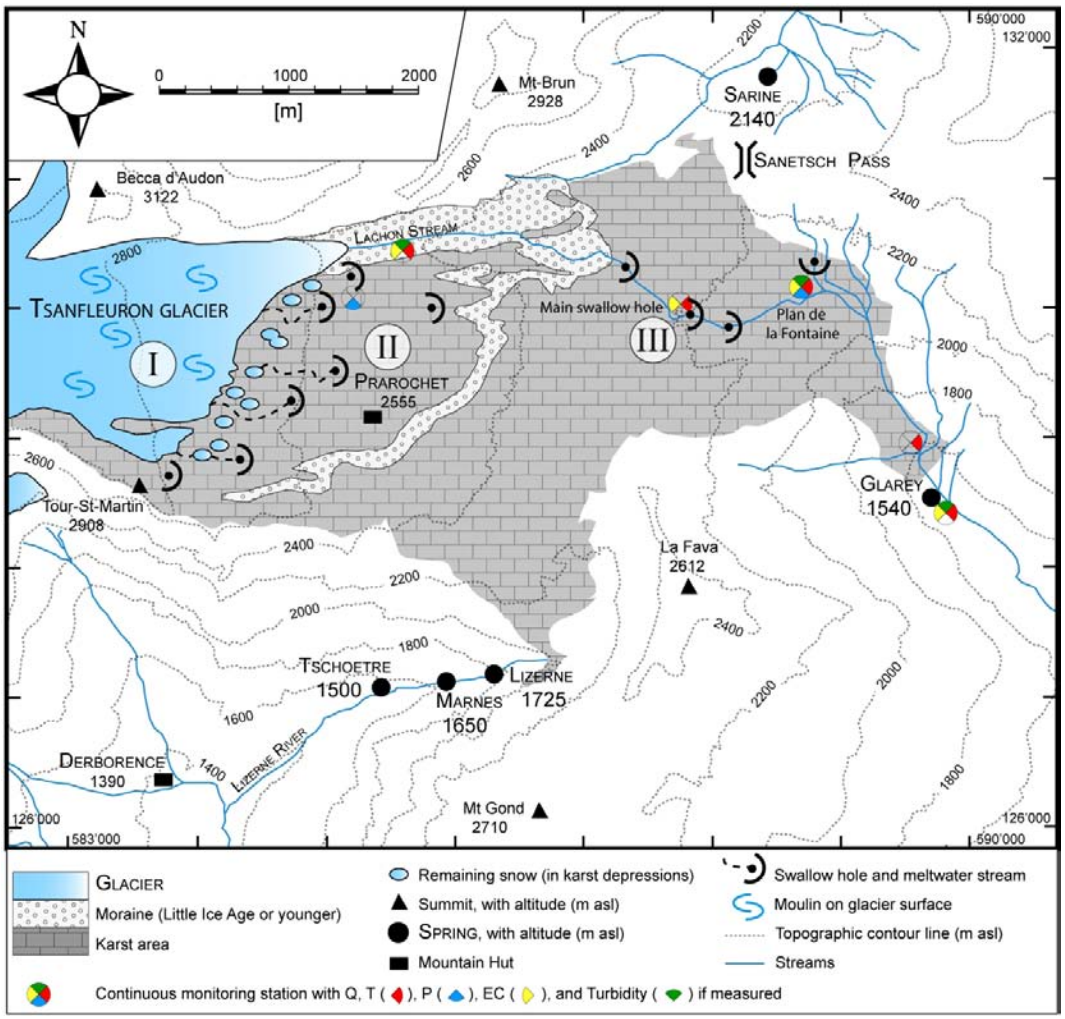

Figure 1.7: Generalised map of the Tsanfleuron area, showing the glacier and its moulins, the different recharge processes, the surface streams, swallow holes, springs and measuring stations. Roman numbers indicate the geomorphologic and recharge zones: I limestone covered by glacier, II polished limestone recently exposed by retreating glacier, III typical alpine karrenfield, below the end moraine of 1855/1860. For measuring stations, red quarter-circles indicate discharge and water temperature instruments, blue is for precipitation and air temperature, yellow for electrical conductivity and green for turbidity.

- The northern Sarine spring is also at the highest elevation (2135 m). The swiss coordinates are [588400;131900], which localize it under the Sanetsch pass in the Berriasian marls below the limit between the Mont-Gond and Diablerets nappes. The Sarine spring discharge is high and stable (annual mean value is about 186 L/s), electrical conductivity and temperature are also seasonnaly stable around 200 $\mu S/cm$ and 2.9 ℃ respectively. Such low electrical conductivity and temperature are witnesses of glacier or snow contribution to this spring. Water is therefore stored in surrounding marl aquicludes as no daily variations are visible.

- The Glarey spring (1553 m) is located at the coordinates of [589650;128650] and is composed of two components. The first one is used as a drinking water resource for the community of

Figure 1.8: Sarine spring that flows out in the berriasian marls in the north east of the karrenfield surface.

Conthey and represents about 10% of the total available outflow (Fig. 1.9(a)). The water is directly captured from the Urgonian-Eocene karst aquifer through a 30 m long artificial drainage gallery. The second is an important overflow 15 meters above, which is only active from May to the end of October (Fig. 1.9(b)).

(a) Structure that drains about 10% of total spring discharge, where the community of Conthey collects fresh water.

(b) Overflow under allochtone stream falls.

Figure 1.9: outflows at Glarey spring.

- The Tschoetre spring (1500 m) is on the south border of the karrenfield, in the Lizerne valley [585375;12775]. It is only active during the spring and summer seasons and flows out at the interface between Malm limestone and Dogger clay 20 meters up from the stream bed.

Figure 1.10: Tschoetre spring with the Lizerne stream below.

- The Marnes spring is also in the Lizerne valley, but outflows 150 m higher than Tschoetre directly in the Lizerne stream. Its coordinates are [586070;127150] for an elevation of 1650 m. It is localized at the same geological limit as the Tschoetre spring, but directly in the Lizerne stream bed.
- The Lizerne spring represents a large part of the Lizerne stream's discharge, at an altitude of 1725 meters and coordinates of [586355;127195].

Chapter 2

Basic concepts and first measurements: a brief overview of test site characteristics

2.1 Introduction

This chapter introduces basic concepts of methods that were used during this work. Subchapters contain general descriptions and explanations for each methodology, sometimes with a theoretical basis to provide an overview of the applications and limitations of each experiment. When necessary, uncertainities, difficulties or errors are mentioned for each method. The chapter will follow this structure:

- Chemical and physical parameters measured in the groundwater are described, with each instrument, its uncertainty and application in the field.
- Description of tracer experiments, their important concepts and parameters and how to apply and analyse tracer experiments in karst areas.
- Alpine glacier dynamics and hydrology are then described, equilibrium processes between snow, ice and water, illustrations of internal drainage structures and an explanation of the ice-water physical processes.
- Radio Magneto Telluric (RMT) principle is developed, how the instrument works, where they are usually used, finishing by some words about investigation depths and contrasts between layers.
- Finally the stable isotope section will present the importance of these natural tracers in alpine catchments, how they are sampled and analysed depending on the water phases and how isotopic ratios are used.

If necessary, some primary field data are exposed in order to introduce characteristics and general parameters of the studied area.

2.2 Chemical and physical parameters

2.2.1 Generalities

To characterize the karst aquifer and in order to correlate physical data with tracer and isotope methods, many physical water parameters were measured (Tab. 2.1). Discharge, electrical conductivity, water temperature, pH and turbidity were monitored continuously (with a time step of 30 min) at Glarey spring from July 2007 till July 2010 and in the Lachon up- and down-stream of the main swallow hole during the warm seasons of 2007 to 2009. Discharge is one of the most useful parameters, as it helps to calculate recovery rates in tracer tests but also to estimate water balance, or hydrograph separation through stable isotopes. Electrical conductivity indicates where water comes from, if it is glacier melt water or aquifer base flow. Temperature may also be used as natural tracer, or help to identify precipitation signals in springs or streams. Precipitations were measured by our own rain gauge station in summer, but annual values are provided by MeteoSwiss. Samples were also collected for chemical characterization of waters. The analyzed ions included K^+, Na^+, Mg^{2+}, Ca^{2+}, HCO_3^-, Cl^-, NO_3^- and SO_4^{2-}. All these parameters are not the main topic of this study, but the foundation of the other methods.

2.2.2 Precipitation

The recharge processes are very important to understand the system. Measuring liquid and solid precipitations is an important input variable of the karst aquifer. Two rain gauges were installed near the glacier front (alt. 2580 m) and at the 'Plan de la Fontaine' alluvial plain (alt. 2120 m) during summers of 2007, 2008 and 2009 (Fig. 1.7). They measured the precipitation sum every 30 minutes. In case of snow or if the temperature is below zero, the time precision of the rain gauge decreases, because snow has to melt before being measured, and water can be stored as ice in the rain accumulator. Known uncertainties for such instruments come mainly from wind exposure (De Jong

Table 2.1: Overview of the monitoring program of continuously (with a time step of 30 min) measured parameters. Discharge (Q), electrical conductivity (EC), temperature (T), total organic carbon (TOC), turbidity (Turb) and precipitations (P) were monitored. For localization of each station, see fig 1.7.

Observation point	Q	EC	T	TOC	$Turb$	P
Glarey community spring	X	X	X	X	X	
Glarey overflow	X		X			
Plan de la Fontaine	X	X	X		X	X
Main swallow hole	X	X	X			
Glacier stream	X	X	X		X	
Glacier front						X

et al., 2002; Rubel et al., 2000; Curtis and Burnash, 1996).

This instrument is made of a 0.24 m diameter metal funnel, which drains water in two buckets of 10 mL balancing on a spindle . Every time one of these bucket is full, the weight of accumulated water empties it, gives an electrical signal to a data taker and places the second bucket in a position to be filled. A simple relation (equ. 2.1) gives precipitations P.

$$P = \frac{B \cdot V}{(\frac{\phi}{2})^2 \cdot \pi} \tag{2.1}$$

where

P : Liquid precipitation (m)
B : Bucket balance counter $(-)$
V : Bucket volume (m^3) $(10\ mL = 10^{-5}\ m^3)$
ϕ : Funnel diameter (m)

Two types of MeteoSwiss stations were used. Daily (and even hourly till end 2007) rainfall data were provided by the station located at the top of Tsanfleuron glacier (station 856; swiss coordinates [581920;130630]) at an altitude of 2966 m. Four annual stations located around the test site gave precipitations for water balance calculations: OldenAlp station at an altitude of 1840 m (station 742, swiss coordinates [585440;133410]), SanetschAlp station located at an altitude of 2043 m (station 110, swiss coordinates [589067;134759]), Sex Rouge station at 2820 m (station 519, swiss coordinates [582250;130675]) and The Cabane des Diablerets station at 2485 m (station 267, swiss coordinates [582750;131910]). Each station provided annual rainfalls between 2003 and 2008.

2.2.3 Discharge

Discharge measurements are as important as the recharge processes, because they show the output of the studied system. Continuous measurements require pressure probes, which measure the pressure of the water column above itself, corrected for atmospheric pressure variations. Occasional manual discharge measurements calibrate the relationship between water level (from pressure probe in mA or directly transformed in m), water on a limnimeter in meters and discharge in $^{L}/_{s}$. Details of calibration curves are available in appendix A.1 and A.2 for Glarey spring and its overflow.

Manual water discharge measurements were made with chemical dilution methods. A known mass M of tracer is injected upstream. Measurements of concentration C of the tracer are made some meters downstream (10 to 100 meters, depending how fast the tracer is mixed homogeneously in the water) during all the time t of the tracer plume. These measurements show a concentration in function of time interval dt. This relation is correct as far as the discharge stays constant during the experiment, and if the total mass of tracer flows through the gauging section. Halite (NaCl) was used here, but the methodology is the same with fluorescent dyes. Because water already has a natural salt equivalent concentration, a baseline has to be subtracted from the concentration signal

to only have the added concentration and not the natural and anthropic signal. The concentration is measured with a field electrical conductivity probe WTW 340i (WTW, Weilheim, Germany) in ($^{\mu S}/_{cm}$) with an uncertainty of 0.05%. Discharge was obtained by dividing the injected salt mass by the surface area under the time-concentration curve subtracted of baseline.The injected mass is conserved hypothetically and the discharge Q is then obtained through the relation 2.2:

$$Q = \frac{M}{\int C \cdot dt} \tag{2.2}$$

where

Q : Discharge ($^{m^3}/_s$)
M : Injected mass (Kg)
C : Measured concentration ($^{Kg}/_{m^3}$)
dt : Time (s)

This method was also used for the occasional measurements that were done on small glacial streams on the test site. Two pressure probes were also installed up- and down-stream the main Lachon swallow hole and calibration strictly follows the methodology described above. Lachon stream calibration curves are available in appendix A.4 and A.5.

At Glarey spring, discharge was continuously measured with a time step of 30 min between July 2007 and July 2010 with two pressure probes (Keller PR46/0.1/8935, Winterthur, Switzerland), one at the community well and the second at its overflow. A correlation between them was established during 2008, which allow to reconstruct previous and next year's discharges, where only community discharge was measured. The best fit for these data (Appendix A.3) was a linear correlation with a regression coefficient of 0.92. The relation between the two measured discharges is presented in equation 2.3

$$Q_{overflow} = 8.89 \cdot Q_{community} - 386.45 \tag{2.3}$$

The total discharge measured at Glarey spring varies from 35 $^{L}/_s$ to 2457 $^{L}/_s$. The uncertainty of the pressure probe method is estimated at about 3% for Glarey spring and 5% for its overflow. The accuracy of total Glarey outflow is then on the order of 10 %.

In Lachon stream, two pressure probes were installed (see fig. 1.7) during the summers of 2007 to 2009 above and below the main swallow hole in order to estimate the infiltration on this bedstream part. The upstream probe measured a maximum of 594 $^{L}/_s$, the minimum was 0 $^{L}/_s$. Downstream, discharges were discontinuous but represent more than 50 % of the upstream water volume (Appendix A.6). During the four summer months, about $4.76 \cdot 10^5$ m^3 arrive at the swallow hole and $2.93 \cdot 10^5$ m^3 are present downstream. Accuracy of discharge values are also about 10 %.

2.2.4 Temperature

Air temperature was measured at the rain gauge places with temperature probes with an incertainty of ±0.5 ℃. These probe measurements are sent to a DT50 datalogger (DataTaker, Rowville, Australia) every 30 minutes. The air temperature indicates whether water is frozen, and therefore if the glacier produces meltwater or stays frozen. Moreover it is also necessary to estimate ice melt components in water balance calculations. Water temperature at Glarey spring is measured through pressure and conductivity probes but also with the field fluorometer GGUN-FL30 at 5 to 15 minutes time intervals. The given uncertainty for the conductivity WTW 340i (WTW, Weilheim, Germany) and the pressure probe are ±0.5 ℃ and ±0.1 ℃ respectively.

Water temperature was continuously monitored at Glarey spring and varies between 3.5℃ during the snow and ice melt season and a stable 4.5℃ during the winter season. The difference may be explained by longer transit times in winter or by lower temperature recharges in summer (glacier or snow meltwater).

2.2.5 Electrical conductivity

Electrical conductivity gives information about residence times in the aquifer (the higher conductivity, the more water stays in the aquifer) and the type of aquifer crossed. Manual electrical conductivity is measured with a field conductivity probe WTW 340i (WTW, Weilheim, Germany) and values are automatically corrected to 25℃. It can measure from 0 $^{\mu S}/_{cm}$ to 500 $^{\mu S}/_{cm}$ with a relative uncertainty of 0.05%. An integrated datalogger allow to store 800 measurements. This instrument was also used for each discharge experiment. A modified WTW conductimeter was coupled with a DT50 datalogger at Glarey spring. A GGUN-FL30 flow-through field fluorometer (University of Neuchatel (Fischer et al., 1987)) continuously measures electrical conductivity with a time step of 5 to 15 minutes. No continuous electrical conductivity measurements were done at its overflow, but many comparisons with chemical analyses and manual conductivity measurements prove that the same water flows at the two locations. Electrical conductivity was also measured in the Lachon stream during winter 2009-2010 in order to characterize the Lachon flow under the snow cover. For this experiment, a modified WTW340i conductimeter coupled to a DT50 datalogger was used.

Electrical conductivity at Glarey spring presents a range between 83 $^{\mu S}/_{cm}$ and 185 $^{\mu S}/_{cm}$ in summer and reaches 420 $^{\mu S}/_{cm}$ in winter. Lachon stream (only measured during the ice melt seasons) has a daily electrical conductivity between 89 $^{\mu S}/_{cm}$ and 116 $^{\mu S}/_{cm}$ if no rain events occur, otherwise it increases to more than 150 $^{\mu S}/_{cm}$. Glacier and snow meltwaters present very low conductivities between 5 and 15 $^{\mu S}/_{cm}$, depending on the transit time before sampling.

2.2.6 Turbidity and particles

Turbidity is a measure of the degree to which water disperses light due to the presence of suspended particles. This parameter is important for water quality, as karst aquifers are often used as drinking water resources. On this site, turbidity variations should help to understand karst aquifer dynamics through primary, secondary or glacial turbidity signals after a precipitation event (Pronk et al., 2006). Primary or autochthonous turbidity is stored inside the aquifer and remobilized during flood

events. Secondary or allochthonous turbidity comes from the surface of the aquifer and is transported through recharge water. The presence of Tsanfleuron glacier adds glacial turbidity that is directly dependent on glacier movements and melt. Does this turbidity belongs to the autochthonous or allochthonous signal? The fact that the glacier is not directly coupled to the aquifer suggests that glacial turbidity should be considered as secondary turbidity, but developments in chapter 6 nuance this first hypothesis.

Measured values at Glarey spring vary from less than 1 NTU to 90 NTU during snowmelt or rain events. In the Lachon stream turbidity ranges from 3 NTU to 28 NTU during summer dry periods and reaches 36 NTU during rainfalls.

Field fluorometers were used to continuously measure turbidity signals (Time steps from 5 to 15 minutes) at the main spring, and in surface streams. They measured a signal from 0.02 to 100 NTU (Nephelometric Turbidity Units). A light beam sent in water will be scattered at 90 ° by all the small particles present. If a lot of particles are present in water, the detector of scattered light receives more intensity than if only few particles are present. The turbidity sensors of the fluorometer were annually calibrated with standards of formazine (ISO 7027) of 0, 1, 10 and 100 NTU.

Turbidity probes WQ750 and WQ710 (Global Water, Gold River, California, United States) coupled with a DT50 datalogger also measured the turbidity values at the Glarey spring and Lachon stream. These probes have a range from 0 to 50 NTU and were also annually calibrated with formazine standards of 0, 1, 5, 10, 25 and 50 NTU. For both instruments, the accuracy is on the order of 10%.

A particle size distribution (PSD) instrument was also available to characterize the repartition of the particles (in a range between 0.9 to 135 μm) in the turbidity signal. The main use of this instrument was to characterize the number and size of the particles that are within the turbidity signal. This device sends a laserbeam through a water volume. Particles crossing the measuring cell attenuate the laser beam intensity (Appendix A.7). This attenuation is then measured and transformed into a volt signal characterizing particles diameters (Ramu, 2010). The maximum number of particles measured per volume sampled is $1.5 \cdot 10^6$ particles per 10 mL. The accuracy of this instrument directly depends on the total amount of particles and their distributions. Below $1.5 \cdot 10^6$ particles per 10 mL, uncertainties are low but above this limit, particles are not more precisely distinguished and particles which are too close together are measured as one bigger one, therefore error sharply increases. Particle numbers at Glarey spring often exceed the accuracy limit of $1.5 \cdot 10^6$ particles per 10 mL and in Lachon stream always exceed this limit. Therefore very few usable data were collected.

2.2.7 Total Organic Carbon

Total organic carbon (TOC) was monitored by the UV LED of field fluorometer GGUN-FL30 at Glarey spring. Fluorescence properties of organic matter have often been investigated (MacCraith et al., 1993; Savoy, 2007; Baker, 2001; Batiot, 2002; Senesi et al., 1991; Pronk, 2008) and reveal that TOC is characterized by a fluorescence emission close to Tinopal, Naphtionate tracer excitation/emission wavelengths. Therefore the UV LED for these dyes in the fluorometer is able to excitate TOC with a 365 nm wavelength and a photodiode detects the 420 to 550 nm wavelengths emitted. The calibration (see appendix A.8) of the field fluorometer was done with manual samples

analyzed in a spectrofluorimeter (LS 50 B, Perkin-Elmer, Waltham, USA). The maximum fluorescence intensities were determined by synchronous excitation/emission scans between wavelengths of 350 and 500 nm with a 0.5 nm steps. Measurements at Glarey spring were confined between 0.1 and 6.1 mg/L. The accuracy of this method is about 10%.

2.2.8 pH

pH was continuously monitored at Glarey spring by a Global Water pH probe WQ201 (Gold River, California, USA) connected to a DT50 datalogger. It was regularly checked by a reference pH probe (Hach HQ40d multi, Dusseldorf, Germany) and calibrated with standard solutions at pH 4, 7 and 10. Measured variations stay in a range of 7.6 (summer) and 8.5 (winter). Accuracy of the pH probe is 0.3.

2.2.9 Chemical sampling

Samples were collected in 500 mL plastic bottles in parallel with tracers or isotope sampling campaigns. They were transported in cool boxes and filtered through 0.45 µm pore size membranes (ME25 mixed cellulose Ester Circles, Whatman, Maidstone, United Kingdoms) before being analyzed in the CHYN laboratory. Anion vials were directly analyzed, but the acid HNO_3 suprapur was added to cation vials to preserve them (pH<2). Major ions were measured through a ionic chromatography instrument (IC DX-120, Dionex, Sunnyvale, United States) for the following cations: Sodium (Na^+) Ammonium (NH_4^+), Potassium (K^+), Magnesium (Mg^{2+}) and Calcium (Ca^{2+}), and anions: Chloride (Cl^-), Nitrate (NO_3^-), Sulfate (SO_4^{2-}). The Bicarbonate anion (HCO_3^-) was measured within 6 hours with HCl 0.1M to a pH of 4.3. Uncertainties are 10 mg/L for Bicarbonates and 0.5 mg/L for ions analyzed by Ionic Chromatography. When the ionic balance had an error below 5 %, the analysis was considered as correct. All measured concentrations can be transformed (equ. 2.4) from mg/L to meq.

Glarey spring water mainly contains Bicarbonate, Sulfates, Magnesium, Sodium and Calcium ions. Minimum and maximum observed concentrations for these five principal elements are presented in table 2.2 (general and detailed chemical tables are also available in appendix A.9).

$$C_{meq} = \frac{C \cdot \chi}{M_m} \tag{2.4}$$

where

C	:	Concentration ($^{mg}/_{L}$)
χ	:	Ionic charge ($-$)
M_m	:	Molecular mass ($^{g}/_{mol}$)

The HCO_3^- and Ca^{2+} ions vary together, with a correlation factor of 0.99 indicating that water mainly flows through calcite minerals in limestone layers. Detritic zones with many impurities containing magnesium-sulfate minerals are most probably in contact with water because a linear relation

Table 2.2: Calcium, Magnesium, Sodium, Sulfate and Bicarbonate concentrations in Glarey spring water (based on 92 samples analysis). Winter values are a mean of measurements taken from December to March. Summer concentrations reflect the extreme variations due to glacier melt between July and mid October.

	Winter (mg/L)	Summer (mg/L)
Calcium	58.9	17.8 to 49.5
Magnesium	6.9	0.9 to 5.1
Sodium	4.1	0.4 to 4.1
Sulfate	33.2	2.5 to 21.9
Bicarbonate	171.4	57.8 to 155.5
Electrical conductivity	420 ($^{\mu S}/_{cm}$)	83 to 185 ($^{\mu S}/_{cm}$)

between Mg^{2+} and SO_4^{2-} is clearly established (correlation at 0.98) in appendix A.11. By correlating Mg^{2+} and Ca^{2+} respectively by HCO_3^- and SO_4^{2-}, a seasonal influence on ion concentrations is illustrated. Samples taken during winter and snowmelt season present a rapid decrease in sulfate and magnesium and reach August's samples. August and September's values have a cloudy repartition, but some of these concentrations already belong to the well defined linear correlation of the October's samples. Therefore the ion concentrations at Glarey spring follow an annual hysteresis between winter values, where water certainly stays longer inside the aquifer, and summer seasons with lower water's residence time (see also appendix A.11 for Ca^{2+}-SO_4^{2-} and Mg^{2+}-HCO_3^- correlations, where higher ionic concentrations decrease between January and June before increasing again at the end of summer season).

2.3 Tracer tests

2.3.1 Tracer generalities

In karst aquifers, tracer tests are often used to obtain a regional knowledge of the groundwater paths, to elaborate conceptual models of karst aquifer systems and to draw limits of spring catchment areas (Kass, 1998). To schedule a tracer test experiment, it is important to characterize the geological, hydrogeological and hydrological structure of the area, sampling and injection points, depending of the aim of the experiment. Then an evaluation of transit times between chosen injection and sampling points is necessary to fix the duration of the sampling. Preliminary or previous tracer test experiments can give information on mean transit times, but it is important in karst aquifers to keep in mind that hydrological conditions can dramatically affect transit times.

A good tracer has to be representative of the water movement and close to the water properties (Schudel et al., 2002). Chemical stability, lowest adsorption and good solubility in water are three important necessary properties. Some practical ones are also relevant, like a very low detection limit, low cost and also cheap analysis of the tracer, little or no polluted charge for environment, and no toxicity for humans, animals and plants. But an ideal tracer, which has all these properties does not exist. Therefore it is important to adjust the quantities and injection conditions to studied cases.

There are three relevant types of tracers. Fluorescent tracers are easily detectable at low concentrations, and are not naturally present in the environment, they often colour water. Salts have higher detection limits and may exist naturally in the environment. They are usually used if water colouration is not acceptable and in shorter distances between injection and sampling points. Artificial particles are mainly used to study transport of pathogens. Here is a list of the fluorescent tracers used in this work, with their general properties and detection limits:

- Uranine is one of the best fluorescent tracers. It has a low detection point of $5 \cdot 10^{-3}\ {}^{\mu g}/_{L}$ but degrades very quickly under the sunlight and is sensible to pH variations.
- Sulforhodamine B and G have a $10^{-2}\ {}^{\mu g}/_{L}$ detection limit and are not influenced by pH variations or sunlight but have a high adsorption. Sulforhodamine B is also ecotoxic and not advisable for surface tracer tests (Behrens et al., 2001). These two tracers belong to the rhodamine dyes family but are not toxic for humans instead of Rhodamine B and WT that are no more used in hydrogeology.
- Naphtionate and Tinopal have a detection limit of $10^{-1}\ {}^{\mu g}/_{L}$ but may easily be confused with organic matter signals. Tinopal is also easily adsorbed.

Halite (NaCl or sodium chloride) is one of the most used salt type tracers. It necessitates very high injection concentrations (10^4 more than uranine) because high background concentrations may often occur in natural environments. This tracer was mainly use for discharge measurements in order to calibrate the pressure probes in the field. Potassium iodate (KI) may be unstable in presence of organic matter and also needs high concentrations to be detected. Lithium chloride is also a good tracer for short distances, because lithium is not an element which is naturally abundant in the environment. These two salts were not used.

Multiple tracer tests consist of the simultaneous injection of at least two tracers, as opposed to single tracer tests which only use one tracer. Uranine, Sulforhodamine B and Naphtionate for example are ideal for multi-tracer tests because they have different excitation wavelengths during analysis. A multi-tracer test with Sulforhodamine B and G, which have similar properties, does not allow a differentiation between the two tracers, and thus between the injection points.

In general, the recommanded quantity of tracer injected for each experiment (Schudel et al., 2002) is given by the simple relation 2.5 (Kass, 1998; Wernli, 1994) .

$$M_i = \alpha_t \cdot L \cdot A \tag{2.5}$$

where

M_i	:	Injected mass (g)
α_t	:	Dye correction factor $({}^{g}/_{m})$
L	:	Distance between injection and sampling points (m)
A	:	Aquifer type dependent parameter $(-)$

For karst aquifers A (equ. 2.6) is related to the discharge Q in ${}^{m^3}/_{s}$ through the relation 2.6.

$$A = 10 \cdot (\frac{Q}{100}) \cdot 0.93 \tag{2.6}$$

The correction factor α_t for uranine is 1; 2 and 4 for Sulforhodamine G and B respectively and 15 for tinopal (Schudel et al., 2002). For the other fluorescent tracers that were not used in this work, this factor may be found in the reference provided.

In the Tsanfleuron area, the quantities were first calculated using equation 2.6, but then modified with existent knowledge coming from previous tracer experiments (Masotti 1989 and 1991). Uranine quantity varies from 200 g for the smaller distances to 1000 g for the injection at the top of the glacier. Suflorhodamine B and G injection mass goes from 450 g to 1000 g. 2000 g of Naphtionate and Tinopal were injected due to higher detection limits and organic matter proximity.

2.3.2 Sampling, analyses and interpretations

Sampling a tracer test experiment needs to follow a strict modus operandi to avoid further interpretation problems. Before the experiment, it is indispensable to take blank samples at each sampling point to characterize the chemical signal of the water, its organic matter content, and if there are no resident dye concentrations from a previous tracer experiment. Then the sampling time step needs to be chosen depending on the knowledge of transit times and the distance between injections and sampling points. It is important to set up the time step to identify the first occurrence of the tracer, the maximum concentration and the tailing of the breakthrough curve. The sampling duration should also be long enough to see possible secondary concentration peaks (Schudel et al., 2002).

This next paragraph focuses on fluorescent dyes, as salt tracers are often easily analysed through field conductimeters or ionic chromatography in laboratories. Fluorescent dyes are organic molecules with the property of emitting a new photon when absorbing a photon with a precise wavelength, instead of only creating heat. The absorption of a photon gives energy to the molecule and it enters in an excited state. This pushes an electron to a state of higher energy (a higher orbital). When it relaxes to the equilibrium state (fundamental state), the molecule sends an emitted photon, which is in a lower energy state than the initial absorbed photon (Fig. 2.1). The lower energy induces a difference between absorbed and emitted wavelenghts, which is a specific parameter for each tracer. This property is known as Stokes shift (Hecht, 1999). In natural water there is no fluorescence in the visible wavelength (between 350 to 800 nm), which creates very good conditions to analyse the tracers.

The instrument used to analyse fluorescence is a laboratory spectrofluorimeter or a field fluorimeter. The detection limits of the spectrofluorimeter is lower by a factor 10 than those of the field spectrofluorimeter. Both instruments measure the emitted photons (Fig. 2.2) after excitation by an initial wavelength. The spectrofluorimeter only measures one tracer per sample. A 10 mL vial is filled with water and undergoes the usual wavelength range for the analyzed tracer. Results are shown in a graph between wavelength and fluorescence intensity in mV. A calibration for each dye transforms light intensities to concentrations. The field fluorimeter measures three tracers at a time inside a 10 mL transparent tube and also provides fluorescent intensity values in mV. Concentrations are directly calculated through stored calibration files inside the datalogger.

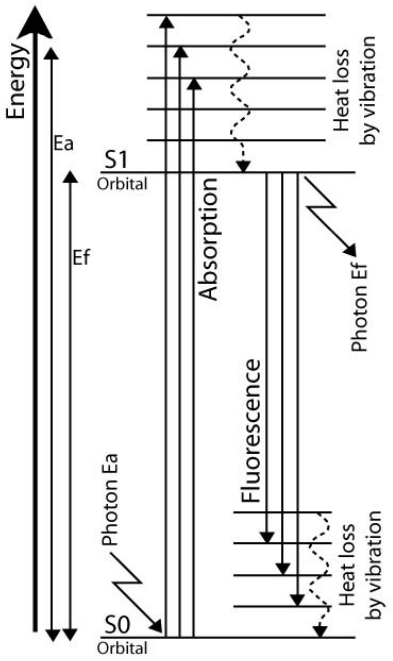

Figure 2.1: Schematic reaction inside the fluorescent tracer molecule by absorption of a photon, which sends an electron of the molecule from orbital (energy state) S0 to S1 or more depending on the wavelength of the initial photon. If more, the electron loses by vibration (by heating) the extra part of its energy to arrive at the orbital S1. When coming back to its initial energy S0, the electron emits a new photon of lower energy and longer wavelength.

Tracer test experiments give multiple information, that are based on the breakthrough curve drawing. The recovery mass M_r (equ. 2.7) is the tracer quantity measured at the sampling point during the experiment's duration. It is an important parameter to calculate and represents the quality of the connection between injection and sampling points. Discharge measurements are necessary for this calculation. The lower the time steps for discharge and concentration measurement, the more precise the recovery rate becomes. Mean estimated discharge may also be used if no instruments are available at the sampling point, but the recovery rate precision sharply decreases. Glarey spring, and the main Lachon swallow hole were instrumented with pressure probes partly for this purpose.

$$M_r = \int C \cdot Q \cdot dt \tag{2.7}$$

$$R = \frac{M_r}{M_i} \cdot 100 \tag{2.8}$$

where

C	:	Concentration at sampling point ($^g/_L$)
Q	:	Discharge at sampling point ($^L/_s$)
t	:	Sampling duration (s)
M_i	:	Injected mass (g)
M_r	:	Recovery mass (g)
R	:	Recovery rate (%)

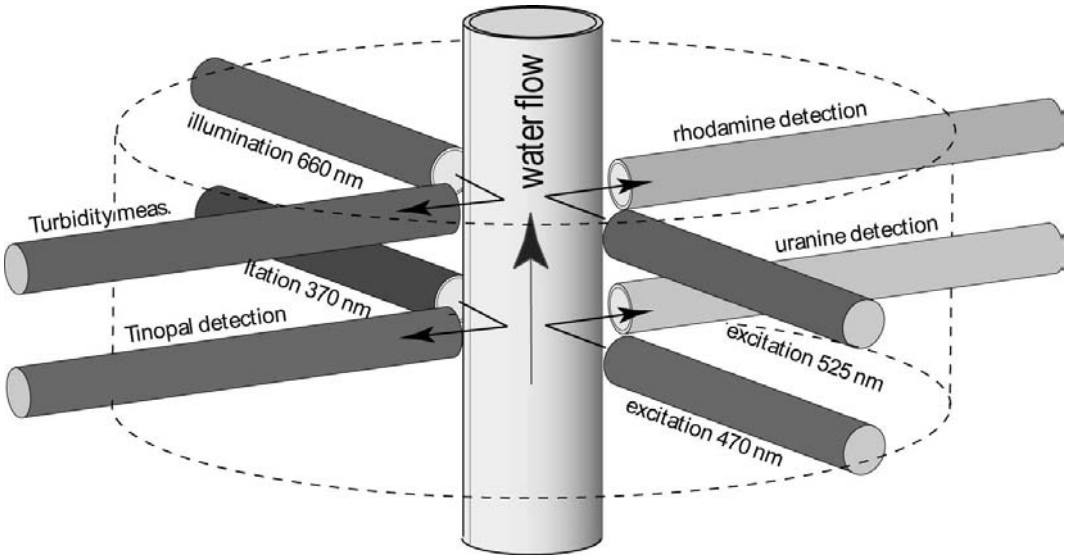

Figure 2.2: Disposition of the light emitters and associated detectors in a field fluorimeter. Each emitter is for one tracer (Uranine, Sulforhodamine and tinopal group of tracers). The water flows in the central tube (Fischer et al., 1987). The fourth light is used for turbidity measurements, which direcly influence the tracer concentration analyses. A laboratory spectrofluorimeter works identically, there is no water flow but a small vat filled with samples, and only one emitter, which analyses a single tracer at a time.

The normalized concentration ${}^{c}/_{M}$ (equ. 2.9) is the ratio of measured concentration by the mass injected. Such a notation helps to compare tracer tests with different injection masses and immediately gives the recovery rate in percent by replacing C in $({}^{g}/_{L})$ by ${}^{c}/_{M}$ $({}^{1}/_{m^3})$. Many results will be presented in this format in the next sections.

$$ {}^{c}/_{M} = \frac{C \cdot 10^{-3}}{M_i} \tag{2.9} $$

The linear maximum flow velocity v_{max} $({}^{m}/_{s})$ is the distance D between the injection and sampling point, divided by the first arrival time t_f. The dominant flow velocity v_p $({}^{m}/_{s})$ is the distance D divided by the first peak time t_p. The median flow velocity vmedian is distance D divided by median transit time. These transit times are illustrated on fig. 2.3.

$$ v_{max} = \frac{D}{t_f} \tag{2.10} $$

$$ v_{peak} = \frac{D}{t_p} \tag{2.11} $$

$$ v_{median} = \frac{D}{t_m} \tag{2.12} $$

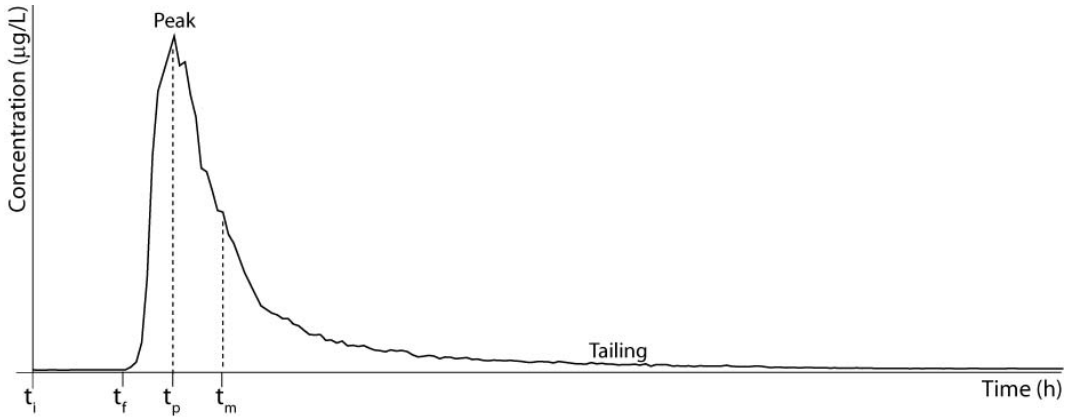

Figure 2.3: Example of a generic breakthrough curve with concentrations in $^{\mu g}/_{L}$. versus time in hours. First arrival time t_f, peak time t_p and median transit time t_m are represented.

2.4 Alpine glaciers, a small review

2.4.1 Generalities

Fresh water is mainly stored in ice, which accumulates in different and distinct environments on the planet. These ice volumes represent 24 millions of km^3 and about 56.5 % of the freshwater reserves on the planet (Benn, 1998). Its most important part is located in high latitudes zones, where temperatures are low, with icecaps on continents or ice-barriers on the sea, and cold glaciers in moutain ranges. Temperate alpine glaciers are only located in mountain ranges, where climatic conditions vary around 0 ℃, and represent an estimated volume of 140 km^3 (Jansson et al., 2003). They mainly developed in high elevation environments and are closely related to climate conditions. Most of them are inside valleys and modeled their morphologies through ice and meltwater flows. They are also the source of many important rivers around the world.

2.4.2 General dynamics of temperate glaciers

The dynamics of temperate alpine glaciers closely follow climate variations. A fragile balance between snow accumulation during cold seasons and snow or ice melt during warm seasons controls the glacier (Fig. 2.4). In the accumulation zone snowfall is higher than snowmelt volumes and a snow layer remains all year round. The ablation zone loses its snow cover and ice surfaces become exposed to melt. In many years, if the accumulated volume is higher than ablation, the glacier grows and its size increases, but if the ablated volume is higher than accumulation, the size and volume of ice decreases and the glacier retreats. The two components may be equal and an equilibrium state is reached: the glacier keeps its current size.

Therefore the state of the glacier always varies over time and parameters that drive the glacier balance are various (Munro, 2005). Snow and ice melt depend on the radiative energy from the atmosphere and sun (temperature) coupled with the albedo of the glacier and surrounding lands. Snow accumulation is highly variable depending on the glacier morphology and climate variations (precipitation). Glacier mass balance is a complex study, which contains many different measurable

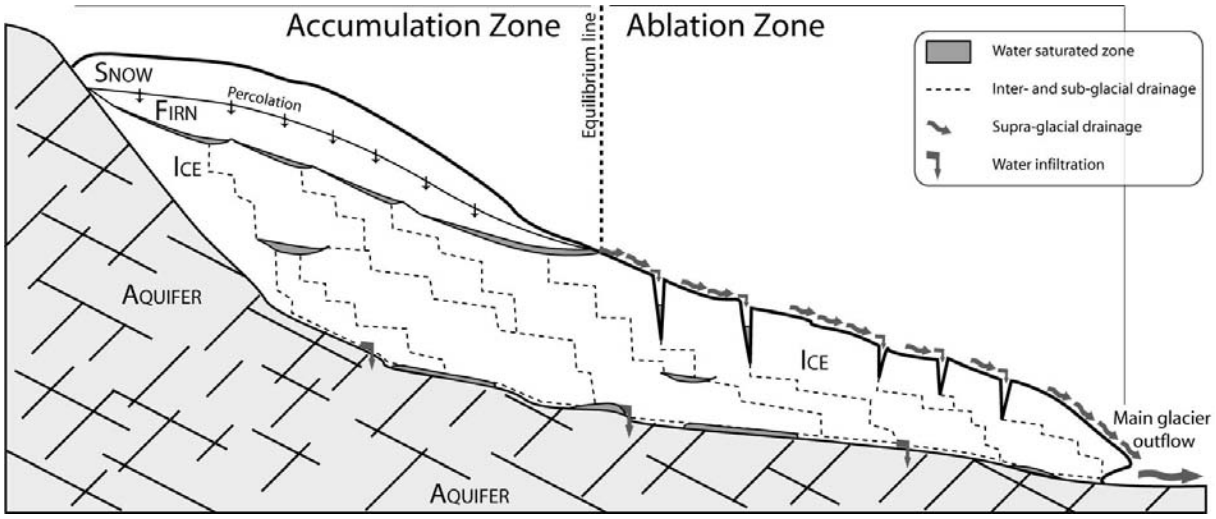

Figure 2.4: Schematic temperate alpine glacier in summer season that presents the accumulation (where snow remains) and ablation (where ice is directly visible) zones, separated by an equilibrium line (or snow limit). Hydrological processes inside the glacier (sub-, en- and super- glacial drainage, saturated layers) and snow (firn, meltwater percolation, saturated zones) are also illustrated. Accumulation of water at the interface between ice and firn drives the englacial network construction. Figure modified from literature (Grust, 2004)

parameters which are spatially heterogeneous.

In most temperate glaciers, meltwater comes mainly from the surface of the glacier (Gurnell and Clark, 1987) and needs to cross chronologically different layers before reaching the main glacier outflow. Depending if water comes from the accumulation zone or ablation zone, some of these layers may not be present. For example during the snow melt season in the ablation zone, melt water will not cross a firn layer. From top to glacier basement, layers are:

- the superficial and sometimes fresh snow layer, whose properties vary according to depth;
- an old and packed snow layer, which is an intermediate stage between snow and ice and is often called firn. This layer has already suffered from two or more melt seasons and contains metamorphized snow cristals;
- The ice layer, composed of many heterogeneous layers has globally a lower hydraulic conductivity than snow or firn if considering only the micro-porosity ;
- Finally the ice-rock interface at the basal limit of the glacier. It is a mix between rocks of various sizes, particles (glacial tills), ice and meltwater.

2.4.3 Glacier hydrology

Snow and ice can be considered as equivalent to porous and karst aquifers respectively but with major and important differences (Hock and Jansson, 2005). A classic porous aquifer is defined by its porosity, hydraulic conductivity and storage capacity. These parameters are fixed and do not

change over time. Moreover it is supplied in water by external recharge. On the contrary, "snow aquifers" are built by solid water and present a dynamic drainage system, which often changes over time (Grust, 2004). Porosity and hydraulic conductivity depend on melt and refreeze rates that are directly proportional to air temperature variations. "Ice aquifers" present an equivalent duality between conduits and matrix as karst systems, but the geometry of the cryokarst network changes every year. In addition, such aquifers are autosupplied in water by melt of the matrix itself. Therefore processes inside these "aquifers" are quite different from classic hydrogeological aquifers and their dynamics require more description. The next paragraphs develop for each solid water layer the corresponding hydrologic processes.

Superficial snow is often vertically heterogeneous, each strata has different properties depending on the climatic conditions during and after deposition. Density, hardness or water content of snow crystals highly differ inside the snow pack and investigations of meltwater hydrologic processes become more difficult. The heterogeneity may be illustrated as more dense snow or even ice layers that create contrasting horizons or preferential flux in the snow (Hock and Jansson, 2005). In the early melt season, these layers induce a lateral distribution of the meltwater in the direction of the glacier's slope. This process decreases during the melt season when snow layers melt, destroy these dense stratas and become globally thinner. The more the melt season advances, the more water transit times in the snow pack decrease and the more water dispersivity decreases by creating preferential pathways through the snow. Finally, at equilibrium, the snow pack contains two water flow systems. A fast one, which uses the preferential water pathways and another, slower, which percolates through the snow porosity.

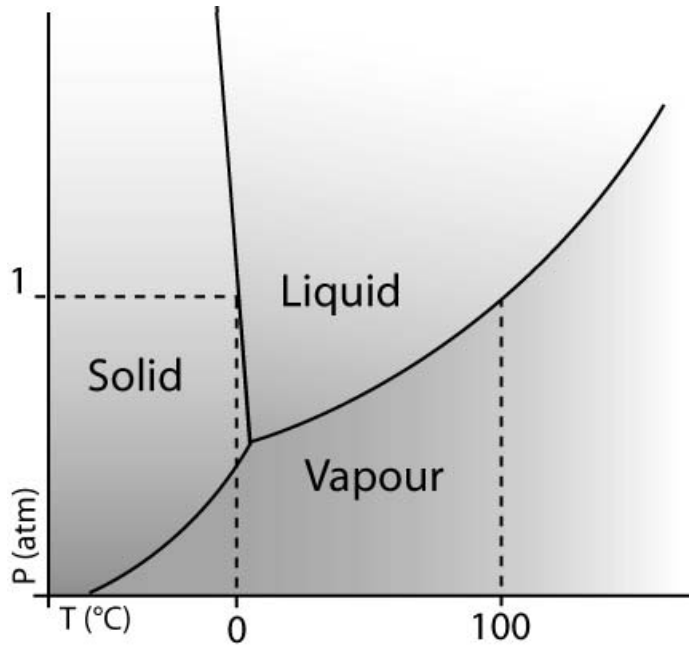

Figure 2.5: Simplified phases diagram for water. By slight pressure variations at 0 °C water is liquid or solid. This physical particularity is important in glacier dynamics (Benn, 1998)

In the firn, the dynamic is equivalent to the snow hydrologic processes, but the physical properties of the packed snow are different. The snow has already suffered from multiple freeze-melt cycles, and its crystallographic structure is close to ice. The density is higher, porosity and hydraulic conductivity

are lower than snow but higher than in ice. This permeability contrast may create saturated zones (Fig. 2.4) at the firn-snow interface (Grust, 2004).

The hydrologic processes of ice are controlled by the equilibrium between the creep pressure P_i of ice (equivalent to a very viscous liquid (Benn, 1998)) and meltwater pressure P_w (Fountain and Walder, 1998). From the water phases diagram (Fig. 2.5), the more pressure increases, the more the melt temperature of ice decreases. When enough water pressure is added to burrying pressure from the ice column, ice starts to melt. If meltwater accumulates in ice structures such as fractures, conduits or on the surface, $P_w > P_i$, the energy E_w from water is used to melt ice and creates new structures depending on ice rheology. The global temperature in the glacier is relatively higher. Conversely during the cold season, water quantities decrease, $P_w < P_i$ and water energy E_w is reduced (temperature in the glacier becomes relatively lower). Ice creeping closes the conduits and fractures that were created during warm season and remaining water cristallizes. If $P_w = P_i$, the equilibrium is reached and no new structures are opened or closed (Fig. 2.6).

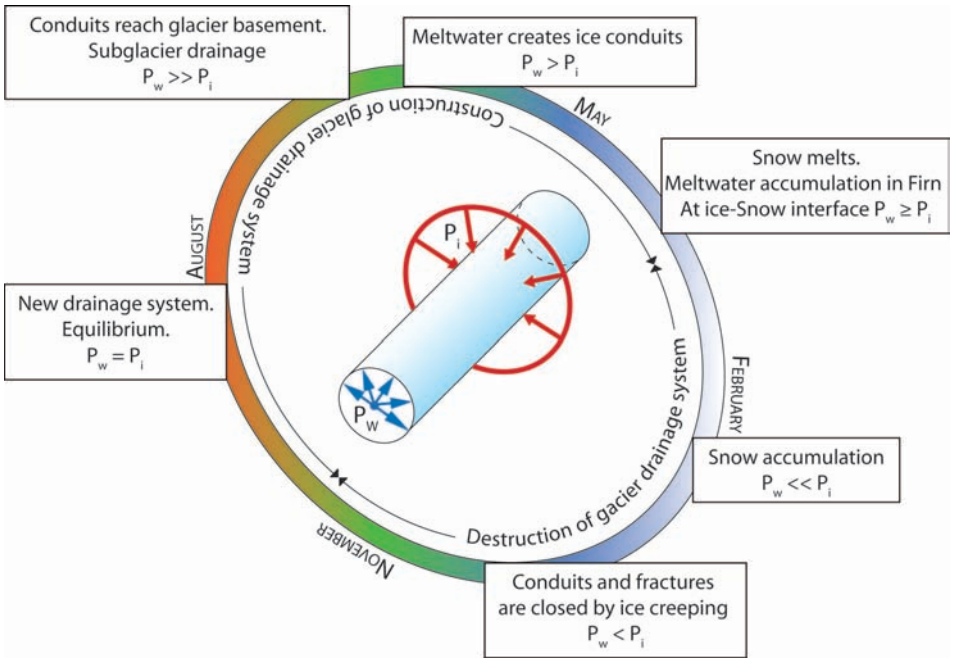

Figure 2.6: Creation and destruction of drainage system in a temperate alpine glacier during one year. P_w and P_i are water and creeping pressure from ice respectively.

When water is stored in the firn (accumulation zone) or in the surface structures (ablation zone), P_w increases and starts to erode the ice. This process creates an englacial drainage system (Rothlisberger channel) in the ice (Fig. 2.4) that sends meltwater to the ice-rock interface at the glacier's base. The internal structure of the glacier is then close to the model illustrated in Fig. 2.4, with sub-horizontal intra-glacial conduits coupled with vertical pathways, where fractures are present (Fountain et al., 2005). These conduits have a tree morphology from the rock basement to the surface (Fountain and Walder, 1998).

At the ice-rock interface, the accumulation of water creates a sub-glacial drainage (Nye or air channels), which drives water to the outflows of the glacier. Tree or random morphology drainage systems connect the existing basal cavities, which are generated by ice flow. Thus as the surface of the bedrock

is not linear, and presents many asperities, accomodation of the ice flux is made by the ice freeze-melt processes, creeping around rock obstacles or by cavity creation (Clark, 2005). The pressure on rocks upstream melts the ice and decreasing pressure downstream of the obstacle rapidly refreezes meltwater. This crystallization of water is more difficult if there are other meltwater influxes. The Nye channels are partially created in glacial tills, bedrock and ice (Grust, 2004). Tracer tests from literature (Fountain and Walder, 1998) show that tree systems have short transit times with low dispersivity, whereas random systems draw multi-peak breakthrough curves with longer transit times and higher dispersivity. A thin layer of water under the glacier helps to displace ice (considered as viscous liquid) from the accumulation zone to the ablation zone and the glacier snout. Two daily processes occur for ice creeping. During warm days, snow melts quickly and mixes with ice melt from the ablation zone. The accumulation of water increases the flow of the glacier, where a great quantity of water is present. On the contrary, during night when temperatures are lower, meltwater velocities and quantities decrease. The flow of the ice therefore decreases (Fountain and Walder, 1998).

With very low meltwater quantities, Nye channels are not present and only cavities remain, as they are not a creation of water and ice pressure equilibrium, but are created by glacier flow. At the beginning of the melt season, the drainage systems of alpine glaciers are therefore dominated by cavities (Fountain and Walder, 1998) and a more efficient drainage network is only created later in the season.

All these processes give a complex view on the hydrology and dynamics of alpine glaciers, and it is now possible to better understand the implications for water transfer to a karstic aquifer underlying a glacier.

2.5 Radio-magneto-telluric method

The RMT method is a rapid geophysical electromagnetic prospection method, which instrument is made of a magnetic coil that measures the magnetic field just over the soil surface, coupled with two electrodes separated by 5 meters (Fig. 2.7). The method uses the properties of Very Low Frequency (VLF) electromagnetic waves to measure the apparent resistivity of the underground. The energy sources are electromagnetic waves emitted by powerful radio transmitters at frequencies of 12-240 kHz. These stations are used in very long range communications and navigational systems.

Such waves are composed of a primary horizontal electrical field E_x and a magnetic field H_y. As soils and rocks are conductive, H_y creates an electrical current in the underground. This secondary electrical field E_s induces a second magnetic field H_s, which overlays the primary one. The measurement of the electrical field E_s and the resultant magnetic field $H_y + H_s$ delivers a value of apparent resistivity ρ_a and phase lag between H_y and $H_y + H_s$. The apparent resistivity is obtained by the equation 2.13.

$$\rho_a = \left(\frac{E_s}{H_y + H_s}\right)^2 \frac{1}{2\pi f \mu_0} \tag{2.13}$$

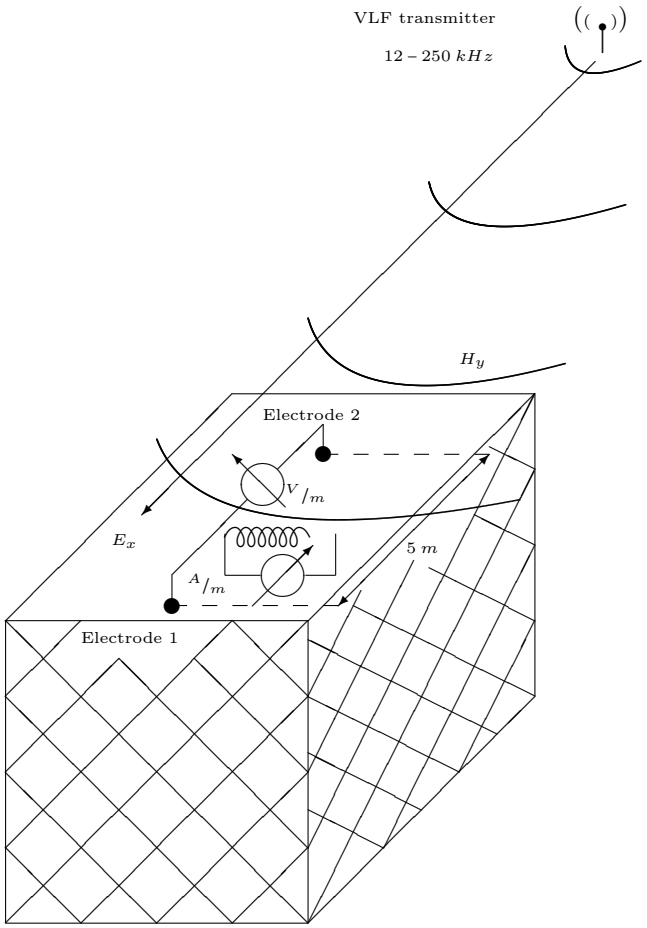

Figure 2.7: Illustration (designed by P.Falco, 2010) of the RMT methods & waves used (Thierrin, 1990)

where

H_y	:	Primary magnetic field $[^A/_m]$
E_s	:	Secondary electric field $[^V/_m]$
H_s	:	Secondary magnetic field $[^A/_m]$
μ_0	:	Magnetic permeability of vacuum = $4\pi 10^{-7}$ $[^{V\,s}/_{A\,m}]$
ρ_a	:	Apparent electrical resistivity $[\Omega\, m]$
f	:	Frequency $[Hz]$

Generally above the soil, E_x is orthogonal $(\frac{\pi}{2})$ to H_y. In a homogeneous soil, the lag between the two phases becomes $\frac{\pi}{4}$, due to interference with H_s. In a stratified soil, the phases determine if a more resistive layer is under (phase under $\frac{\pi}{4}$) or above (phase higher than $\frac{\pi}{4}$) the considered depth. The higher the frequency, the better the resolution but the shallower the investigation depth (Bechtel et al., 2007). The apparent resistivities ρ_a and phase lag values of each frequency can be inverted to produce a model of true resistivity versus depth below each measurement point (vertical sounding):

$$d \cong 503 \cdot \sqrt{\frac{\rho_a}{f}} \tag{2.14}$$

Where d is investigation depth or skin depth (m), ρ_a is resistivity (Ωm) and f is frequency (Hz). This method is generally often applied for hydrogeological prospection or contaminated sites in porous lithologies (Thierrin, 1990).

2.6 Stable isotopes

2.6.1 Isotope properties

Atoms are constituted of neutrons, protons and electrons. Neutrons are not charged, protons have a positive and electrons a negative charge. At equilibrium state, atoms are neutral with an equal number of protons and electrons. The nuclear mass A (Equ. 2.15) of an element is the sum of its protons and neutrons.

$$A = Z + N \tag{2.15}$$

Where Z and N are the quantity of protons and neutrons in the core of the atom. Each element X is then written as ${}^{A}X$. In the light elements of the periodic table of the elements (Mendeleïev table), the same quantities of protons and neutrons are present in order to stabilize the repulsive electric forces between each positively charged proton. For example, the core of a stable carbon atom is made of 6 protons, 6 neutrons and 6 electrons to have a neutral charge. The element carbon will be written ${}^{12}C$. For heavier elements in the periodic table, the number of neutrons often surpasses that of protons. ${}^{208}Pb$ for example only has 82 protons for 126 neutrons (AIEA, 2008; Hecht, 1999).

Stable or unstable isotopes are built on neutrons excess in the core of the element. The elements can be stable as ${}^{2}H$, ${}^{13}C$, ${}^{15}N$ and ${}^{18}O$ or unstable as ${}^{3}H$ and ${}^{14}C$. The natural creation of these isotopes is very improbable and they exists only at very low concentrations. For water elements, the abundance in the total hydrosphere of ${}^{1}H$, ${}^{2}H$ and ${}^{16}O$, ${}^{18}O$ is described in Tab. 2.3. This creates water molecules with different masses and natural occurrences (Tab 2.4). Molecules mixing two or more stable isotopes such as ${}^{1}H^{2}H^{18}O$, ${}^{2}H^{2}H^{18}O$ and ${}^{2}H^{2}H^{16}O$ are extremely rare and therefore neglected. ${}^{2}H$ is often written as Deuterium or abbreviated as D (AIEA, 2008).

Table 2.3: Isotopic abundance of water isotopes.

Isotopes	${}^{1}H$	${}^{2}H$	${}^{16}O$	${}^{18}O$
Abundance (%)	99.99	0.015	99.8	0.2

Table 2.4: Weight related isotopic abundance of the light and heavy water molecules, with their correspondant molecular masses.

Water molecule	$^{1}H^{1}H^{16}O$	$^{1}H^{2}H^{16}O$	$^{1}H^{1}H^{18}O$
Abundance (%)	99.7	0.03	0.2
Molecular mass (g/mol)	18	19	20

Isotopic abundance is usually defined through isotope ratios ^{A}R: the rare isotopic abundance is divided by the common isotopic abundance. The values of these ratios are very low (Equ. 2.16 and 2.17), and a high level of precision is necessary to measure them.

$$^{2}R = \frac{^{2}H}{^{1}H} \tag{2.16}$$

$$^{18}R = \frac{^{18}O}{^{16}O} \tag{2.17}$$

^{18}R equals $2.0052 \cdot 10^{-3}$ in the ocean, $1.9851 \cdot 10^{-3}$ in evaporated water, whereas ^{2}R equals $1.5575 \cdot 10^{-4}$, in ocean water and $1.4329 \cdot 10^{-4}$ in evaporation. These ratios are not absolute values because they depend on the sensitivity if the instruments when measuring them and also of fractionation conditions.

To have a better idea of the variations of these ratios, the relative $\delta - notation$ (in ‰) is used, with a reference to chosen standards. The reference is the ocean (VSMOW, Vienna Standard Mean Ocean Water) for ^{18}O and ^{2}H. It means that $\delta^{2}H$ and $\delta^{18}O$ equal 0 ‰ in the sea. Here are two relations (Equ. 2.18 and 2.19) for water isotopes, with $^{A}R_{m}$ the measured isotope ratio, and $^{A}R_{std}$ the standard ratio, which equals $2.0052 \cdot 10^{-3}$ for oxygen and $1.5575 \cdot 10^{-4}$ for hydrogen.

$$\delta^{18}O = \frac{^{18}R_{m} - ^{18}R_{std}}{^{18}R_{std}} \cdot 1000 \tag{2.18}$$

$$\delta^{2}H = \frac{^{2}R_{m} - ^{2}R_{std}}{^{2}R_{std}} \cdot 1000 \tag{2.19}$$

A negative $\delta^{2}H$ or $\delta^{18}O$ indicates lower abundance of the rare isotope than in the reference standard, and positive value a higher abundance.

2.6.2 Fractionation processes

Variations of $\delta^{2}H$ or $\delta^{18}O$ variations occur during phases change in a natural environment. The higher mass of the stable isotopes affects their mobility. The kinetic energy of a molecule is dependant on the temperature (in Kelvin) (Hecht, 1999).

$$k_b \cdot T = \frac{1}{2} \cdot M \cdot \nu^2 \tag{2.20}$$

where

k_b : Boltzmann constant $= 1.38 \cdot 10^{-23}$ $\left({}^{m^2 kg}/_{s^2 K}\right)$
M : Molecular mass $\left({}^{g}/_{mol}\right)$
ν : Mean molecular speed $\left({}^{m}/_{s}\right)$
T : temperature (K)

This equation indicates that each molecule in an equilibrium temperature environment has the same kinetic energy, independently of its mass. Therefore molecules with higher molecular mass have lower speeds. Thus the diffusion speed of these heavier molecules and collisional frequency with others molecules are lower. Heavier molecules tend to stay in the lower energy phases (Clark and Fritz, 1997). This process is called fractionation. It occurs between heavy and light isotopes of a same element or molecule. For water, light elements are molecules of ${}^1H_2^{16}O$ and heavy elements are ${}^1H^2H^{16}O$ and ${}^1H_2^{18}O$ when working with ${}^2H$ and ${}^{18}O$ ratios respectively.

For example, lighter molecules are more volatile and have a slight preference for evaporation, whereas heavier molecules will stay in the water. In contrast, water drops are isotopically heavier than water vapour (AIEA, 2008). In snow, light isotopes are leached out by melt water or by evaporation and heavy isotopes stay in the solid phases (Fig 2.12). It is possible to describe this reaction with a chemical equilibrium equation and an equilibrium constant α (Etcheverry, 2002). For ${}^{18}O$ between water and vapour, the equilibrium isotope fractionation factor equals:

$$\alpha_{liquid-vapour} = \frac{{}^{18}R_l}{{}^{18}R_v} = 1.0098 \;\; at \;\; 20°C \tag{2.21}$$

Where ${}^{18}R_l$ and ${}^{18}R_v$ are the ${}^{18}O$ isotopic ratio of liquid water and vapour. The isotopic enrichment factor ϵ is then defined as :

$$\epsilon = (\alpha - 1) \cdot 1000 \tag{2.22}$$

For kinetic isotope fractionation, or non equilibrium fractionation, of water isotopes, humidity is a major influencing factor (AIEA, 2008). When considering liquid water to vapour phase transformation (or evaporation), humidity reaches 100% at the interface between the two phases, and rapidly decreases at higher distances. On this small interface layer, the equilibrium fractionation works very well, but the transfer to an equilibrium mixed air and water vapour induces a transitional volume between the 100% humidity zone and the atmosphere, where light isotopes move faster than heavier. This creates a ϵ_{trans} dependant on humidity h (Clark and Fritz, 1997). The kinetic enrichment factor is the sum of the transitional zone and the equilibrium interface ϵ_{equ} enrichment factors :

$$\epsilon_{kin} = \epsilon_{equ} + \epsilon_{trans} \cdot (1 - h) \approx \delta^{18}O_{liquid} - \delta^{18}O_{vapour} \tag{2.23}$$

2.6.3 Analyses

All isotope samples were measured through high precision laser spectroscopy (OA-ICOSL for Off-Axis Integrated Cavity Output Spectroscopy Laser). This instrument (Fig. 2.8) works on very small quantities. It transforms 1 mL liquid water samples to vapour for analysis. Compared to IRMS, it provides simultaneous ^{2}R and ^{18}R ratio measurements directly on H_2O molecules, with no conversion to H_2, CO or CO_2 (Lis et al., 2008).

Figure 2.8: OA-ICOSL instrument in the CHYN Laboratory (black box) and the automatic samples injector on its right.

The instrument is made of a 1 meter long cavity, in which water vapour is injected. At each side of the cavity are mirrors, which reflect the emitted laser beam, enough times to have a path length of several kilometers inside the cavity (Fig. 2.9).

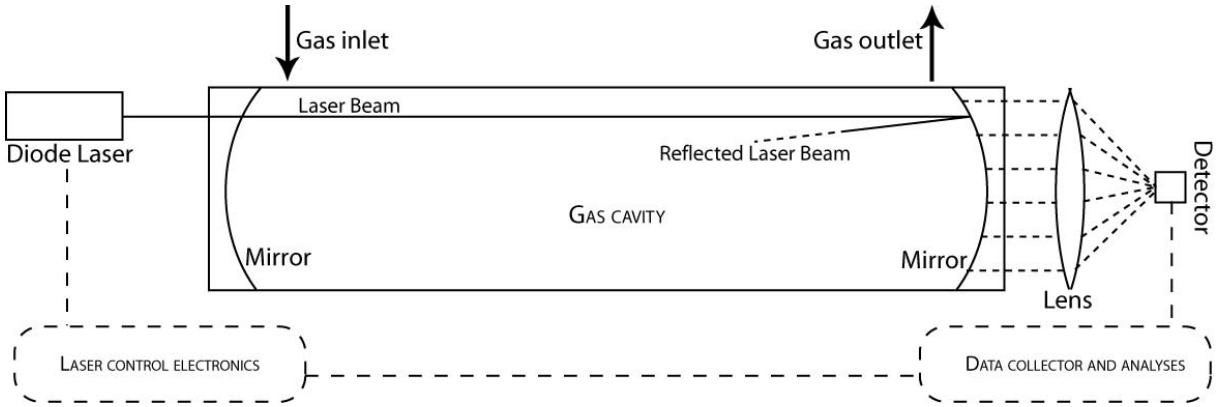

Figure 2.9: Schematic figure of the instrument. Water vapour is injected in the cavity, where the laser beam is reflected several times. Then attenuated lasers are focused on a detector and analysed.

Thus the laser crosses the water molecules several times. This procedure increases the precision of the measures. The analysis uses the natural vibrations of the water molecules, which absorb the light wavelengths. The symmetrical, asymmetrical and bend vibrational movements are considered (Fig. 2.10).

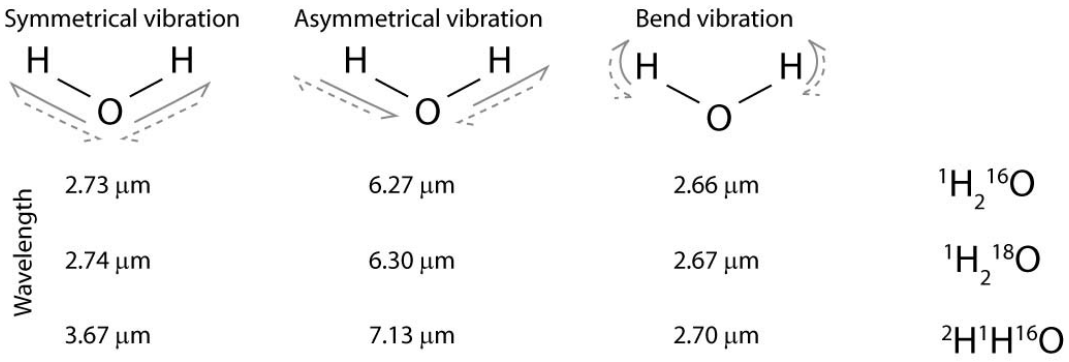

Figure 2.10: Vibration types of a water molecule. Each absorbs a known laser wavelength (here values in µm), which is different for heavy molecules and light molecules.

The analysis protocol was etablished following literature (Lis et al., 2008). Four waters, with known stable isotope values were used as standards. Each sample is analyzed five times to completly replace the vapour in the cavity and avoid mixing with the previous sample. This mixing is called memory effect and was found to be negligible after the third injection (Lis et al., 2008). The two first analyses are rejected and the last three need to have a mass yield that equals $3.1 \cdot 10^{16} \pm 0.1$ H_2O molecules. If not, they were discared and analyzed a second time. The mean of the three injections is then used to calculate δ-values. At the beginning of a series, standards are analysed first and also repeated after two samples to correct instrumental drift.

2.6.4 Water isotopes use

All isotopic studies with δ^2H and $\delta 18O$ start with rain, because it is the initial input signal. It varies with location, temperature and altitude (Criss et al., 2007). Globally the world rain samples are localized on a global water meteoric line, which was built by plotting δ^2H and $\delta 18O$ together (Clark and Fritz, 1997) :

$$\delta^2H = 8 \cdot \delta 18O + 10 \tag{2.24}$$

This linear relation is considered as a norm, but every location has its own local meteoric line. Then, for every study, a local line needs to be traced to understand the origin and pathway of groundwater. They are established with local rain samples. The slope is often the same as the global line, but the intercept,which is also known as deuterium excess ${}^2H_{excess}$ may differ.

$${}^2H_{excess} = \delta^2H - 8 \cdot \delta 18O \tag{2.25}$$

Temperature is one of the major factors in local meteoric water line changes. It is clearly visible in seasonal variations (Fig. 2.11). The relation between $\delta 18O$ and temperature is not linear in the range

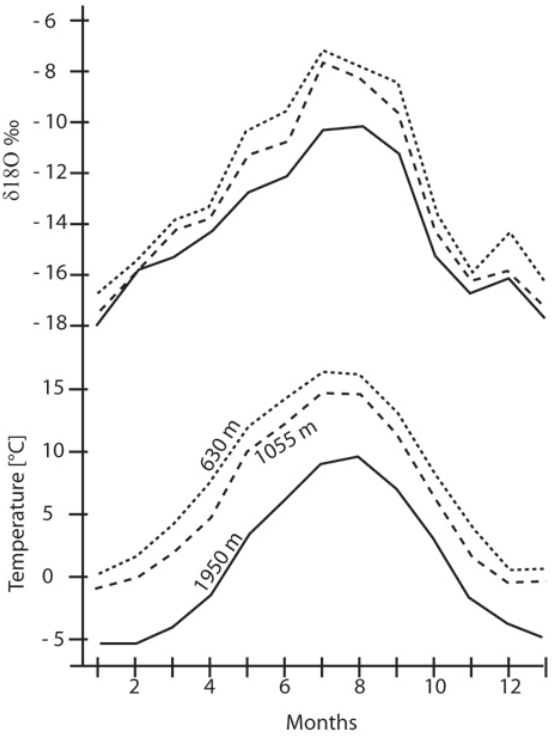

Figure 2.11: Typical seasonal variability of isotopic signals in Switzerland (Etcheverry, 2002).

of - 4°C and + 28°C, but linearity is often accepted for usual temperature differences (Etcheverry, 2002).

The altitude effect is also dependent on the temperature. As altitude increases, the temperature decreases and precipitation becomes more and more depleted in heavy isotopes. Precipitation is also lighter because of a general decrease of heavy elements in the initial vapour (Fig. 2.12) but at the same time heavier if evaporation occurs on the rain drops. All these processes result in a linear correlation between elevation and $\delta 18O$ (see also Fig. 5.1).

These considerations have a consequence on the relation between altitude and $\delta 18O$. At higher altitude, rain often has a lower $\delta 18O$, but if samples are taken on the leeward side of mountains (not exposed to wind and weather) this altitude gradient is not visible anymore due to fewer changes in humidity (Moran et al., 2007). When humidity content changes with altitude or latitude, the isotopic value of water vapour differs considerably.

In temperate glaciers, the isotopic signal is completely smoothed and does not show seasonal variations (Taylor et al., 2002). This comes from the frequent melt-refreeze cycles. During the snow-ice transformation, a large part of the light isotopes are wiped out and the isotopic ratio tends to be heavier than in the initial precipitation. Snow meltwater has a relatively long transit in the snow pack and a part of this meltwater refreezes many times before flowing out. Therefore the fractionation mainly occurs during the freeezing processes as water molecules are not mobile in snow or ice. Comparisons at an elevation of 3500 m were performed at the Jungfraujoch (Switzerland). Isotopic signals in precipitations with common seasonal variations show a mean snowfall $\delta 18O$ value of -15.9 ‰ while a temperate and wind exposed glacier, where melt and freeze cycles often occur, has a mean

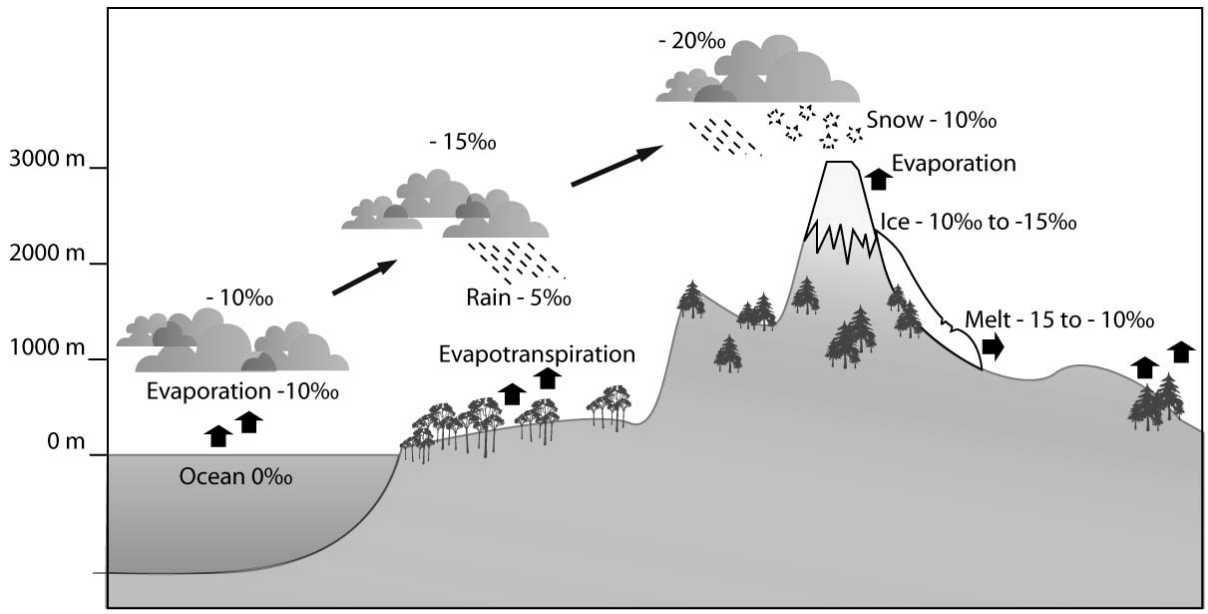

Figure 2.12: Schematic fractionation illustration between the standard isotopic value of the ocean and the rainfall and snowfall in mountain ranges. Variations also occur during water transformation (snow to ice, or snow to water) on the mountain's surface.

value at a similar altitude of -12.5 ‰(Schotterer et al., 2002). For this study, fractionation in the snow pack is illustrated in appendix D.1.

The table 2.5 below shows the range of isotope ratios measured in rain and snow falls at Tsanfleuron glacier and Glarey spring in 2008 and 2009. Fractionation processes are clearly visible in the differences between each type of sample, especially between rain and snow falls.

Table 2.5: Range in the values measured at Glarey spring and in the precipitations (liquid and solid) during the isotopic campaign on the Tsanfleuron Karrenfield between 2008 and 2009. Glacier values collected did not show significant variations.

	$\delta^2 H$	$\delta^{18} O$
Tsanfleuron glacier	-91.0 ‰	-12.7 ‰
Glarey spring	-67.6 to -110.4 ‰	-8.0 to -15.3 ‰
Rainfalls	-80.2 to -106.4 ‰	-11.5 to -15.0 ‰
Snowfalls	-73.6 to -148.5 ‰	-9.1 to -21.0 ‰

Chapter 3

From geological structure and tracer experiments to a conceptual flow model of the Tsanfleuron karst aquifer[1]

3.1 Introduction

In alpine regions, the importance of karst aquifers for water resources is well known (COST-65, 1995). To improve the management and use of alpine karst aquifer systems, a detailed hydrogoeological understanding is necessary (Kralik, 2001). Thus, a geological study in order to create maps and cross-sections, forms a precondition for developing concepts about how the structure of the strata influences the dynamic of the aquifer. In this chapter, the geology of the Tsanfleuron area will be detailed with a description of the stratigraphy in the main tectonic structures, a geological map and many hydrogeological cross-sections giving an overview of relations between defined hydrogeological units. Tracer tests are a very inexpensive and reliable method to obtain connections between springs and different points localized on the upper stratigraphic layers. Coupled with a knowledge of geological structures, it helps to build catchments of the springs and flow pathways inside a hydrogeological conceptual model. Then characteristics and dynamics of the karst aquifer are known which is primordial for developing future works and studies.

[1]This chapter is based on Hydrogeology Journal paper:
Gremaud, V., Goldscheider, N., Savoy, L., Favre, G. and Masson, H. (2009) Geological structure, recharge processes and underground drainage of a glacierised karst aquifer system, Tsanfleuron-Sanetsch, Swiss Alps. *Hydrogeology Journal*, 17(8): 1833-1848.

3.2 Geological framework

3.2.1 Nappe tectonics

The Tsanfleuron-Sanetsch area belongs to the Helvetic domain of the Alps (appendix B.1) and is formed by a pile of several nappes made of Mesozoic and Paleogene rocks, among which limestones take an important place. The region is a classical example of nappe tectonics (Lugeon, 1914). The present geological knowledge and terminology were established by many studies (Lugeon, 1940; Badoux et al., 1959; Badoux et al., 1990; Escher et al., 1993; Steck et al., 1999; Steck et al., 2001). Large parts of the study area are formed by the Diablerets nappe, while the adjacent areas to the N, E and SE belong to the overlying Mont-Gond nappe (Fig. 3.1, Fig. 3.3). In the study area, the Diablerets nappe is generally little deformed, while the Mont-Gond nappe has a thin and strongly deformed overturned limb, connected to the Diablerets nappe by a large isoclinal syncline. Its hinge is clearly discernible south of Tsanfleuron, near the Glarey spring.

The basal thrust of the Diablerets nappe follows a Middle Jurassic (Aalenian) clay formation known for its ductility and low permeability (Crespo-Blanc et al., 1995). The tectonic complex below includes parts of the Morcles nappe and several other units. The top of the Morcles nappe is formed by thick and clayey Oligocene flysch. For these reasons, it can be assumed that the Diablerets and Morcles nappes form two separated hydrogeologic systems. The entire pile of nappes is gently folded and forms a huge anticlinorium in the Tsanfleuron-Sanetsch area (Steck et al., 2001). The axial plunge of this structure is between 5 ° and 10 ° to the ENE. The dips of the strata rarely exceed 10 to the NW and 25 to the SE.

3.2.2 Stratigraphy

The Diablerets nappe below the Tsanfleuron karrenfield (lapiaz) is 1200 m thick; 150 m are due to tectonic repetition by an internal low-angle thrust that obliquely cuts most of the series (Fig. 3.3). The stratigraphy is well exposed in the high cliff SW of the lapiaz and comprises Middle and Upper Jurassic, Lower Cretaceous and Tertiary sedimentary formations.

The sequence (Fig. 3.2) starts with 60-100 m of Middle Jurassic (Dogger) black pelites (Aalenian), clayey siltstones, fine-grained sandstones and calcarenites. The overlying Upper Jurassic and Cretaceous series is principally composed of four limestone formations (two of which are in direct contact) separated by two thick marly formations; these are, from base to top:

- Massive, micritic limestone of 200 m thickness (Malm);
- Above a sharp stratigraphic contact follows a 200-250 m thick alternation of marls and mudstones of earliest Cretaceous age (Berriasian);
- This alternation gradually passes into a 150 m thick formation of bioclastic calcarenites (Late Berriasian to Valanginian);
- Above a sharp contact follows 150 m thick siliceous limestone (Hauterivian);
- With clear contact follows 100 m thick alternation of marls and marly limestones (early Barremian);

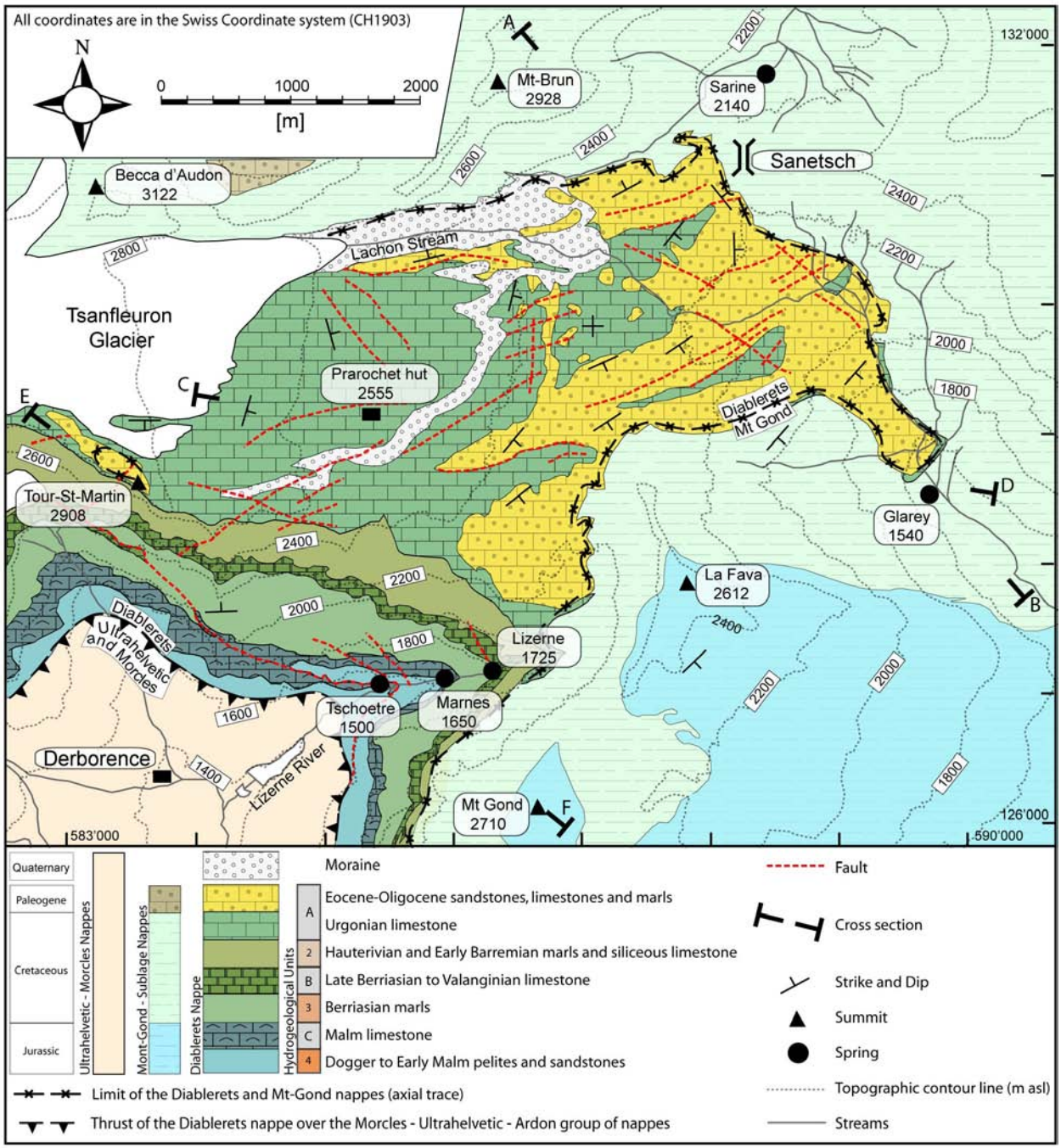

Figure 3.1: Geological map of the Tsanfleuron-Sanetsch area (with Swiss coordinates). Large parts of the study area belong to the Diablerets nappe and mainly consist of Cretaceous Urgonian limestone. The stratigraphy of the over- and underlying nappes is strongly simplified. Relations to hydrogeological units defined in fig. 3.2 are illustrated beside the stratigraphic legend. Relevant springs and streams are also shown; elevations are in meters above sea level.

- This alternation passes upwards into the 120 m thick Urgonian formation (late Barremian to early Aptian), consisting of pure and massive limestone that is quite resistant to mechanical erosion, but highly karstifiable, as discussed in the introduction.

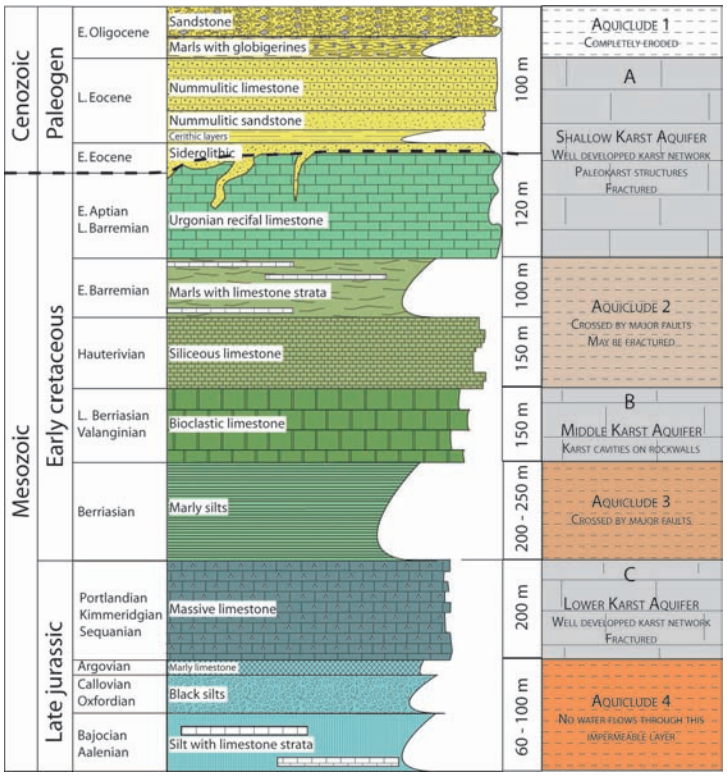

Figure 3.2: Stratigraphy log from Jurassic to Paleogene. It is more detailed than the geological map (Fig. 3.1) or than the cross sections (Fig. 3.3). Aalenian to Argovian formations are mixed with only one colour without figurative drawings on the map and cross-section. Berriasian marls are also without figurative drawings on the geological map. Cenozoic formations are represented only by nummulitic limestone on map and cross-sections to simplify reading of both two figures. The right column shows the karst aquifer formations in grey, and aquicludes in different oranges

A major stratigraphic gap, resulting from uplift and regression starting at the beginning of the Palaeogene, separates the Urgonian from the overlying Eocene to Oligocene formations. The ensuing erosion removed the entire Upper Cretaceous, leaving the Urgonian limestone exposed at the surface. The overlying sediments represent a marine transgression and include, from base to top: sporadic continental (karstic and lacustrine) deposits; brackish sediments (Weidmann et al., 1991); shallow marine sandstones and nummulitic limestones (Menkveld-Gfeller, 1994); Globigerina marls; and finally flysch, consisting of sandstone with abundant volcanic rock debris. The nummulitic limestone looks similar to the Urgonian limestone and is also karstifiable, but can be distinguished by means of fossils. In the study area, the total thickness of the Palaeogene sediments never exceeds 100 m.

Sporadic but sometimes spectacular paleokarst can be observed both on top and inside the Urgonian limestone. It formed during the continental period preceding the Eocene transgression mentioned above. Paleodolines, karren and solutionally-enlarged fractures are filled by continental (often residual) sediments, such as fine-grained, iron-rich sandstones (Wieland, 1976). Similar paleokarst phenomena have been studied more thoroughly in the Morcles nappe (Masson et al., 1980; Linder, 2005). At its SW margin, the Tsanfleuron karrenfield breaks off in steep cliffs from 2900 m to 1400 m, exposing the entire stratigraphic sequence (Fig. 3.1). A rockfall of $5 \cdot 10^6\ m^3$ emanated from these cliffs in 1714, destroying the village of Derborence. The Swiss writer C. F. Ramuz wrote a novel about this disaster (Derborence), but there is little scientific literature available.

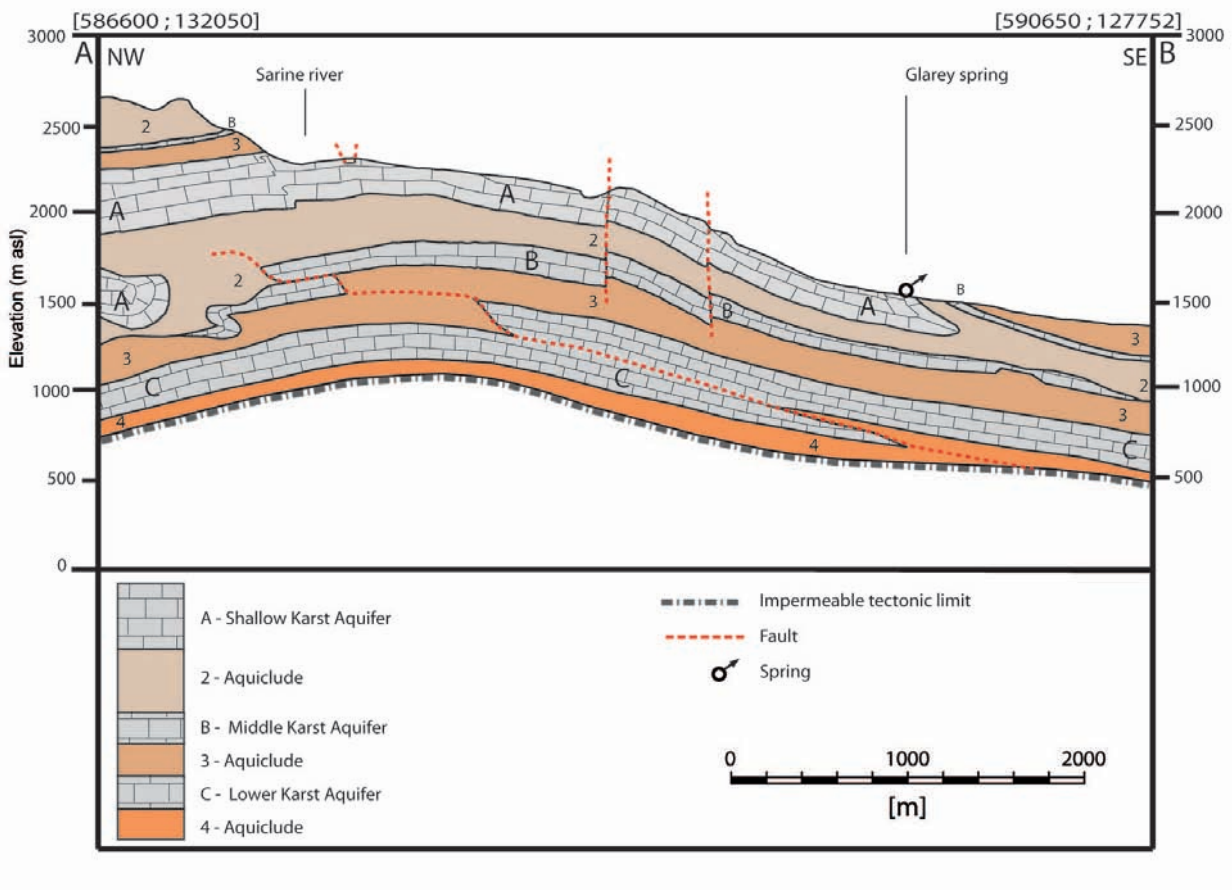

Figure 3.3: Cross-section of the test site area towards the Glarey spring. A is the main karst aquifer. B is an intermediate one that is only visible on southern rockwalls and presents karst cavities. C is the lowest karst aquifer that can be reached by meltwater. Aquicludes 2 to 4 separate the aquifers. On appendix B.2, which presents the geology instead of hydrogeological units, the isoclinal syncline connecting the Diablerets nappe and the Mt. Gond nappe is clearly visible.

3.2.3 Fault tectonics

Fractures of different types and ages are numerous in the study area (Franck et al., 1984). The oldest are synsedimentary, revealed by abrupt variations of layer thickness and, occasionally, by the presence of pebbles and blocks. These fractures were active before and during the deposition of the Eocene sediments and have influenced paleokarst development, as demonstrated by paleodolines in the Urgonian limestone aligned along an ENE direction. Paleokarst development was stopped by the marine transgression, and then by the thrusting of the overlying nappes. Kinematic reconstructions suggest a tectonic overburden of 12 to 14 km (Escher et al., 1993). The Rhone-Simplon Line is a major tectonic discontinuity, which follows the Rhone valley and splits into a number of ENE-WSW to E-W dextral strike-slip faults ((Masson et al., 1980); (Steck and Hunziker, 1994); (Steck et al., 1999)). Some of these faults nearly reach the study area, such as a prominent 15 km long fault, known as the "CCA fault", which has a displacement of 200 m east of Tsanfleuron and branches westward into a multitude of minor fractures (Badoux et al., 1959). In the Tsanfleuron area, just

as in the entire region, the main system of relatively young (i.e. post-nappe) extensional fractures and small-scale conjugate shear zones indicates a stress field with a NW-SE (130-160) maximum compression. This stress field is still active today, as revealed by focal mechanisms of numerous micro-earthquakes recorded along a seismic zone approximately following the CCA fault ((Pavoni, 1980); (Franck et al., 1984); (Masson et al., 1980); (Pavoni et al., 1997). The influence of this fault zone on groundwater circulation can be observed in a nearby gallery (Rawil), which encountered a zone of water-bearing fissures between two dry sectors when crossing the CCA fault ((Badoux, 1982)).

3.2.4 Surface karst development

The Urgonian limestone outcrops of the Tsanfleuron area can be subdivided into three zones of karst development (figs. 3.4 and 1.7), also characterised by different recharge processes (see below). Zone I is where the retreating glacier overlies the limestone. Zone II is located between the glacier front and the end moraine from 1855/60, which indicates the glacier front during the 'Little Ice Age' (Greene et al., 1999; Hubbard et al., 2000). This zone offers the opportunity to observe limestone recently exposed by the glacier and to infer the structure of the ice-rock interface below the glacier. Polished rock surfaces predominate, partly covered by some rock debris representing a thin and patchy melt-out till. There are also meander karren, solutionally enlarged faults, vertical shafts, and large rocky depressions, often 100s of meters wide and 10s of meters deep. Conspicuous elongated calcite crystals on the limestone surface near the glacier front have formed below the ice (Hubbard and Hubbard, 1998).

Zone III, below the end moraine, constitutes a typical alpine karrenfield that began forming at the end of the Pleistocene glaciations, uninterrupted by the Little Ice Age, similar to many other alpine karst systems. A great variety of karren and other karst landforms can be observed, with a soil and vegetation cover that increases with decreasing altitude. The differences between Zones II and III are not only due to the Little Ice Age but also reflect a general change in karst development with altitude and temperature. Small lakes in Zone II and small wetlands in Zone III are due to paleodolines filled with low permeability deposits, as described above.

There are about one hundred caves in the area, most of which are very small but some approach 1 km in length. With one exception, none of these caves reach the active conduit network of the karst aquifer. Although caving teams have done much work, the regional speleological inventory is far from being complete. Most caves developed in Urgonian limestone, but some are also present in Eocene limestone. Cave entrances often consist of vertical shafts, but many caves also include sub-horizontal passages, parallel to the stratification.

3.3 Hydrogeological setting

3.3.1 Aquifers and aquicludes

The sequence of aquifers and aquicludes can be inferred from the stratigraphy described above and illustrated in Fig. 3.2, complemented by field observations. The most important aquifer is the pure, competent, intensively fractured and karstified Urgonian limestone, which outcrops on large parts

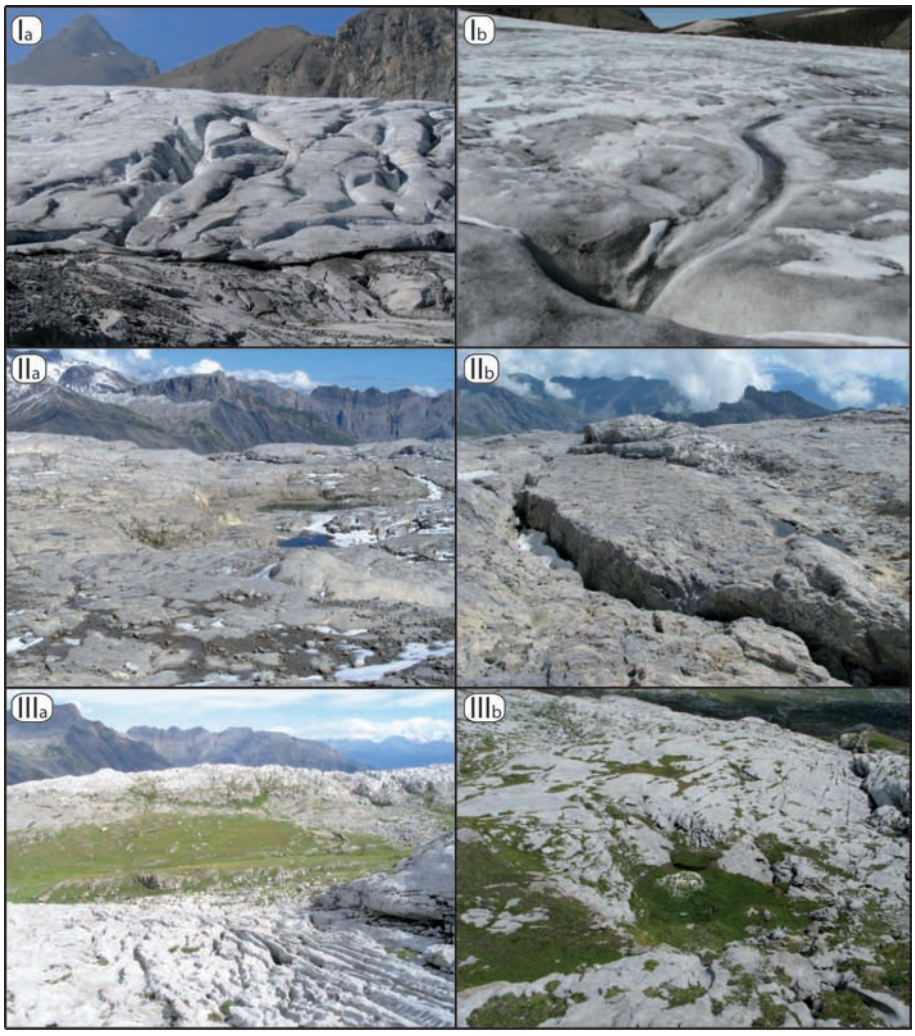

Figure 3.4: Ia and Ib illustrate the glacier cover karst zone, with moulins and front infiltration in the karst. IIa and IIb, the zone without glacier since the Little Ice Age, with small karren and deep dolines. IIIa and IIIb present the well developed karrenfield, with grassy dolines. (Photography Ib and IIIb from N. Goldscheider).

of the land surface. The limestone within the locally overlying Eocene and Oligocene formations is also karstified. Hydrological and speleological observations indicate that the two limestones form the connected **Shallow Karst Aquifer A** (Fig. 3.2).

The underlying Barremian marls coupled with the Hauterivian siliceous limestone also constitute a regional aquiclude in other parts of the Helvetic zone (Goldscheider, 2005). However, the thickness of these two formation is about 250 m in the Tsanfleuron area and has partly been reduced due to tectonic movements as can be seen in the profile in Fig. 3.3; furthermore, the vertical displacements of some faults exceed the thickness of this formation. Therefore, the hydraulic effectiveness of this formation as a regional aquiclude is not immediately apparent. But without considering preferential pathways and relatively to the Shallow Karst Aquifer A, the general hydraulic conductivity of this **Aquiclude 2** layer is low.

Below this first aquiclude unit, Late Berriasian to Valanginian limestone (bioclastic calcarenites) shows proofs of karstification on southern rockwalls, where cavities and small resurgence are present. Water flowing from fractures or faults of Aquiclude 2 uses existent karst conduits. Many major faults and fractures also cross this **Middle Karst Aquifer B** (Fig. 3.2) creating good conditions for karst network development.

Following Berriasian marly silts have a common aquiclude facies but are crossed by the same major faults. The situation is similar to the Barremian marls described above. Water may flow through the 200 m of silts only along preferential pathways on fault or fracture planes. This unit is named **Aquiclude 3** (Fig. 3.2).

In other regions of the Alps and Jura Mountains, the Malm limestone forms a major regional karst aquifer (Herold et al., 2000). However, it is not immediately obvious if the Malm limestone is actually karstified in the Tsanfleuron region. Karstification requires water circulation, but the entire sequence below the Barremian marls appears to be largely shielded against recharge and outcrops only in the steep cliffs south of the Tsanfleuron karrenfields (Fig. 3.1). However, springs that emerge from this limestone formation indicate that a good karst network is present. Hydrogeologically this limestone formation forms the **Lower Karst Aquifer C** (Fig. 3.2).

The last **Aquiclude 4** unit includes the Aalenian to Callovian silts above a major tectonic limit. These formations are considered in this study as completely impermeable and isolate the hydrogeological system from the Ultrahelvetic nappes. Moreover, the important faults that cross the entire stratigraphy are stopped by these more ductile formations.

Observed deep sub-vertical faults might form hydraulic connections from the land surface down towards the deeper limestone aquifers (from Karst Aquifer A to Karst Aquifer B and C), across the entire stratigraphic sequence. This hypothesis was later confirmed by tracer tests.

3.3.2 Recharge processes

A great variety of recharge processes can be observed in the Tsanfleuron-Sanetsch area (Fig. 1.7), some of which are specific to glacierised karst aquifer systems and have rarely or never been described in the literature. The recharge processes are related to the geomorphologic zones of the Urgonian limestone described above, and are closely linked to the meltwater production and drainage system of the Tsanfleuron glacier.

Glaciers typically consist of an accumulation zone and an ablation zone. During the past few years, the entire surface of the Tsanfleuron glacier has often acted as an ablation zone, i.e. the firn line was above the highest point of the glacier, which means that the glacier is not simply retreating but vanishing. The northern sector of the glacier has a pronounced glacier tongue, and a glacier mouth that gives rise to the principal glacier stream, the Lachon. The southern sector consists of a shallow ice sheet on top of the karst limestone (Hubbard et al., 2000). Numerous meltwater streams can be observed at the glacier surface during summer (supra-glacial drainage). Some of them sink into so-called moulins (glacial swallow holes). The moulins in the northern sector are probably connected to the glacier mouth and are thus tributary to the Lachon stream, while those in

the southern sector are most likely connected to swallow holes below the glacier, i.e., the meltwater contributes to subglacial point recharge of the karst aquifer. Many paleo-subglacial swallow holes can be observed below the recent glacier front. The Lachon glacier stream displays significant seasonal and diurnal discharge variations. Below the glacier mouth, it first flows over moraine and then over Urgonian limestone, where it sinks underground via swallow holes at different places, depending on the hydrological conditions (Fig. 1.7). Only during the maximum early-summer snowmelt or storm rainfall, does it form a continuous stream, ultimately tributary to the Rhone River. In the southern sector, many supra-glacial meltwater streams reach the glacier front, where they join with emerging subglacial meltwaters that flow at the ice-rock interface, sometimes as sheet flow. Below the glacier front, these meltwater streams first flow over limestone for short distances (typically 10s of meters), often via meander karren or over polished rock surfaces, and then sink into swallow holes, often in the form of vertical shafts. Due to the rapid glacier retreat, this is the most rapidly changing zone in the entire area.

Similar recharge processes can be observed in the entire Zone II during snowmelt or intense rainfall, when innumerable streams flow over limestone for short distances before sinking underground via swallow holes. This is a fundamental difference between Zone II and Zone III, where all water immediately infiltrates through the epikarst zone. The diffuse infiltration and percolation of water through soil and epikarst has already been studied (Pronk et al., 2009), while recharge into glacier-polished limestone has never been described in detail. The karst aquifer also receives allogenic recharge from the adjacent non-karst area to the east, mostly via streams that sink underground when they reach the karst area (Fig. 1.7). As this zone is used for cattle pasture, the swallow holes represent a potential source of microbial spring water contamination, as was demonstrated for other karst systems (Pronk et al., 2006).

3.3.3 Springs

Five main springs drain the Tsanfleuron-Sanetsch karst aquifer system (Fig. 1.7). Small springs that are not relevant for regional drainage are not described here. The Glarey spring [Swiss Coordinates: 589'650; 128'650; altitude: 1553 m] is situated on the axis of the syncline connecting the Diablerets and Mont-Gond nappes (Fig. 3.3). It is used as a drinking water source for the community of Conthey, and for irrigation. Water from the Shallow Karst Aquifer A is captured by means of a 30 m long artificial drainage gallery with multiple branches. In winter, the mean discharge and electrical conductivity are 30 $^{L}/_{s}$ and 450 $^{\mu S}/_{cm}$, respectively, while higher mean discharges (180 $^{L}/_{s}$) and lower electrical conductivities (100 $^{\mu S}/_{cm}$) occur during summer, due to snow and glacier melt; the water temperature is relatively stable at 4 °C. When the discharge of the main spring exceeds 40 $^{L}/_{s}$, an overflow spring becomes active, directly discharging into the Lachon stream 100 m upstream of the main spring. Both show identical diurnal variations of physicochemical characteristics. The discharge of the overflow can exceed 3000 $^{L}/_{s}$, but has only been measured continuously by means of a pressure probe since 2008. For earlier years, it is possible to reconstruct estimates of the overflow discharge using an empirical relation between the discharge of the main spring and the overflow that has been established in 2008.

Tschoetre spring [585'375; 127'075; 1500 m] and Marnes spring [586'070; 127'150; 1650 m] are located near the limit between the Malm karst aquifer and the Dogger aquiclude, which outcrops twice due

to tectonic repetition (Fig. 3.1). Lizerne spring [586'355; 127'195; 1725 m] discharges from the base of the Valanginian limestone. The mean annual electrical conductivity and temperature of the Tschoetre spring are 200 $^{\mu S}/_{cm}$ and 5 ℃, respectively. As the spring forms a waterfall in a steep gorge, discharge measurements are difficult. The estimated mean discharge during summer is 500 $^{L}/_{s}$. The two other springs directly discharge into the Lizerne Stream; measurements of conductivity, temperature and discharge are not available.

The Sarine spring [588'400; 131'900; 2135 m] is located north of the Sanetsch pass and seems to discharge from Berriasian marl near the base of the Mt. Gond nappe, not far from the thrust contact to the tectonically underlying Urgonian limestone of the Diablerets nappe. The mean spring discharge is 150 $^{L}/_{s}$; much higher than could be expected from a marl formation, suggesting inflow from a karst aquifer. However, the discharge is stable, and electrical conductivity (200 $^{\mu S}/_{cm}$) and water temperature (3 ℃) show no significant variability.

All springs show similar chemical composition, with Ca^{2+}, Mg^{2+} and HCO_3^- as the main ions, which is typical for groundwater from limestone and marl stratigraphy.

Table 3.1: Summary of the main springs around Tsanfleuron karrenfield, with Swiss coordinates, altitude, main discharge, electrical conductivity and temperature. A minimal-maximal range is shown for Glarey and Sarine springs because of the large observed variations. A large amount of samples were available for these two springs (four years for Glarey spring and 1 year for Sarine spring). Tschoetre spring was only promptly measured during tracer tests experiments and only a mean discharge value was measured. Due to the morphology of Lizerne and Marnes spring, no discharge measurements were available (na).

Springs	X (m)	Y (m)	Z (m)	Q $(^{L}/_{s})$	EC $(^{\mu S}/_{cm})$	T (℃)
Glarey	589650	128650	1553	30 *to* 2457	83 *to* 420	3.5 *to* 4.5
Sarine	588400	131900	2135	50 *to* 1850	200 *to* 250	3 (*stable*)
Tschoetre	585375	127075	1500	200	200	5
Marnes	586070	127150	1650	*na*	*na*	*na*
Lizerne	586355	127195	1725	*na*	*na*	*na*

3.4 Tracer test experiments

3.4.1 Overview and experimental design

Between 2005 and 2008, 19 tracer injections were carried out in the Tsanfleuron area, in order to delineate the catchments of the five main springs, to determine transit times and flow velocities, to obtain information about interactions between the glacier, surface waters and groundwater, and to assess the possible impacts of contaminant releases on the Glarey spring.

Four different fluorescent dyes were used as tracers, due to their favourable properties (Kass, 1998): Uranine, Sulforhodamine B and G, and Tinopal. Uranine was the preferred choice for single tracer tests, but Sulforhodamine B or G was used when two injections were too close in time. Uranine and

Sulforhodamine B were used for multi-tracer tests with two injection points; Tinopal or Naphtionate was used as the third tracer. Tab. 3.2 summarises the injection points (#1-19), the tracer types and quantities, and the experimental conditions. Fig. 3.5 shows the location of the injection points, along with the results that will be discussed in the next section.

For the 19 tracer experiments, springs were sampled for up to three weeks after injection, which is sufficient in this karst area where transit times are generally very short (Masotti, 1989; Masotti, 1991). Automatic samplers (ISCO), manual sampling, field fluorimeters (GGUN-FL30) and charcoal bags were used for monitoring. To validate results, at some sampling points, instruments were doubled, for example using field fluorimeters with automatic samplers. All water and charcoal samples were analysed in the CHYN laboratory with a spectrofluorimeter (PERKIN ELMER LS 50 B). A field fluorimeter stayed during 3 years at the Glarey and measured the dye concentration, electrical conductivity and temperature in the spring water at a time intervals of 5 to 15 minutes.

Injection #1 is the release of Tinopal into a cave stream that seems to show relatively little flow variations. The injection was done by speleologists. Tracer test #2 is the injection of uranine into the washbasin of the Prarochet mountain hut. Systematic flushing with tap water lasted only about 30 minutes; afterwards, flushing occurred in an irregular manner, as a function of the use of the washbasin. This tracer test also aimed at assessing the potential impact of the mountain hut on the Glarey spring. Injection points #3-5, #12, #13, #17 and #18 are located near the southern and eastern margin of the glacier, where numerous small meltwater streams sink into karstified limestone. At several other sites, naturally flowing water is usually not available. Injection points #6 to #8 are dry dolines, shafts or inactive swallow holes. For the tracer injections, several m^3 of flushing water were delivered by tank trucks. Sites #9 and #10 are inaccessible for vehicles so that the injections were done during rainfall and snowmelt. At four times, a tracer was injected into the main glacial stream (Lachon) at the glacier mouth (injections #11 and 14-16) in order to determine transit times between the glacier and the Glarey spring during different flow conditions. The main swallow holes are 3 km downstream (Fig. 1.7) so the tracers were exposed to sunlight and, thus, photolytic decay. Therefore, calculated tracer recoveries represent minimum values, as indicated in Table 3.2 A degradation experiment at this altitude revealed an Uranine loss of 40% in 5 hours under sunlight (appendix B.5). As a function of the different hydrological and meteorological conditions, degradation was lower for injection #11 but very high for injection #16. Sulforhodamine G, used for injection #15, is known to be less sensitive to daylight (Kass, 1998). Experiment #19 is the injection of Uranine directly into the main swallow holes of the glacial stream, in order to avoid photolytic decay and to obtain realistic values of tracer recovery. Tracers injected in points #20 to #22 correspond to galcier infiltration experiments and use moulins or crevasse structures on the ice surface. Meltwater was used to help infiltrating the three dyes, uranine, Sulforhodamine G and Naphtionate. These tracer tests are discussed in chapter 4 and do not appear in table 3.2.

3.4.2 Discussion of tracer results

Positive results were obtained for all of the 19 tracer tests. Table 3.2 presents a summary, with the times of maximum concentration (peak times), the maximum normalised concentrations, the tracer recoveries and the linear distances between injection and sampling points. Fig. 3.5 shows the connections demonstrated by these tracer tests, and the peak times. Fig. 3.6 and Fig. 3.7 present

Table 3.2: Summary of the experimental setup and results of the tracer tests in the Tsanfleuron area. Results include tracer recovery (R), time of maximum concentration (t), normalized maximum comcentration (c/M) and distance (D).

Injections	1	2	3	4	5	6	7	8	9	10	11[a]	12	13	14[ac]	15[a]	16[a]	17	18	19
Date		03.9		18.9			02.8		13.8	15.8		24.7		29.8	30.8	11.9	26.7	07.8	26.8
		2005		2005			2006		2006	2006		2007		2007	2007	2007	2008	2008	2008
Alt.(m)	2300	2555	2847	2700	2845	2128	2249	2284	2197	2460	2439	2532	2603	2439	2382	2439	2840	2196	2196
Dye	*T*	*U*	*SB*	*SB*	*U*	*T*	*U*	*SB*	*U*	*SB*	*U*	*SB*	*T*	*U*	*SG*	*U*	*U*	*SB*	*U*
M_i(g)	2000	200	450	500	500	2000	300	500	1000	1000	200	500	2000	300	700	600	1000	1000	200
P(mm)	–	–	–	–	–	+	+	+	+	+	+	+	+	++	+	–	–	–	–
Results																			
Glarey																			
D (m)	2500	4400		5900		2000	3150				5213	4945	5196		4848	5213	6250		2274
t (h)	31.4	54.8	ND	57	ND	33	29.5	ND	ND	ND	5.8	10.3	12.8	ND	5.4	15.3	12.9	ND	6.1
c/M ($10^{-6}m^{-3}$)	88.8	8.93		70.5		2.9	3.3				31.4	1.8	?[b]		29.9	7.4	46.1		69.8
R (%)	80	50		42		65	20				50	5	?[b]		55	20	58		75
Sarine																			
D (m)							590	1227											
t (h)	ND	ND	ND	ND	ND	ND	37	11.5	NS	NS	ND	ND	ND	X	ND	ND	NS	NS	NS
c/M ($10^{-6}m^{-3}$)							2.9	240											
R (%)							0.8	71.4											
Tschoetre																			
D (m)			2900		3100														
t (h)	ND	ND	16.2	ND	32.3	NS	NS	NS	NS	NS	ND	ND	ND	NS	NS	NS	ND	ND	NS
c/M ($10^{-6}m^{-3}$)			17		21.2														
R (%)			47		35														
Marnes																			
D (m)																			
t (h)	NS	NS	NS	NS	NS	NS	NS	NS	X	X	NS	NS	NS	NS	NS	NS	ND	X	NS
c/M ($10^{-6}m^{-3}$)																			
R (%)																			
Lizerne																			
D (m)																			
t (h)	NS	NS	NS	NS	NS	NS	NS	NS	X	X	NS	NS	NS	NS	NS	NS	ND	NS	NS
c/M ($10^{-6}m^{-3}$)																			
R (%)																			

Comments

Tracers: U Uranine, T Tinopal, SG/SB Sulphorhodamine G and B.
Precipitation: -, + and ++ mean no, moderate and intended rainfall, respectively.
ND sampled but not detected, X connection demonstrated by means of charcoal bags, NS not sampled.
[a] Exposure to sunlight and photolytic decay, recoveries are minimum values.
[b] Due to interferences with organic carbon, Tinopal concentrations cannot be determined.
[c] Due to very high flow rates, the main swallow hole of the Lachon stream probably acted as a spring, so that the tracer did not enter the aquifer.

the breakthrough curves at Glarey and Tschoetre spring respectively. Only few tracers arrived at more than one spring at the same time, such as the uranine injected into #7, which was detected both at the Glarey spring and the Sarine spring. Most other injection points are connected to one spring only; furthermore, the tracer flow paths do not cross each other, i.e., most proven connections are simple point-to-point connections. This helps to delineate the spring catchment areas, as shown in Fig. 3.5. Moreover no significant differences were observed between rainy or dry conditions. Mean transit velocities in the aquifer are identical except for tracer experiments that partially use the Lachon streambed, where velocities are higher. Meltwater flowing in the Lachon stream is about 3.5 faster than groundwater. Rain events do not influence the transfer dynamics of the karst aquifer, unless water levels reach the surface (see fig. 3.8) and stop the infiltration processes.

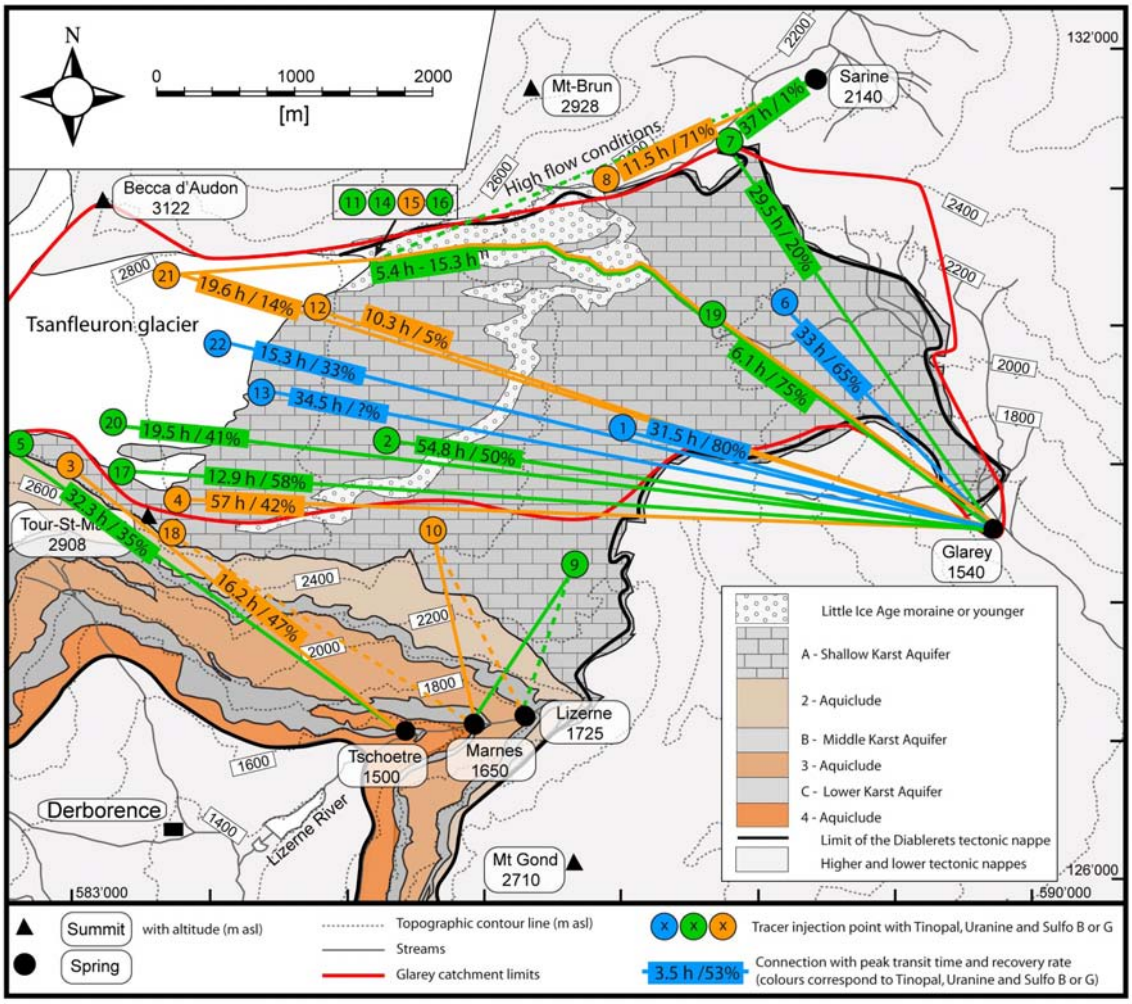

Figure 3.5: Underground connections demonstrated by tracer tests with peak times and catchment boundaries. Injections #1 to #19 are treated in this chapter (table 3.2). Injections #20 to #22 are discussed in chapter 4. In the background of the map are illustrated the karst aquifers and aquicludes discussed in fig 3.2.

The tracer tests demonstrate that the catchment of the Glarey spring comprises large parts of the Tsanfleuron karrenfield and glacier, while the four other springs (Sarine, Marnes, Lizerne, and

Tschoetre) drain only very marginal parts of the karrenfield with very small contribution of the meltwater from the glacier. Its area is about 13 km^2. The transit times in the conduit system, obtained from the peaks of the breakthrough curves, are very short, ranging from 5.4 hours to 57 hours. The shortest times were observed between the main glacier stream (Lachon) and the Glarey spring (injections #11, 15 and 19), suggesting that the principal swallow hole of this stream is connected to a well-developed karst conduit. In the catchment of the Glarey spring, there is no correlation between distance and transit time, which illustrates the high degree of heterogeneity that is characteristic for karst aquifer systems. For example, the tracer injected at site #1 takes 31.4 hours for a 2500 m linear distance, while tracer #17 takes 12.9 hours for 6250 m (Tab. 3.2, Fig. 3.5). The karst system drained by Glarey spring has a low dispersive capacity (many peaks do not exceed 24 hours). Peaks have sharp borders and do not expand on the time axis. Only experiment #11 present a larger surface under the curve. This is explained by the very low water volume available at the injection point, which was localized near the glacier's front. Injection time was then longer than 30 minutes and certainly creates higher dispersivity.

Tracer recoveries at the Glarey spring (including the contribution of the overflow), range from 5% (#12) to 96% (#4). High recoveries indicate a straightforward conduit connection between the injection point and the spring. Lower recoveries may have different reasons, such as photolytic decay for injections #11, #15 and #16, or tracer loss at the injection site due to the absence of naturally flowing water (#6, #7 and #11). However, when a conservative tracer is directly injected into the conduit network, typically via a swallow hole, recoveries can be used to obtain additional information on the underground flow system. Recoveries lower than 100% mean that the missing part of the tracer and water went elsewhere. In the present case, the low recoveries for some of the injected tracers may indicate deep infiltration into subvertical fractures, in the north side of the general anticline and/or continued flow in the Urgonian karst aquifer towards the east, where the Diablerets nappe plunges under the tectonically higher nappes. The rapid connections from injection points #3 and #5, located at the top of the Urgonian limestone karrenfield at 2850 m altitude, towards the Tschoetre spring, which discharges from the Lower Karst Aquifer C at 1500 m, shows that deep infiltration via fractures does actually occur, across the entire stratigraphic sequence.

Some breakthrough curves (BTC) show multiple peaks with 24-hour periodicity, indicating an influence of glacier melt. Fig. 3.6 presents #1 and #2 curves observed at the Glarey spring during the same multi-tracer test, i.e. during identical hydrological conditions. Uranine was injected into the washbasin of the mountain hut (#2), and Tinopal into a cave stream (#1). Both tracers arrived at the spring after about 30 hours (time of first detection); the Tinopal BTC essentially shows a single peak, while Uranine displays at least six peaks, in 24 h intervals. It is hypothesised that the Uranine was transported through the unsaturated zone towards an active karst conduit directly connected to the glacier. The diurnal variability of water level and flow rate in this conduit causes a stepwise mobilisation of the tracer; intense rainfall on the eighth day seems to wash out the remaining tracer, illustrated by an additional and final Uranine peak. Tinopal, on the other hand, was transported in a cave stream far away from the glacier, without intermediate storage in the unsaturated zone and without significant diurnal variability. The connections from injection points #9, #10 and #18 to the Marnes spring were established by very high tracer concentrations found in charcoal bags placed downstream in the Lizerne River. Tracers #9 and #10 were also detected in a charcoal bag that was placed upstream from the spring, but at lower concentration levels. This finding pointed to the presence of an important spring farther upstream, the Lizerne spring, which was previously unknown.

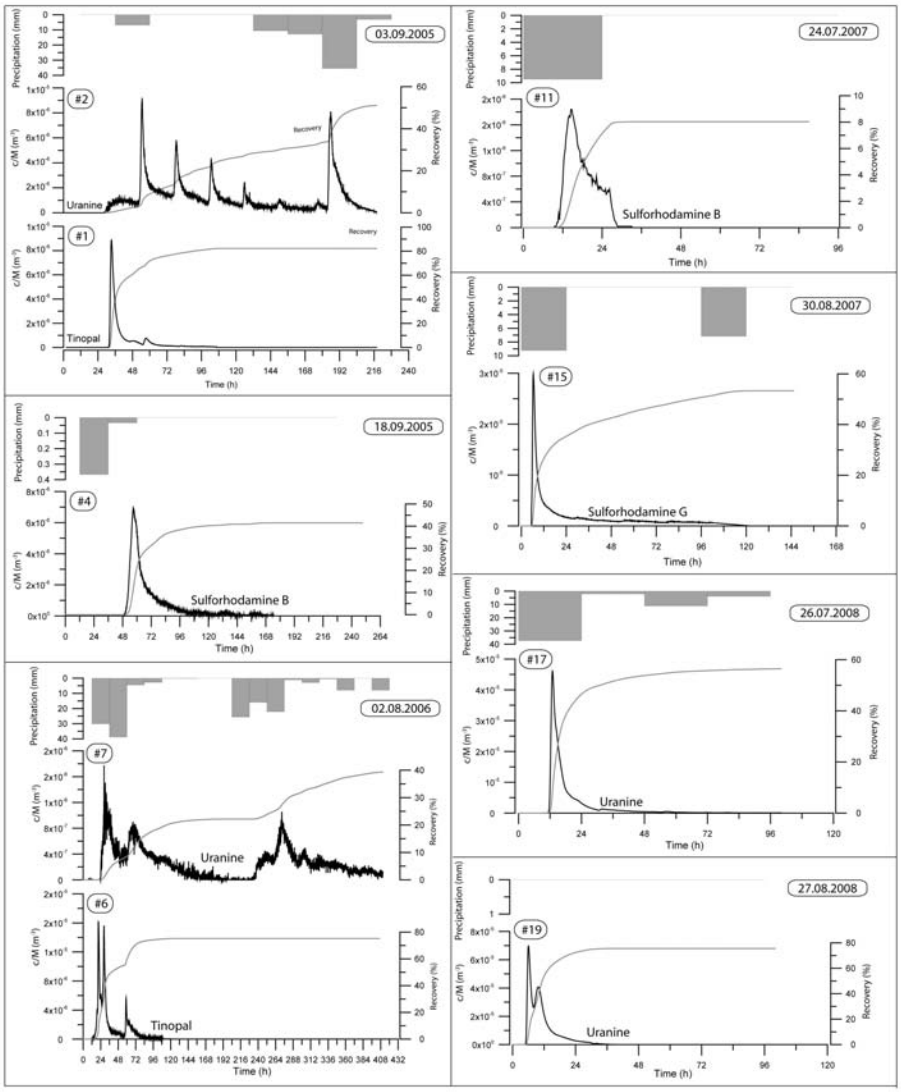

Figure 3.6: Breakthrough curves monitored at the Glarey spring, along with recoveries and daily precipitation, resulting from injections #1, #2, #4, #6, #7, #11, #15, #17 and #19. Tracers arrived at Glarey spring in a range of 5.4 h to more than 55 h with recoveries between 5% and 80%. #2 shows several peaks in 24-h intervals, indicating influence of the diurnal variations of glacier melt. It is the only breakthrough curve that obviously illustrates the melt cycles at Glarey spring. Precipiation were found to flush the tracers out of the aquifer by reducing water transit times and increasing water level inside the aquifer. Dispersivity remains globally low, peaks have sharp borders and do not expand on the time axis.

Although discharge is not continuously monitored at the Tschoetre spring, the multi-peak uranine BTC resulting from injection #5 clearly illustrates the influence of the diurnal variability of the small glacier part that melts into this spring (Fig. 3.7). The tracer pathway crosses several unsaturated limestone and marl formations, obviously along deep vertical fractures, before it reaches the active flow system of the Marl karst aquifer. Intermediate tracer storage in the unsaturated zone and periodic flushing by meltwater can also explain the observed BTC because injection #3 does not present the same characteristics of diurnal variations. Dispersivity is here higher than in the Glarey

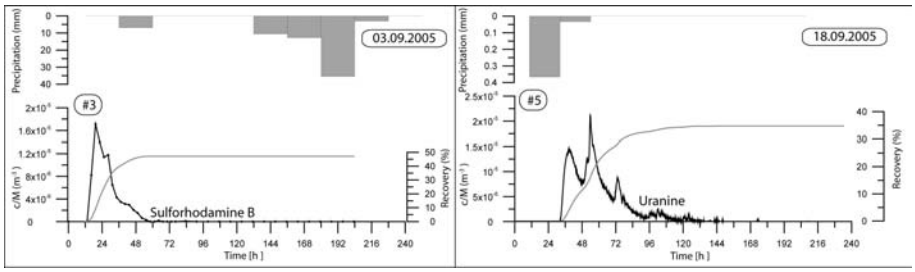

Figure 3.7: Sulforhodamine B and Uranine breakthrough curves monitored at Tschoetre spring, resulting from injection #3 and #5. The multi-peak behaviour of the Uranine is attributed to the diurnal variability of glacial meltwater production.

catchment with larger peaks (peaks widths are about 48 hours) that are probably due to the geological pathways through strata.

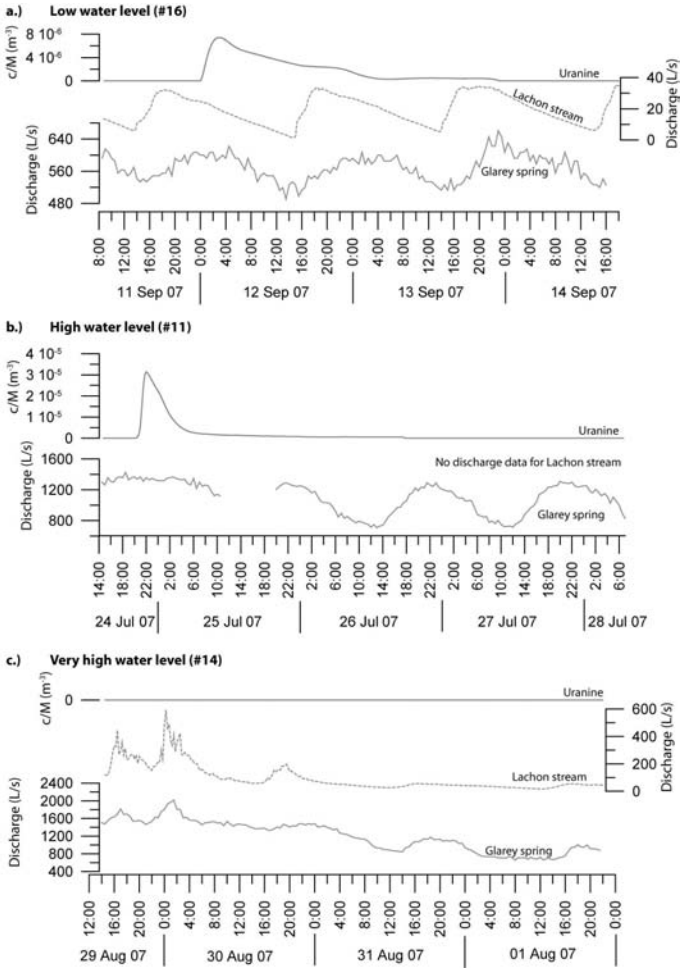

Figure 3.8: Discharge monitored at the Glarey spring and the Lachon stream (if available) during three different tracer tests carried out during different hydrologic conditions, and resulting Uranine BTCs, monitored at the Glarey spring: (a) injection No. 16, (b) injection No. 11 and (c) injection No. 14 (see also Table 1 and Fig. 6). During high-flow conditions, shorter transit times and a higher recovery were observed than during low-flow. During very high flow conditions, the tracer did not reach the spring as the swallow holes were obviously not active or were transformed into springs (act as estavelles). c/M is the uranine concentration normalized by the injected mass

The tracer injections in the Lachon stream near the glacier mouth made it possible to better characterise the glacier-stream-aquifer-spring relations during different hydrologic conditions (Fig.

3.8). As described above, the tracers were exposed to daylight between the injection site and the swallow hole so that partial photolytic decay has occurred. During low-flow conditions (injection #16), the tracer peaked after 15 h but the recovery was only 20%, indicating substantial photolytic decay in the slow-flowing surface stream. During high-flow conditions (#11), the maximum tracer concentration occurred only 5 h after injection and the recovery was substantially higher (50%) indicating less tracer loss by photolytic decay due to shorter residence times in the stream. Due to the short transit times (the breakthrough was largely completed within about 15 h), the BTC from this injection shows no discernible influence of the diurnal glacier-melt variations, unlike the BTCs presented in Fig. 3.6 and Fig. 3.7. During very high flow conditions, when little photolytic decay is expected, the tracer did not arrive at the spring, indicating that the swallow holes were not active but probably transformed into springs, i.e. they act as estavelles.

3.5 Conceptual model of karst drainage

Based on geological considerations, hydrologic observations and tracer test results, a conceptual model of the underground drainage pattern of this glacierised karst aquifer system was established as illustrated in two hydrogeological cross-sections (Fig. 3.9, Fig. 3.10). The Hydrogeological unit A, namely Shallow Karst Aquifer A (fig. 3.2), constitutes the main regional karst aquifer, limited by the underlying aquiclude 2, which is relatively thick (250 m) but crossed by faults and fractures. Various processes contribute to aquifer recharge, including sinking streams from adjacent non-karst areas (allogenic recharge), diffuse infiltration of rain and snowmelt water, infiltration of glacial meltwater underneath the glacier and near its front, as well as sinking of the main glacier stream far downstream from the glacier mouth (autogenic recharge). Large parts of the area are mainly drained by the Glarey spring, but marginal zones drain towards four other springs (Fig. 3.5). Structurally, Shallow Karst Aquifer A forms a large anticline with a poorly defined axis and a wide crest, plunging towards the ENE below tectonically higher structures (see appendix B.2), with an axial plunge of 5-10 °. The southward adjacent isoclinal syncline, on the other hand, has a well-defined axis and forms a narrow trough. The Glarey spring is located where a deeply incised valley cuts this syncline at a low topographic position (1553 m).

It is assumed that underground drainage essentially occurs near the base of the shallow karst aquifer, on top of the underlying marl, and follows the fracture network and the dip of the strata (Fig. 3.9). The karst waters partly flow towards the ENE, following the gentle plunge of the wide anticline, but eventually turn southward, where the isoclinal syncline acts as a major drainage structure, collecting and conveying the water towards the Glarey spring. Some tracer tests resulted in high recoveries, indicating straightforward connection between the respective swallow holes and the Glarey spring, via well-developed conduits. Other tracers, although directly injected into the conduit network via swallow holes, reappeared at substantially lower recoveries (sometimes only 5%), suggesting that the remaining part of the tracer and, thus, an important part of the water, went elsewhere. It is generally known that high mountain areas often act as recharge zones for large, deep groundwater circulation systems (Toth, 1963; Toth, 1999). However, infiltration into these systems can rarely be observed. In the Tsanfleuron area, two types of deep infiltration can be hypothesised, supported by geological and hydrological considerations, and tracer test evidence:

- Continued groundwater flow in Shallow Karst Aquifer A following the general plunge of the

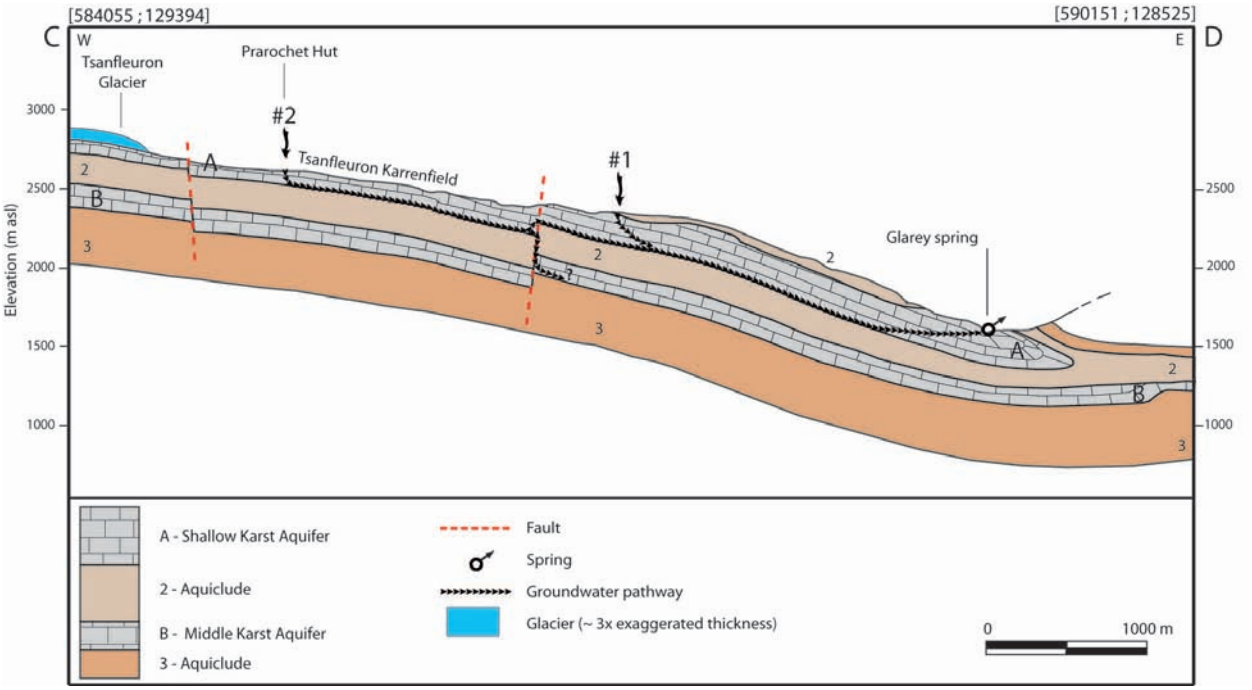

Figure 3.9: Conceptual model of karst drainage from the Tsanfleuron glacier and karrenfield towards the Glarey spring, confirmed by tracer tests (injection points #1 and #2 are shown, also see Fig. 3.5). Water flow occurs near the base of Karst Aquifer A on top of the underlying Aquiclude 2 towards the isoclinal syncline that collects all water and conveys it to the spring. Infiltration into deeper aquifers along faults is assumed (section line see Fig. 3.1). Appendix B.3 presents the geology instead of hydrogeological units.

Diablerets nappe towards the ENE.

- Deep infiltration via subvertical fractures and faults, across the relatively thin Barremian marl aquiclude and the underlying formations

The first type can only be indirectly deduced from the geological structure and the low tracer recoveries, but cannot be observed directly, because the Diablerets nappe plunges below tectonically higher nappes east of the Sanetsch pass and there are no accessible sampling points farther to the east, where the re-emergence of groundwater from the study area could be observed.

The second type of deep infiltration, however, is confirmed by the two positive tracer tests between the surface of Shallow Karst Aquifer A and the Tschoetre spring, which discharges from Lower Karst Aquifer C, 1350 m below (Fig. 3.10). Between the injection points and the spring, the tracers crossed about 800 m of marl and limestone stratigraphy in less than two days, which is only possible via open, subvertical fractures and faults. As a consequence of the steep topography in this part of the area, fractures probably opened by gravitation, enabling rapid water percolation. The catastrophic rockfalls, which plunged from these cliffs in 1714 and 1749, further support the supposed existence of open fractures. The failed tracer test from a nearby swallow hole can eventually be explained by deep infiltration into vertical fractures, which are, however, not connected to the Tschoetre spring. Both the Tschoetre and the Glarey springs receive inflow from the glacier and rapidly react to the temperature-driven diurnal variations of meltwater production.

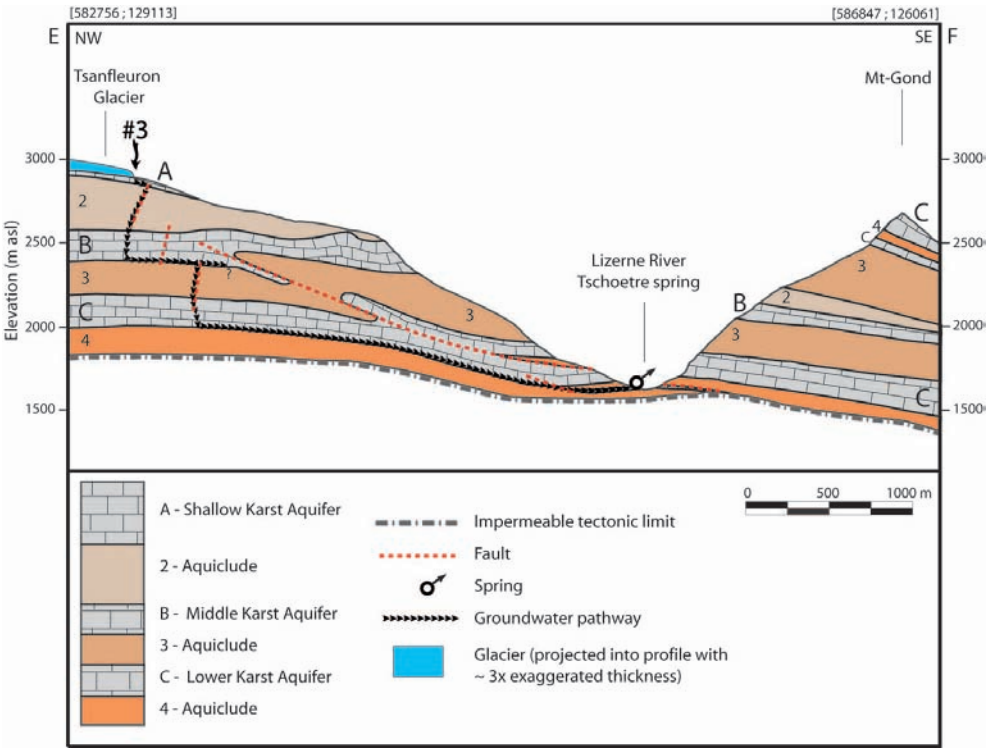

Figure 3.10: Conceptual model of flow from the upper part of the Tsanfleuron glacier and karrenfield towards the Tschoetre spring, confirmed by tracer tests (injection point #3 is shown; see also Fig. 3.5). The tracer crossed the entire stratigraphic sequence, including several aquiclude formations, in less than two days along deep fractures that opened due to the steep topography (glacier projected into section, see Fig. 3.1). Appendix B.4 shows an identical section with geological strata.

Flow towards the Lizerne and Marnes springs follows pathways similar to those towards the Tschoetre spring, i.e. from Shallow Karst Aquifer A along fractures across marl aquicludes 2 and 3 towards Middle and Lower Karst Aquifers B and C, respectively. The Sarine spring, located near the tectonic contact between two nappes, seems to discharge from Aquiclude 3 but receives inflow from the Tsanfleuron karst area, as demonstrated by tracer tests. The crest of the anticlinorium, although not precisely defined, acts as water divide between the catchments of the Sarine spring and Glarey spring. One tracer injection went to both springs; during high flow conditions, there is also inflow from the glacier stream to the Sarine spring. The spring is characterised by high but stable discharge, and stable physicochemical parameters. It is hypothesised that the spring is connected to a karstified limestone imbricate thrust that drains the surrounding marl aquitards and is also connected to the main aquifer. More research is necessary to confirm this hypothesis, but unfortunately no equivalent water level conditions were available during the next two years and the experiment could not be done again.

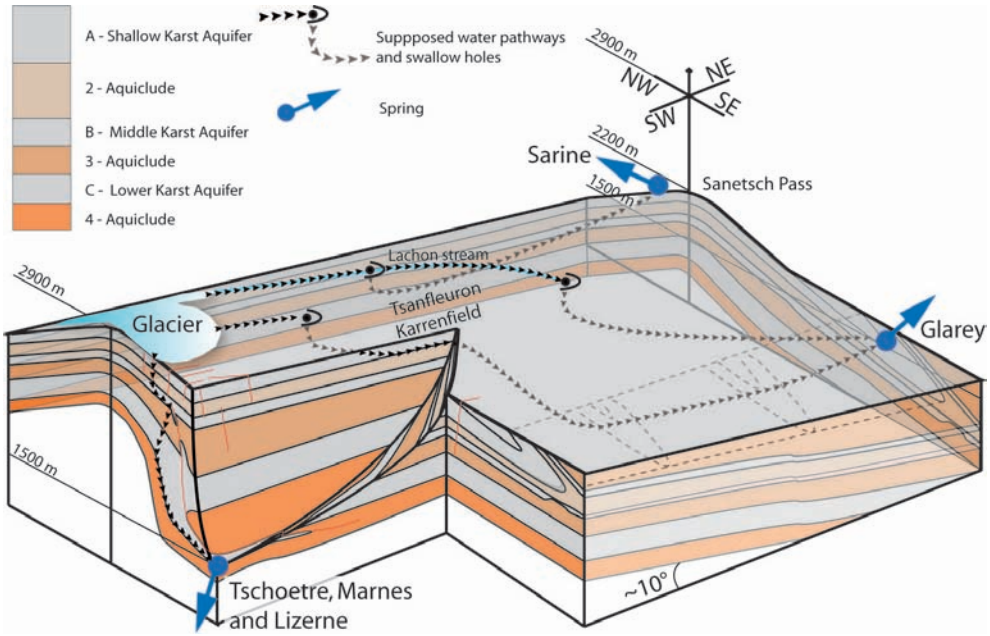

Figure 3.11: Schematic fence diagram illustrating the hydrogeological units and drainage of the Tsanfleuron glacier-karst system. Arrows indicate inferred schematic flow paths toward three groups of springs: Glarey spring drains most of the area; the other springs drain marginal parts. Connections have been established by the 19 tracer tests, but precise pathways are not known. A geological conceptual model is available on appendix B.7

3.6 Conclusions

Apart from the immediate relevance for a better understanding of regional hydrogeology and for the delineation of protection zones for the Glarey spring, this chapter also allows several conclusions of more general relevance to be drawn. Groundwater flow in alpine karst aquifer systems consisting of marl and limestone formations often follows the stratification. Therefore, fold structures have a major influence on groundwater flow in shallow karst systems, as already demonstrated by means of tracer tests in several alpine karst systems (Goldscheider, 2005). Some authors (Butscher and Huggenberger, 2007) used geologic 3D modelling in combination with a conceptual flow model approximating underground drainage of shallow karst systems by open surface flow on top of the underlying aquiclude. In the Tsanfleuron-Sanetsch karst system, the anticlinorium is part of the continental water divide between the catchments of the Rhône and Rhine Rivers; the isoclinal syncline acts as a regional drainage structure, conveying water towards the Glarey spring. Due to the presence of fractures and faults, there is also flow across the stratification. It was possible to demonstrate rapid flow across an 800 m sequence of marls and limestone, towards the Tschoetre spring, in less than two days. Catastrophic rockfalls occurred in this part of the area in historic times. The tracer tests indicate the presence of open fractures and thus the risk of future rockfalls, enhanced by permafrost thawing and glacier retreat. Not all recharge water reappears at accessible springs, but part of the water feeds deeper and larger regional flow systems. In the Tsanfleuron-Sanetsch area, two types of deep infiltration can be supposed, and partly demonstrated: (1) parallel to the stratification, following the plunge of the Diablerets nappe towards the ENE below tectonically higher nappes; (2) across the

stratification, along subvertical fractures, at least down to the Malm limestone.

Intense interactions between the glacier and the karst aquifer, including specific recharge processes, were observed. Diurnal variations in glacial meltwater production influence tracer transport in the aquifer, confirming the importance of hydrologic variability for contaminant transport processes in karst aquifer systems (Goppert and Goldscheider, 2008). The delineation of the Glarey spring catchment shows that Tschoetre and Sarine springs do not drain large part of the Tsanfleuron glacier and of the karrenfield's surface. On the basis of these observations, the next part of this work will focus:

- On a better characterisation of the influence of the glacier on Shallow Karst Aquifer A, how meltwater infiltrates in the system and its importance to Glarey spring variations;
- On the influence of diurnal and seasonal variability of glacier melt upon groundwater flow in the aquifer, using stable isotope tracers and simple hydrograph separations;
- Finally on prognoses for the impact of climate-change induced glacier retreat on the availability and quality of water at Glarey spring.

Chapter 4

Geometry and drainage of Tsanfleuron glacier recharging the karst aquifer[1]

4.1 Introduction

Glaciers have a great impact on the surface morphology of alpine areas, and their current rapid melt induces higher run-off (Lambrecht and Mayer, 2009) and therefore increases the recharge of connected aquifers. Many human communities currently use this amount of water for hydropower or irrigation (Loukas et al., 2002; Viviroli and Weingartner, 2004). The general decrease of glacier volumes provides excess discharge, which will not be available if the current trend of climate change goes on. Many modeling studies have investigated the potential streamflow in glacierized catchements (Braun et al., 2000; Schaefli et al., 2007; Huss et al., 2008) but impacts on aquifers are not discussed. An investigation of such relations was set up in order to characterize available freshwater volumes and connections of meltwater pathways with the aquifer. To date glaciology and hydrogeology are separate disciplines, only a few studies investigated glacier-aquifer relations, e.g. numerical simulations of large-scale groundwater flows beneath ice masses (Flowers et al., 2003). Published studies evaluating climate change impacts on glacier-aquifer dynamics on a catchment scale are scarce. The relations between glaciers and karst aquifers have previously been studied in the Rocky Mountains of Alberta, Canada (Smart, 1983; Smart, 1996; Smart, 1997; Smart and Ford, 1986). The Tsanfleuron site remains ideal for studying glacier-aquifer interrelations and for evaluating possible impacts of glacier retreat on connected freshwater resources. Glaciologists have already well studied the Tsanfleuron glacier, focusing on its temperature distribution, rheology, and ice-flow dynamics (Chandler et al., 2008; Hubbard, 2002; Hubbard et al., 2000; Sharp et al., 1989), but no real investigation of ice volume and meltwater flow through ice and on the glacier-karst interface has been done yet.

[1]This chapter is based on Acta Carsologica paper:
Gremaud, V., Goldscheider, (2010) Geometry and drainage of a retreating glacier overlying and recharging a karst aquifer, Tsanfleuron-Sanetsch, Swiss Alps. *Acta Carsologica*, 39/2:289-300.

This chapter combines glaciological geophysic and hydrogeological methods to focus on the role of the glacier as an intermediate freshwater storage reservoir recharging the aquifer and ultimately contributing to drinking water supply. Thus the aims are:

1. Determine the geometry of the glacier, i.e. its surface area and average thickness, so as to determine the ice volume and the equivalent freshwater quantity

2. Obtain information on the structure and morphology of the glacier-limestone interface, i.e. the hidden karst landscape below the glacier

3. Investigate, characterize and classify recharge processes by which meltwaters enter the aquifer underneath the glacier and beyond its front

4.2 Experimental area, overview and limits

The goals were obtained by a geophysical and hydrogeological campaign during the summers of 2007 and 2008, using radiomagnetotellurics (RMT) to determine ice thickness, tracer tests to characterise recharge processes and a wide use of the chapter 3 contents that describe and introduce geological and hydrogeological characterization of the site and defines the main aquifer layers.

The main features of the Glarey spring catchment, which contains Tsanfleuron glacier, were defined in the previous chapter: the glacier overlies Cretaceous limestone (Barremian-Aptian) 100 to 120 m thick that outcrops on large parts of the land surface. Locally, the Cretaceous is overlain by thinly-bedded Eocene nummulitic limestone and other rock types (fig. 3.2), which are interconnected and were defined as a unique Shallow Karst Aquifer A. The major part of the karst surface and glacier is drained by the Glarey spring in the SE (Fig. 4.1), with a discharge ranging from 30 L/s in winter to a maximum of 2457 L/s during snowmelt and storm rainfall, with a mean annual discharge of 667 L/s (2004-2009). Underground water flow toward this spring occurs parallel to the stratification, near the base of the Cretaceous aquifer, on top of underlying marl and are collected in the narrow syncline in the south-east that conducts water to the Glarey spring. Dominant transit times are in a range of 5-57 h (obtained from peak times of tracer breakthrough curves) with recoveries of 5-80 %.

Three morphological types of karst surface were defined in the previous chapter. (I) underneath the glacier, (II) between the glacier front and the end moraine from 1855/1860 ("Little Ice Age") and (III) below this moraine (Fig. 4.1). The present chapter focuses on the two highest zones, which contain the glacier, its specific recharge processes and the unaccessible and unobservable limestone surface underneath the ice. But as the glacier is rapidly retreating (Fig 4.2 and appendix C.1), 300 m length were lost between 2000 and 2008 and about 100 m between 2008 and 2009 (SGMN, 2009), observations near the glacier front provide insight into subglacial geomorphology and hydrology. In this zone, rock surfaces are polished and the epikarst has been partially removed by glacial erosion. Dolines and large karst conduits from paleo-networks are certainly present, close to the morphology of the recently deglaciated zone II.

The basal ice includes plucked material that creates striations on limestone surfaces. In zone II, this rock debris forms a thin, discontinuous ablation till. Carbonate precipitates occur on lee

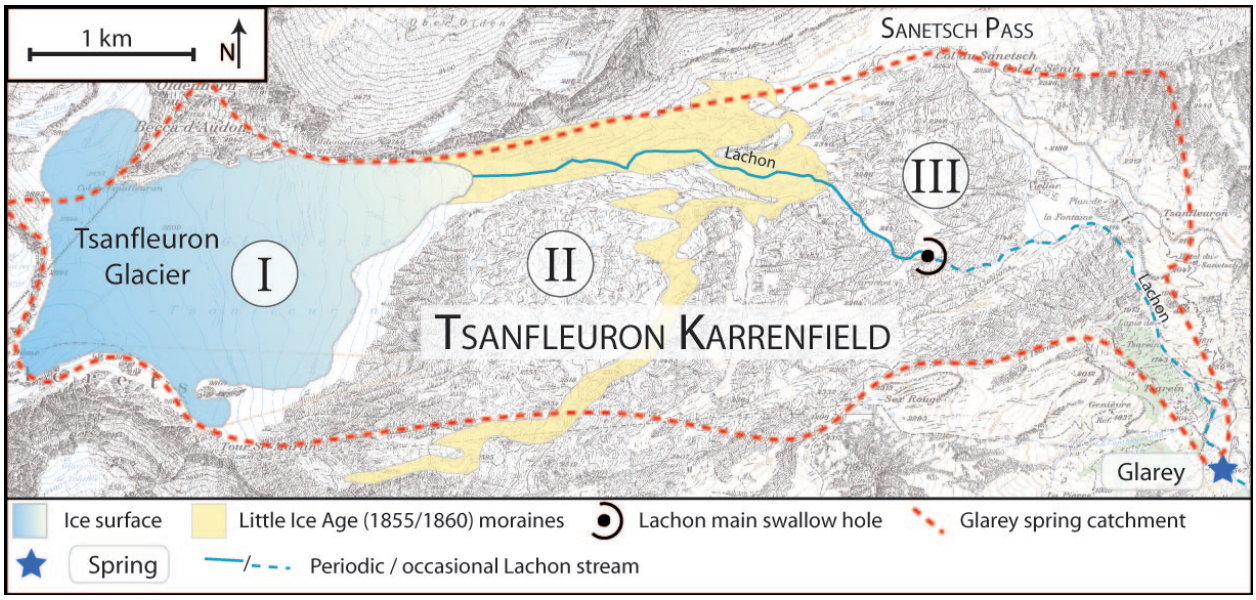

Figure 4.1: The major part of Tsanfleuron glacier is included in the Glarey catchment (see chapter 3). The karst area was subdivided into three zones (fig. 1.7): I. glacier on top of the karst aquifer; II. limestone between the current glacier front and end moraine from 1855/60; III. limestone exposed since the end of the Würm Ice Age. This chapter focuses on the two higher zones. The main glacier stream (Lachon) typically sinks into swallow holes in zone III; only during extreme high-flow conditions, does it continue beyond this point.

sides of subglacial bedrock hummocks, now exposed below the current glacier front (Hubbard and Hubbard, 1998). Nye channels cut into the rock surface by meltwater indicate that at least parts of the subglacial drainage occur along the ice-rock interface (Bates et al., 2003; Grust, 2004). After glacier retreat, meltwater streams often flow several tens of meters in these channels or over polished limestone surfaces before sinking into shafts or fractures. Such swallow holes are present everywhere in the area, mainly relics of a paleokarst conduits that were used for meltwater or closed by glacier sediments. During spring and early summer snowmelt, the zone of active swallow holes is extensive; but in dry summer and autumn periods, active swallow holes can only be found near the glacier front. Rainfall activates swallow holes across zones II and III.

In many alpine areas, the combined action of mechanical erosion by glaciers and flowing waters has formed the landscape; in karst areas, most water drains underground, so that the result of pure glacial erosion can be observed. Zone II of the study area includes large depressions, hundreds of meters wide and tens of meters deep. Some of them are bordered by steep walls, caused by plucking of fracture-bound limestone blocks by the flowing glacier. Similar geomorphologic and hydrologic phenomena have been observed in a glacierised karst region of the Canadian Rocky Mountains (Ford, 1983).

In zone III, the landscape has been exposed to karstification at least since the end of the Würm Ice Age, about 10,000 years ago, but also probably between each earlier Ice Age (Riss, Mindel or Günz). Karrenfields are partly covered by thin soil and alpine vegetation, explaining the name Tsanfleuron, which comes from the French "champ fleuri" and means flower meadow. Due to a well-developed

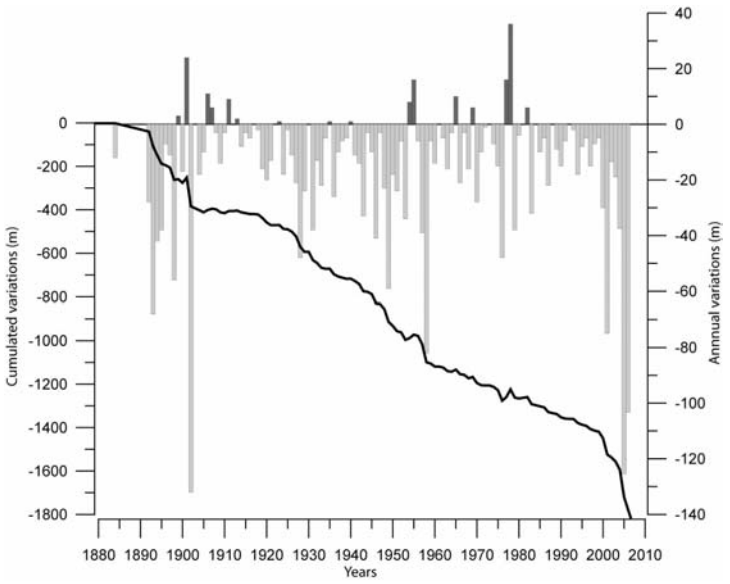

Figure 4.2: Glacier annual and cumulated variations between 1884 and 2009. The glacier has lost about 250 m in length in the last 5 years and more than 1850 m since the Little Ice Age (SGMN, 2009).

epikarst, diffuse infiltration predominates, with two exceptions: The main glacier stream (Lachon), which first flows over moraine, sinks into several swallow holes in the centre of zone III (Fig. 4.1). At the eastern margin of the area, several allogenic streams sink underground near the marl-limestone contact.

4.3 Detailed method application

4.3.1 Geophysical measurement of glacier thickness

Glacier thickness was measured using the radiomagnetotelluric (RMT) method. Georadar and seismics are often used for glacier surveys: Seismics allows for greater investigation depth; georadar is efficient for imaging shallow glacier structures (Senechal et al., 2003). RMT was selected for this study because the equipment is portable, and the method delivers robust information on layer thickness (provided resistivity contrasts are sufficiently high). For the general principle of the instrument please refer to chapter 2. Four frequencies were used 234, 183, 77.5 and 19.6 kHz. Deep ice resistivity can reach 10^6 to 10^9 Ωm (Assier and Evin, 1995; Hubbard and Hubbard, 1998; Kulessa, 2007). In contrast, shallow ice resistivity critically depends on meltwater saturation and consequently varies with temperature. Therefore the investigation depth was very variable (Kulessa, 2007) and our method presents a high risk of dealing more with shallow ice layers than representating the entire ice thickness.

A two-layer model was used for the data inversion: glacier ice overlying limestone, where ice thickness (Z), ice resistivity (ρ_1), and limestone resistivity (ρ_2) are the three fit parameters (Fig. 4.3). Variable ice resistivity poses no problem, as it is always significantly lower than limestone resistivity, i.e. the contrast is sufficiently high. The chosen frequencies (Table 4.1) allow a total investigation of the ice layer. Only in the case of meltwater totally saturating the ice (with resistivty about 100 Ωm) is the investigation too limited and may minimize the thickness of the ice layer. Many of these points were eliminated before and during data inversion processing.

Table 4.1: Corresponding depth for each frequency and ice resistivity by using the equ. 2.14

ρ_1	frequencies [Hz]			
	19600	77500	183000	234000
100	$36m$	$18m$	$12m$	$10m$
1100	$119m$	$60m$	$39m$	$34m$
2100	$165m$	$83m$	$54m$	$48m$
2700	$187m$	$94m$	$61m$	$54m$

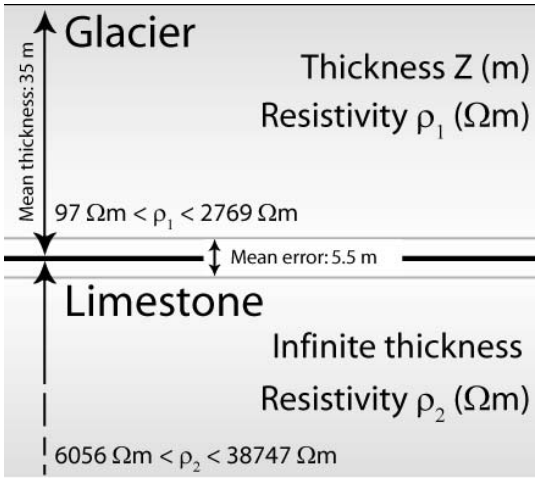

Figure 4.3: Illustration of the two-layer model used for the RMT icethickness mapping. The fit parameters include ice thickness, ice resistivity, and limestone resistivity. Ranges of obtained resistivity values are indicated. Ice resistivity varies as a function of water saturation, but the resistivity contrast is always sufficiently high to obtain clear results, confirmed by repeated measurements at selected points in 2007 and 2008 (tab. 4.2), which delivered reproducible results (mean error 5.5 m).

During two glacier surveys in the summers of 2007 and 2008, RMT measurements were done at 226 points, located by means of GPS with a precision of 2 m horizontally and 3 m vertically. The two campaigns took place on the area where the snow pack completely vanished from the glacier's surface in order to have a direct contact between our electrodes and ice, and to keep a two-layers model. The mean distance between measurement points is 90 m, but the distribution is heterogeneous, because of crevasses and other terrain difficulties. Some points were measured in both years or during different times of the day, and delivered reproducible results with a mean error of 5.5 m (tab. 4.2). Two software tools developped at the University of Neuchâtel were used for data inversion: FITVLF2 (Thierrin, 1990) and Gmin (Fischer et al., 1987). When the two codes delivered inconsistent results, the respective data points were eliminated. Simple interpolation (kriging) of the measured ice thickness at all 187 valid measurement points (appendix C.2 and C.3) yielded a map of ice thickness in 2007/2008 [2] (Fig. 4.6). The limits of the glacier's surface were taken by GPS measurements and represent the 2008 limits in end September. A thickness of zero meters was arbitrary defined for this limit in order to constrain the interpolation method even if observed thicknesses at some points of the glacier border were estimated at 2 or 3 meters. Due to rapid glacier retreat, this map is only a snapshot. The thickness and limits of the glacier will change in the next

[2]The thickness of the glacier is certainly higher than the results of this method. Between 50 to 80 meters were found to miss in our method compared with georadar campaigns (Hubbard and Hubbard, 1998; Nath Sovik and Huss, 2010). Our method therefore mainly illustrates the shallow ice layers

years.

Table 4.2: Comparison between same measured points in 2007 and 2008 RMT campaigns.

Point	Year	Time	modelled Z (m)	Mean value (m)	Abs error (m)	Rel. Error (%)
199	2008	12h	22	23.4	2.8	12.0
37	2007	10h	24.8			
72	2007	14h	28.5	26.4	4.2	15.9
200	2008	12h	24.3			
66	2007	13h	48.2	50.75	5.1	10.0
215	2008	15h	53.3			
67	2007	13h10	43.6	39.55	8.1	20.5
96	2007	16h	35.5			
85	2007	14h30	53.3	51.3	4	7.8
219	2008	16h	49.3			
170	2008	18h	31.2	29.6	3.2	10.8
203	2008	13h10	28			
64	2007	12h30	18.2	19.4	2.4	12.4
94	2007	16h30	20.6			
175	2008	8h00	14.3	13.45	1.7	12.6
214	2008	14h50	12.6			
69	2007	13h30	36.1	27	18.2	67.4
97	2007	17h	17.9			
				Mean	5.52	18.8

4.3.2 Multi-tracer test experimental design

Apart from the 19 tracer experiments discussed in chapter 3, three new tracer injections were done at the Tsanfleuron glacier on 11 September 2008 during dry weather. The fluorescent dyes Uranine, Sulforhodamine G (SulfoG) and Naphthionate were used as tracers. The three injection sites represent different recharge pathways (Figs. 4.4 and 4.5): Uranine (#20) was injected at the top of the glacier, near its southern edge, into a moulin with a constant estimated flow rate of 5 L/s. This structure had a diameter of 6 cm, a vertical orientation, which certainly sends meltwater deep inside the glacier. SulfoG (#21) was injected into the branch of a tree stream (15 L/s) that drains a shallow depression and finally sinks into a long and deep crevasse oriented in the north-south direction. This injection point was located in the northern part of the glacier, 1.4 km west of the glacier terminus. Naphthionate (#22) was injected near the central part of the glacier front into a large meltwater surface stream (100 L/s) sinking into a deep moulin, that belongs to a larger collapsing area about 20 m of radius and collecting many identical streams.

The monitoring campaign began in dry weather but more than 15 mm of rain occured over the next days. A field fluorometer (GGUN-FL30, Neuchâtel, Switzerland) was installed into the main glacier stream (Lachon), 860 m downstream of the glacier mouth (M1, Fig. 4.5); charcoal bags were put in

(a) Uranine (b) SulfoG (c) Naphtionate

Figure 4.4: Illustration of the three injection points on the Tsanfleuron glacier. Uranine was injected in a typical moulin structure at the top of the glacier (a), Sulforhodamine G in a long crevasse, where many meltwater streams infiltrate (b) and Naphtionate inside a large and deep collapse moulin (c).

12 meltwater streams, including M1 (for comparison between fluorometer and charcoal results), two tributaries of the main stream (M2, M3) and 9 streams emerging at the glacier front and sinking into the karst aquifer via swallow holes (M4-M12, Fig. 4.5). Charcoal bags were selected for monitoring because of the large number and remoteness of sites. Usually, charcoal bags are not recommended for Naphthionate detection because of interference with organic carbon (Goldscheider et al., 2008), but glacial meltwaters contain very little organic carbon and the expected tracer concentrations were high. The Glarey spring was monitored using an auto-sampler (6712C, ISCO, Lincoln, USA) and a field fluorometer. All samples were analysed in the CHYN laboratory (University of Neuchatel) with a spectrofluorometer (Perkin Elmer LS50B).

Table 4.3: Summary of flow rates (meltwater streams sinking into moulins), tracers (U uranine, SG sulphorhodamine G and N naphtionate) at the injection points on the Tsanfleuron glacier in September 2008. Localizations of injection sites are on fig 4.5

Tracers	20	21	22
Elevation Z (m)	2850	2738	2700
Tracer quantity (g)	200	400	1000
Estimated flow rate (L/s)	5	15	100

4.4 Results and discussion

4.4.1 Glacier thickness and subglacial karst morphology

Fig. 4.6 presents the ice thickness map of the Tsanfleuron glacier in summers 2007/2008, based on 187 valid RMT measurements and a glacier borehole at the SW corner of the area. As snow did not melt in this zone, no RMT measurement were done near this borehole that would have allowed comparison. Information was obtained about this borehole only recently, after completion of the

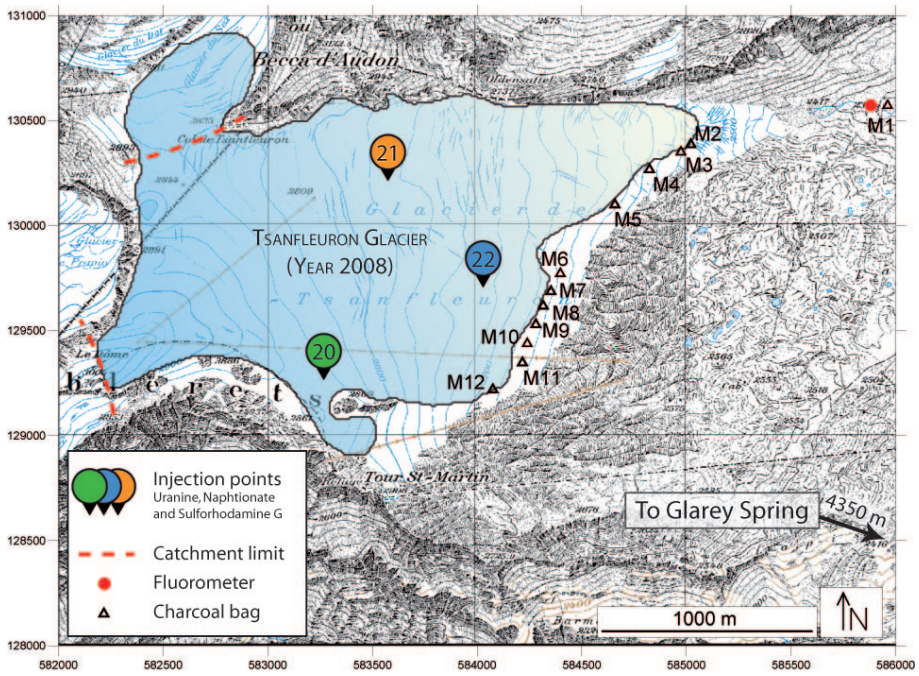

Figure 4.5: Location of the injection points for Uranine (#20), Sulforhodamine G (#21) and Naphthionate (#22), and the monitoring sites (M1 to M12). The Glarey spring (outside the map) is the principal drainage point of the groundwater system and was also monitored.

field surveys. As the reproducibility of the results has been confirmed by repeated measurements in two subsequent years (described above and in table 4.2, illustrated in Fig. 4.3), the method is sufficiently precise to estimate an ice volume and characterise the geometry of the glacier and subglacial morphology. However due to the important probability of measuring only the saturated layer of the glacier, the map is reproducible but may only represent a model of the shallow ice layers. Next values therefore need to be considered with precautions. The mean ice thickness was found to be 35 m, with a maximum of 138 m near the northern margin of the glacier and only 15 near its centre. The missing thickness, compared with radar profiles, is not homogeneous and can therefore not simply be added. We decide finally to use our glacier model, but we keep in mind that it only represents a minimum volume. Based on this map and field observations, the glacier can be subdivided into two parts. A thick northern part, which fills a W-E trending valley (Fig. 4.8) and forms a glacier tongue in its lowest part. In this part the ice carves softer Eocene rocks, which follow the tectonic limit of the Diablerets nappe (Fig 3.3 and 3.1). This area of the glacier was already considered as the principal ice flow zone (Grust, 2004). Deep dolines are expected to be present in this part, where the morphology of the substrate creates depressions. The central and southern zone consists of a thin layer of ice overlying a shelf of Urgonian limestone (Fig. 4.6). The subglacial bedrock topography contains depressions and knobs, especially in the northern part, where the geology is heterogeneous and also includes softer rocks, resulting in differential glacial erosion. The southern sector also shows several wider oscillations. The subglacial morphology (zone I) consequently resembles the karst landscape in the glacier forefield (zone II) with karst depressions, dolines creating identical but more active water infitration processes.

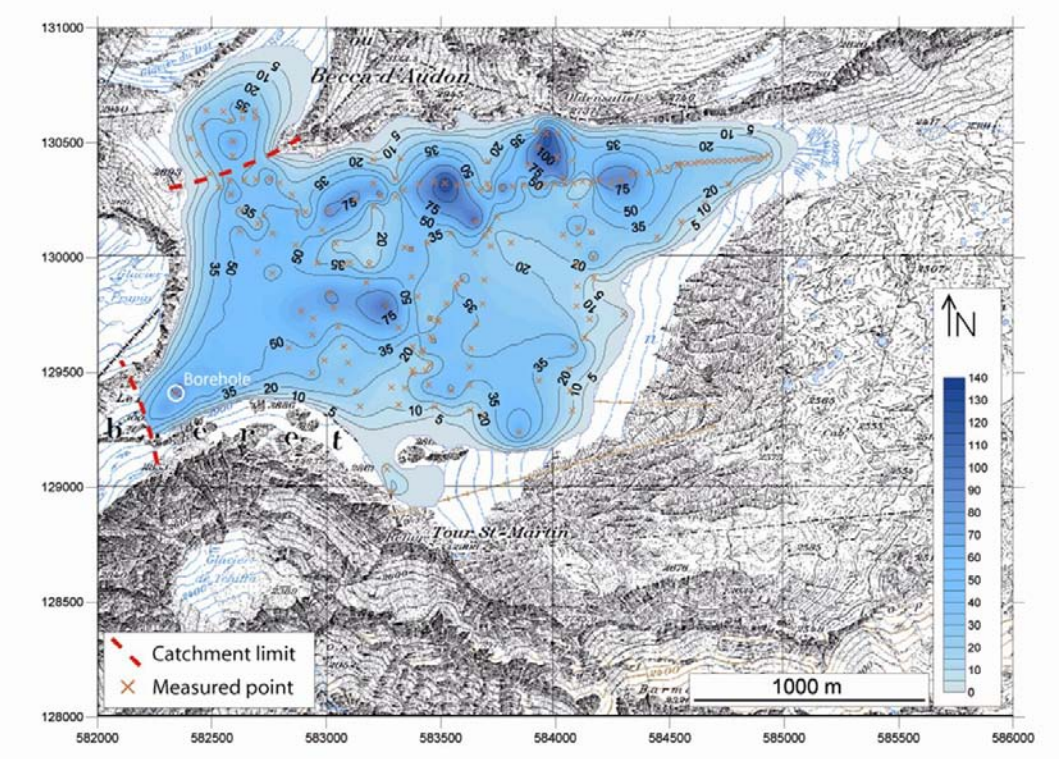

Figure 4.6: Ice thickness map of the Tsanfleuron glacier in 2007/2008, based on 187 valid RMT soundings and a glacier borehole. A recurrent error was made about the resistivity of ice and this map only shows the shallow layers, which are saturated by meltwater. But the massive ice was not measured and the map shows only minimum thicknesses. The NW zone of the glacier is probably not within the catchment of the Glarey spring (based on bedrock geology and topography) and was not included in the estimations of the ice volume. The thick northern part forms a glacier tongue; the southern sector is a thin ice layer overlying limestone. The heterogeneous pattern of ice thickness reflects the uneven rock surface relief below the glacier. Limestone-glacier interface morphologies are certainly close to the typical geometry of the forefield karst.

4.4.2 Glacial water storage

Based on the map of glacier thickness (and considering measurement accuracy and uncertainties resulting from interpolation and system boundaries), the ice volume within the catchment of the Glarey spring (as indicated in Fig. 4.6) is estimated at $1.0 \cdot 10^8$ $m^3(\pm 10\%)$, corresponding to $0.92 \cdot 10^8$ $m^3(\pm 10\%)$ of water available for recharge, assuming an ice-water density ratio of 0.92 (Benn, 1998). Data from the Swiss Glacier Monitoring Network (2009) and field observations indicate that the glacier currently loses a mean of 15 m in length and more than 1.5 m in thickness per year. In 2008, the glacier occupied 2.8 km^2, so the current estimated annual ice loss is $4.2 \cdot 10^6$ m^3 ($3.9 \cdot 10^6$ m^3 of freshwater). Sublimation and evaporation losses from glaciers are small compared to meltwater production (Benn, 1998; Lang, 1981; Strasser et al., 2008). Therefore, most of this volume is presumed to contribute to aquifer recharge if sufficient aquifer storage is available, which is the case here. This quantity represents a transient surplus of water that is available during periods of glacier retreat but will be missing when the glacier has disappeared. The annual water volume discharged at Glarey spring is $1.8 \cdot 10^7$ m^3, so a first estimation of the missing water volume corresponds to ca.

20 % of the current annual spring flow and will slowly decrease in the next years as the glacier area reduces.

4.4.3 Glacier to aquifer drainage pathways

The tracer injections delivered positive results and gave insights into the relations between the glacier, the aquifer, and the spring. Results obtained from charcoal bags installed at 12 meltwater streams around the glacier (M1-M12, Fig. 4.5) are summarised in Tab. 4.4. SulfoG was found in monitoring sites M1 and M3, contributing to the main glacier stream (Lachon). Naphthionate was detected at very high levels at M6, M10 and M12, demonstrating the connection between the supraglacial meltwater streams sinking into the moulin (#22 in Fig. 4.5) and three subglacial meltwater streams emerging at the glacier front, then sinking into three swallow holes several tens of meters downhill. Ice is therefore heterogenous and presents impermeable layers (Grust, 2004) that can drive meltwater to various directions inside the glacier. Uranine was not detected in any of the 12 monitoring sites around the glacier, suggesting that all meltwaters sinking into this moulin (#20 in Fig. 4.5) infiltrate into the underlying karst aquifer via subglacial swallow holes.

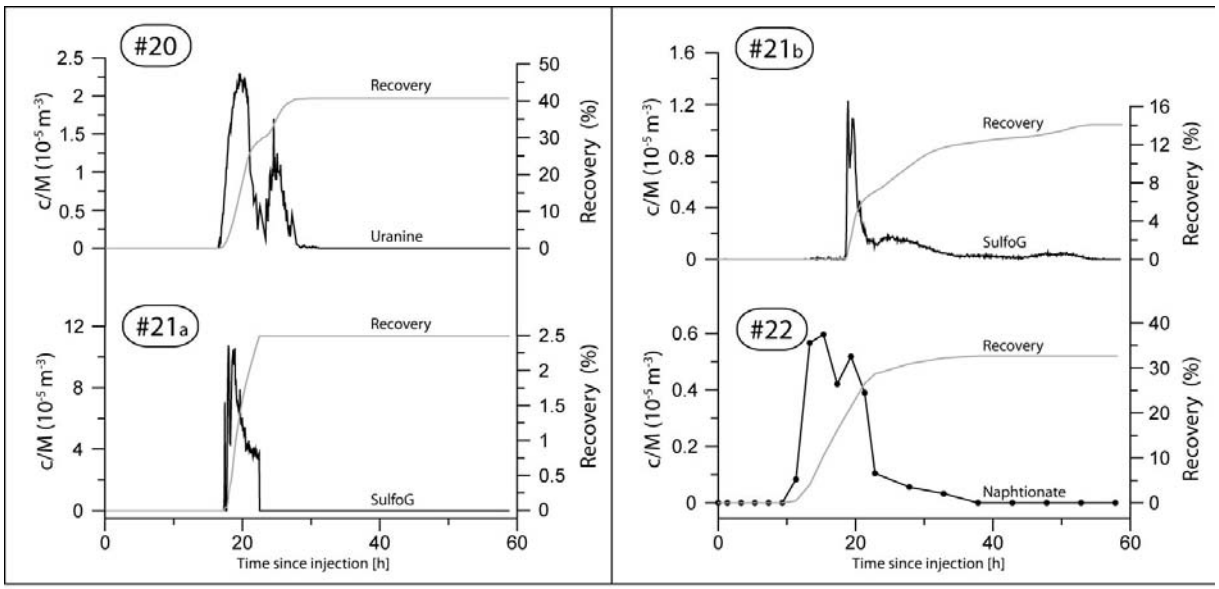

Figure 4.7: Breakthrough curves and tracer recoveries obtained for the three injections at the Tsanfleuron glacier. To enable comparison, normalised concentrations are shown, i.e. concentrations divided by injection mass (c/M). #20 Uranine at Glarey spring, #21a SulfoG in the main glacier stream (Lachon), #21b SulfoG and #22 Naphthionate at Glarey spring. The abrupt decrease of SulfoG in the Lachon stream is not an artefact but presumably the result of a meltwater wave flushing all tracer previously stored in stagnant zones of the streambed. It may also come from a deplacement of the device out of the streambed by higher discharge.

The field fluorometer installed in the Lachon stream (M1, Fig. 4.5) recorded a SulfoG breakthrough curve (BTC; Fig. 4.7), while the other two tracers were not detected. This is consistent with the hypothesis that only the northern zone of the glacier, which forms the glacier tongue, drains

Table 4.4: Results of charcoal bags installed at monitoring sites M1-M12 (location see Fig. 6). Legend: + means positive results, / means tracer not detected.

Samples	$M1$	$M2$	$M3$	$M4$	$M5$	$M6$	$M7$	$M8$	$M9$	$M10$	$M11$	$M12$
Altitude (m)	2380	2519	2537	2570	2607	2636	2646	2644	2645	2648	2649	2674
#20	–	–	–	–	–	–	–	–	–	–	–	–
#21	+	–	+	–	–	–	–	–	–	–	–	–
#22	–	–	–	–	–	+	–	–	–	+	–	+

Table 4.5: Summary of tracer test results at the main glacier stream (Lachon) and the Glarey spring. $^{c}/_{M}$ means maximum concentration normalised by injected tracer mass.

Results	Lachon stream	Glarey spring		
	21	20	21	22
D(m)	2460	6570	6325	5785
t (h)	17.9	19.5	19.6	15.3
$^{c}/_{M}$ $(10^{-6}m^{-3})$	11	23	12	6
R (%)	2.5	40.7	14.1	32.7

toward the principal glacier stream, while the central and southern part are drained by the immediately underlying karst aquifer. The irregular shape of the BTC can be explained by the highly variable flow rate of this meltwater stream. The peak time is 17.9 h and the recovery rate is only 2.5 %, suggesting that large parts of the tracer went elsewhere (Tab. 4.5). All three tracers were detected at the Glarey spring (Tab. 4.5), where a fluorometer and auto-sampler were installed, confirming that this spring is the main drainage point of the entire Tsanfleuron glacier and karst system. Uranine was only detected at this spring but not at any monitoring site around the glacier, confirming direct and rapid connection between the glacier moulin and the spring, presumably via subglacial swallow holes. The two distinct peaks of the Uranine BTC may point to the presence of two subglacial swallow holes connected to different karst conduits (Fig. 4.7). However, high diurnal meltwater discharge variations can also create multi-peak BTCs (see also capter 3). With these tracer results and surface stream observations, infiltration types may be spatially separated. About half of the glacier meltwater production in the higher western zone (fig 4.8) flows directly inside the aquifer subglacially, without reaching the glacier snout. The other half of meltwater production partially infiltrates under the glacier but also flows into the Lachon stream along the glacier front. This second zone also contains the surface streams that come from the first zone. Softer rocks and important depressions are witnesses of a higher glacial erosion in the northern area, where the glacier is thicker, and therefore a possible excess of sediments is expected to accumulate and colmate many swallow holes or dolines. It would partly explain why recovery rates were lower for sulforhodamine G (#21) as described below.

SulfoG recovery is higher at the Glarey spring (14.1 %) than in the Lachon stream (2.5 %), while transit times are similar, although the distance to the spring is 2.6 times larger than to the

monitoring site in the stream (Tab. 4.5 and Fig. 4.7). These findings demonstrate that there are two recharge pathways between the northern part of the glacier and the spring. An infiltration into subglacial swallow holes with a direct underground passage in the karst aquifer toward the spring (19.6 h for 6,325 m), and a drainage near the glacier base towards the main glacier stream (17.9 h for 2,460 m), which sinks underground via swallow holes 3 km farther downstream. These swallow holes are connected to the spring, as demonstrated by tracer test #19 (6.1 h for 2,274 m). The second peak of the SulfoG BTC (Fig. 4.7) can be interpreted as the arrival of tracer that travelled along this second pathway and was largely dispersed.

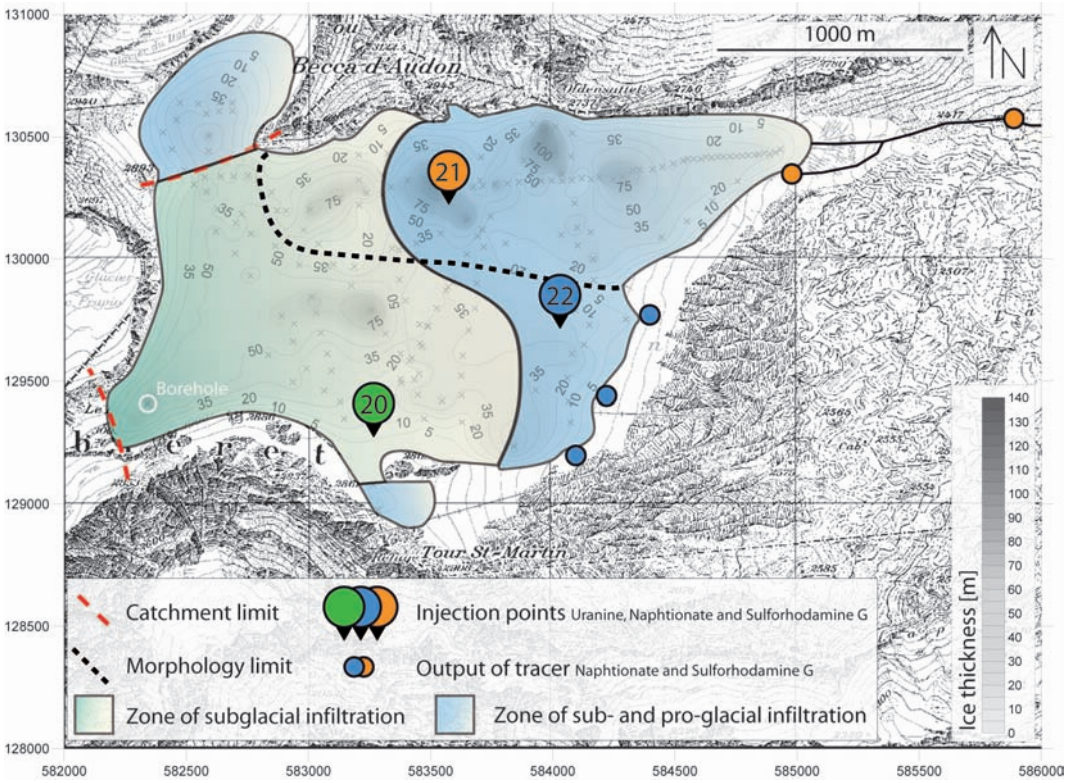

Figure 4.8: Summary map with morphologic and infiltration zones on the Tsanfleuron glacier. Black tilled line separates the main glacier tongue with higher thicknesses from the southern area, where the glacier is flat and less thick. Blue and green zones represent the estimated area of subglacial and partly sub- and pro-glacial infiltrations. Background is illustrated with thickness measurements. Tracer injections and positive charcoal bags are also represented.

Naphthionate was detected in three charcoal bags installed at the glacier front and also arrived at the Glarey spring, which allows the identification of the relevant pathways: The supraglacial meltwater stream sinking into the glacier moulin (#22 in Fig. 4.5) flows at the glacier-limestone interface along three different Nye channels, reappears at the glacier front and then sinks underground into three swallow holes, which are connected to the spring. The Naphthionate BTC (obtained from laboratory analyses of water samples, which are more reliable for this dye than measurements with field fluorometers) displays two peaks, which may correspond to different Nye channels and swallow holes (Fig. 4.7).

4.5 Conclusions

The combined use of geophysical and hydrogeologic methods made it possible to assess the geometry and volume of the Tsanfleuron glacier, estimate the stored freshwater volume, characterise hydrologic glacier-aquifer relations, and make preliminary prognoses concerning the future availability of freshwater from the Glarey spring, which is used for drinking water supply and irrigation. The glacier can be subdivided into a northern zone forming a glacier tongue, and a thin, "pancake-like" central to southern zone. The subglacial morphology includes depressions and mounts, similar to the karst landscape below the recent glacier front that has been exposed due to rapid glacier retreat since 1855/1860. The northern zone of the glacier partly drains via subglacial swallow holes and partly contributes to the main glacier stream that sinks underground 3 km downstream of the glacier mouth (Fig. 4.9A). The central and southern part drains via numerous swallow holes underneath the glacier and near its front (Fig. 4.9B). Similar drainage patterns have been described for glacierised karst systems in the Rocky Mountains, Canada (Smart 1983, 1997).

In 2007/2008, the Tsanfleuron glacier included about $100{\cdot}10^6 m^3$ of ice ($92{\cdot}10^6 m^3$ water equivalent). Glaciers accumulate snow and ice in winter and release meltwater in summer. Under equilibrium conditions (no retreat or advancement), glaciers do not exert much influence on the long-term water budget of a hydrologic basin, as there is balance between accumulation and ablation by sublimation, evaporation and meltwater production, the latter contributing to runoff and recharge. Glaciers at equilibrium mainly influence the variability of connected freshwater resources by delivering meltwater during warm periods. However, retreating glaciers do alter the water balance: The Tsanfleuron glacier currently loses 1.5 m thickness per year, corresponding to $3.9 \cdot 10^6 m^3$ of water. This is a transient quantity that is available today but will be missing when the glacier disappears. Although reliable prognoses concerning climate change and glacier retreat are problematic, simple extrapolation of the current trend suggests that this small glacier might have disappeared by 2030. However our glacier model presents a recurrent error in the thickness by not considering the deep resistive layers of ice. Moreover the glacier retreat leaves ice at higher altitude, where it melt slowlier. The glacier is therefore not expected to disappear before 2050 or 2070. The disappearance of the glacier will reduce the present-day annual discharge of the Glarey spring ($2.1 \cdot 10^7 m^3$) by ca. 20%. Preliminary water balance estimations (that will be refined and will be presented in detail in chapter 6) suggest also a possible loss of 20%. Nearly all of this spring flow loss would occur during summer and autumn, causing possible temporary water shortages.

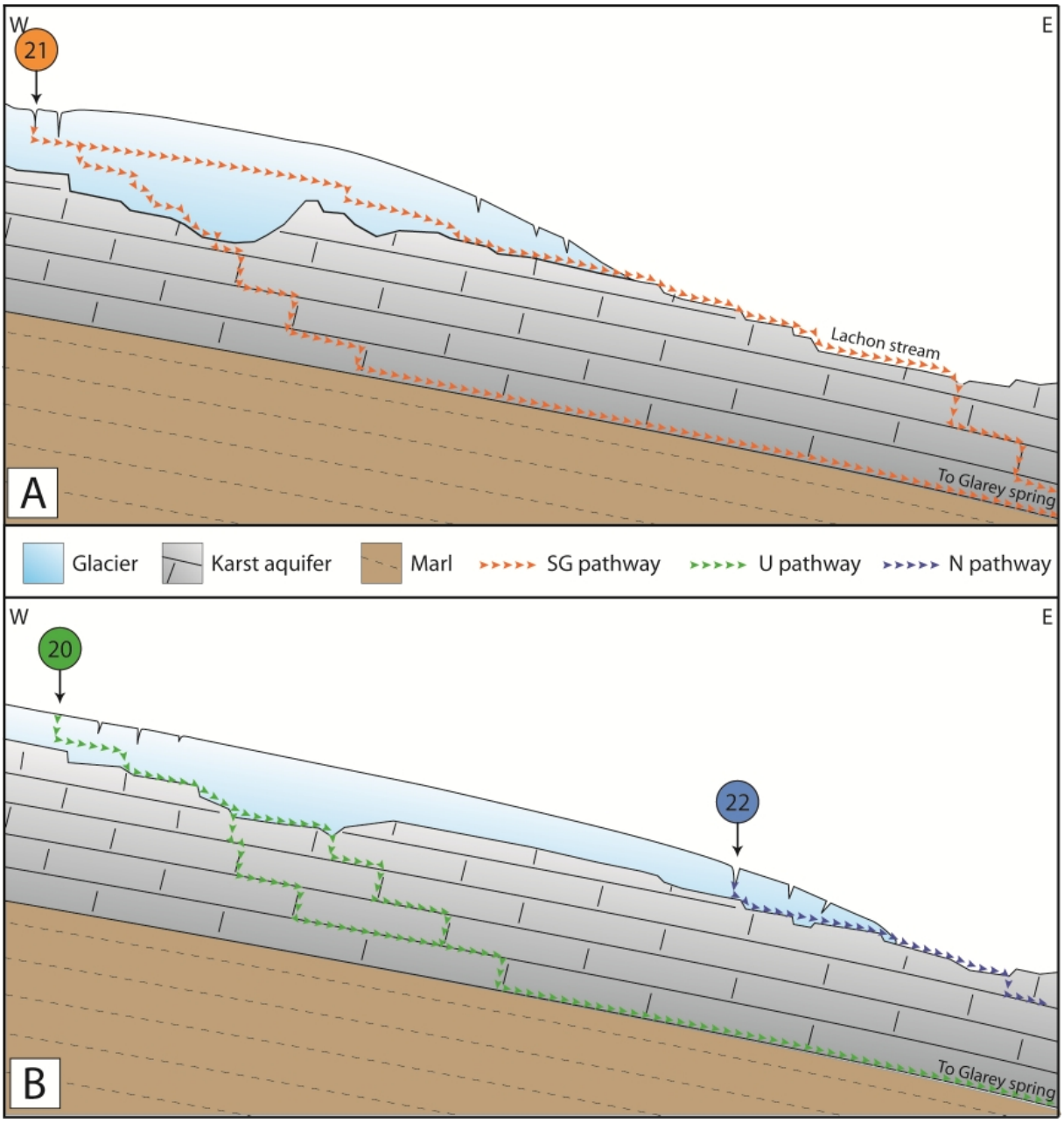

Figure 4.9: Schematic illustration of glacier-aquifer relations (A) in the northern zone, and (B) in the central to southern zone of Tsanfleuron glacier, based on geophysical glacier surveys and tracer tests with Sulforhodamine G (#21), Uranine (#20) and Naphthionate (#22). On the right side of the illustrations, the limestone layer continues towards the Glarey spring.

Chapter 5

Use of stable water isotopes to characterize the relationship between glacier melt and karst aquifer dynamics

5.1 Introduction

In alpine catchments, where high elevation differences are common and water is present in different phases (ice, snow and liquid), water stable isotopes allow to differenciate the different contributions of a sampled spring. Because isotope ratios vary with altitude, temperature and phases, water volumes at the output can be separated into different contributions corresponding to their own isotopic input (Huth et al., 2004). Stable isotopes are used here as natural tracers (Falcone et al., 2008). Ice, snow and rain samples therefore have to be taken in order to have a good view of the isotopic ratios for each phase and altitude. Regular spring samples allow to establish seasonal variations and compare these to common regional seasonal variation curves.

The first step of the water stable isotope campaign was to differentiate ratios of water coming from ice, snow or rain, and water from the aquifer base flow at Glarey spring. These ratios were then compared with the time series measured at the output of the system. Moreover hydrograph separation may be produced with this information (Taylor et al., 2002). One of the aims of this campaign was to distinguish the different contributions at Glarey spring and their repartition during seasons, but also to analyse the temporal shift between infiltration of each component and the isotopic signal variations at the output. Such knowledge also helps to produce the water balance but this subject will be developped further in chapter 6.

5.2 Local isotopic variations

5.2.1 Sampling methods

More than 290 samples of the three water phases available on the test site (water, snow and ice) were taken between 2008 and 2010, at different altitudes, during variable weather events and in the three available water phases in the test site (liquid, snow and ice). Water was immediately sampled in 1.5 mL glass vials closed with impermeable septum caps. For snow samples, the aim was to take the whole thickness. A long instrument made of a 2 m long steel tube was created. It allows to dig about 1.5 to 1.8 m and to keep the snow core, which is representative of the stable isotope values along the snow profile. Snow samples are much bigger and were taken in plastic bags that can be hermetically closed. After melt in a low temperature room (4°C) to minimize evaporation, they were stored in large vials of 100 mL. Ice samples were only taken in the 10 first centimeters of the glacier and stored in the 1.5 mL vials. All samples were kept in a freezer to avoid evaporation. The sampling campaign was separated in three types.

- Manual sampling of the different types of recharge to estimate the input values including surface streams, snow cover, ice melt (on moulins for example) and ice;
- Cumulative rainfall samples were taken at different elevations to calibrate the local relation between altitude and stable isotopes. Water was collected in a 2 L recipient with a funnel on its top. The diameter of the funnel was chosen to collect rain during many months. A parafin oil layer of 2 cm was added in the recipient in order to avoid evaporation between rain events in the field;
- Times series were done to establish daily variations at the Glarey spring, along with seasonal sampling to characterize annual variations. For this purpose, samples were taken manually or through automatic samplers.

5.2.2 Rainfall, local meteoric water line and elevation gradient

Rain samples were taken in summer 2008 and twice in summer 2009 in order to establish the altitude isotope ratio correlation but also to compare with the already available meteoric water lines. For the Rhône valley the line was established at $\delta^2H = 7.58 \cdot \delta^{18}O + 5.2$ (Fette et al., 2005) and for northern Switzerland at $\delta^2H = 7.55 \cdot \delta^{18}O + 4.8$ (Pearson et al., 1991). The $\delta^{18}O - \delta^2H$ relation (see also fig. 5.3) obtained for this work is:

$$\delta^2H = 7.02 \cdot \delta^{18}O - 1.34 \tag{5.1}$$

During the first sampling campaign (summer 2008) only small parts of the rainfall were taken and the correlation between altitude and stable isotopes were unusable because of high temporal variations occurring during rain events. These results had significantly higher isotopic values, but they kept linearity with the next rain samples taken in 2009. For the second and third sampling campaigns in summer 2009, a cumulative rain gauge with a system to avoid evaporation, was used

during one month to measure the average value for precipitation at different elevations (1550, 2120, 2300 and 2550 m). Results (Equ. 5.2) are very similar to the literature relations (Equ. 5.3) from Fette et al. (2005) and give an isotopic gradient per 100 meters of -0.34 ‰ for $\delta^{18}O$.

$$Z = -298.1 \cdot \delta^{18}O - 1913.9 \ (summer) \quad Z = -282.8 \cdot \delta^{18}O - 3076 \ (winter) \tag{5.2}$$

Tsanfleuron data

$$Z = -298 \cdot \delta^{18}O - 1648.2 \ (summer) \quad Z = -285.3 \cdot \delta^{18}O - 3406.1 \ (winter) \tag{5.3}$$

Regional data (Fette et al., 2005)

Winter data were collected below Glarey spring (at elevations between 1100 and 1550 m) and at the top of studied site (2650 to 2800 m). Sampling campaigns were chosen in order to collect snow as fresh as possible. Results (Equ.5.2) after removal of outliers (too old snow) are close to the elevation line of this area (Fette et al., 2005). The snow's isotopic values change rapidly, and even after some cold days a large divergence from this linear relation is observed.

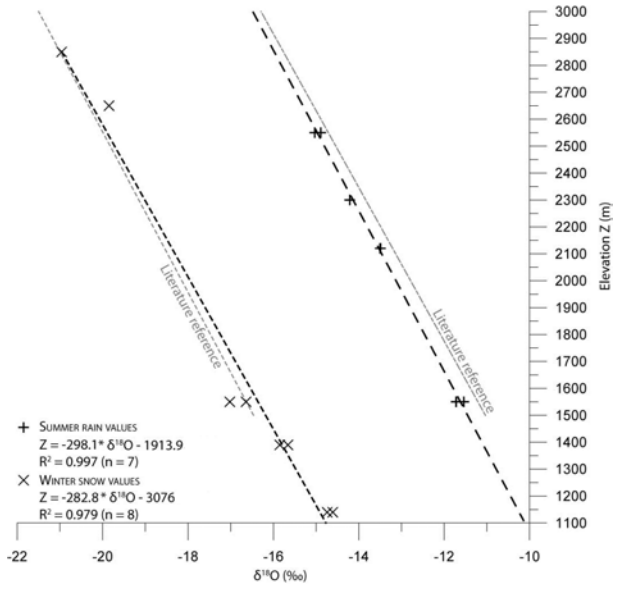

Figure 5.1: $\delta^{18}O$ values at different elevations. The Tsanfleuron results for summer season ($Z = -298.1 \cdot \delta^{18}O - 1913.9$) are the small black crosses, very close to the (Fette et al., 2005) summer linear relation ($Z = -298 \cdot \delta^{18}O - 1648.2$ in double dashed grey line). Winter samples ($Z = -282.8 \cdot \delta^{18}O - 3076$) are also equivalent to the winter linear relation ($Z = -285.3 \cdot \delta^{18}O - 3406.1$ in simple dashed grey line) given in the literature.

The altitude gradient for snow is -0.35 ‰/ per 100 meters, slightly higher than for summer rain. An inverse (positive) gradient with light isotopic compositions at low altitude and heavy precipitation a high elevations may theoretically be observed (Moran et al., 2007). As it was not possible to immediatly collect the exact snowfall values, and since isotopic ratios in snow change very fast after deposition, such gradients were not measured. In different alpine zones, much lower snow gradients (0.05 per 100 meters) were obtained (Novel et al., 1999; Siegenthaler and Oescheger, 1980; Dray et al., 1990) but rarely inverse gradients. Therefore this gradient will be used in order to

characterize the snow deposition (table 5.1), even if some doubts remain concerning the heterogeneity and freshness of analyzed snowpacks.

In order to characterize the recharge as precisely as possible, it is necessary to define elevation zones that correspond to the isotopic ratios obtained by rain samples. To simplify, the karrenfield surface was separated into 15 iso-altitude zones inside the Glarey spring catchment limits (Appendix D.2). Table 5.1 shows the value in m^2 of each area and their mean isotopic input values based on equations 5.2.

Table 5.1: Isotopic input values on the Glarey spring catchment, based on elevation zones and the winter and summer relations described in Equ. 5.2. The summer values are corrected by glacier areas that cover the considered zone. Mean values for all of the catchment are weighted by the zone's percent

Zone (m)	*Area* (m^2)	*Area ratio* (%)	*Glacier* (%)	$\delta^{18}O$ (*Summer*)	$\delta^{18}O$ (*Winter*)
Below 1600	26993	0.2	0	−11.62 ‰	−16.45 ‰
1600 - 1700	73269	0.5	0	−11.95 ‰	−16.80 ‰
1700 - 1800	100263	0.7	0	−12.29 ‰	−17.15 ‰
1800 - 1900	173532	1.3	0	−12.63 ‰	−17.51 ‰
1900 - 2000	77125	0.6	0	−12.96 ‰	−17.86 ‰
2000 - 2100	273797	2.0	0	−13.30 ‰	−18.22 ‰
2100 - 2200	1430685	10.7	0	−13.63 ‰	−18.57 ‰
2200 - 2300	2163380	16.1	0	−13.97 ‰	−18.92 ‰
2300 - 2400	1611930	12.0	0	−14.30 ‰	−19.28 ‰
2400 - 2500	1480816	11.0	5	−14.55 ‰	−19.63 ‰
2500 - 2600	1773894	13.2	8	−14.80 ‰	−19.98 ‰
2600 - 2700	998779	7.4	40	−14.56 ‰	−20.34 ‰
2700 - 2800	1353558	10.1	60	−14.54 ‰	−20.69 ‰
2800 - 2900	1685199	12.6	70	−14.63 ‰	−21.04 ‰
Above 2900	185102	1.4	90	−14.60 ‰	−21.40 ‰
	Sum			*Mean*	*Mean*
	13408324			−14.28 ‰	−19.66 ‰

In order to calculate the real area values a surface weighted average was built added with glacier input when necessary. The glacier area is 2.7 km^2 and it covers the highest elevation zones. 90% of the 2900 zone, 70% of the 2800 to 2900 m zone and 60% of the 2700 to 2800 m zone, 40% of the 2600-2700 m zone, 8% of the 2500-2600 m zone and 5% of the 2400-2500 m are covered by ice. It is then possible to produce a correction factor when glacier melt occurs in these areas (Tab. 5.1).

5.2.3 Glacier isotopic values

The glacier is composed of different ice layers illustrating the snowfall history and the melt of the ice. Therefore it should present many different isotopic values. However, it is globally not the case (Fig. 5.2), the ice of Tsanfleuron glacier has a mean -12.7 ‰ and -91 ‰ for $\delta^{18}O$ and $\delta^{2}H$ respectively (Hubbard et al., 2000). These values also correlate with the surface ice isotopic ratios of our own samples. Some heterogeneities appear in the ice-core analysed in the literature, especially in some ice-layers and at the interface between limestone and ice. The provenance of such differences inside the glacier are the consequences of isotopically light ice layers, which were supposed to have been formed as a crevasse fill near the ice's surface or by accumulating meltwater in an englacial cavity, creating a perched water table. The basal zone, where heavier ratios were found, is debris-rich, close to melt-out till, and suffers from many melt - refreezing processes (Hubbard et al., 2000). These examples prove that even if Tsanfleuron glacier seems globally homogeneous, some specific ice-layers, when melting, may generate various isotopic ratios.

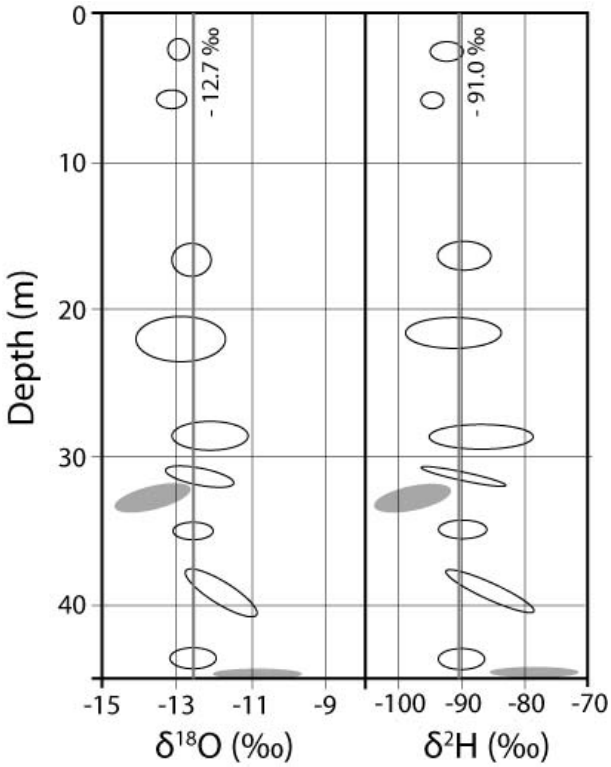

Figure 5.2: Ice core isotopic values in a 44 meter long ice core. Clouds of samples are identified by black ellipses. These samples are globally on the -12.7 ‰ and -91.0 ‰ lines. Only at 33 meters and on the base of the glacier (grey zones) were different isotopic values measured (Hubbard et al., 2000).

The linear regression of bivariate co-isotopic plots defines a relation of $\delta^{2}H = 6.90 \cdot \delta^{18}O - 3.5$ (Hubbard et al., 2000) for ice samples. The explanation for such general homogeneity is probably that glacier flows on the bedrock and slowly sends ice from an altitude of 3000 meters to 2600 meters at the front, completely mixing the isotopic signals (Taylor et al., 2002). Observations of its equilibrium line show that only a very small part of the ice's volume is made of new ice and the major part of the glacier has already suffered multiple freeze and melt cycles.

5.2.4 Isotope ratios at Glarey spring

Glarey samples can aslo be plotted on a $\delta^{18}O - \delta^{2}H$ graph and show a linear relation of:

$$\delta^2 H = 6.86 \cdot \delta^{18}O - 4.72 \tag{5.4}$$

The slope of the line is lower than the local water meteoric line ($\delta^2 H = 7.02 \cdot \delta^{18}O - 1.34$), proof of evaporation or mixing processes between rainfall and spring water.

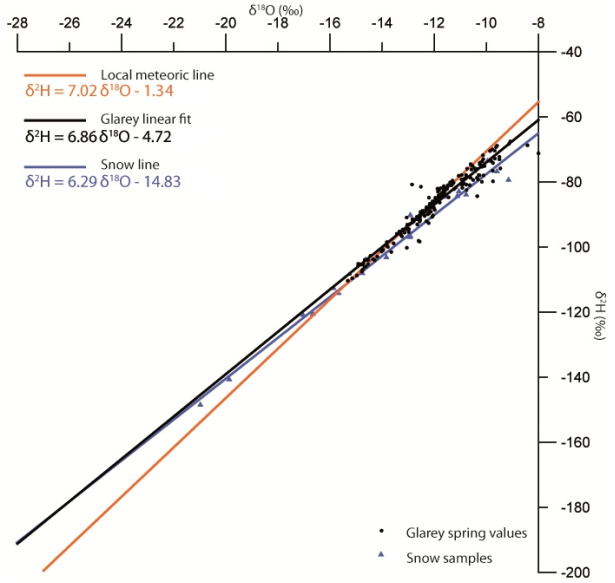

Figure 5.3: Difference between liquid precipitation in orange ($\delta^2 H = 7.02 \cdot \delta^{18}O - 1.34$), snow in blue ($\delta^2 H = 6.29 \cdot \delta^{18}O - 14.83$) and the isotopic composition of Glarey spring water in black ($\delta^2 H = 6.86 \cdot \delta^{18}O - 4.72$). Some evaporation or mixing processes occur during water pathways to the spring as the slope of the Glarey spring line is lower than the local meteoric water line.

Some samples from Glarey spring were removed because they present a characteristic evaporation line ($\delta^2 H = 1.99\delta^{18}O - 58.04$) with a smaller slope. These evaporative samples are considered as outliers because they belong to time series data (time step was 1 hour) and the previous and next samples do suffer from this. As isotopic value could not change so rapidly, evaporation certainly occured during transport and storage of these samples.
Time series samples at Glarey spring provide two ranges of variations. Seasonal variations (Fig. 5.4) contains all the different isotopic ratios measured at Glarey spring between 2008 and 2010 (Tab. 5.2) and present an annual $\delta^{18}O$ range from -15.3 ‰ to -8.0 ‰ and a $\delta^2 H$ from -110.4 ‰ to -59.0 ‰. During winter season, some periods with the highest electrical conductivity values allow a sampling of baseflow values. They were about -11.2 ‰ for oxygen and -81.7 ‰ for hydrogen. Snow deposition during winter are more depleted in heavy molecules with mean theoretical values for $\delta^{18}O$ and $\delta^2 H$ of -19.7‰ (Tab. 5.1) and -139.7‰.

The isotopic ratio of meltwater coming from snow pack is highly variable over time. Isotopic values early in the season are lower than later in the season. Therefore hydrograph calculations using a mean value will overestimate the melwater fraction at the beginning of melt season but underestimate them towards the end. This is a consequence of isotopic fractionation between solid and liquid phases (Taylor et al., 2002). A fractionation factor $\alpha_{solid-liquid}$ between snow and water (Equ. 5.5) enables

an estimation of the oxygen 18 value of the released water (Suzuoki and Kimura, 1973) during snow melt season. This process only occurs in new meltwater, when the heaviest part of it refreezes and the lightest part is washed out. No fractionation processes can occur in the solid phases, as molecules do not have a significant veolocity.

$$\alpha_{solid-liquid} = \frac{^{18}R_{solid}}{^{18}R_{liquid}} = 1.0028 \quad at\ 0℃ \tag{5.5}$$

$$^{18}R_{solid} = (\frac{\delta^{18}O}{1000} .^{18}\ R_{VSMOW}) +^{18}\ R_{VSMOW} \tag{5.6}$$

$$^{18}R_{liquid} = \frac{^{18}R_{solid}}{1.0028} \tag{5.7}$$

The mean δ-notation obtained for snowfall should then be transformed using a general isotopic ratio (Equ. 5.6). The meltwater ratio is calculated with equ. 5.7. Finally to obtain δ-notation once again for liquid and solid phases, equ. 2.18 is applied. Theoretically the global volume of snow equals 1 and for the first meltwater percents removed, calculation gives a result of -22.44 ‰for meltwater that flows ou of the snow pack, but a part is refreezing at -19.67 ‰ (appendix D.1). At the end of snow melt season, all the snow mass has melted into an equivalent mass of water, and if no evaporation has occured, total meltwater should have the same isotopic value as the primary snow volume. The enrichment factor $\epsilon_{solid-liquid}$ is -2.8 ‰ (Suzuoki and Kimura, 1973). At Glarey spring, the measured isotopic values during snow melt season reach the lowest observed values with a $\delta^{18}O$ of -15.3 ‰ and a $\delta^{2}H$ of -110.4 ‰. The process is the same for the glacier, where refreezing processes may change the estimated uniform isotopic ratios of the released meltwater. As no exhaustive experiments were done for daily melt, it was difficult to estimate the amount of refreezing processes inside the Tsanfleuron glacier. A uniform value was taken, but it is important to keep in mind that it is a sharp simplification.

Aquifer baseflow was found to be heavier than all the other parameters. Water should come from lower elevation than the measured recharges. But no area was found to respect our $\delta^{18}O$-elevation line. Such low values are expected to infiltrate at an altitude lower than 1500 meters, lower than Glarey spring. An other hypothesis is some evaporation processes inside the aquifer during a very long residence time of this water.

For summer season it is more difficult to separate glacier melt from rainfall as only mixed isotopic values arrive at Glarey spring. In order to have a better understanding of this, daily variations during summer season were analyzed, when the glacier is melting. Here isotopic ratios range from -96.3 ‰ to -76.0 ‰ and -13.3 ‰ to -10.7 ‰ for $\delta^{2}H$ and $\delta^{18}O$ respectively. The samples were first taken during tracer test experiments, which do not allow to adapt for meteorological conditions or time step variations. Many of the 2008 samples series were thus difficult to interpret. In two dry periods (early July and early September) of summer 2009, automatic samplers were deployed during five days with a two hour time step in order to characterize the glacier's contribution and isotopic

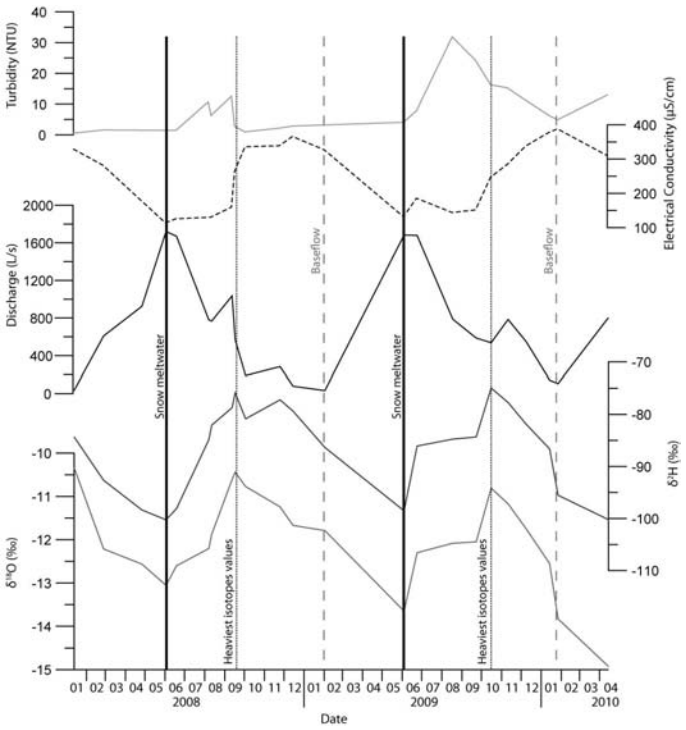

Figure 5.4: Two year time series, with selected $\delta^{18}O$, $\delta^{2}H$, discharge, electrical conductivity and turbidity values. When snow melts, the isotopic values decrease and reach a minimum in early June. Then fractionation has left heavy water in remaining snow and the signals increase to a maximum in end September or early October. Minimum discharge at Glarey spring indicates baseflow in end January. Baseflow does not coincide with the heavy isotopes. It may be a proof that snow melts enough in winter to decrease the isotopic signals or that there is a mix between heavy ice meltwater and snow meltwater in winter. The isotopic peaks correspond to the increase of electrical conductivity and decrease of turbidity at the end of the ice melt season.

values.

Each signal varies every 24 hours, but maxima and minima occur at different times. Discharge peaks occur between 18h30 and 20h30. Electrical conductivity peaks, which illustrate water with a longer residence time in the aquifer, occur two or four hours earlier. The minimum of conductivity corresponds to the maximum arrival of glacier meltwater, which has very low ion concentrations, occurs two to four hours after maximum discharge. Glacier meltwater should also have the isotopic ratios observed for ice (with a $\delta^{18}O$ of -12.7 ‰ and a $\delta^{2}H$ of -91 ‰) but it takes about 10 hours more to reach this baseline (Fig. 5.5). One hypothesis to explain this specificity is that the first water infiltrating the aquifer is contained in the basal interface of the glacier, where melt and refreeze processes often occur (Hubbard et al., 2000). This water is isotopically heavier than usual glacier meltwater, postponing the arrival of the isotopic reference for the glacier but not the minimum of electrical conductivity.

5.3 Hydrograph analyses

5.3.1 Methodology

By using stable isotope values, it is possible to separate the "new water" contribution (from a snow, rain fall or glacier melt event) from the "old water" (pre-event water or aquifer baseflow) in the spring hydrograph (Taylor et al., 2002). The method uses two-component mass balance equations describing the water and the isotopic fluxes at a spring (Lakey and Krothe, 1996).

Table 5.2: Summary of the mean isotopic ratios for each water component at Glarey spring. Rainfall values contain glacier melt during the precipitation event (see Tab. 5.1). Fresh and old snow melt values come from theoretical relations between altitude and isotopes and were calculated with fractionation processes between early light isotopic release and heavy isotopes that are refreezed in solid phase. Aquifer baseflow was measured during the highest electrical conductivity periods and glacier meltwater is based on ice core drilling (Hubbard et al., 2000) and surface sampling

Water component	$\delta^{18}O$	$\delta^{2}H$	Electrical Conductivity (EC)
Aquifer baseflow (n=35)	-11.2 ‰	-81.7 ‰	420 µS/cm
Fresh snow meltwater (n=19)	-22.4 ‰	-158.2 ‰	15 µS/cm
Old snow meltwater (n=19)	-17.1 ‰	-121.1 ‰	15 µS/cm
Glacier meltwater (n=8)	-12.7 ‰	-91.0 ‰	5 µS/cm
Mean rainfall (n=20)	-14.3 ‰	-101.8 ‰	25 µS/cm

$$Q_{sp} = Q_{nw} + Q_{ow} \tag{5.8}$$

$$Q_{sp} \cdot \delta_{sp} = Q_{nw} \cdot \delta_{nw} + Q_{ow} \cdot \delta_{ow} \tag{5.9}$$

In equations 5.8 and 5.9, Q_{sp} is the output measured discharge, Q_{nw} the amount of new event water and Q_{ow} the amount of pre event water. The δ-notations correspond to $\delta^{18}O$ or $\delta^{2}H$ values for output, event water or pre event water (respectively δ_{sp}, δ_{nw} and δ_{ow}). The solution of this equation system is:

$$Q_{nw} = Q_{sp} \cdot \frac{\delta_{sp} - \delta_{ow}}{\delta_{nw} - \delta_{ow}} \tag{5.10}$$

A problem observed for this method is that only few parameters are considered. In equation 5.10 only δ values are used and their properties highly influence the hydrograph's separation. This method might give negative discharge values. Daily time series illustrates that glacier meltwater arrival is driven by many parameters, mainly electrical conductivity. Occulting such parameters decreases the accuracy of the calculation and to improve the results, two different parameters were used. Therefore, calculations do not directly concern discharge values, but new relative factors ζ and κ, which are used to weight the spring discharge. Temperature, $\delta^{2}H$ or any other parameter can be used. Electrical conductivity was chosen because this parameter is closely correlated to meltwater from snow or ice.

$$\delta^{18}O_{sp} = \zeta \cdot \delta^{18}O_{nw} + \kappa \cdot \delta^{18}O_{ow} \tag{5.11}$$

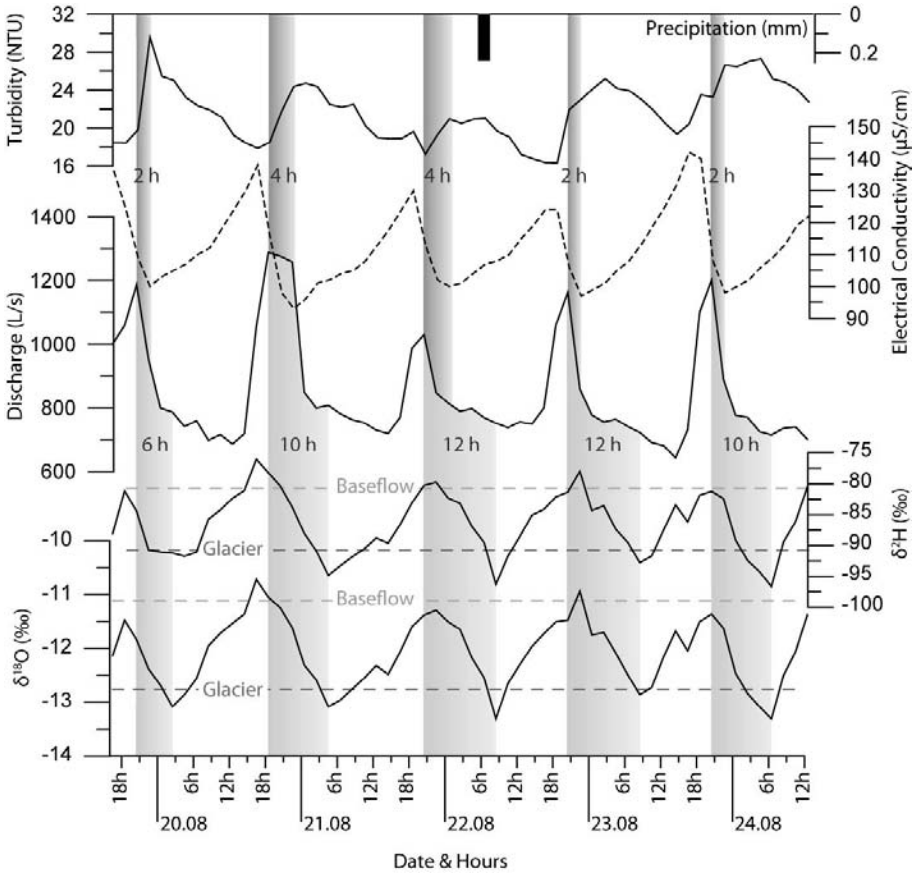

Figure 5.5: Variations of isotopic ratios at Glarey spring, discharge, electrical conductivity and turbidity during five days without rain. Mean isotopic ratios observed for baseflow and glacier melt (we assume here that glacier produces a uniform isotopic ratio) are drawn in light and dark grey dashed line respectively. Discharge peaks occur 2 or 4 (dark grey boxes) hours before the minimum electrical conductivity, which represent the arrival of glacier water with low conductivity. Curiously the isotopic ratios reach the glacier baseline only 10 hours later (light grey boxes). This lag is perhaps an issue of our uniform isotopic value for ice melt.

$$EC_{sp} = \zeta \cdot EC_{nw} + \kappa \cdot EC_{ow} \tag{5.12}$$

In relations 5.11 and 5.12 , $\delta^{18}O_{sp}$ and EC_{sp} respectively represent the isotopic ratios and the electrical conductivity of water flowing at Glarey spring, the "old water" parameters are $\delta^{18}O_{ow}$, EC_{ow} and the quantity in Glarey spring equals κ. The "new water" parameters are $\delta^{18}O_{nw}$, EC_{nw} weighted by ζ. Factors ζ and κ represent the water available at the spring in percent, thus their sum must equal 1. These factors weight the measured Glarey discharge Q_{sp} and give the proportion of each water component.

We work here with only two inputs, event and pre event water. If another event is added in the system (rainfall and glacier melt or snowfall and glacier melt) the equations need to have more terms, depending how many input events are observed. More physical parameters have to be defined, because

each term that is added in the equation increases the quantity of equations necessary to solve the system.

5.3.2 Application and limits

Two time series were taken during the summer 2009 during dry weather periods in order to see the glacier's variations. From 10 to 15 July at the beginning of ice meltwater production and from the 19 to 24 August (Fig. 5.5) during ice melt season. Therefore a two-component equation system (Equ. 5.11 and 5.12) is applied with electrical conductivity (Equ. 5.14) and $\delta^{18}O$ (Equ. 5.13). Glacier melt and baseflow parameters used here are taken from table 5.2, but depend on the considered components. Rain or snowmelt may replace glacier meltwater.

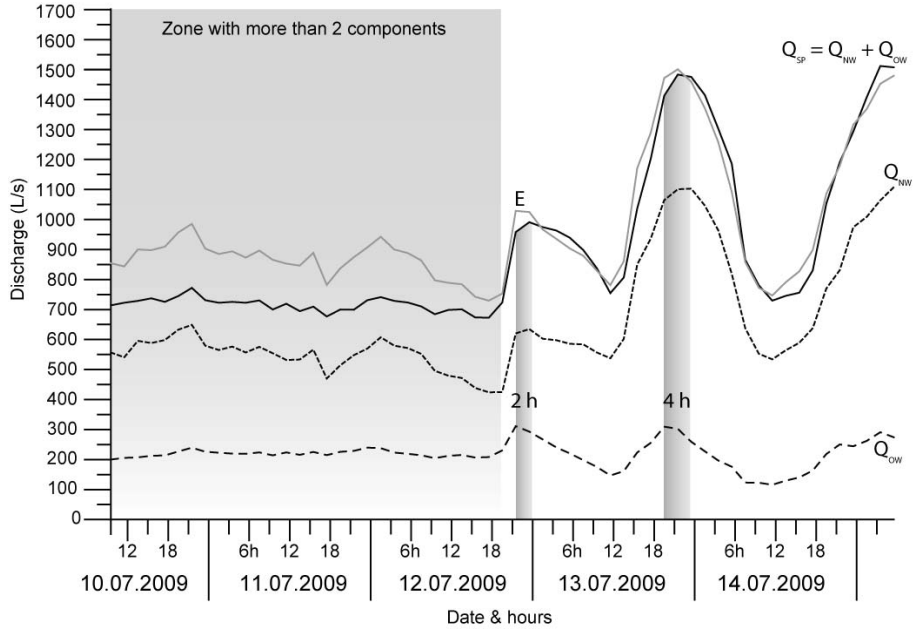

Figure 5.6: Hydrograph at Glarey spring (Q_{sp}) between 10.07.2009 at 9:30 to 15.07.2010 at 5:30. The two tilled lines represent the pre event water Q_{ow} and the event (here glacier meltwater input) Q_{nw} water. The grey line is the sum of the Q_{ow} and Q_{nw} water and illustrates the error E of the method. From 10 to 12 July, the error is high due to the previous days' precipitation and low air temperature. After this, the daily variations due to ice melt occur again and a time lag from 2 to 4 hours between the maximum of Q_{ow} and Q_{nw} respectively, is represented by grey boxes. It illustrates pressure pulse effects in the karst aquifer.

$$\delta^{18}O_{sp} = -12.7 \cdot \zeta - 11.2 \cdot \kappa \tag{5.13}$$

$$EC_{sp} = 5 \cdot \zeta + 420 \cdot \kappa \tag{5.14}$$

The factor κ hypothetically equals $(1-\zeta)$ and their sum must be 1. The divergence of the sum represents the uncertainty of the method, which was between 0 % to 25 %. When the error E between the measured discharge and the sum of the two components (see fig. 5.6) is more than 5 %, the accuracy of this method becomes unsatisfaying, due to other components that contribute to the spring discharge. These results are then eliminated. Equations 5.15 and 5.16 present the solutions of the two component systems, which depend on the measured electrical conductivity and $\delta^{18}O$ at Glarey spring.

$$\zeta = \frac{4 \cdot EC_{sp} + 150 \cdot \delta^{18}O_{sp}}{1885} \tag{5.15}$$

$$\kappa = \frac{127 \cdot EC_{sp} + 50 \cdot \delta^{18}O_{sp}}{52780} \tag{5.16}$$

By replacing EC_{sp} and $\delta^{18}O_{sp}$ with the Glarey spring measurements, ζ values ranges from 0.562 to 0.867 and κ from 0.210 to 0.400. These factors were applied on discharge measurements from July and August, quantifying water quantity from each provenance. About 74 % of the water comes from the glacier, and only 26 % from the aquifer. Same calculations were done for other seasons (unfortunately without time series analysis) in order to characerize the aquifer dynamics. Interpretation and discussion are presented in the next section.

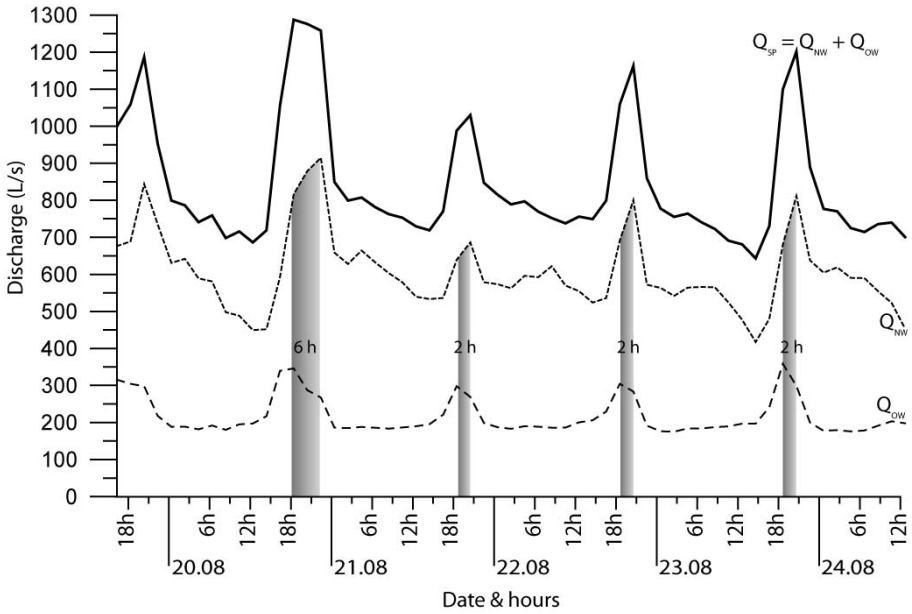

Figure 5.7: Hydrograph at Glarey spring (Q_{sp}) between 19.08.2009 at 16:30 to 24.08.2010 at 12:30. The two tilled lines represent the pre event water Q_{ow} and the event (here glacier meltwater input) Q_{nw} water. As the error is here below 5%, the sum of the two components is not represented but follows the Glarey discharge measurements line. The time lag (from 2 to 6 hours) between the maximum of Q_{ow} and Q_{nw} respectively, is represented by grey boxes.

In July, at the beginning of daily ice meltwater production, the first two days (10 to 12 July) show an error higher than 5 % and indicates that aquifer dynamics are not only influenced by glacier meltwater but by one or more other components. More than 25 mm of snow and rainfall occured the previous five days and mean temperatures of this early July were below 0 °C. The $\delta^{18}O$ values was between -15.32 ‰ and -13.04 ‰ during these two days, which correspond more to snowfall values. Therefore our hydrograph separation does not work for the beginning of the month to the end of 12.07.2009 because at least a third component (snow melt) contributes to Glarey spring discharge (Fig. 5.6). For dry periods of the ice melt season (the second part of fig. 5.6 and all fig. 5.7) a time lag of 2 to 6 hours separates the discharge peaks between the two water components. The first peak comes from the pre event water, followed by the event water peak (glacier ice melt), which is also contemporary with the total discharge maximum. This observation illustrates pressure pulse processes, created by daily glacier meltwater infiltrations (Fig. 5.7).

5.4 Conceptual seasonal aquifer dynamics

5.4.1 Ice melt season

During this season (July to middle October), the last snow finishes to melt but the ice melt is the major recharge of the aquifer between precipitation events. But even if temperature decreases, rainfall creates good conditions for higher melt rates because ice melts faster in contact with water than with air at equivalent temperatures (Hock and Jansson, 2005). The glacier rapidly melts during warm days with hot temperatures but also during rainfall events. Therefore the discharge signal for precipitation is closely related to glacier meltwater as soon as precipitation is not snow deposit on the glacier. During such cases the ice is protected from melting by snow and the precipitation input in the aquifer is delayed, dependent on a sufficient temperature increase. Snow melt at constant altitude is enriched in $\delta^{18}O$ during the beginning and the end of the melt (snow disappearance) by 3.5 to 5.6 ‰ (Taylor et al., 2002). But in summer, because of high melt rates, these temporal variations occur at very small time steps and do not really influence the mean season ratio.

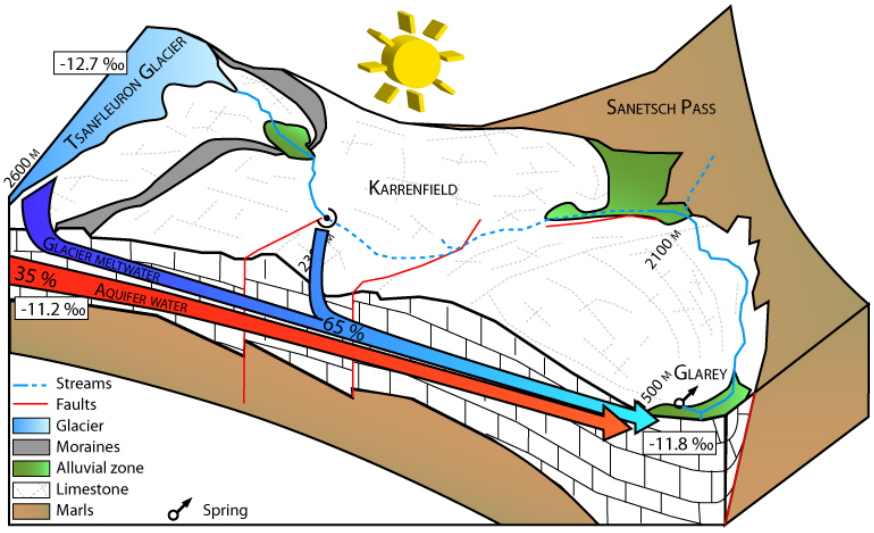

Figure 5.8: Illustration of the water components during a schematic dry ice melt season, with the mean measured isotopic values during the considered season. About 65% of Glarey water comes from the Tsanfleuron glacier. The pre event water is reduced to 35%.

The mean $\delta^{18}O$ values at Glarey spring (-11.8 ‰) are close to the basal isotopic zone of Tsanfleuron glacier (Hubbard et al., 2000) (Fig. 5.2), where values are between -12 ‰ and -10 ‰. As mentioned, the basal water of the glacier arrive to the spring first, followed only 10 hours later by the inner glacier ice meltwater. The hydrograph separation during dry periods, where only the glacier contributes to the spring's discharge, was composed of 74% glacier meltwater and 26% aquifer water (Fig. 5.7). The water coming from the aquifer was considered as baseflow, as no other summer standard values were available, but it was certainly already a mix between glacier and real aquifer baseflow components. With a mean value representing the ice melt season, this effect is more visible and reduces the glacier water amount in this first conceptual model. The main contributions were estimated at 65% for the glacier and about 35% for the aquifer (Fig. 5.8), but it is certainly a minimal estimation.

When rain events occur, the percent of each contribution stays close to that of dry periods (Fig. 5.9) but seems to be slighty lower. About 64% of Glarey spring water comes from the surface of the karrenfield, and represents a mix of glacier melt and rainfall (see Tab. 5.1). Water coming from the aquifer is 36 %. The mixing effect is also present here but can not be clearly evaluated.

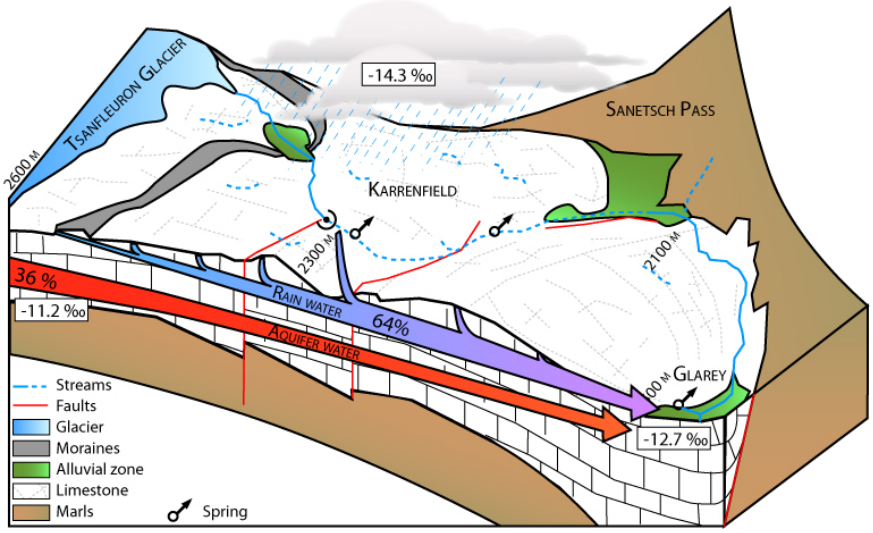

Figure 5.9: In this case, glacier and rainfall were considered as one input (see table 5.1) of -14.3‰. 64% of Glarey spring water comes from the karst surface, quite equivalent to the glacier's only input.

5.4.2 Snow cover season

During the first part of the winter season (from mid October to mid December), the glacier has globally stopped melting and snow starts to accumulate on the glacier and karrenfield surfaces, until the whole area is covered by a large amount of snow (about 2 meters). However the glacier's base is still melting due to thermal flux (about 3 °C from the karst aquifer. The melt rate is about 1 mm per month, which reported to the glacier area recharges the aquifer with about 1 $^{L}/_{s}$. The same process occur for the snow pack, probably at an equivalent melt rate with an input volume of about 4 $^{L}/_{s}$. A constant recharge is therefroe present during winter. At Glarey spring the water volume decreases despite this recharge and reaches its lower values at less than 30 $^{L}/_{s}$. A baseflow recession factor k permits to calculate a hypothetical long term outflow without recharge following the simple exponential law, illustrated in the equation 5.17. Based on fig. 5.10, k equals $-9.7 \cdot 10^{-4}$ and it would

take theoretically about 10 years to totally empty the aquifer of its water. Discharge observed during two or three baseflow months in winter is close to linearity but also presents some significant peaks, indicating that parts of the snow pack at lower altitude sometimes melt. An important melt event is therefore excluded except the basal and continuous melt mentionned above.

$$Q_t = Q_0 \cdot e^{-kt} \tag{5.17}$$

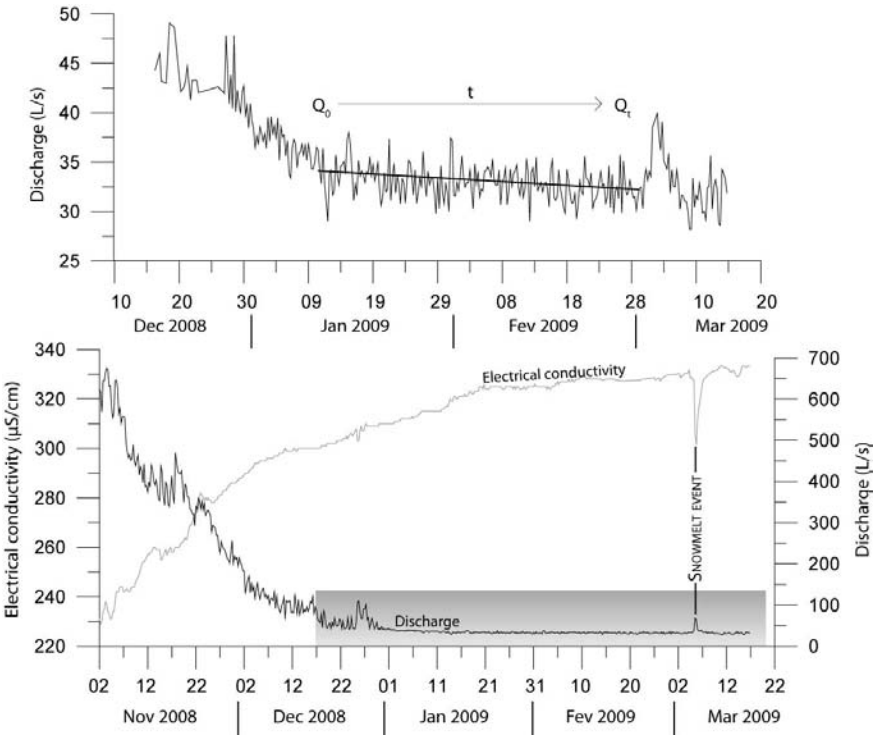

Figure 5.10: Period with minimal discharge between November 2008 and March 2009. A selected part of the curve (grey area of the second graph) is used for calculating the recession factor k using equation 5.17. Q_0 is the discharge at the beginning of the stable part, Q_t the discharge at time t after Q_0.

Discharge and electrical conductivity at Glarey spring reach a supposed aquifer baseflow value. The second part of winter season (from mid December to the end of February) snowmelt events increase, even if new snow is often released. No glacier meltwater is available to recharge the aquifer, glacier dynamics are in standby, protected from air temperature variations by the snow pack. Snow precipitations have a mean $\delta^{18}O$ of -19.7‰ and if small periods of melt occur lighter isotopic water (-22.3‰) is released in the aquifer.

The output signal at Glarey spring is then very high compared to meltwater input. Snow melt recharge is thought to be minimal to help keep the isotopic signal close to the aquifer baseflow. A mean of winter isotopic values during lowest electrical conductivities gives a base flow estimated at -11.2 ‰. Therefore, based on equations 5.11 and 5.12 with parameters from table 5.2, the snow melt contribution to the spring in winter is estimated at 15% (Fig. 5.11), whereas the aquifer flow contributes to 85% of the spring water.

The main observation here is that even in winter, about 15% of Glarey spring's water quantity comes

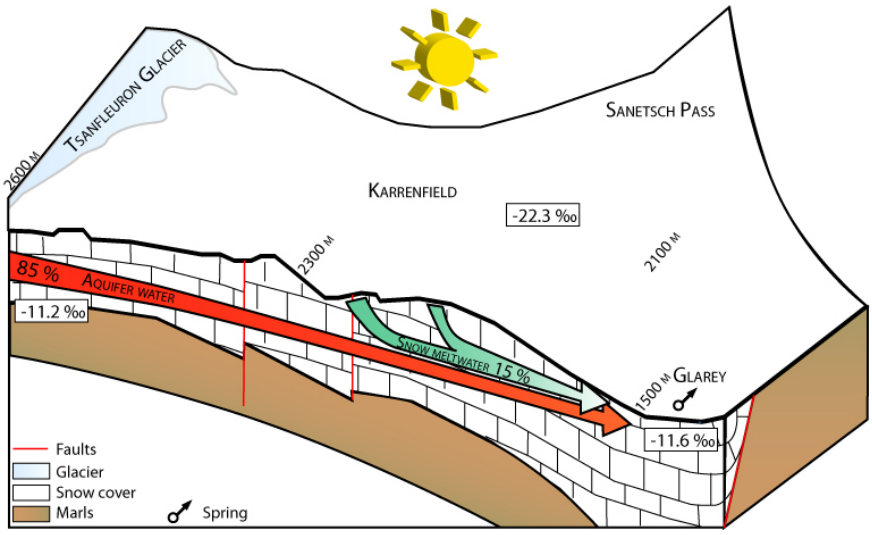

Figure 5.11: Very little meltwater is produced during winter season. Snowfall melts and contributes to the aquifer's output in an order of 15%. The major part of the Glarey water comes from the aquifer's baseflow.

from snow melt. Temperature are sufficiently high to produce snow meltwater and during enough time to transfer it to the aquifer. Probably only the lower part of the catchement suffers from this melt. The quantity of meltwater from snow should certainly be higher compared to the melt area if it would have been possible to localize an elevation limit, where snow does not melt in winter.

5.4.3 Snow melt season

At the end of the snow cover season (from March to July), snow disappears first from the lower then at higher elevations. Isotopic signals are highly variable during this season and interpretation is quite complex. Low elevation snow packs become more rapidly enriched with heavy isotopes than at higher elevations, but liquid precipitation events also mix with old snow meltwater. Faster melt processes occur when snow or ice is in contact with liquid water (Hock and Jansson, 2005), increasing melt but also buffering the snow's isotopic values. Later in the season, in places where snow cover already disappeared, precipitation is not mixed anymore and give typical isotopic signals. To simplify, only snow melt during dry weather was considered. Fractionation processes occur and a mean $\delta^{18}O$ of -17.1‰ for old snow meltwater was defined (with an enrichment factor of 2.6‰ from snow deposition). In this case, more than the half of Glarey water (53%) comes from snow, the rest belongs to aquifer baseflow (Fig. 5.12).

This period also has the highest discharge. Thus this result is certainly not correct because not all parameters have been considered. Many fractionation processes occur and snow does not have a spatially homogeneous melt. Many snow zones remain during the ice melt season and disappear only in mid august.

5.5 Conclusions

Glacierized aquifer systems in alpine regions are very complex. The two forms of precipitation interact differently with glacier, karrenfield or snow cover, if present. Therefore the major difficulty is to understand the implication of every interaction and their consequences for aquifer dynamics.

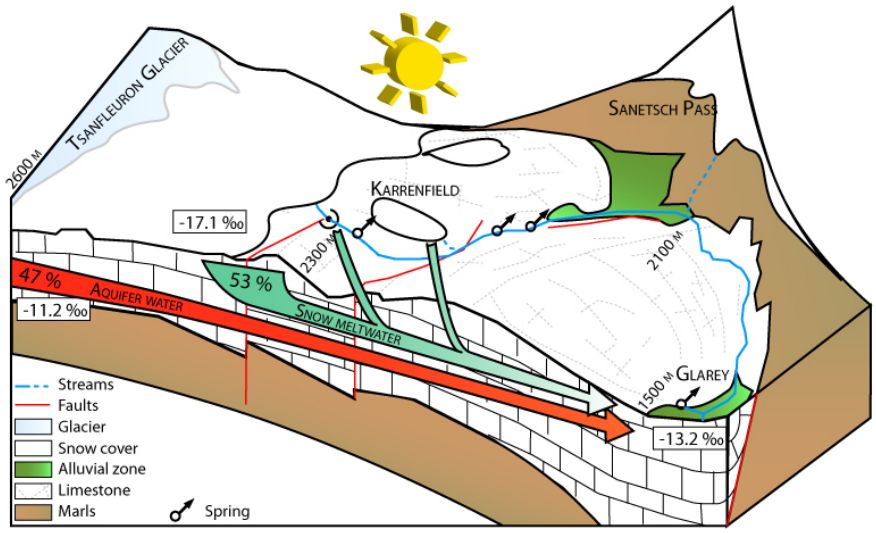

Figure 5.12: When snow cover disappears, fractionation occurs and the mean isotopic ratio of remaining snow is heavier than initial snow precipitation. A 2.6‰ enrichment creates a mean meltwater isotopic value of -17.1‰. 53% of Glarey water comes from the snow melt.

Good natural tracers may help to distinguish every process that occur during the hydrological year. Stable isotopes of water present many advantages for this purpose, but the application creates many difficulties. Fractionation of solid phases are spatially and temporally hard to understand, even with daily air temperature measurements. When does snow or ice start to melt? In which proportion? Does this meltwater immediately reach the aquifer or is it stored before? Does it suffer from freeze-melt cycles and how many times? How do pathways through snow or ice layers affect the initial isotope ratio? Many questions that are partially resolved in this work, but have to be completly in order to best characterize the seasonal and daily behavior of the aquifer.

Apart from these difficulties many information about seasonal and weekly aquifer dynamics were available. The major water components were defined and estimation of their quantities at Glarey spring for each season illustrate input-output properties of the karst aquifer. In November and December snow rapidly accumulates on the karrenfield surface, the aquifer is in standby and does not receive any major input. January and February present the first snow melt events and the first input at Glarey Spring (about 15%). From March to the end of June, the snow cover completely melts and creates a fairly permanent high water level condition in the aquifer. From July to October, the glacier is a continuous input (more than 65%) for the karst aquifer, even during rain events.

Shorter time steps during the glacier melt season introduce time lags between various signals. A pressure pulse delays the minimal electrical conductivity in comparison with discharge maximum. The isotopic signatures corresponding to glacier's inputs are themselves delayed by 10 hours after the maximum of discharge. The heterogeneity of some ice layers and the melt-refreeze zone at the base of the glacier are suspected to be the cause of such differences. These information give an overview of the meltwater processes during the pathway to the aquifer. It partially answers the questions above but more precision and specific measurements are needed for a perfect comprehension of these processes.

Finally all information and characteristics regarding karst aquifer dynamics will be used to achieve one of the principal goals of this study, which is to estimate future water availability in case of

the glacier's disappearance. This will be the subject of the next chapter where a comprehensive but simplified water balance will be developped and long term continuous monitoring curves will be analysed. A hydrograph simulation without glacier for future water availability will also be discussed and compared with these primary input/ouput conceptual models.

Chapter 6

Consequences of retreat and disappearance of a small alpine glacier for the future quality and availability of water[1]

6.1 Introduction

Since the maximum of the "Little Ice Age" in the middle of the 19th century, all alpine glaciers have lost much of their length and volume (Greene et al., 1999; Paul et al., 2004). Glacier retreat has already, and will continue to influence the availability and temporal variability of hydraulically-connected groundwater resources, with implications for ecosystems (Cannone et al., 2008), drinking water supply, agriculture and hydropower (Loukas et al., 2002; Viviroli and Weingartner, 2004). Glaciers store water as snow and ice during cold periods and release it during warm periods (Benn, 1998). During times of glacial retreat, increased meltwater production can lead to temporarily higher freshwater availability in connected streams and aquifers. However, from a long-term perspective, a loss of glaciers as intermediate storage reservoirs is expected to result in local or temporary water shortages, particularly during long dry summers (Schaefli et al., 2007; Seidel et al., 1998).

Climate change impacts on variability and balance of alpine catchments are of first importance to estimate future influences on water resources. But long-term observations are necessary to explain the current evolution of glaciers in reaction to climate variations (Escher-Vetter et al., 2005), often only periods lasting over decades allow a complete overview of climate processes. Unfortunately complete data at the Tsanfleuron test site is only available for about 5 years from 2004 to 2009. However glacier variation data has been collected for more than a century (from 1884 to 2009) clearly illustrating the

[1]This chapter will be published in Hydrology Journal in 2011

climate's impact on alpine ice volumes (Fig. 4.2 and appendix C.1). With such a lack of data only a short term trend is estimated, based on discharge and precipitation variations. Though five years of measurements are sufficient enough to characterize an estimated response of the aquifer upon short and long periods.

The goals of this last chapter are to observe aquifer variations in order to determine its reaction to various input signals at different time steps, but also to discuss the glacier's impact on future water resources. Continuous monitoring at Glarey spring of discharge, conductivity, organic matter and turbidity, as well as daily and annual rainfall measurements at MeteoSwiss stations were mainly used to achieve these objectives.

6.2 Water input, output and transit properties

6.2.1 General catchment overview

Karst alpine catchments are frequent in the Alps, but few of them allow direct access to a complete recharge and drainage system, including glacier, main springs and surface streams. The Tsanfleuron area presents an easily accessible retreating glacier overlying and recharging the upper part of a karst aquifer. The system is mainly drained at its lowest southeastern point by Glarey spring used for drinking water supply and irrigation purpose. Four other springs drain parts of the system. Tschoetre, Marnes and Lizerne springs collect water coming from the southern border of the karrenfield and cross a large part of the stratigraphy (Fig. 3.5). On the North West, Sarine spring drains a small area at the karrenfield limit.

Geologically the test site belongs to the Helvetic zone of the Alps, which contains many karst aquifer systems in Mesozoic limestone, especially in late cretaceous formations. Detailed geological structure of the aquifer and underground drainage were studied in chapters 3 and 4 and allow the delimitation of the catchments of each spring or spring group (Fig. 3.5). The main karst system is built in late Barremian "Urgonian" (Schrattenkalk) and Eocene limestone with a well developed karst, mainly based on a paleokarst network. It was previously defined as Shallow Karst Aquifer A. Underlying this aquifer, alternate earlier Cretaceous marl, sandstone and limestone are present reaching the Jurassic formations at the bottom of the geological unit. The Shallow Karst Aquifer A has a mean thickness of about 120 m and outcrops the entire catchment surface with typical glacial and karst morphologies. Meander karren, polished rock surfaces, dolines, karstic depressions and deposits are common on the Tsanfleuron karrenfield. Under the aquifer, 250 m thick marl and siliceous limestone strata were defined as Aquiclude 2. At the south east of the catchment a sharp syncline closes the aquifer, where the Glarey spring has sprung. Many vertical fractures also allow water to cross aquiclude strata and finally infiltrate deeply. An evidence of this process was the connection between the southern border of the karrenfield and the Tschoetre spring located 1500 m below, through the whole stratigraphy (Fig. 3.10).

The Glarey spring catchment area, obtained by the mean of 22 tracer tests (see also chapter 3) is estimated about $13.7 \cdot 10^6$ m^2. Transit times were between 5 to 57 hours, with recovery rates increasing from 6% in the northwestern part of the site to 75% in the South East (Fig. 6.1).

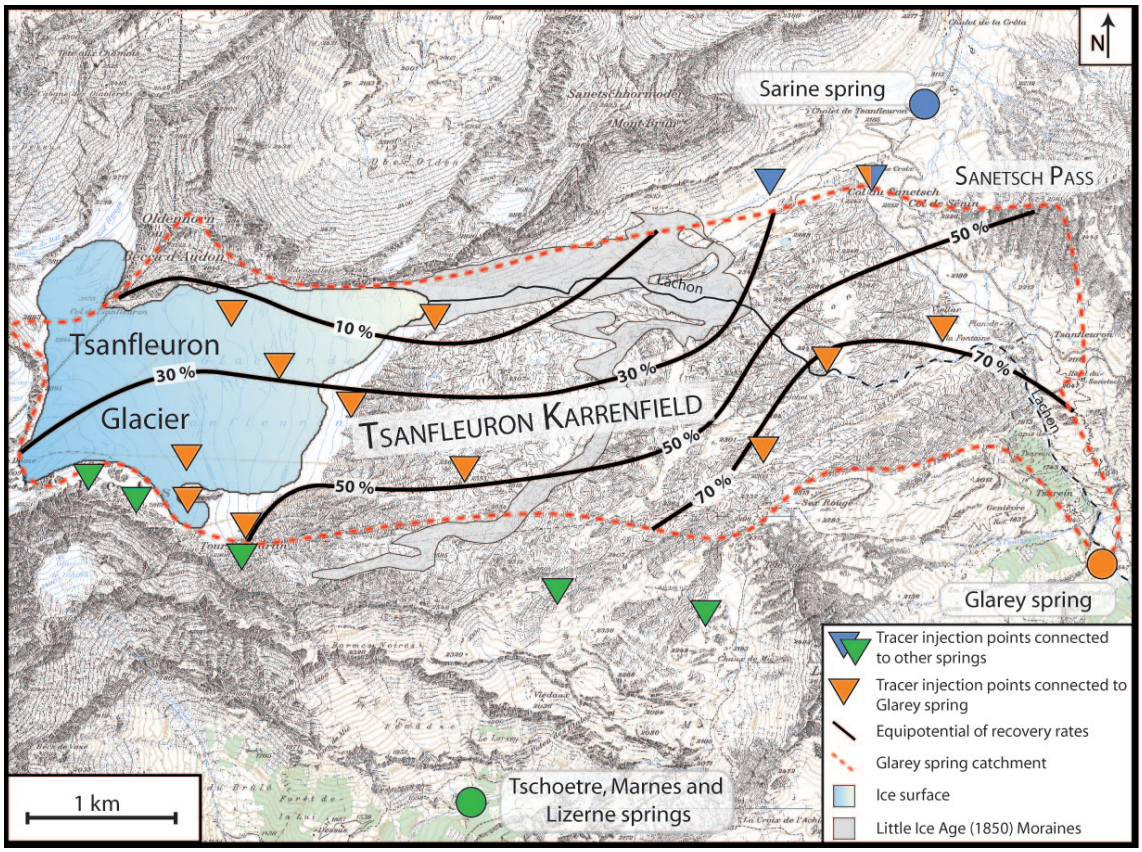

Figure 6.1: Summary of tracer experiments, with injection points distributed to springs catchments. Recovery rates of each tracer experiment are illustrated by estimated isolines inside the Glarey catchment (Copyright of the foreground map: Swisstopo)

6.2.2 Meteorological heterogeneity

Glarey catchment altitudes are between 1500 and 3000 meters above see level, therefore precipitation and temperatures have great variations and a high heterogeneity repartition. At 2550 meters, temperatures may reach 14 / 5 ℃ (max/min in 24 hours) in August but decrease to 4 /-5 ℃ in October. 550 meters below, temperatures were measured in August at 20/8 ℃ and 7/-2 ℃ in October. Globally, mean measured precipitation are 1580 mm per year, and depending on temperature and humidity conditions during precipitations the limit between rain and snow varies in altitude (Appendix E.1) and may create a storage effect in case of important snowfall (no direct infiltration). However the exact precipitation amount is not known, only a large estimation is given in this study. Some authors showed that rain gauge measurements should highly be discussed (Rubel et al., 2000; De Jong et al., 2002) with sometimes as much as 30 % of real rainfall missing from collected data. The accuracy of a rain gauge depends on the distinction between liquid and solid phases, wind exposure and rain intensity.

With two rain gauges installed at 2100 and 2550 meters during 2007 to 2009 summer seasons, one Swiss Meteorological Survey rain gauge that was measuring rain and snowfall with a daily time step

and four rain gauges with annual time steps distributed around the test site, errors on precipitation estimation are many and various. Statistical corrections could be applied, but these necessitate more instruments to measure wind direction, air humidity or have enough stations to create a network of rain gauges in order to interpolate the data. Therefore, no correction will be applied in this work, but these large uncertainties need to be kept in mind.

Evaporation is a process of high specific energy requirement. 2500 J/g for water at O °C and 2833 J/g for ice and snow are necessary to get vapour. Melting snow or ice needs only a specific energy of 333 J/g (Lang, 1981). Therefore evaporation is very low at these altitudes, estimated at less than 10% of the rainfall and neglected during snow cover seasons (Escher-Vetter et al., 2005; Curtis and Burnash, 1996).

6.2.3 Glacier and meltwater flow settings

The glacier covers 20% of the karst aquifer's surface included in the Glarey catchment. Its volume (2008) was about $1{\cdot}10^8$ m^3 of ice for an area of $2.7{\cdot}10^6$ m^2 (see chapter 4). The Tsanfleuron glacier has been retreating very quickly these last years (Fig 4.2). About 103 meters length were lost in 2009 and annual estimations of mean thickness loss are about 1.5 m per year (observations from Glacier3000 company, responsible for tourism and skilift.), equivalent to an estimated water volume of $4.1{\cdot}10^6$ m^3. First progonosis about glacier melt and a model from B. Hubbard (email communication) estimates the disappearance of Tsanfleuron glacier in a time range between 20 to 70 years. However no glacier balance measurements were available in this study, and only melt estimations based on discharge data are available.

Glacier meltwaters were found to follow three different pathways through the ice before infiltrating the aquifer (see chapter 4). Direct aquifer infiltrations occur in the upper part of the glacier, while at lower elevations, meltwater first flows out at the glacier front before infiltrating inside swallow holes. The northern part of Tsanfleuron glacier is thicker and a part of its meltwater production is drained by the Lachon stream. Summer water volumes in this stream were measured at $5.4 \cdot 10^5$ m^3 between July and October (ice melt season). If this water volume corresponds to 10% of the glacier's surface as estimated in the literature (Grust, 2004), total meltwater production would match our first estimation with an annual ice thickness loss of 1.43 m ($3.6 \cdot 10^6$ m^3 of meltwater).

By also considering also snow melt volumes, the annual amount of water flowing in the Lachon stream is estimated at $1.6 \cdot 10^6$ m^3 ($1.4 \cdot 10^6$ m^3 from snow or ice melt, and $1.6 \cdot 10^5$ m^3 from springs along the streambed). About 55% of this volume does not infiltrate the aquifer and follows the streambed outside the system. Only 45% really recharges the aquifer, perhaps less because 10% of the total volume already comes from the aquifer through the streambed springs.

Water infiltrations are directly dependant on meteorological conditions, especially observed in the Lachon stream during three tracer experiments (Fig. 3.8). At low flow conditions, water infiltrates in the main swallow hole (Fig. 1.7) after 16 hours, but with high dispersion. When water level increases in the system, transit times and dispersion decrease. At very high flow conditions, no more infiltrations were observed. Many swallow holes were transformed into springs (estavelle), while new connections were established to other important springs. Hydrological conditions therefore easily

alter the connections, transit times and transport in the glacial streams flowing over the karrenfield area.

6.2.4 Water residence time distribution

If considering the tracers injection points inside the Glarey catchment, 12 breakthrough curves were available to characterize a general transfer function through the aquifer (Fig. 6.1). Each curve was first normalized by the injection mass, then multiplicated by discharge at Glarey spring. The calculation creates a probability density functions (PDF) of the water transit (equ. 6.1) for each specific tracer experiment (Brissaud et al., 1999).

$$P = \frac{C}{M_i} \cdot Q \tag{6.1}$$

where

P : probability $(^1/_s)$
C : Concentration $(^{kg}/_{m^3})$
M_i : Injected mass (kg)
Q : Discharge $(^{m^3}/_s)$

Therefore each curve represents the probability for infiltrated water to arrive at the output in a considered time. These PDFs are unit functions, where the surface below the curve theoretically equals 1. It is not always the case if the considered experiment does not have a recovery of 100 % (all the infiltrated tracer arrives at the output). To obtain a global transit function ψ over time, a weighted mean based on real recovery rates in percent (see fig. 6.1 and tab. 3.2) creates a unique curve including every tracer experiment information (equ. 6.2). This transfer function is built to be unitary and to illustrate the distribution of residence times in the aquifer (Fig. 6.2), more precisely the probability of an infiltrating water volume to reach the spring in a precise time step.

$$\psi = \frac{\sum R_j \cdot P_j}{\sum R_j} \quad with\ 1 \leq j \leq 12 \tag{6.2}$$

where

ψ : Global PDF $(^1/_s)$
P_j : PDF from experiment j $(^1/_s)$
R_j : Recovery rate from experiment j (%)

About 50% of infiltrated water reaches the spring in 31.25 hours and 75% in 67 hours, indicating that flow rates are rapid in this karst system (Fig. 6.2). After 10 days, 100 % the water is supposed to have reached the output point of the aquifer. However many uncertainties are present during

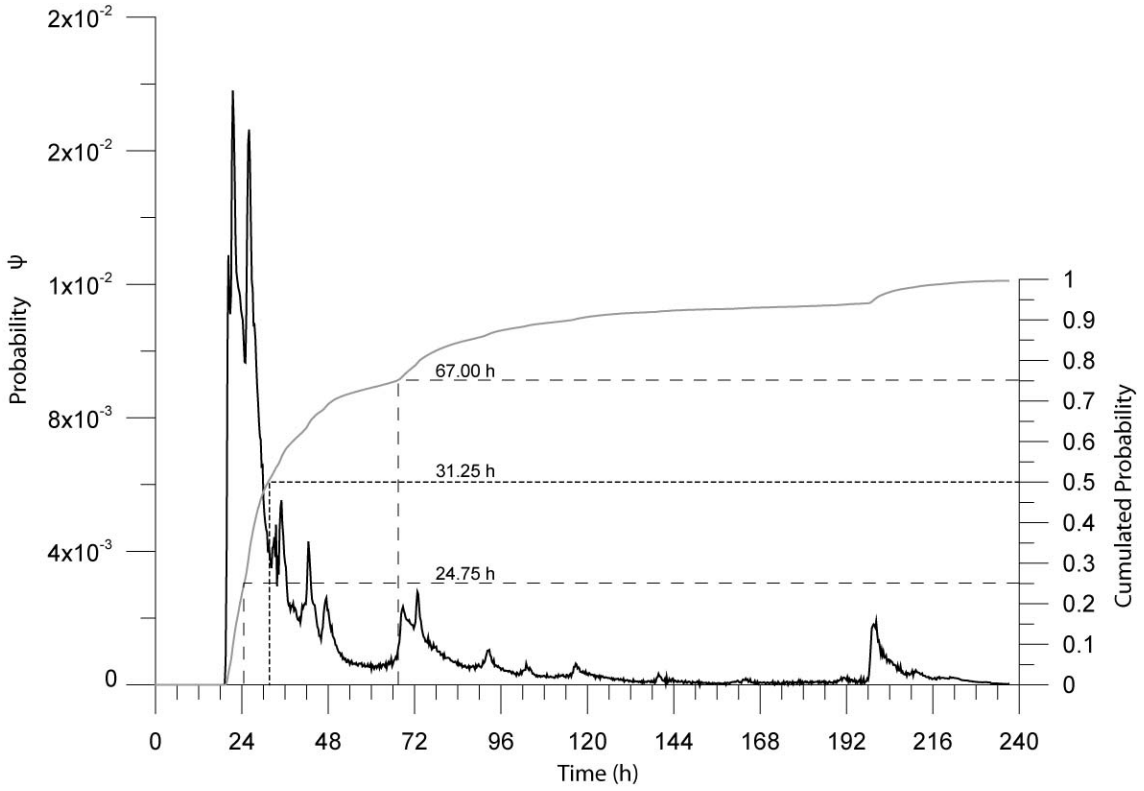

Figure 6.2: Probability density function of water residence times in the aquifer based on tracer breakthrough curves. 50% of infiltrated water flows out at Glarey spring in about 31 hours, and 75% in 67 hours. After 10 days all infiltrated water is supposed to have flown out of the aquifer.

the calculation (limits of tracer detections, discharge errors, difference in precipitation, water level variations). Therefore the probability of 1 is not exactly reached after 10 days but the curve of cumulated probability should finally converges asymptotically to 1 after some weeks.

The selected injection points are also not representative of the whole karrenfield's surface, even if they are sufficiently well distributed on the catchment area. Infiltration and aquifer pathways may sharply differ some meters beside an injection point. It is important to be aware that the map on fig. 6.1 presents important simplifications, but is consistant with the anticline axis located approximatively near the 30% isoline. Therefore groundwater is driven to the northern part of this structure or reaches the Glary spring in the south. This map is a possibility for representing such divergence of water inside the aquifer and illustrates the observed deep infiltrations (Fig. 3.11) or groundwater escapes toward the East of the area.

6.3 Temporal variations at Glarey spring

6.3.1 Seasonal series

The Tsanfleuron glacier has a great impact on the aquifer dynamics during warm seasons. Continuous measurements of electrical conductivity, turbidity, discharge and temperature were made between 2007 and 2010. To improve comprehension of the processes in the next sections, three seasons were defined (see also chapter 5). From 15^{th} October to end February is winter season with the entire field surface covered by snow and a minimum of snowmelt events. The major part of snow melts between March and 30^{th} June during the so called snowmelt season (usually spring season), and then from the 1^{st} July to 14^{th} October in the ice melt season (summer and autumn), where only glacier and rainfalls recharge the aquifer.

At seasonal and annual time scales, variations are more dependent on snowfall and summer glacier melt. Winter months do not show significant variations in physical parameters, but in spring months snowmelt starts and highly increases the discharge at the spring (Appendix E.2). Summer and autumn seasons are then driven by glacier melt (Fig. 6.3), which recharges the aquifer until middle October.

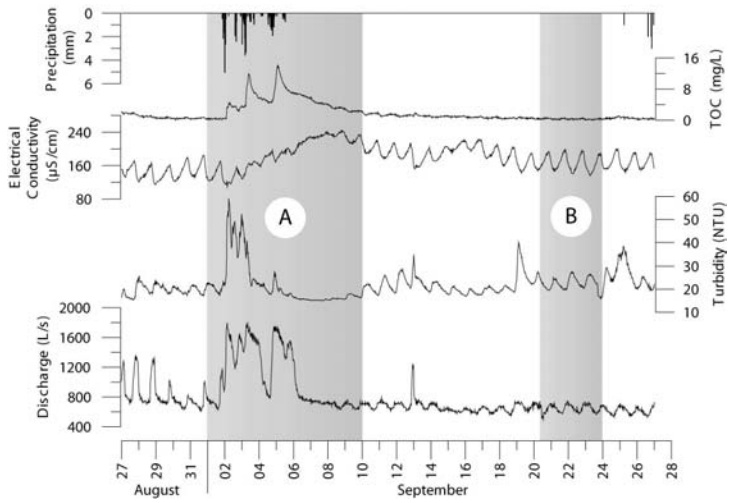

Figure 6.3: Temporal variations at the Glarey spring with electrical conductivity ($\mu S/cm$), discharge (L/s), Turbidity (NTU), TOC (mg/L) and precipitation (mm). Diurnal cycles are smoothed during rainfalls (but stay clearly visible on the electrical conductivity signal), disappear with snowfalls and if temperature is low enough (A, see fig. 6.5). Between precipitation events, diurnal glacier melt drives aquifer dynamics (B, fig. 6.4).

6.3.2 Daily observations

At small time scales and without rainfall, diurnal variations dominate the dynamic of the aquifer (Fig. 6.4). A maximum of meltwater is released at 2 pm from the glacier each warm day and enters the aquifer. It creates a pressure pulse that pushes water already present in the aquifer to the spring in about 8 hours. This water has a relatively higher electrical conductivity compared to ice meltwater. Effective transport of meltwater, illustrated by minimal electrical conductivity, takes about 16 hours since the estimated maximum of recharge. Between these two significant events the maximum of turbidity occurs about 6 hours after the maximum of discharge. This signal is not related to aquifer turbidity, as it did not vary close to the increase in discharge, but is defined as glacial turbidity

because it begins and stops precisely with electrical conductivity variations. Primary or secondary turbidity signals from the karst aquifer (Pronk et al., 2006) are not visible on turbidity signals during dry weather periods. With the particle counter device a time shift of the maxima for each size class were observed (appendix E.3). The pressure pulse mobilizes big particles with water already present inside the aquifer and can be considered as primary turbidity. The real transport of meltwater, represented by a decrease in electrical conductivity, conducts smaller particles and creates glacial turbidity signals. The contribution of small particles to total turbidity is more important than large particles and hides the primary turbidity when only the global signal is observed.

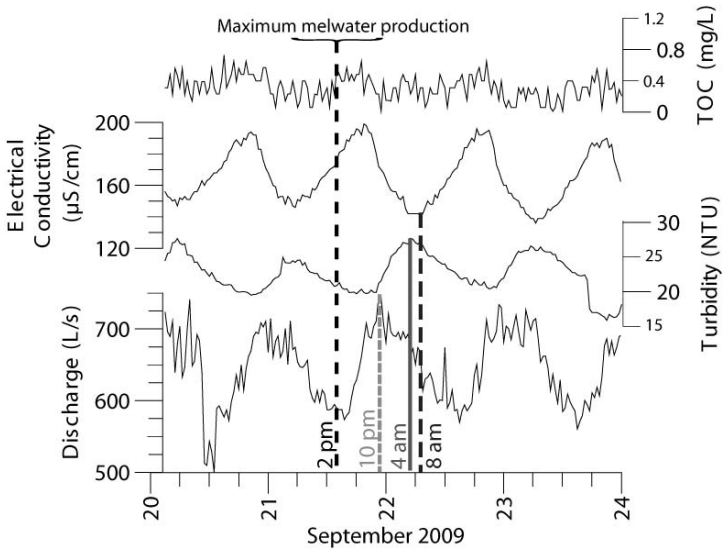

Figure 6.4: Part B from fig. 6.3. Electrical conductivity ($\mu S/cm$), discharge (L/s), Turbidity (NTU), TOC (mg/L) and precipitation (mm) at Glarey spring between 20 to 24 September 2009. Without rain perturbation, estimated maximums of glacier meltwater production occur at 2 pm and create a discharge maximum after 8 hours (10 pm), a glacial turbidity peak after 14 hours (4 am) correlated with the electrical conductivity minimum after 16 hours (6 am).

On the other hand, rain events completely alter the hydrogeological regime of the aquifer for many days. During rainfalls, variations sharply increase for all parameters except electrical conductivity, which slowly increase until glacier meltwater once again replaces "oldwater" inside the aquifer. Discharge and turbidity are flattened in the following days, as a consequence of lower air temperature and possible snow accumulation in the highest elevation zones. Discharge highly increases and primary turbidity is immediately washed from the karst network. Primary turbidity is often merged with glacial turbidity and both are difficult to distinguish during precipitation events. Secondary turbidity is nevertheless perceptible through the Total Organic Carbon (TOC) (Pronk et al., 2006), which only varies with precipitation or snowmelt. The distinction between autochthone and allochthone turbidity signals is therefore very difficult because rainfalls do not stop glacier melt processes. Only if ice is covered by snow and with low temperature are daily variations stopped. Otherwise every 24 hours, melt occurs, decreases electrical conductivity, adds and transports particles inside the aquifer (Fig. 6.5).

6.3.3 Annual and long term variations

Water balances were calculated with hourly discharge and precipitation data during 5 years. In order to represent annual variations, monthly water volumes and balances were used (Equ. 6.3). The mean annual water volume at Glarey spring is $18.2 \cdot 10^6\ m^3$. Precipitations were evaluated at 1507 mm on a catchment area of $13.7 \cdot 10^6\ m^2$, which represents an input volume of $20.6 \cdot 10^6\ m^3$. Even if evaporation

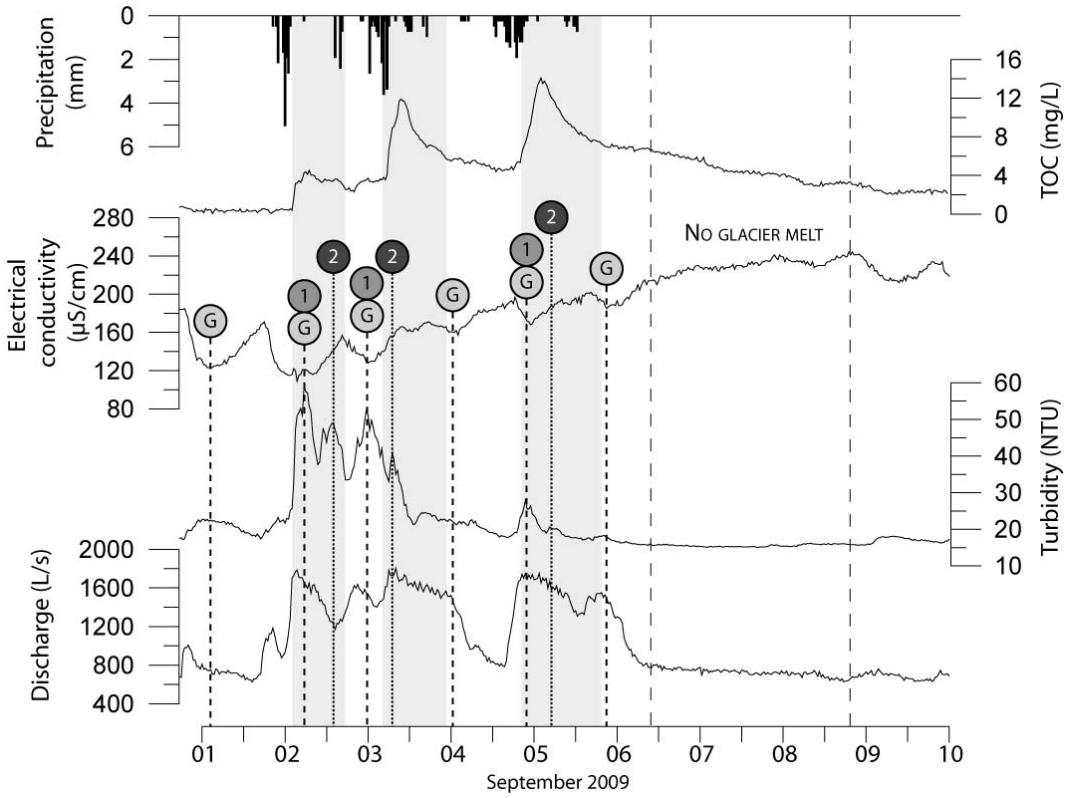

Figure 6.5: Part A from fig. 6.3. 10 days (from 1 to 10 September 2009) monitoring of electrical conductivity ($^{\mu S}/_{cm}$), discharge ($^{L}/_{s}$), Turbidity (NTU), TOC ($^{mg}/_{L}$) and precipitation (mm) at Glarey spring. (G), (1) and (2) correspond respectively to glacial, primary and secondary turbidity. 24h cycles of electrical conductivity minima indicate that glacier continues to melt under rainfalls. Glacial turbidity was observed to correlate with these minima (Fig. 6.4). Primary turbidity increases in parallel with discharge and is here mixed with glacial turbidity signals. Secondary turbidity follows the primary turbidity by 3 to 4 hours.

is minimal at higher elevations, an estimation of 10% is applied, corresponding to many alpine areas (Strasser et al., 2008; Lang, 1981). Therefore precipitation input after evaporation is $18.6 \cdot 10^6\ m^3$, but is substracted of $0.85 \cdot 10^6\ m^3$ corresponfing to rainfall volume catched by Lachon stream, that flows out the system without infiltrating. Input volume was finally calculated at $17.7 \cdot 10^6\ m^3$.

$$\sum Q_d = E \cdot S \cdot \sum p_d \tag{6.3}$$

where

Q_m : Daily discharge ($^{m^3}/_{day}$)
E : Evaporation (%)
p_m : Daily precipitations ($^{m^3}/_{day}$)
S : Catchment area (m^2)

Without considering glacier contributions, which are only estimated, the balance between input and output is already equilibrated inside the Glarey spring catchment. Only a small mean water deficit of about 2% in the input volume was observed during the five years considered. However many approximations and uncertainties are present in such balance calculations and results should be carefully analyzed. Uncertainty values were estimated at ±20% for the catchment area and ±15% for precipitations. For output, discharge calculation methods and calibrations induce uncertainties of about ±10%.

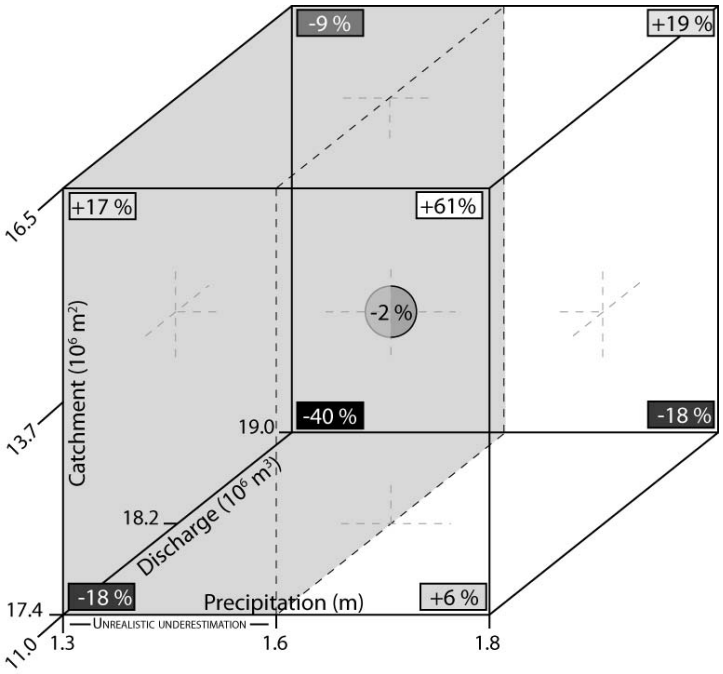

Figure 6.6: Uncertainties allow to build a 3-axis graph with the possible variations for precipitation, discharge and catchment area. The central value is water balance calculated without using uncertainties, with an excess of 2% in output. All around values are combinations with the minimum and maximum discharge, catchement area and precipitation. Left grey part represents lower rainfall than measured, which was calculated but are not convenient with measurements error as described in literature. Normally precipitation measurements may not exceed real precipitations and are expected to be about 20% lower. Right part of the figure therefore represent a more realistic uncertainty and will be developped further.

Each parameter for the balance calculation presents uncertainties that are described and discussed.

For precipitation measurements, wind-induced errors and spatial variations of precipitation are considered (De Jong et al., 2002; Rubel et al., 2000; Curtis and Burnash, 1996). Precipitation data from the Hydrological Atlas of Switzerland are estimated at more than 2000 *mm* per years (Fig. 1.5), values that were never measured during field campaigns. Correcting input data (snow-rain differenciation (Rubel et al., 2000), see appendix E.1) require more instruments that were not available during this work. Experimental evaporation factors could also replace the estimated evaporation from literature (Strasser et al., 2008; Lang, 1981) in order to precisely determine the infiltration volumes.

Discharge uncertainties also highly influence the balance calculation, like precipitation variations. These uncertainties can therefore not be improved because they are directly dependant of instruements and calibration methods.

Surface limits for the Glarey catchment based on punctual tracer tests also over- or underestimate the total rainfall input value. Large modifications of the catchment area are however difficult be-

cause morphology of the karrenfield and geological structure largely constrain the water pathways (see chapter 3), only small adjustments can be done but they have a great influence on the balance calculation (Fig. 6.6) inducing variations of 40% between lower and higher values.

Water balances were calculated and illustrated in the fig. 6.6 with the different uncertainty combinations. The water amount ($8.5 \cdot 10^5$ m^3) that does not infiltrate the aquifer through the Lachon stream was also considered. However such examples illustrate the difficulties to obtain precise estimation of water balances in glacierised alpine catchments without a good glacier balance campaign. Direct relations between input and output values is illustrated in percent, where input equals output 100% is obtained. The highest water deficit (-40%) corresponds to minimum catchment surface, minimum precipitation and maximum discharge. On contrary, a water excess of 61% is obtained with the higher catchment area, maximum precipitation and minimum discharge. The first of these two extremes does not match with field observations: even the highest glacier contribution is not able to replace such a lack with its meltwater. It would represent a net ice thickness loss at the glacier surface of 3 m each year. Moreover, measurements of precipitation are expected to be underestimated rather than overestimated (De Jong et al., 2002; Rubel et al., 2000; Curtis and Burnash, 1996). The second extreme induces a loss of more than twice of Glarey's annual water volume, which may be realistic with the observed and estimated limit of 1.5 m of ice melt each year, like the other more reasonable scenarios. These cases present three possible relations with glacier meltwater.

1. For high water deficit cases (-18%), where more water flows out than enters the system, Tsanfleuron glacier completes the volume of water to reach equilibrium and few volumes are expected to be lost inside the aquifer. This hypothesis is not really compatible with such a fracturated aquifer and aquiclude geometry, and with the fact that the Shallow Karst Aquifer A continues under higher tectonic structures in the East.

2. If glacier meltwater is added to excess volumes (+61%, +19% and +6%), important volumes are expected to be lost in the northern and eastern part, where no karst springs were discovered. Deep infiltrations through the stratigraphy also decrease the volume of water available at Glarey spring. No incidences are therefore expected after the glacier's disappearance.

3. When meltwater is added into a balance (-2%) which is already close to equilibrium, it represents a water volume corresponding to usual excesses in alpine water balances that are reported to glacier retreat and may reach 20% (Lambrecht and Mayer, 2009; De Jong et al., 2002). When necessary this meltwater partially completes the deficit but mostly contributes to volumes that flow elsewhere and are not measured.

The worst possible deficit, if removing unconsistent extremes and the calculated balances with overestimated precipitations, is illustrated in fig. 6.7. For this case the maximum glacier contribution completes about 18% of Glarey's annual volume and corresponds to a water volume of $3.7 \cdot 10^6$ m^3 or mean ice thicknesses of 1.4 meters. It is very close to the observed 1.5 meters of ice loss that should produce $4.1 \cdot 10^6$ m^3 of meltwater (23% of the annual volume at Glarey spring) or to estimated meltwater flowing in the Lachon stream and reported to glacier surface. As no glacier balance was measured or available, these estimations will be used as annual glacier volume loss. Its volume was measured in 2008 (see chapter 4) at $100 \cdot 10^6$ m^3, and this value was taken as a 100% reference in fig.

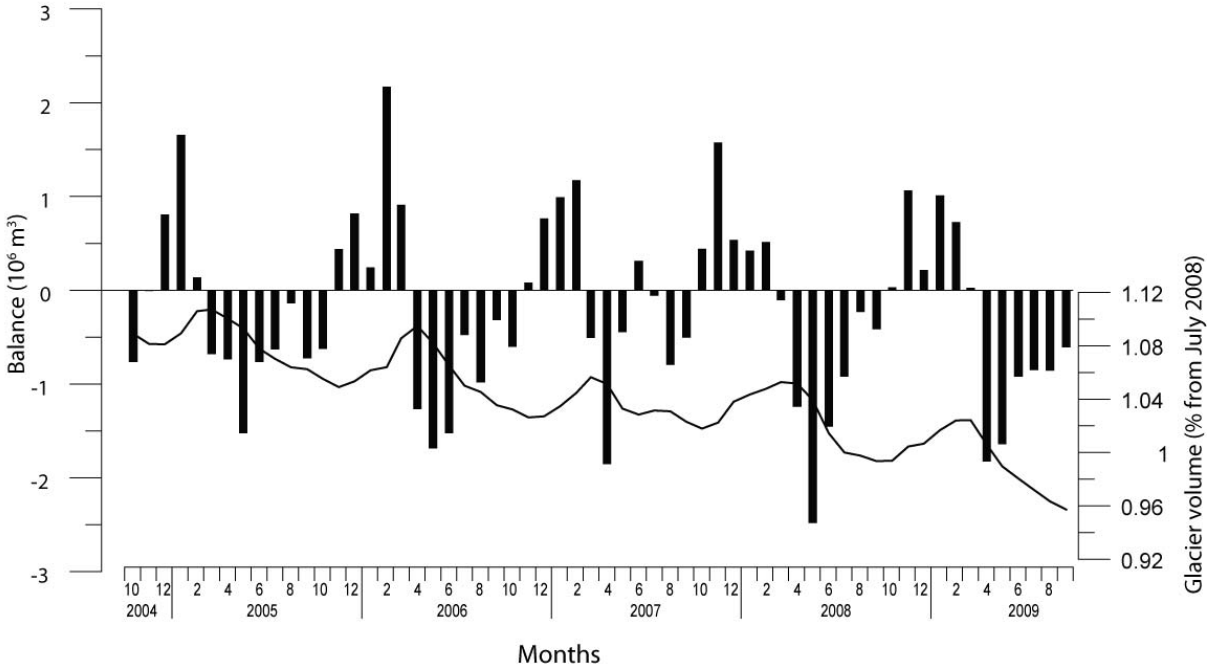

Figure 6.7: Water balance representing the worst possible case, where the glacier has to complete 18% of deficit in the water balance. The black line represents the deviation in percent from the water volume stored as ice inside the glacier in July 2008. The variations illustrate the annual removed volume of ice necessary to equilibrate this type of balance each year.

6.7. Glacier volume before and after this reference are calculated by positive or negative results in the water balance for each month during the five years measured. The annual snow accumulation is considered as a positive part of the glacier and acts like a reserve before the glacier starts to melt. However the distribution of the thickness loss is not homogeneous on the glacier's surface and a maximum of ice is lost at the front of the glacier and a minimum at the top, where snow melts later and temperatures are lower.

For lower contributions (balance at -2%), a part of the meltwater contributes to groundwater volumes that flow elsewhere than to the Glarey spring. If considering the 18% calculated above as real glacier recharge, excess water would be about 16%. When the balance already presents a water excess without glacier contribution, meltwater increases the unmeasured outflows, which could therefore reach 79% (61% of precipitation excess and 18% of glacier meltwater).

Many scenarios are exposed and none of them is more probable than the others without complete

and exhaustive glacier balance calculations. It is therefore not possible to privilege one or the other. Discussion in the next section will mainly focus on the high deficit case in order to characterize the worst case scenario. But developments about unmeasured water volumes in water excess scenarios are also illustrated.

6.4 Consequences for water availability

6.4.1 Climate parameters

Currently climate changes in the Alps are clearly visible due to fast glacier retreat and the increase in altitude of perennial snowfields. Water stored in these frozen masses is released and increases the water volume available for hydropower, rivers or aquifers in an order of 10% to 45% (Lambrecht and Mayer, 2009) depending on the percentage of catchment surface covered by snowfields or glaciers. The climate prognoses for 2050 are less precipitation during summer but more in winter, with more extreme rainfall events. Temperature is also expected to increase about 1℃ with the immediate consequence of elevating the snow-rain limit altitude by about 150 m (if considering a temperature gradient of $0.6℃/_{100m}$). Recent climate research (Hohmann et al., 2007) distribute precipitation variations on 4 seasons. From December to February an increase of 8% is forecasted. A decrease will occur during the next three seasons, about -1% from March to May, -17% in June to August period and -6% during September, October and November. Moreover such differences in the precipitation are expected to slow down the current rate of glacier recession.

Table 6.1: Example of parameters to estimate discharge and precipitation for 2050 at Glarey spring, based on the highest possible deficit case (-18%).Q_m: Mean monthly discharge for the 2004 to 2009 period, V_{ice}: mean seasonal ice volume contributing to spring discharge, p_m mean monthly precipitation for the 2004 to 2009 period, $\Delta\ p$: prognosed precipitation differences per month in 2050, p_{2050} and Q_{2050}: monthly in and output volumes prognosed in 2050.

Month	Deficit values 2004-2009				Estimated values 2050		
	Q_m ($m^3/_{month}$)	V_{ice} ($m^3/_{month}$)	p_m ($m^3/_{month}$)	p_m+V_{ice}/Q_m (–)	$\Delta\ p$ (%)	p_{2050} ($m^3/_{month}$)	Q_{2050} ($m^3/_{month}$)
1	$2.6 \cdot 10^5$	0	$1.4 \cdot 10^6$	5.4	7	$1.5 \cdot 10^6$	$2.8 \cdot 10^5$
2	$2.7 \cdot 10^5$	0	$1.5 \cdot 10^6$	5.7	12	$1.7 \cdot 10^6$	$3.0 \cdot 10^5$
3	$1.5 \cdot 10^6$	0	$1.3 \cdot 10^6$	0.9	8	$1.4 \cdot 10^6$	$1.6 \cdot 10^6$
4	$2.9 \cdot 10^6$	0	$1.1 \cdot 10^6$	0.4	–1	$1.1 \cdot 10^6$	$2.9 \cdot 10^6$
5	$3.7 \cdot 10^6$	0	$1.7 \cdot 10^6$	0.5	–10	$1.6 \cdot 10^6$	$3.3 \cdot 10^6$
6	$3.2 \cdot 10^6$	$2.9 \cdot 10^5$	$2.2 \cdot 10^6$	0.8	–14	$1.9 \cdot 10^6$	$2.5 \cdot 10^6$
7	$2.8 \cdot 10^6$	$1.3 \cdot 10^6$	$2.1 \cdot 10^6$	1.2	–17	$1.7 \cdot 10^6$	$1.4 \cdot 10^6$
8	$2.3 \cdot 10^6$	$1.2 \cdot 10^6$	$1.5 \cdot 10^6$	1.1	–20	$1.2 \cdot 10^6$	$1.1 \cdot 10^6$
9	$1.7 \cdot 10^6$	$6.7 \cdot 10^5$	$9.3 \cdot 10^5$	0.9	–18	$7.7 \cdot 10^5$	$8.0 \cdot 10^5$
10	$1.4 \cdot 10^6$	$2.9 \cdot 10^5$	$9.1 \cdot 10^5$	0.9	–4	$8.8 \cdot 10^5$	$1.0 \cdot 10^6$
11	$6.0 \cdot 10^5$	0	$1.4 \cdot 10^6$	2.3	4	$1.4 \cdot 10^6$	$6.2 \cdot 10^5$
12	$2.7 \cdot 10^5$	0	$1.1 \cdot 10^6$	4.1	5	$1.2 \cdot 10^6$	$2.8 \cdot 10^5$
somme	$2.1 \cdot 10^7$	$3.7 \cdot 10^6$	$1.7 \cdot 10^7$			$1.6 \cdot 10^7$	$1.6 \cdot 10^7$
	100%	18%	82%			78%	78%(–22%)

6.4.2 Future hydrograph estimation

For cases where water balances present an excess in precipitation, an estimation of the future hydrograph is not possible. No real differences occur as recharge is always sufficiently higher than discharge, therefore only excess volume will decrease. But for cases where water excess is lower than 20%, glacier melt will induce a deficit in water balance. It becomes possible to discuss a future estimated hydrograph. Water availability prognosis is developped here for the worst case (-18%), which is presented in fig. 6.8.

The Tsanfleuron glacier is assumed to have completely vanished and precipitation variations are distributed for each month depending on seasonal prognosis (Hohmann et al., 2007) in table 6.1. The ice contribution to Glarey spring is first removed from the mean monthly discharge during years 2004 to 2009 ($Q_{mean} - V_{ice}$). This contribution is distributed according to the season, with an observed maximum melt during July and August. Moreover the difference in precipitation is applied on this result (Equ. 6.4) to illustrates the climatic change and creates the estimated hydrograph (Fig. 6.8 and tab. 6.1).

$$Q_{2050} = \frac{p_m + p_m \cdot \Delta p}{\frac{p_m + V_{ice}}{Q_m}} \tag{6.4}$$

where

Q_{2050}	:	Monthly volumes (2050) ($^{m^3}/_{month}$)
Q_m	:	Monthly volumes (2004-2009) ($^{m^3}/_{month}$)
V_{ice}	:	Ice volume lost in 2008 and distributed per month ($^{m^3}/_{month}$)
p_m	:	Monthly precipitation volumes (2004-2009) ($^{m^3}/_{month}$)
$\Delta\ p$	:	Difference in precipitations per month (%)

Many uncertainties remain with such a simple method, and some slight differences may occur depending on ice volumes' distribution in summer. However these differences do not alter the general shape of the hydrograph curve. If precipitations are snowfalls, the decrease in May and June may be balanced by stored increases during the winter period, which is partly reported to the following months. Disappearance of the Tsanfleuron glacier would have an important influence on the future volumes of water at Glarey spring, always if only considering deficit balances. Without glacier about 18% of the current annual water volume in summer season would be removed. The climatic effect remove 4% more to the annual volume loss, conducting to an annual volume loss of $4.9 \cdot 10^6\ m^3$ (22%) at Glarey spring. The major consequences of climate change on water resources in alpine catchment would depend more on a general temperature increase inducing snow and glacier melt than from precipitation differences (Appendix E.4). Highest discharge values will continue to occur in year 2050 as currently, but the meltwater volume of four months (from March to June, snowmelt season) would reach 64 % of the annual water volume. Today this proportion is only 54 %, leaving more water resources during summer.

Separation between aquifer water and glacier meltwater (see chapter 5) using stable isotopes illustrates that aquifer only contributes to 35% to the water volumes at Glarey spring during the

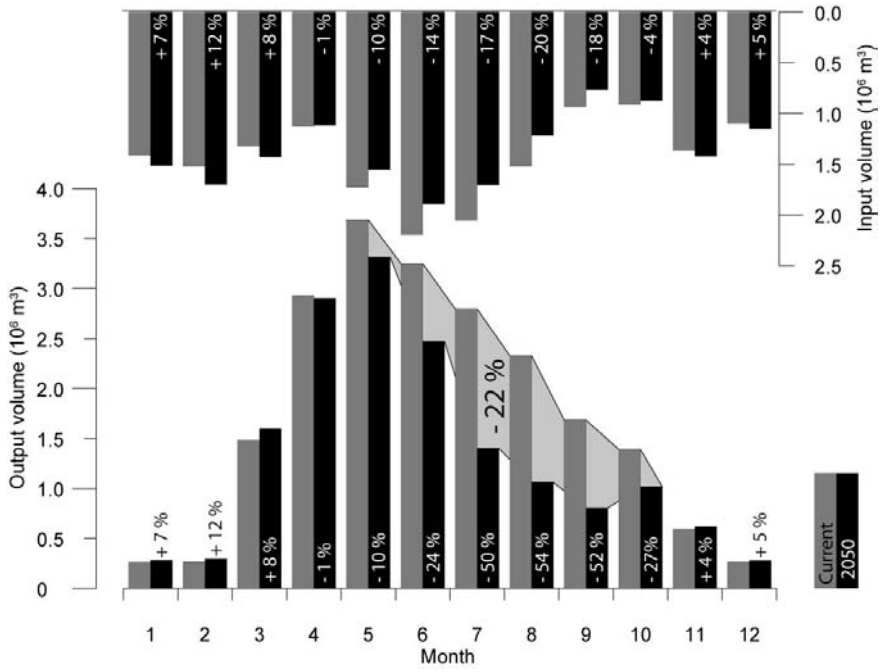

Figure 6.8: Prognosis of water volume loss and repartition for high deficit case (minimum catchement area, maximum discharge and precipitation) if Tsanfleuron glacier disappears. Precipitations and discharge are based on 2004 to 2009 mean values and summed per month. About 22% ($4.9 \cdot 10^6\ m^3$) of the annual volume of water at Glarey spring is expected to miss.

summer season, glacier completing the 65% that remains. This ice melt contribution was found to correspond to 25% of the annual water volume at Glarey spring, which is close to the highest deficit obtained through water balance. Moreover, equilibrium or excess balance scenarios are really difficult to mix with stable isotopes results. This observation consolidates the deficit scenario which is presented in table 6.1 anf illustrated in fig. 6.8.

6.4.3 Repercussion on aquifer dynamics

By losing glacier meltwater volumes, the dynamics of the aquifer will especially change during the summer season. Snow cover and snowmelt season will not really be influenced by the disappearance of the glacier. Although Tsanfleuron glacier is not active in cold season, it acts as an impermeable layer that can store snow meltwater longer than if snow is directly in contact with karrenfield's surface. Therefore without glacier, meltwater will probably arrive to the spring faster and create huge discharge signals at the main output of the system.

In summer, water volumes available could decrease if deficit balances are verified or stay close to current volumes but in all cases the diurnal cycle will disappear. Turbidity dynamics will therefore completely be altered, because the main source of particles will disappear even if the relics of glacier presence will take longer to vanish. Currently many small particles and rocks are present in the proglacial area of the glacier and are slowly brought inside the aquifer by rain or snow falls. Lachon stream will only be active during the snowmelt season and perhaps very strong rainfalls. The particles stored inside its bed will stay on the surface of the karrenfield and modify the particle volumes at Glarey spring. In order to have the best drinking water resources, such hypothesis are good, but without regular washing of the aquifer by glacier melt many particles will accumulate in the karst network and arrive at higher concentrations in the spring during high water events.

Diurnal pressure pulses due to glacier melt will also disappear, water transit times inside the aquifer will then be longer with the consequence of increasing the summer electrical conductivity at last to winter values (420 $^{\mu S}/_{cm}$). Only the snowmelt season will keep a lower electrical conductivity (about 80 to 100 $^{\mu S}/_{cm}$).

Without the glacier, the Tsanfleuron aquifer will have a dynamic close to karst at lower elevations such as the Siebenhengste system. The main difference will come from the volume and duration of snowpack on the surface, which controls the meltwater quantity in spring season. In the Siebenhengste system, the snowmelt volume represents about 77% (Jeannin, 2001; Corbel, 1957) of the annual water discharge (at the Beatuhöhle spring), a situation close to our prognosis about the Tsanfleuron's future.

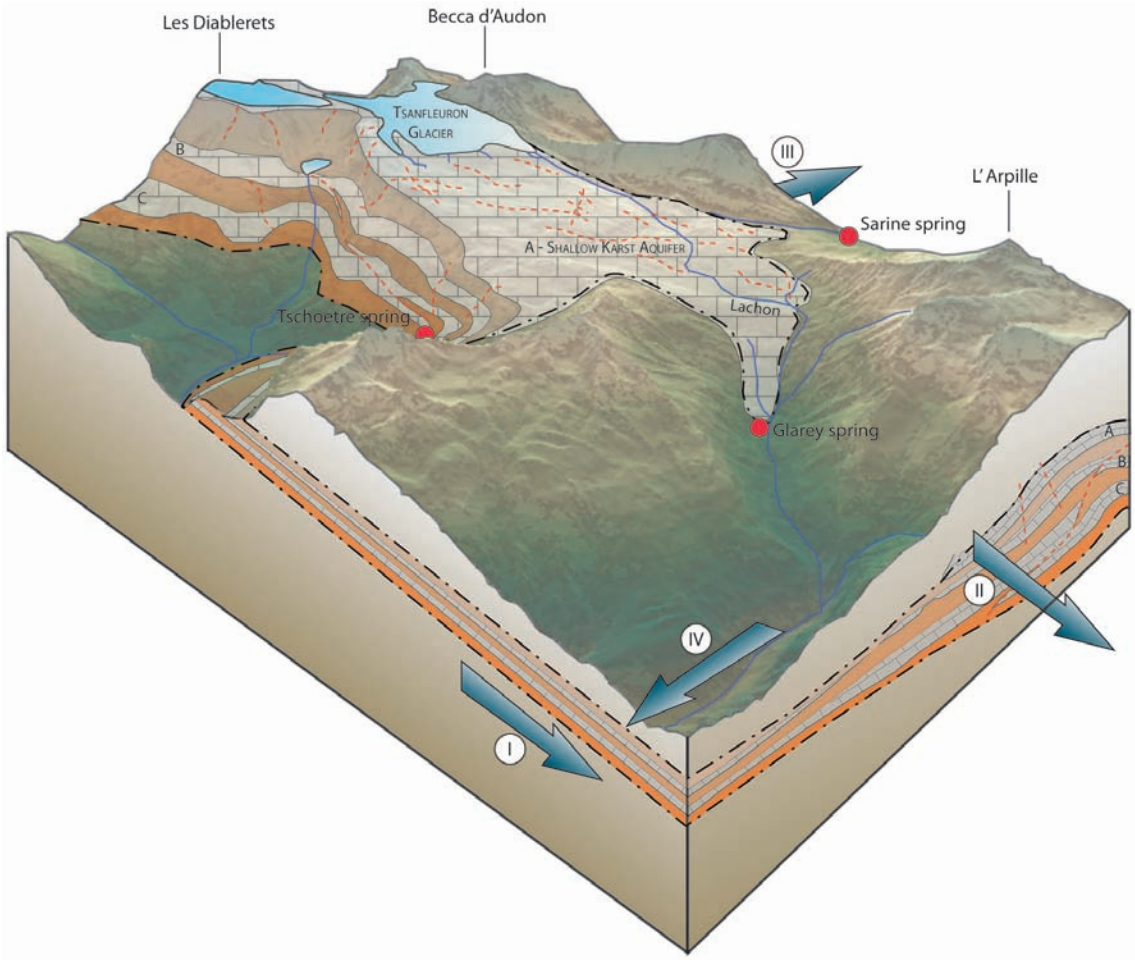

Figure 6.9: Possibility of water loss around Tsanfleuron karst system. Deep infiltrations through fractures and faults distribute surface water from the Shallow Karst Aquifer A, Middle Karst Aquifer B and to the Lower Karst Aquifer C (I.). These three structures plunge under higher tectonic structures to the east and never outcrop again. Water follows the dip of the strata and is lost eastward, where no correlated springs were found (II.). On the north the large anticline is closed by multiple folds, again burried under higher tectonic structures. Some outcrops are however apparent, and springs were discovered there in summer 2009. Therefore large volumes of meltwater from the glacier may flow to the north (III.). Finally a non negligible amount of water was found to be lost through the Lachon stream. Cumulated with unknown and unestimated exfiltrations around Glarey spring, a part of water flowing in the south direction is perhaps lost in the valley and reaches the Rhône river (IV.).

6.4.4 Hypothesis for water volume loss

For equilibrium and excess balance cases, but also for deficit cases where there is enough glacier meltwater to create also excess volumes, various amounts of water are lost and flow elsewhere than to Glarey spring (Fig. 6.9). These volumes, completed with glacier contributions, vary between an excess of 79% (excess case with 61%, with high precipitation estimation, lowest discharge and biggest catchement surface) to equilibrium at 0% (deficit case with 18%, discussed above). Water was found to cross the entire stratigraphy in southern border of the karrenfield, flowing in fractures and faults and crossing the aquicludes (see chapter 3, especially figs. 3.9 and 3.10). Therefore the middle and lower Karst Aquifers B and C drain probably a part of this lost volume. No springs were found, but the dip of these strata certainly drives water to the east (I. in fig. 6.9) with a same process as in the Shallow Karst Aquifer A (II. in fig. 6.9). A large and consequent volume is certainly lost following the dip of the aquifers and flowing to the east below overlying tectonic structures, where no karst springs are present.

Some small springs were found in year 2009 in the north part of the studied area, and as the structure of the aquifer plunge in multiple folds under overlying tectonic structure, a part of the glacier's meltwater is certainly lost there. The important dolines observed by geophysical campaign in the northern part of the glacier are certainly connected with these outflows, located in the other side of the Becca d'Audon (III. in fig. 6.9).

Finally a large amount of water is lost through the Lachon streambed, and reaches directly the Rhône Valley. Some diffuse exfiltrations may also exist along the downstream part of the Lachon, from the main swallow to Glarey spring (IV. in fig. 6.9).

6.5 Conclusions

Based on continuous monitoring of springs and precipitations, a general water balance was built. However many difficulties emerged during treatment of the data, especially concerning meteorological and catchment values. With direct measurements, input volumes were estimated at $18.6 \cdot 10^6$ m^3 with 10% of evaporation, if not considering glacier melt infiltrations. Ouput volumes at Glarey spring represent $18.2 \cdot 10^6$ m^3. As no glacier balance and therefore no glacier contribution to Glarey spring were available, the calculated water deficit of 18% in one case (corresponding to $3.7 \cdot 10^6$ m^3 of water) was considered as the glacier's contribution as it is equivalent to observations on the field and to calculations from Lachon stream's discharges. This volume was used to equilibrate the input and output of the karst aquifer. Tsanfleuron glacier is currently rapidly retreating and last available measurements show a loss of 100 meters in length between years 2008 and 2009. This meltwater volume is equivalent to usual alpine glacier contributions in delimited catchements.

These continuous monitoring experiments and field observations also allow to estimate the future water resources for the Tsanfleuron karst aquifer. Current and prognosed annual groundwater and surface flows are described, and in the case of the glacier's disappearance, the probable consequences for water dynamics are discussed. The general shape of the hydrograph curve would be most probably modified during the summer season (July to early October) but would also present a shorter and more concentrated snow-melt season. In general the disappearance of the glacier will induce many

impacts on groundwater dynamics, especially:

- The current diurnal specificity of primary, secondary and glacial turbidity will be changed to lower elevation springs dynamics, where particle distributions are mainly driven by storm events as described in literature (Pronk et al., 2006).
- Electrical conductivity will be increased by a factor of 4 illustrating longer transit times;
- Discharge will sharply decrease.

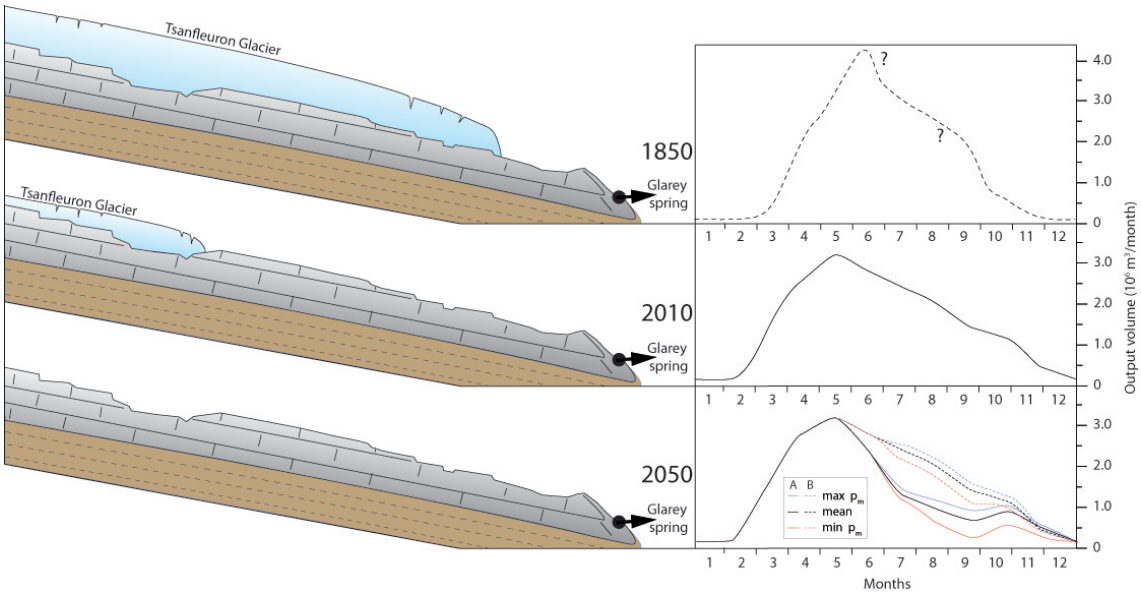

Figure 6.10: Three hydrographs for the Little Ice Age (1850, maximum volume and expansion of the Tsanfleuron glacier), current (2010) and future (2050, without glacier) periods. The first hydrograph is schematic as no data were available. Curve of monthly volumes for 2010 are an average of 2005 to 2009. The curve for 2050 is based on the table 6.1 with also mean data from 2005 to 2009. A. is the worst deficit case (developed in tab. 6.1) and B. the equilibrium scenario (only influenced by precipitation differences). The blue and red lines corresponds to equivalent calculations but with maximum and minimum monthly precipitation.

Only snow pack volumes and melt rate differences will affect the snowmelt (March to June) and the snow cover season (end of October to February). Climate impacts on the catchments primary depend on temperature elevations, which control glacier melt rates. For higher deficit cases about 80 % of the estimated differences between current and 2050 hydrograms come from the glacier disappearance and only 20% come from precipitation variations (fig. 6.10). The precipitations were supposed to be higher in winter and lower during summer season, but our calculation minimized the impact of these changes at the scale of small alpine catchements. Winter discharges will not significantly exceed the current values and therefore not completely alter the monthly balances. The negative difference of summer water volumes due to the glacier's disappearance is increased but not the direct result of precipitation variations. On the other hand, for lower deficit cases, the influence of precipitation and glacier become equal at respectively 47% and 53%.

To conclude, it appears that many cases present no real impact of glacier's disappearance on water volumes in the future. However our discussion focuses on the worst cases that have the same probability to occur as others in order to see the consequences on water availability. In these cases the probability of occasional water shortages during rare but more intense rainfall periods will strongly increase (fig. 6.10), especially if water demands for human activity also increase. But glacier's disappearance will undoubtly have many impact on water quality, and on the annual repartition of water at Glarey spring.

Chapter 7

Conclusions, summary and perspectives

7.1 Review of the main objectives

The management of karst groundwater resources in alpine catchments requires a complete knowledge of aquifer geometry and water transfers from the surface of the system towards springs and drinking water supplies. Snow fields and glacier covered areas represent a huge water storage system and if overlying karrenfield, they are a direct extension of alpine karst aquifers. Moreover the water volume stored inside these frozen structures is slowly released and recharges the aquifer during warm seasons. Artificial and natural tracer experiments on the karrenfield and glacier's surface, water balance calculations and time series analysis are therefore perfectly suitable to characterize catchment drainage systems and the relations with the frozen water stored on its surface.

Aims of this work were to investigate:

- the influence of the aquifer geometry on meltwater flow and pathways, especially in relation with Tsanfleuron glacier;
- the spatial and temporal surface recharge and aquifer transport, and the consequences for the parameters of the water at the main output;
- the impacts of glacier retreat and precipitation variations on the dynamics of a karst aquifer, with a focus on the availability of freshwater;
- the specificity of current hydrographs in comparison with prognosed repartition of water in the future;

These objectives were investigated through different methods and techniques during 5 years (from summer 2005 to spring 2010). Each aim was partially or completelly achieved by using a mix of field experiments, that are described in table 7.1.

Table 7.1: Methods that were used to achieve each of the initial objectives during the 3 years of fieldwork

Domain of investigation	Techniques related
Aquifer geometry and water pathways	Dye tracing on karrenfield and glacier surface Geological campaign Discharge monitoring at the main springs
Recharge and water transport	Continuous multi-parameter measurements Rainfall and air temperature measurements Water stable isotopes
Impacts of glacier retreat	Geophysical campaign on glacier surface Continuous multi-parameter measurements Dye tracing on glacier surface Water balance calculation
Future water availability	Estimation of glacier volume Water balance calculation Climate change application Hydrograph comparisons

This chapter is a summary of the main findings and compiles the implications of the thesis and also presents the limitations and perspectives for future research.

7.2 Conclusive summaries

7.2.1 Aquifer geometry, water pathways and recharge estimation

The karst aquifer structure is constrained by geological parameters and stratigraphy. An alternance of karstifiable limestones, marls and sandstone layers characterize the Diablerets and neighbouring nappes. At the surface, middle-Createceous and Eocene limestone generously outcrop and represent the studied karrenfield. A large anticline approximatively located under the Tsanfleuron glacier is expected to drive meltwater to the northern and southern part of the system. The southern isoclinal syncline closes the aquifer and acts as a groundwater reservoir. Moreover the fold structures were found to have a major influence on groundwater flow in the shallow karst system, while fractures and faults drive water across the whole stratification to reach deep karst networks.

Three catchements were defined by the mean of 22 tracer tests on the Tsanfleuron karrenfield and glacier. The major part (a surface about $13.7 \cdot 10^6$ m^2) of the karrenfield and Tsanfleuron glacier is drained by Glarey spring. Water flows along the superficial aquifer, parallel to stratification. Water infiltrated at the southern border of the karrenfield crosses 800 m of stratigraphy and flows out in the Tschoetre, Lizerne and Marnes springs. Deep faults enlarged by mass movements created pathways through marls and sandstone strata and allow water to reach basal karst aquifers. Finally a small and thin northern part is drained by the Sarine springs located in another tectonic nappe composed at this location of highly impermeable lithologies. Parts of Lachon stream and karrenfield near the Sanetsch pass are linked with this spring, which present stable electrical conductivity and temperature.

Glacier meltwater production was found to control the flow and transport inside the karst system. Seasonal and diurnal variations were observed. By considering annual time scales, the aquifer is highly dependent on snow and ice melt. Snow cover or winter season presents a very low recharge of the aquifer, with the highest observed electrical conductivities and heavier stable isotope values. Snow and ice melt seasons (spring, summer and autumn) represent a large part of the annual discharge at Glarey spring. Low electrical conductivity and lighter stable isotopes characterize these water volumes. If not altered by rainfalls, diurnal variations are clearly visible during snow and ice melt seasons, where volume of glacier meltwater is maximum at 2 pm, creating a pressure pulse inside the aquifer, followed by a minimum of electrical conductivity when meltwater finally arrives at the spring. Glacial turbidity signals vary 2 hours before electrical conductivity, partly pushed by the initial pressure pulse but mainly transported with glacier meltwater. In case of rain events, discharge, TOC and turbidity show great variations. Autochthonous and glacial turbidity are mobilized together before allochthonous turbidity and TOC signal. Electrical conductivity slowly rises during but especially after rainfalls, indicating an increase of water residence time in the aquifer.

Seasonal recharge contributions were investigated through water stable isotopes, which were used to describe the different processes inside each element constituting the system. Snow melt fractionation creates a variable isotopic input during the spring season. First meltwater is composed of light isotopes, but as the snow cover melts, heavier isotopic ratios are measured in meltwater. Multiple freeze and melt layers inside the glacier, especially the rock-ice interface, postpone for about 10 hours (in comparison with electrical conductivity) the arrival of the typical glacier isotopic signature at Glarey spring. About 65% of Glarey spring flow comes from glacier meltwater during the ice melt season. This proportion decreases to 15% during the snow cover season. Due to isotopic variations during snow melt, the estimation for spring season is more uncertain but was estimated at 55%.

7.2.2 Impact of glacier retreat on future water availability

The substrate geometry and volume of the Tsanfleuron glacier were assessed through combined use of geophysical and hydrogeological methods. For about 180 points, ice thickness was measured during summers 2007 and 2008. By interpolating the measurements, ice volume was estimated at $100{\cdot}10^6\ m^3$, which corresponds to a freshwater storage of $92 \cdot 10^6\ m^3$. Per year an estimated thickness of $1.5\ m$ is lost, corresponding to $3.9{\cdot}10^6\ m^3$ of water if reported to the glacier area in 2008 ($2.8{\cdot}10^6\ m^2$). Simple linear extrapolation based on these data suggests that the disappearance of Tsanfleuron glacier would induce 20% less water at Glarey spring.

Water volumes that enter the system were estimated through mean precipitation data for 2005 to 2009, the catchment area and an evaporation of 10 %. The annual input ($17.7 \cdot 10^6\ m^3$) was found to be close to the mean measured output at Glarey spring, evaluated at $18.2{\cdot}10^6\ m^3$. The difference between in and output is 2%. Many balance scenarios were produced by combining catchment, discharge and precipitation uncertainties and glacier production was found to complete a deficit in input volume of $3.7 \cdot 10^6\ m^3$ in the worst case, or to increase input excess by an equivalent volume. Moreover since winter snow accumulation is completely removed before the end of September, new ice is not created from firn. If such a water volume is removed from the Tsanfleuron glacier every year in the next decades, coupled with climate change prognosis, the ice volume is expected to vanish before 2050.

A comparison between current and future hydrographs illustrates the differences of water repartition during each season. For the worst case, based on uncertainties variations, about 82% of the observed differences comes from the glacier's disappearance, when 18% is a consequence of rainfall alteration. Therefore no important variations would occur between mid October to the end of June. Snow cover and snow melt seasons keep their described specificities. Namely very low recharge from November to the end of February even if rainfalls occur at higher altitude, and high recharge from March to June. Then no glacier meltwater will sustain water volumes in the summer season but only reduced rainfalls will recharge the aquifer. Turbidity dynamics will be altered and electrical conductivity will increase, due to higher residence times in the aquifer. Moreover the glacial Lachon stream will only be active during important rain events. Currently snow accumulation represents 55% of the total annual volume available at Glarey spring and without the glacier's contribution snow melt from March to June could reach 65% of the annual water quantity.

7.3 General conclusions

The objectives were globally achieved, even if many improvements should have been applied for better results. The next section will expose the necessary limitations and improvements of this work. Four years of observations, measurements, interpretations and discussions develop a complete knowledge of the Tsanfleuron test site. Primarily only glacier retreat was studied, but the equilibrium line of the Tsanfleuron glacier was localised at a higher elevation than glacier's summit. Therefore this work deals more with a vanishing than a rapidly melting glacier. The basal motion of the ice was already reduce to a minimum in year 2001 (Grust, 2004), but without new ice creation very few glacier dynamics are expected. Therefore Tsanfleuron glacier may be considered as a frozen water reservoir, distributing a certain amount of water every summer. This approach is consistent with the observed meltwater quantity released during warm seasons, which is about 1.5 more than other glacierized alpine sites with equivalent ice cover (Lambrecht and Mayer, 2009). Without a stabilization of the temperature increase due to climate change in the following years, the current melt trend will certainly accelerate and exceed our simple linear prognoses, presumably result in a rapid glacier's disappearance. This type of situation will alter the dynamics of the karst aquifer and its capacity of water supply for human communities. The first and most important consequence will be temporary water shortages diuring long dry warm periods, while aquifer parameters, namely electrical conductivity, turbidity or microbial communities, will affect the quality of this drinking water resource. As water residence times will increase, rapid flushing of possible contaminations will disappear, inducing higher dispersions and also longer periods of water treatment.

7.4 Limitations and perspectives

Catchement areas are never completely known in such alpine karst systems. Even with many new tracer experiments, doubts always subsist about the exact limits of each spring drainage surface due to karst sensibility on differences in water level. Furthermore infiltration conditions are highly variable between snow and ice melt seasons. Certainly more than 95% of swallow holes present on the karrenfield surface are only active during snow melt periods or strong rainy events. In the remaining 5%, many are unaccessible under the glacier when others create the meltwater infiltration belt visible

at the front of the glacier, which is a particularity that changes every summer. A high temporal and spatial heterogeneity characterizes water infiltration, inducing high difficulties to obtain a complete overview of the studied site. Complex physical processes between snow and ice, aquifer and ice or rain and ice were described and discussed, but involved such different approaches that even a comprehensive hydrogeological study is not enough to precisely determine the complete relations between precipitation, glacier and aquifer. Therefore many improvements are necessary in case of future research dealing with karst aquifer in high alpine areas, opening new perspectives for a better comprehension of such systems.

- More detailed and systematic glacier observations are inevitable in order to grasp relationships between rain, snow and glacier, but also to build a more affordable transfer concept between ice and karst aquifer. Building a general glacier balance would remove a large part of uncertainty about recharge volumes from ice melt.

- New dye tracing on the glacier's surface may result in a more precise localisation of catchment limits on the ice's surface and perhaps develop the drainage comprehension of the northern karst system. Linked with such experiments, new knowledge about retreating glacier hydrology would be expected and may include improved descriptions about meltwater transfers between the glacier and karst aquifer. A distinction of the three characteristic infiltration types developped in this work and their corresponding area could be interesting.

- Snow pack settings also need many improvements. Spacial knowledge of which part of the snow pack is melting and in which proportion. Internal melt process comprehension are also required to specify snow hydrology and its impact on karst dynamics. Transformation steps from fresh snow to firn and ice (metamorphism of snow pack) linked with air temperature and water saturation in snow pack are of first interest for such research.

- Meteorological stations should be installed on many parts of the field in order to quantify sun radiations (and estimate albedo factors), new snowfall thickness and temperatures, as well as wind strength and directions. These data allow to correct rain gauging deviations that are of great importance to equilibrate the water balance of the system.

- Modeling this glacierized system is also a possibility to characterize the internal parameters and the developement of the karst network. A good opportunity, as the major part of the system was found to be drained by Glarey spring.

References

AIEA (2008). *Isotopes de l'environnement dans le cycle hydrologique*. Agence atomique internationale de l'energie atomique, Vienne.

Assier, D. and Evin, M. (1995). Cryokarst and glacial outbursts at the Chauvet Glacier (Haute-Ubaye, French Southern Alps). In *Annales Litteraires*, volume 561 of *3rd international symposium on glacier caves and cryokarst in Polar and high mountain region*, pages 83–87.

Badoux, H. (1982). Des evenements de Zeuzier et de la galerie de sondage du Rawyl RN6. *Bull. tech. Suisse romande*, 12:155–167.

Badoux, H., Bonnard, E., Burri, M., and Vischer, A. (1959). Feuille St-Leonard et Notice explicative. Technical report, Atlas Géologique Suisse.

Badoux, H., Gabus, J., and Mercanton, C. (1990). Feuille 1285 Les Diablerets. Technical report, Service Géologique National Suisse.

Baker, A. (2001). Fluorescence excitation emission matrix characterization of some sewage-impacted rivers. *Environmental Science and Technology*, 35(5):948–953.

Bates, P., Siegert, M., Lee, V., Hubbard, B., and Nienow, P. (2003). Numerical simulation of three-dimensional velocity fields in pressurized and non-pressurized nye channels. *Annals of Glaciology*, 37:281–285.

Batiot, C. (2002). *Etude experimentale du cycle du carbone en régions karstiques. Apport du carbone organique et du carbone mineral a la connaissance hydrogéologique des systemes.* PhD thesis, University of Avignon and Pays de Vaucluse, France.

Bechtel, T., Bosch, F., and Gurk, M. (2007). *Methods in karst hydrogeology*, chapter Geophysical methods, pages 171–199. Taylor & Francis.

Behrens, H., Beims, U., Dieter, G., Eikmann, T., Grummt, T., Hanisch, H., H., H., Kass, W., Kerndorf, H., Leibundgut, C., Muller-Wegener, U., Ronnefahrt, I., Scharenberg, B., Schleyer, R., Scholz, W., and Tilkes, F. (2001). Toxicological and ecotoxicological assessment of water tracers. *Hydrogeology Journal*, 9:321–325.

Beniston, M., Diaz, H., and Bradley, R. (1997). Climatic change at high elevation sites: an overview. *Climatic Change*, 36:233–251.

Beniston, M., Keller, F., Koffi, B., and Goyette, S. (2003). Estimates of snow accumulation and volume in the Swiss Alps under changing climatic conditions. *Theor. Appl. Climatol.*, 76:125–140.

Benn, D. (1998). *Glaciers and Glaciation.* Arnold Publishers.

Boulton, G., Slot, T., Blessing, K., Glasbergen, P., Leijnse, T., and Vangijssel, K. (1993). Deep circulation of groundwater in overpressured subglacial aquifers and its geological consequences. *Quat Sci Rev*, 12(9):739–745.

Braun, L., Weber, M., and Schulz, M. (2000). Consequences of climate change for runoff from Alpine regions. *Annals of Glaciology*, 31:19–25.

Brissaud, F., Salgot, M., Bancole, A., Campos, C., and Folch, M. (1999). Residence time distribution and disinfection of secondary effluents by infiltration percolation. *Water Science and technology*, 40(4/5):215–222.

Butscher, C. and Huggenberger, P. (2007). Implications for karst hydrology from 3d geological modeling using the aquifer base gradient approach. *J Hydrol*, 342(12):184–198.

Cannone, N., Diolaiuti, G., Guglielmin, M., and Smiraglia, C. (2008). Accelerating climate change impacts on alpine glacier forefield ecosystems in the European Alps. *Ecological Applications*, 18(3):637–648.

Chandler, D., Hubbard, B., Hubbard, A., Murray, T., and Rippin, D. (2008). Optimising ice flow law parameters using borehole deformation measurements and numerical modelling. *Geophysical Research Letters*, 35(12):L12502.

Clark, G. (2005). Subglacial processes. *Annual Review Earth Planet*, 33:247–276.

Clark, I. and Fritz, P. (1997). *Environmental isotopes in hydrogeology.* Lewis Publishers.

Corbel, J. (1957). Karsts alpins de moyenne altitude: Interlaken, Beatenberg. *Revue de Gographie de Lyon*, 32(1):43–56.

COST-65 (1995). *Hydrogeological aspects of groundwater protection in karstic areas, Final report.* European commission, directorat general XII Science, Research and development, Report EUR 16547, Brussels, Luxembourg.

Crespo-Blanc, A., Masson, H., Sharp, Z., Cosca, M., and Hunziker, J. (1995). A stable and 40Ar/39Ar isotope study of a major thrust in the Helvetic nappes (Swiss Alps): evidence for fluid flow and constraints on nappe kinematics. *Geol Soc Am Bull*, 107(10):1129–1144.

Criss, R., Davidsson, L., Surbeck, H., and Winston, W. (2007). Isotopic methods. In *Methods in karst hydrogeology*, pages 123–144. Goldscheider and Drew.

Curtis, D. and Burnash, R. (1996). Inadvertent rain gauge inconsistencies and their effect on hydrologic analysis. In *California-Nevada Conference*, pages 1–4. ALERT user group.

De Jong, C., List, F., and Ergenzinger, P. (2002). Experimental hydrological analyses in the Dichma based on daily and seasonal evaporation. *Nordic Hydrology*, 33(1):1–14.

Dray, M., Parriaux, A., and Dubois, J. (1990). Image synchrone de la composition isotopique de la couverture neigeuse des Alpes de Suisse occidentale. *Proc. and Reports IAHS*, pages 447–454.

Escher, A., Masson, H., and Steck, A. (1993). Nappe geometry in the Western Swiss Alps. *J Struct Geol*, (15):501–509.

Escher-Vetter, H., Braun, L., Siebers, M., and Weber, M. (2005). Water balance of the Vernagtferner high alpine basin based on long-term measurements and modelling. *Landschaftökologie und Umweltforschung*, 48:19–32.

Etcheverry, D. (2002). Valorisation des méthodes isotopiques pour les questions pratiques liées aux eaux souterraines, isotopes de l'oxygene et e l'hydrogene. Technical report, Swiss federal office for environment.

Fairchild, I.-J., Killawee, J.-A., Hubbard, B., and Dreybrodt, W. (1999). Interactions of calcareous suspended sediment with glacial meltwater: a field test of dissolution behaviour. *Chem Geol*, 155(34):243–263.

Fette, M., Kipfer, R., Schubert, C., Hohn, E., and Wehrli, B. (2005). Assessing river-groundwater exchange in the regulated Rhône river (Switzerland) using stable isotopes and geochemical tracers. *Applied geochemistry*, 20:701–712.

Fischer, G., Schnegg, P., Ma, J., Mueller, I., and Burkhardt, M. (1987). Etude VLF-R du remplissage quaternaire de la vallée de Gastern (Alpes Bernoises, Suisse). *Eclogae geol. Helv.*, 80(3):773–787.

Flowers, G., Bjornsson, H., and Palsson, F. (2003). New insights into the subglacial and periglacial hydrology of Vatnajokull, Iceland, from a distributed physical model. *J Glaciol*, 49(165):257–270.

Ford, D. (1983). The physiography of the Castelguard karst and Columbia icefields area, alberta, canada. *Arctic and Alpine Research*, 15(4):427–436.

Ford, D. and Williams, P. (2007). *Karst hydrogeology and geomorphology*. Wiley, Chichester.

Fountain, A., Schlichting, R., Jansson, P., and Jacobel, R. (2005). Observations of englacial water passages: a fracture-dominated system. *Annals of Glaciology*, 40:25–30.

Fountain, A. and Walder, J. (1998). Water flow through temparate glaciers. *Review of Geophysics*, 36(3):299–328.

Franck, P., Wagner, J., Escher, A., and Pavoni, N. (1984). Evolution des contraintes tectoniques et sismique dans la region du col du Sanetsch, Alpes Valaisannes Helvetiques. *Eclogae Geol Helv*, 77(2):383–393.

Goldscheider, N. (2002). *Hydrogeology and vulnerability of karst systems - Example from the Northern Alps and the Swabian Alb.* PhD thesis, Angewandte Geologie Karlsruhe.

Goldscheider, N. (2005). Fold structure and underground drainage pattern in the alpine karst system Hochifen-Gottesacker. *Eclogae Geol Helv*, 98(1):117.

Goldscheider, N., Meiman, J., Pronk, M., and Smart, C. (2008). Tracer tests in karst hydrogeology and speleology. *International Journal of Speleology*, 37(1):27–40.

Goppert, N. and Goldscheider, N. (2008). Solute and colloid transport in karst conduits under low- and high-flow conditions. *Ground Water*, 46(1):61–68.

Greene, A., Broecker, W., and Rind, D. (1999). Swiss glacier recession since the little ice age: reconciliation with climate records. *Geophys Res Lett*, 26(13:1909–1912.

Gremaud, V. and Nessi, J. (2006). Etude structurale et hydrogeologique de la region du Col du Sanetsch et du Lapiaz de Tsanfleuron (Suisse). Master's thesis, University of Lausanne, Switzerland, (unpublished).

Gruber, S. and Haeberli, W. (2007). Permafrost in steep bedrocks slopes and its temperature-related destabilization following climate change. *J. Geophys. Res.*, 112(f2):F02S18.

Grust, K. (2004). *The hydrology and dynamics of a glacier overlying a linked-cavity drainage system*. PhD thesis, Dpt of Geography and geomatics, University of Glasgow.

Gurnell, A. and Clark, M. (1987). *Glacio-fluvial sediment transfert: An Alpine perspective*. Wiley and sons, Chichester.

Haeberli, W., Hoelzle, M., Paul, F., and Zemp, M. (2007). Integrated monitoring of mountain glaciers as key indicators of global climate change: the European Alps. *Ann. glaciol.*, 46:150–160.

Hecht, E. (1999). *Physique*. De Boeck and Larcier, Bruxelles.

Herold, T., Jordan, P., and Zwahlen, F. (2000). The influence of tectonic structures on karst flow patterns in karstified limestones and aquitards in the Jura Mountains, Switzerland. *Eclogae Geol Helv*, 93(3):349–362.

Hock, R. and Jansson, P. (2005). Modeling Glacier Hydrology. In *Encyclopedia of Hydrological Sciences*, pages 2647–2655. Anderson MG.

Hohmann, R., Thalmann, E., Muller-Ferch, G., Neu, U., Ritz, C., and Kull, C. (2007). Les changements climatiques et la Suisse en 2050, Impacts attendus sur l'environnement, la société et l'économie. Report, OcCC - Organe consultatif sur les changements clismatiques.

Hubbard, B. (2002). Direct measurement of basal motion at a hardbedded, temperate glacier: Glacier de Tsanfleuron, Switzerland. *J Glaciol*, 48(160):18.

Hubbard, B. and Hubbard, A. (1998). Bedrock surface roughness and the distribution of subglacially precipitated carbonate deposits: implications for formation at Glacier de Tsanfleuron, Switzerland. *Earth Surf Proc Land*, 23(3):261–270.

Hubbard, B., Hubbard, A., Tison, J.-L., Mader, H., Nienow, P., and Grust, K. (2003). Spatial variability in the water content and rheology of temperate glaciers: Glacier de Tsanfleuron, Switzerland. *Ann Glaciol*, 37:16.

Hubbard, B., Tison, J., Jannsens, L., and Spiro, B. (2000). Ice core evidence for the thickness and character of clear facies basal ice: Glacier de Tsanfleuron, Switzerland. *J Glaciol*, 46(152):140–150.

Huselmann, P., Otz, M., and Jeannin, P. (2003). A review of the dye tracing experiments done in the Siebenhengste karst region (Bern, Switzerland). *Eclogae Geol Helv*, 96(1):23–36.

Huss, M., Farinotti, D., Bauder, A., and Funk, M. (2008). Modelling runoff from highly glacierized alpine drainage basins in a changing climate. *Hydrological Processes*, 22:3888–3902.

Jansson, P., Hock, R., and Schneider, T. (2003). The concept of glacier storage: a review. *Journal of Hydrology*, 282(1):116–129.

Jeannin, P. (2001). Modeling flow in phreatic and epiphreatic karst conduits in the Hölloch cave (Muotatal, Switzerland). *Water Resour Res*, 37(2):191–200.

Kass, W. (1998). *Tracing technique in geohydrology*. Balkema, Rotterdam.

Kleinn, J., Frei, C., Gurtz, J., Luthi, D., Vidale, P., and Schar, C. (2005). Hydrologic simulations in the Rhine basin driven by a regional climate model. *J Geophys Res Atmos*, 110:D04102.

Klotz, M. (2007). Partikelzählsysteme: Des Worst-Case Lässt sich vermieden - Prüfung der technischen Sauberkeit von Hydraulikflüssigkeiten. *Fluid Spezial*, Hydrauliköle:24–26.

Kralik, M. (2001). *Strategie zum Schutz der Karstwassergebiet in Öesterreich*. Umweltbundesamt GmbH, Vienna.

Kulessa, B. (2007). A critical review of the low-frequency electrical properties of ice sheets and glaciers. *Journal of Environmental & Engineering Geophysics*, 12(3):23–36.

Lakey, B. and Krothe, N. (1996). Stable isotopic variation of storm discharge from a Perennial Karst spring, Indiana. *Water Resources Research*, 32:721–731.

Lambrecht, A. and Mayer, C. (2009). Temporal variability of the non-steady contribution from glaciers to water discharge in western Austria. *Journal of Hydrology*, 376:353–361.

Lang, H. (1981). Is evaporation an important component in high alpine hydrology? *Nordic Hydrology*, 12:217–224.

Linder, P. (2005). An Eocene paleodoline in the Morcles Nappe of Anzeindaz (Canton de Vaud, Switzerland). *Eclogae Geol Helv*, 98(1):51–61.

Lis, G., Wassenaar, L., and Hendry, M. (2008). High-Precision Laser Spectroscopy D/H and $^{18}O/^{16}O$ measurements of microliter natural water samples. *Anal. Chem.*, 80:287–293.

Loukas, A., Vasiliades, L., and Dalezios, N. (2002). Climatic impacts on the runoff generation processes in British Columbia, canada. *Hydrology and Earth System Sciences*, 6(2):211–227.

Lugeon, M. (1914). Les Hautes Alpes calcaires entre la Lizerne et la Kander (Wildhorn, Wildstrubel, Balmhorn et Torrenthorn). Technical report, Service Gologique National Suisse.

Lugeon, M. (1940). Feuille Diablerets et Notice explicative. Technical report, Service Géologique National Suisse.

MacCraith, B., Grattan, K., Connolly, D., Briggs, R., Boyle, W., and Avis, M. (1993). Cross comparison of techniques for the monitoring of total organic carbon (TOC) in water sources and supplies. *Water Science and Technology*, 28(11-12):457–463.

Marechal, J., Perrochet, P., and Tacher, L. (1999). Long-term simulations of thermal and hydraulic characteristics in a mountain massif: the Mont Blanc case study, French and Italian Alps. *Hydrogeol J*, 7(4):341–354.

Masotti, D. (1989). Sources de Glarey, zones de protection. Mandat, rapport 02/89, Commune de Conthey.

Masotti, D. (1991). Contribution l'étude scientifique du karst de Tanfleuron, Valais. In *Actes du 9e congrs national de la SSS*.

Masson, H., Baud, A., Escher, A., Gabus, J., and Marthaler, M. (1980). Compte rendu de l'excursion de la societe géologique suisse du 1 au 3 octobre 1979 : coupe Préalpes-Helvetique-pennique en Suisse Occidentale. *Eclogae Geol Helv*, 73(1):331–349.

Menkveld-Gfeller, U. (1994). Die Wildstrubel-, die Hohgant- und die Sanetsch-Formation: Drei neue lithostratigraphische Einheiten des Eocaens der helvetischen Decken. *Eclogae Geol Helv*, 87(3):789–809.

Moran, T., Marshall, S., Evans, E., and Sinclair, K. (2007). Altitudinal gradients of stable isotopes in lee-slope precipitation in the Canadian Rocky Moutains. *Arctic, Antarctic and Alpine Research*, 39(3):455–467.

Munro, S. (2005). A revised Canadian perspective: Progress in glacier hydrology. *Hydrological Processes*, 19:231–245.

Nath Sovik, K. and Huss, M. (2010). Glaciological investigations on three glaciers at Les Diablerets, Alpes Vaudoises. In *Abstract Volume, 8th Swiss Geoscience Meeting*.

Novel, J., Dray, M., Fehri, A., Jusserand, C., Nicoud, G., and Olive, P. (1999). Homogenization processes affecting isotopic signals (18O and 3H) in a mountainous hydrological system: The Aoasta Valley (Italy). *Revue des sciences de l'eau*, 12(1):3–21.

OcCC (2008). Le climat change, que faire? Le nouveau rapport des Nations Unies sur le climat (GIEC 2007) et ses principaux résultats dans l'optique de la Suisse. Report, OcCC - Organe consultatif sur les changements clismatiques.

Paul, F., Kaab, A., Maisch, M., Kellenberger, T., and Haeberli, W. (2004). Rapid disintegration of Alpine glaciers observed with satellite data. *Geophys Res Lett*, 31:L21.

Pavoni, N. (1980). Comparison of focal mechanisms of earthquakes and faulting in the Helvetic zone of the Central Valais, Swiss Alps. *Eclogae Geol Helv*, 73(2):551–558.

Pavoni, N., Maurer, H.-R., Roth, P., and Deichmann, N. (1997). Seismicity and seismotectonics of the Swiss Alps. In *Deep structure of the Swiss Alps: results of NRP 20*, pages 241–250, Basel. Pfiffner AO.

Pronk, M. (2008). *Origin and behaviour of microorganisms and particles in selected karst aquifer systems*. PhD thesis, Science Faculty, Centre of Hydrogeology, University of Neuchatel, Switzerland.

Pronk, M., Goldscheider, N., and Zopfi, J. (2006). Dynamics and interaction of organic carbon, turbidity and bacteria in a karst aquifer system. *Hydrogeol J*, 14(4):473–484.

Pronk, M., Goldscheider, N., Zopfi, J., and Zwahlen, F. (2009). Percolation and particle transport in the unsaturated zone of a karst aquifer. *Ground Water*, 47(3):361–369.

Ramu, S. (2010). Use of a particle-counter to characterize transport and dynamics of glacial turbidity in a glacier-karst-aquifer system, Tsanfleuorn, Swiss Alps. Master's thesis, University of Neuchatel, Switzerland, (unpublished).

Rubel, F., Ungersbock, M., Skomorowski, P., Auer, I., Rudolf, B., Fuchs, T., and Rapp, J. (2000). On the correction of systematic rain gauge measurement errors. In *Mesoscale Alpine Programme, Climate workshop*.

Savoy, L. (2007). *Use of natural and artificial reactive tracers to investigate the transfer of solutes in karst systems*. PhD thesis, Science Faculty, Centre of Hydrogeology, University of Neuchatel, Switzerland.

Schaefli, B., Hingray, B., and Musy, A. (2007). Climate change and hydropower production in the Swiss Alps: quantification of potential impacts and related modelling uncertainties. *Hydrol Earth Syst Sci*, 11(3):1191–1205.

Schotterer, U., Stocker, T., Burki, H., Hunziker, J., Kozel, R., Grasso, D., and Tripet, J. (2002). Das Schweizer isotopen messnetz, trend 1992-1999. *Gas-Wasser-Abwasser*, 80:3–11.

Schudel, B., Biaggi, D., Dervey, T., Kozel, R., Müller, I., JH, R., and Schindler, U. (2002). Utilisation de traceurs artificiels en hydrogologie. *Report from Federal Office for Environment and Swiss Society for Hydrogeology (SSH)*.

Seidel, K., Ehrler, C., and Martinec, J. (1998). Effects of climate change on water resources and runoff in an Alpine basin. *Hydrological Process*, 12(10-11):1659–1669.

Senechal, G., Rousset, D., Salome, A., and Grasso, J. (2003). Georadar and seismic investigations over the Glacier de la Girose (French Alps). *Near Surface Geophysics*, 1(1):5–12.

Senesi, N., Miano, T., Provenzano, M., and Brunetti, G. (1991). Characterization, differentiation, and classification of humic substances by fluorescence spectroscopy. *Soil Science*, 152(4):259–271.

SGMN (2009). The Swiss Glaciers, Yearbooks of the Cyosperic Commission of the Swiss Academy of Sciences. http://glaciology.ethz.ch/swiss-glaciers/.

Sharp, M., Gemmell, J., and Tison, J. (1989). Structure and stability of the former subglacial drainage system of the Glacier de Tsanfleuron, Switzerland. *Earth Surface Processes and Landforms*, 14(2):119–134.

Siegenthaler, U. and Oescheger, H. (1980). Correlation of 18O in precipitation with temperature and altitude. *Nature*, 285:314–317.

Smart, C. (1983). The hydrology of the Castleguard Karst, Columbia Icefields, Alberta, canada. *Arctic and Alpine Research*, 15:471–486.

Smart, C. (1996). Statistical evaluation of glacier boreholes as indicators of basal drainage systems. *Hydrol Process*, 10(4):599–613.

Smart, C. (1997). Hydrogeology of glacial and subglacial karst aquifers: Small River, British Columbia Canada. In Jeannin, P., editor, *6th conference on Limestone Hydrology and Fissured Media*, pages 315–318. Universit de Franche-Comte.

Smart, C. and Ford, D. (1986). Structure and function of a conduit aquifer. *Canadian Journal of Earth Sciences*, 23:919–929.

Spicher, A. (1980). Carte tectonique de la Suisse 1:500000. Publication cartographique, Service gologique national Suisse.

Steck, A., Bigioggero, B., Dal Piaz, G., Escher, A., Martinotti, G., and Masson, H. (1999). Carte tectonique des Alpes de Suisse occidentale et des régions avoisinantes 1:100000. Technical report, Service Gologique National Suisse.

Steck, A., Epard, J., Escher, A., Gouffon, T., and Masson, H. (2001). Carte tectonique des Alpes de Suisse occidentale et des regions avoisinantes 1:100000. Notice explicative, Service gologique national Suisse.

Steck, A. and Hunziker, J. (1994). The Tertiary structural and thermal evolution of the Central Alps: compressional and extensional structures in an orogenic belt. *Tectonophysics*, 238:229–254.

Strasser, U., Bernhardt, M., Weber, M., Liston, G., and Mauser, W. (2008). Is snow sublimation important in the alpine water balance? *The Cryosphere*, 2:53–66.

Suzuoki, T. and Kimura, T. (1973). D/H and 18O/16O fractionation in ice-water system. *Mass Spectroscopy*, 72:229–233.

SwissGEO (2008). www.swissgeo.ch.

Taylor, S., Feng, X., Williams, M., and McNamara, J. (2002). How isotopic fractionation of snowmelt affects hydrograph separation. *Hydrol. Process*, 16:3683–3690.

Thierrin, J. (1990). *Contribution l'étude des eaux souterraines de la region de Fribourg (Suisse Occidentale)*. PhD thesis, Science Faculty, Centre of Hydrogeology, University of Neuchatel.

Toth, J. (1963). A theoretical analysis of groundwater flow in small drainage basins. *J Geophys Res*, 68(16):4795–4812.

Toth, J. (1999). Groundwater as a geologic agent: an overview of the causes, processes and manifestations. *Hydrogeol J*, 7(1):114.

Viviroli, D. and Weingartner, R. (2004). The hydrological significance of mountains: from regional to global scale. *Hydrol Earth Sys Sci*, 8(6):1016–1029.

Weidmann, M., Franzen, J., and Berger, J. (1991). Sur l'âge des Couches a Cerithes ou Couches des Diablerets de l'Eocene alpin. *Eclogae Geol Helv*, 84(3):893–919.

Wernli, H. (1994). Markierversuche in der Molasse. *Gas-Wasser-Abwasser*, pages 15–22.

Wieland, B. (1976). *Petrographie eozaener siderolithischer Gesteine des Helvetikums der Schweiz: ihre Diagenese und schwache Metamorphose*. PhD thesis, Univ. Bern.

Zemp, M., Haeberli, W., Hoelze, M., and Paul, F. (2006). Alpine glaciers to disappear within decades? *Geophys. Res. Lett.*, 33(13):L13504.

Zoetl, J. (1974). *Karsthydrogeologie*. Springer.

Appendix A

Appendix from chapter 2

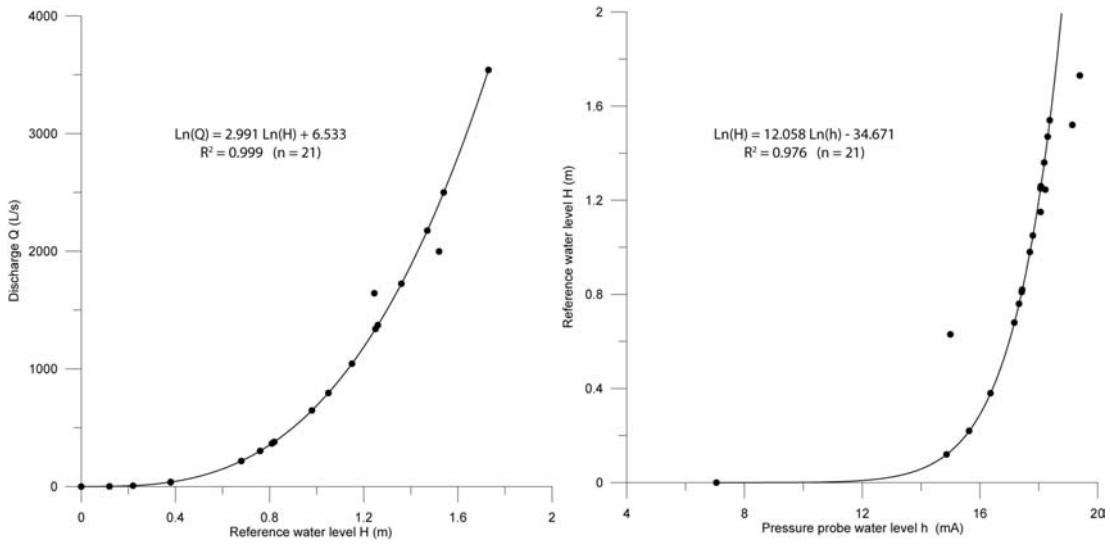

Figure A.1: Glarey overflow discharge calibration.

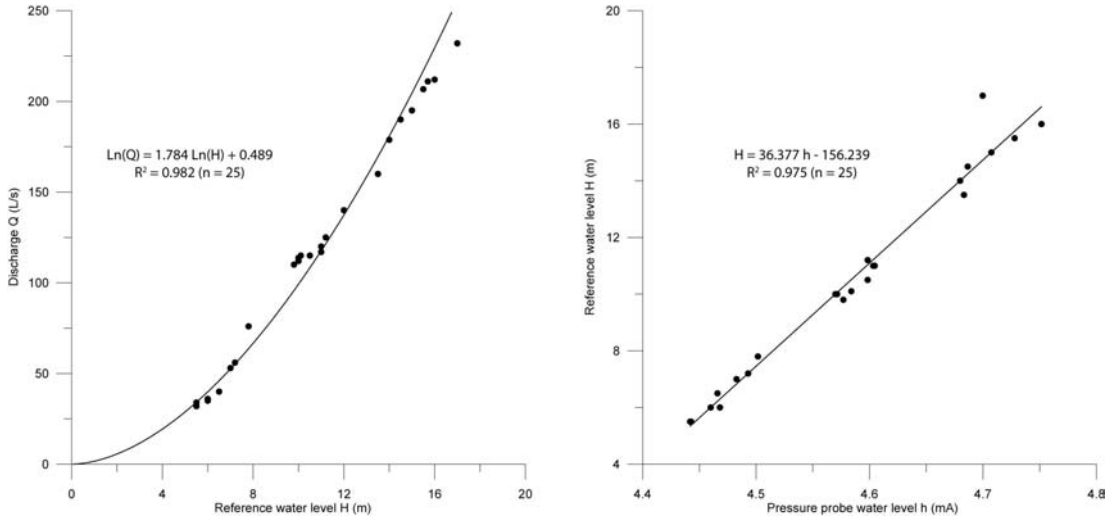

Figure A.2: Glarey discharge calibration.

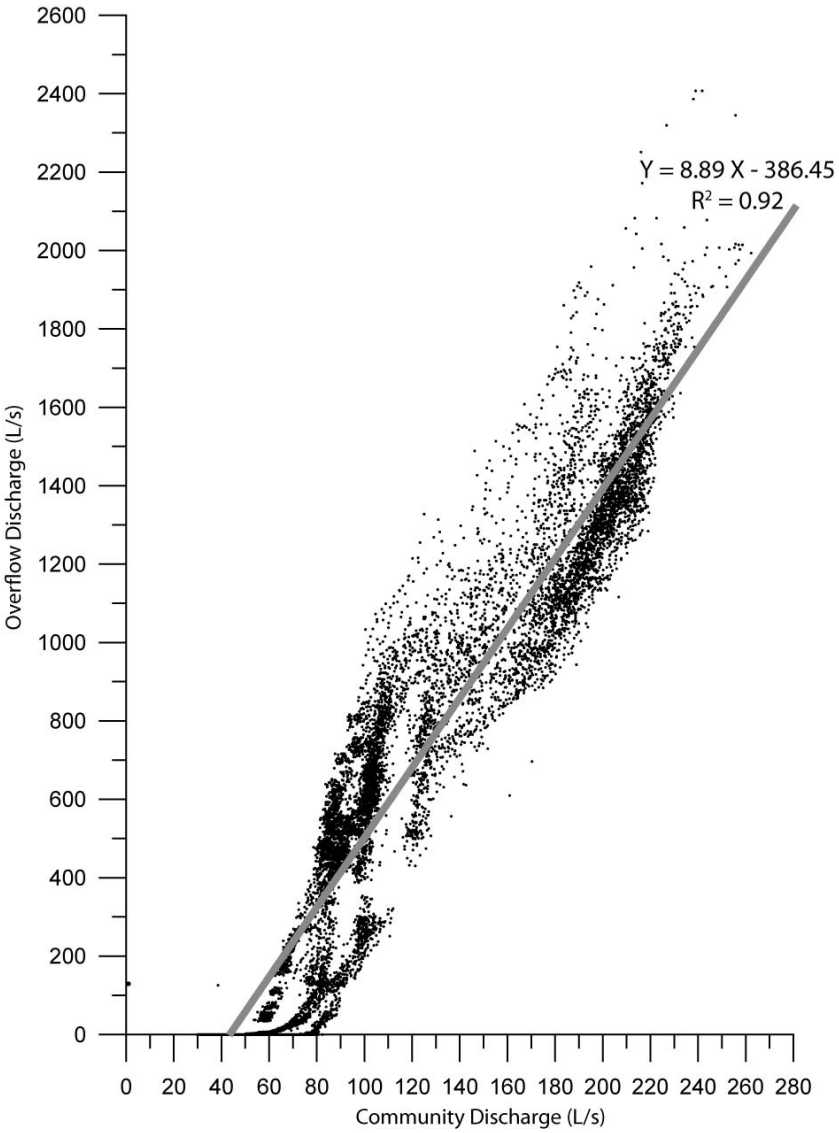

Figure A.3: Correlation between Glarey discharge and its overflow.

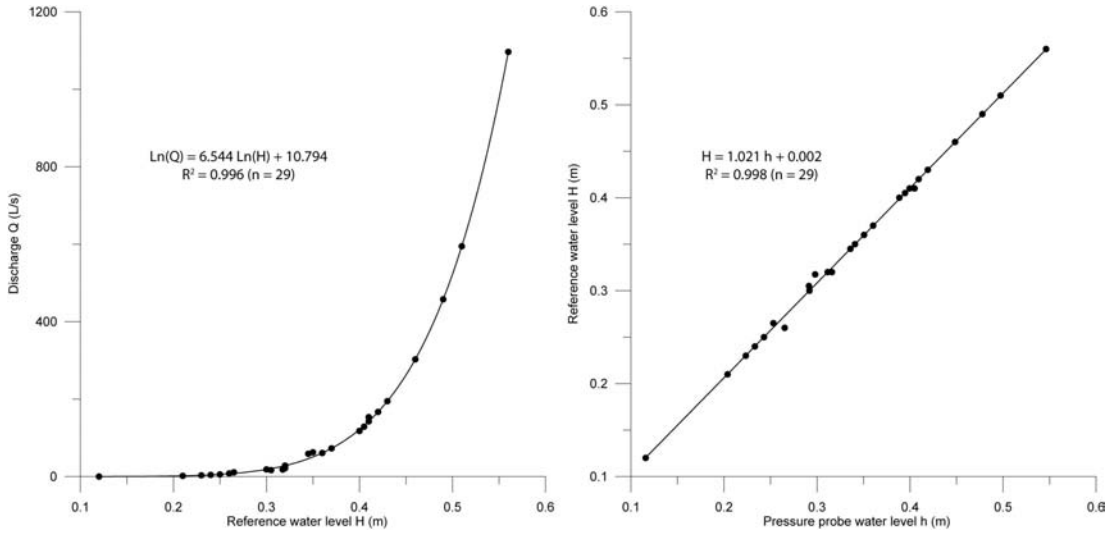

Figure A.4: Calibration curve at Lachon main swallow hole.

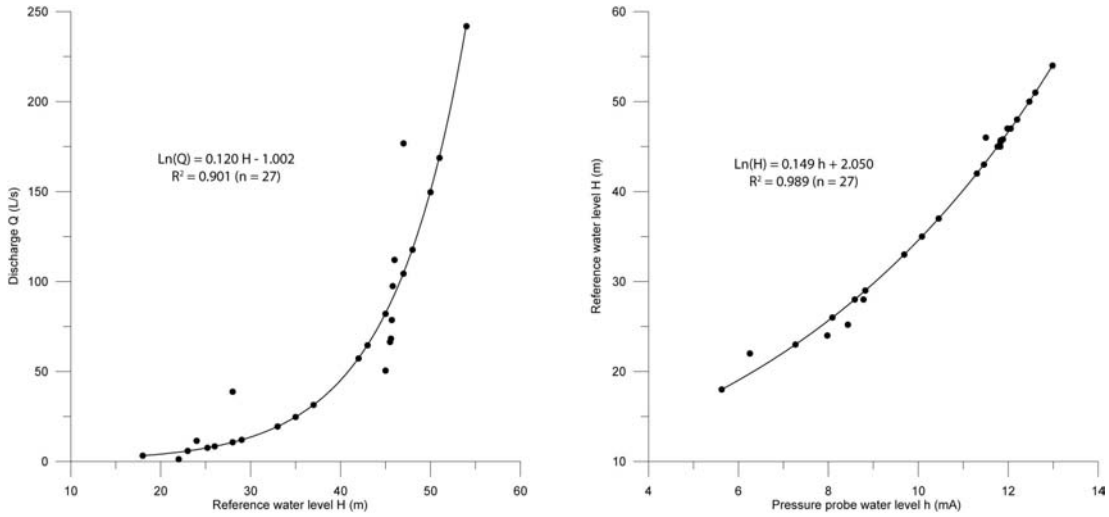

Figure A.5: Calibration curve at Lachon stream at Plan de la Fontaine.

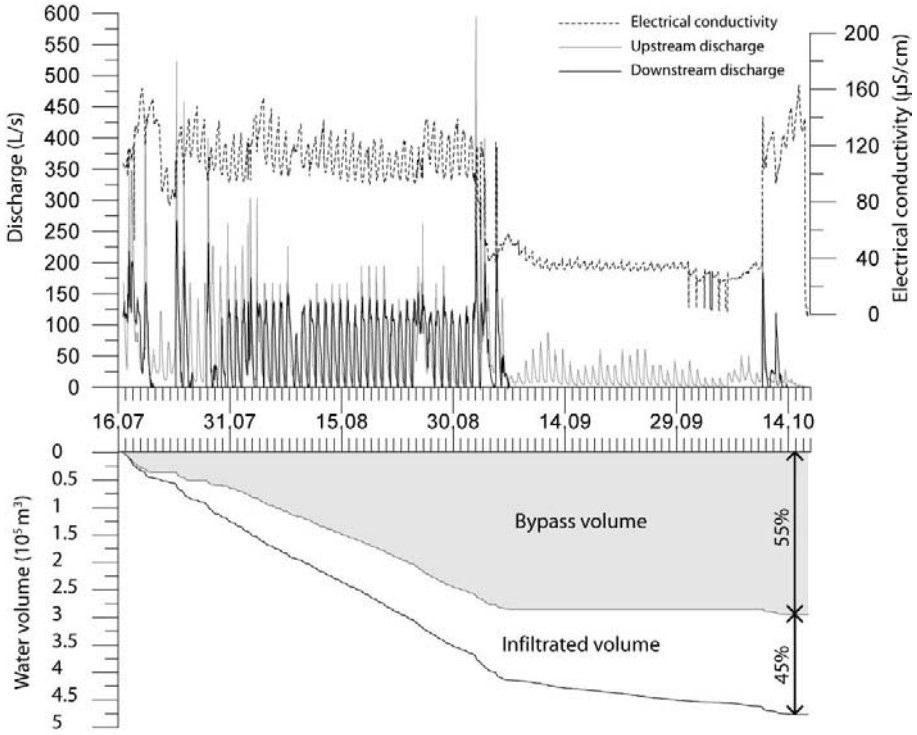

Figure A.6: Infiltration of Lachon stream in the main swallow hole. Less than 40% of the Lachon continues in the streambed during 4 summer months.

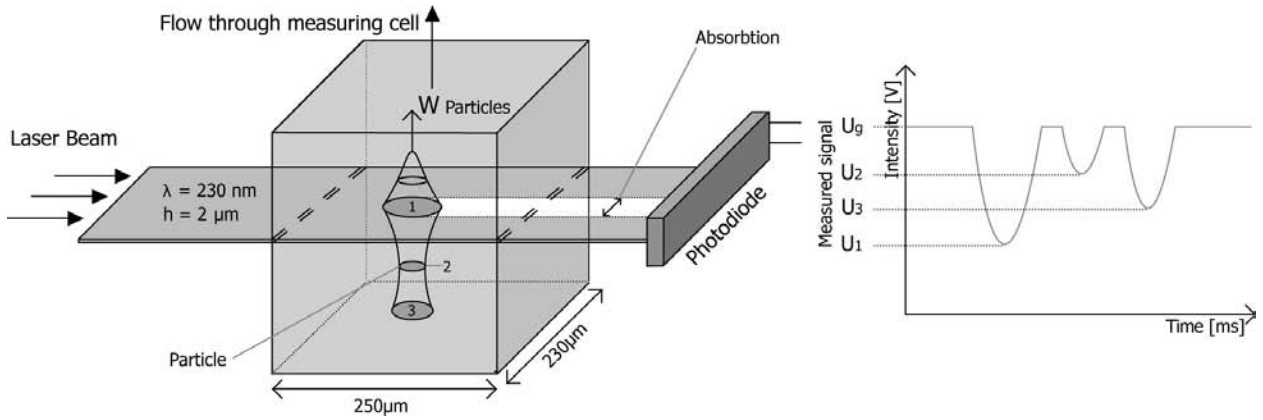

Figure A.7: Particle counter instrument. A laser beam crosses the particles'trajectory and its intensity decreases proportionally to the size of the particles. A correlation between intensity and time allows to count the particle numbers and specifiy their size. Modified from literature (Klotz, 2007).

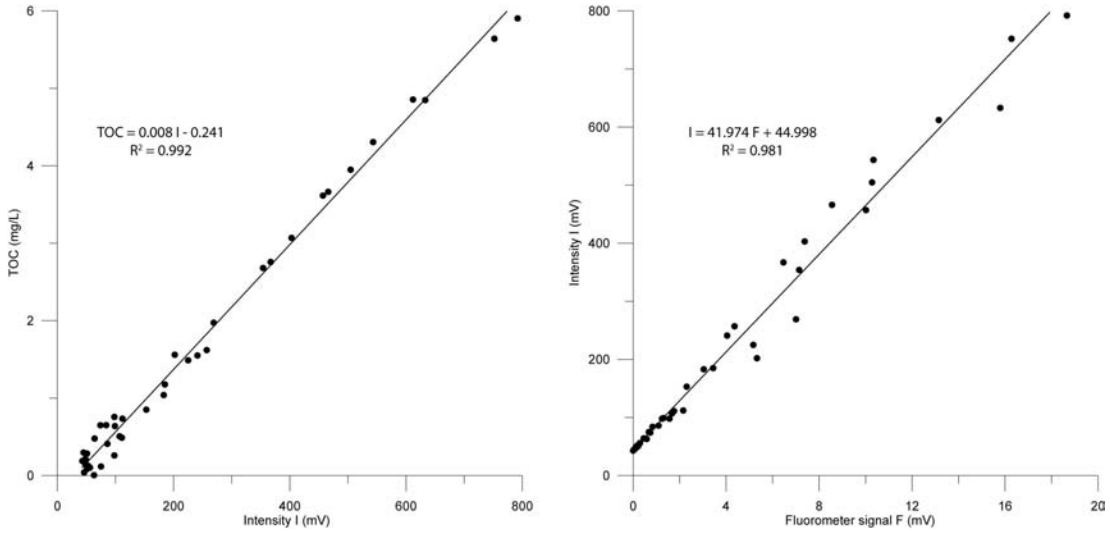

Figure A.8: Calibration of field fluorometer to measure TOC. Samples are analyzed on the spectrofluorimeter, which give an intensity I corresponding to a concentration in TOC. This intensity is then correlated to the continuous monitoring of the field fluorometer F.

Figure A.9: Analysed anions and cations at Glarey spring, in meq.

	Cations					Anions				
	Sodium	Ammonium	Potassium	Magnesium	Calcium	Fluoride	Choride	Nitrate	Sulfate	Bicarbonate
Date and hours	meq	meq	meq	meq	meq	meq	meq	meq	meq	meq
13.01.2008 11:15	0.178	0.006	0.008	0.575	2.861	0.246	0.004	0.010	0.691	2.675
27.02.2008 12:30	0.086	0.006	0.004	0.334	2.944	0.247	0.021	0.007	0.285	2.810
26.04.2008 10:48	0.048	0.004	0.004	0.232	2.373	0.247	0.003	0.013	0.200	2.195
02.06.2008 12:15	0.018	0.004	0.002	0.094	1.331	0.000	0.003	0.007	0.132	1.305
18.06.2008 16:30	0.037	0.003	0.002	0.093	1.394	0.000	0.007	0.008	0.073	1.434
11.08.2008 11:15	0.037	0.005	0.002	0.089	1.324	0.000	0.002	0.000	0.077	1.372
11.08.2008 12:15	0.030	0.001	0.002	0.084	1.227	0.000	0.005	0.003	0.076	1.270
11.08.2008 13:15	0.030	0.001	0.001	0.077	1.117	0.000	0.002	0.000	0.070	1.169
11.08.2008 14:15	0.035	0.003	0.002	0.089	1.629	0.000	0.002	0.000	0.064	1.691
11.08.2008 15:15	0.031	0.002	0.002	0.076	1.253	0.000	0.001	0.002	0.059	1.304
11.08.2008 16:15	0.030	0.002	0.002	0.078	1.312	0.000	0.002	0.002	0.060	1.363
11.08.2008 17:15	0.029	0.002	0.002	0.074	1.239	0.000	0.001	0.000	0.055	1.286
11.08.2008 18:15	0.027	0.002	0.002	0.073	1.231	0.000	0.002	0.001	0.054	1.269
11.08.2008 19:15	0.029	0.003	0.002	0.074	1.279	0.000	0.002	0.000	0.056	1.323
11.08.2008 20:15	0.030	0.002	0.002	0.073	1.255	0.000	0.001	0.001	0.052	1.319
11.08.2008 21:15	0.031	0.000	0.001	0.079	1.316	0.000	0.001	0.000	0.054	1.364
11.08.2008 22:15	0.030	0.004	0.001	0.076	1.296	0.000	0.003	0.000	0.057	1.356
11.08.2008 23:15	0.032	0.004	0.002	0.079	1.328	0.000	0.001	0.000	0.059	1.373
12.08.2008 00:15	0.036	0.000	0.001	0.081	1.343	0.000	0.001	0.000	0.062	1.408
12.08.2008 01:15	0.035	0.002	0.002	0.081	1.350	0.000	0.002	0.000	0.064	1.416
12.08.2008 02:15	0.034	0.002	0.002	0.084	1.363	0.000	0.003	0.000	0.068	1.402
12.08.2008 03:15	0.035	0.002	0.002	0.088	1.385	0.000	0.001	0.000	0.071	1.437
12.08.2008 04:15	0.035	0.004	0.002	0.087	1.380	0.000	0.002	0.000	0.074	1.430
12.08.2008 05:15	0.040	0.001	0.002	0.096	1.448	0.001	0.001	0.000	0.080	1.517
12.08.2008 06:15	0.044	0.007	0.002	0.110	1.627	0.000	0.002	0.000	0.088	1.681
12.08.2008 07:15	0.040	0.001	0.002	0.105	1.458	0.001	0.001	0.000	0.094	1.516
12.08.2008 08:15	0.081	0.001	0.003	0.117	1.130	0.000	0.002	0.000	0.094	1.242
12.08.2008 10:30	0.081	0.001	0.003	0.117	1.130	0.000	0.020	0.007	0.114	1.193
12.08.2008 12:30	0.061	0.001	0.004	0.112	1.131	0.000	0.002	0.005	0.114	1.195
12.08.2008 14:30	0.058	0.001	0.003	0.116	1.181	0.000	0.002	0.008	0.118	1.235
12.08.2008 16:30	0.043	0.000	0.002	0.117	1.173	0.000	0.003	0.005	0.121	1.213
12.08.2008 18:30	0.049	0.001	0.002	0.119	1.182	0.000	0.003	0.012	0.121	1.224
12.08.2008 20:30	0.055	0.024	0.084	0.119	1.182	0.000	0.125	0.016	0.135	1.196
12.08.2008 22:30	0.044	0.001	0.003	0.107	1.103	0.000	0.002	0.005	0.112	1.149
13.08.2008 00:30	0.041	0.004	0.003	0.098	1.055	0.000	0.003	0.006	0.101	1.102
13.08.2008 02:30	0.048	0.001	0.025	0.089	1.000	0.000	0.002	0.005	0.088	1.060
13.08.2008 04:30	0.042	0.003	0.021	0.083	0.941	0.000	0.025	0.007	0.084	0.962
13.08.2008 06:30	0.051	0.001	0.002	0.078	0.892	0.000	0.002	0.004	0.078	0.947
13.08.2008 08:30	0.045	0.004	0.008	0.081	0.928	0.001	0.008	0.006	0.087	0.971
13.08.2008 10:30	0.034	0.001	0.002	0.082	0.938	0.001	0.001	0.005	0.085	0.969
13.08.2008 12:30	0.031	0.002	0.003	0.084	0.960	0.000	0.002	0.005	0.088	0.991
13.08.2008 14:30	0.072	0.005	0.003	0.092	1.076	0.000	0.003	0.006	0.093	1.140
12.09.2008 09:40	0.038	0.005	0.002	0.126	1.967	0.000	0.002	0.007	0.109	2.029
12.09.2008 14:40	0.038	0.005	0.003	0.104	1.847	0.002	0.004	0.010	0.096	1.895
12.09.2008 19:40	0.035	0.002	0.002	0.105	1.775	0.000	0.002	0.008	0.103	1.817
13.09.2008 00:40	0.041	0.002	0.002	0.111	1.744	0.000	0.002	0.006	0.109	1.796
13.09.2008 05:40	0.046	0.006	0.002	0.126	1.845	0.000	0.003	0.006	0.123	1.906
13.09.2008 10:40	0.044	0.005	0.003	0.132	2.053	0.000	0.002	0.006	0.114	2.133
13.09.2008 15:40	0.030	0.005	0.003	0.120	2.170	0.000	0.002	0.004	0.090	2.254
13.09.2008 20:40	0.041	0.005	0.002	0.123	2.176	0.000	0.001	0.008	0.105	2.255
14.09.2008 01:40	0.051	0.000	0.003	0.145	2.341	0.000	0.001	0.007	0.130	2.391
14.09.2008 06:40	0.056	0.000	0.006	0.152	2.311	0.000	0.003	0.005	0.138	2.378
14.09.2008 11:40	0.052	0.002	0.003	0.163	2.347	0.000	0.001	0.007	0.152	2.399
14.09.2008 16:40	0.055	0.001	0.003	0.176	2.427	0.000	0.002	0.004	0.167	2.476
14.09.2008 21:40	0.051	0.000	0.002	0.172	1.935	0.000	0.002	0.007	0.179	1.956
15.09.2008 02:40	0.056	0.000	0.003	0.179	1.947	0.000	0.006	0.008	0.179	1.986
15.09.2008 07:40	0.063	0.000	0.006	0.179	1.913	0.000	0.002	0.006	0.188	1.984
15.09.2008 12:40	0.069	0.000	0.006	0.187	1.937	0.000	0.001	0.006	0.196	2.010
15.09.2008 17:40	0.053	0.000	0.003	0.191	1.954	0.000	0.000	0.008	0.208	1.995
15.09.2008 22:40	0.082	0.000	0.009	0.201	1.970	0.000	0.002	0.008	0.213	2.052
16.09.2008 03:40	0.060	0.000	0.003	0.200	1.940	0.000	0.001	0.007	0.210	1.976
16.09.2008 08:40	0.090	0.000	0.012	0.207	1.962	0.000	0.001	0.008	0.220	2.040
16.09.2008 13:40	0.067	0.000	0.003	0.209	1.976	0.000	0.001	0.007	0.217	2.027
16.09.2008 18:40	0.083	0.000	0.007	0.218	2.001	0.000	0.001	0.009	0.228	2.065
16.09.2008 23:40	0.076	0.000	0.008	0.223	2.009	0.001	0.006	0.009	0.228	2.067
17.09.2008 04:40	0.083	0.000	0.003	0.242	2.473	0.001	0.001	0.009	0.234	2.549

Figure A.10: Analysed anions and cations at Glarey spring, in meq. (part 2)

	Cations					Anions				
Date and hours	Sodium	Ammonium	Potassium	Magnesium	Calcium	Fluoride	Choride	Nitrate	Sulfate	Bicarbonate
02.10.2008 10:24	0.160	0.000	0.005	0.416	2.385	0.002	0.024	0.010	0.442	2.477
02.10.2008 14:24	0.153	0.000	0.005	0.416	2.382	0.002	0.021	0.011	0.444	2.465
02.10.2008 18:24	0.152	0.000	0.005	0.415	2.366	0.002	0.021	0.011	0.449	2.440
02.10.2008 22:24	0.158	0.000	0.006	0.417	2.375	0.002	0.026	0.011	0.456	2.445
03.10.2008 02:24	0.173	0.000	0.005	0.422	2.390	0.002	0.038	0.011	0.454	2.467
03.10.2008 06:24	0.180	0.000	0.005	0.422	2.382	0.002	0.046	0.011	0.449	2.461
03.10.2008 10:24	0.157	0.000	0.005	0.414	2.364	0.002	0.032	0.012	0.444	2.428
03.10.2008 14:24	0.146	0.000	0.005	0.401	2.335	0.002	0.023	0.011	0.430	2.398
03.10.2008 18:24	0.138	0.000	0.005	0.391	2.306	0.002	0.017	0.013	0.430	2.392
03.10.2008 22:24	0.125	0.000	0.004	0.376	2.258	0.002	0.012	0.011	0.417	2.326
04.10.2008 02:24	0.114	0.000	0.004	0.360	2.227	0.002	0.011	0.013	0.396	2.292
04.10.2008 06:24	0.107	0.000	0.004	0.350	2.230	0.002	0.010	0.012	0.382	2.299
04.10.2008 10:24	0.098	0.000	0.004	0.333	2.177	0.002	0.010	0.013	0.363	2.224
04.10.2008 14:24	0.093	0.000	0.004	0.321	2.144	0.002	0.008	0.013	0.350	2.191
04.10.2008 18:24	0.090	0.000	0.004	0.314	2.154	0.001	0.010	0.013	0.334	2.206
04.10.2008 22:24	0.085	0.000	0.003	0.282	2.001	0.002	0.003	0.014	0.318	2.038
05.10.2008 02:24	0.085	0.000	0.004	0.297	2.108	0.002	0.012	0.013	0.320	2.150
05.10.2008 06:24	0.080	0.000	0.004	0.293	2.105	0.002	0.003	0.015	0.312	2.155
05.10.2008 10:24	0.088	0.000	0.003	0.282	2.066	0.002	0.008	0.015	0.303	2.117
05.10.2008 14:24	0.060	0.004	0.006	0.315	2.156	0.001	0.009	0.016	0.283	2.249
05.10.2008 18:24	0.047	0.004	0.005	0.266	2.170	0.001	0.008	0.014	0.219	2.258
05.10.2008 22:24	0.046	0.004	0.005	0.265	2.145	0.001	0.003	0.015	0.227	2.239
06.10.2008 02:24	0.045	0.004	0.006	0.263	2.125	0.001	0.008	0.015	0.221	2.218
06.10.2008 06:24	0.043	0.004	0.006	0.245	2.099	0.001	0.008	0.012	0.208	2.177
21.10.2008 18:00	0.046	0.004	0.008	0.268	2.061	0.001	0.009	0.009	0.276	2.088

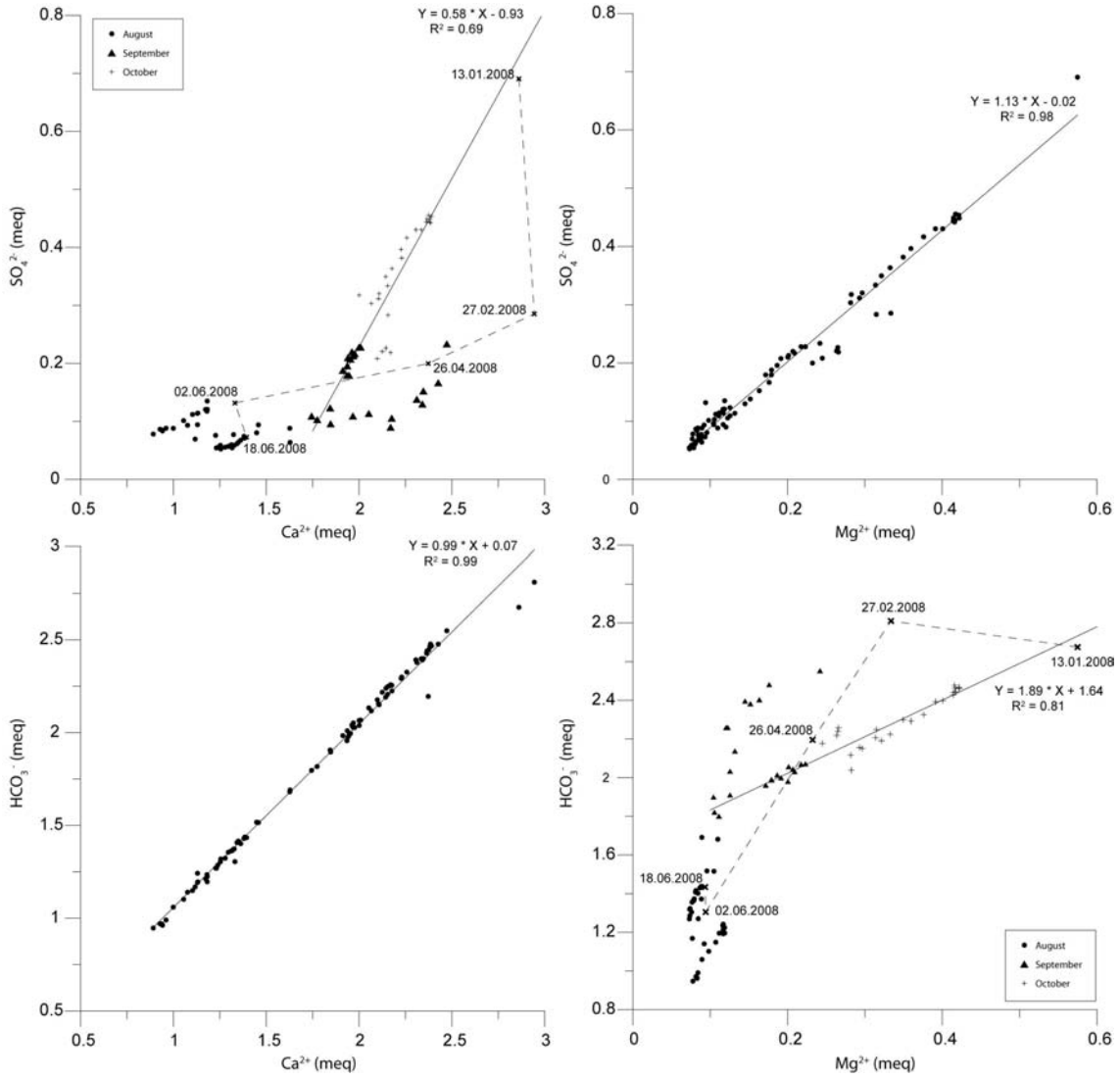

Figure A.11: Very good correlations between HCO_3^- and Ca^{2+}, and between Mg^{2+} and SO_4^{2-} illustrate that water mainly flows through limestone layers but is also in contact with detritic zones with many impurities containing magnesium-sulfate minerals. By correlating Mg^{2+} and Ca^{2+} respectively with HCO_3^- and SO_4^{2-}, the seasonal influence of ionic concentrations is illustrated. Samples taken during the winter season present a rapid decrease in sulfate and magnesium during snow melt. August and September values have a cloudy repartition, but some of these concentrations belong to the well defined linear correlation of October's samples.

Appendix B

Appendix from chapter 3

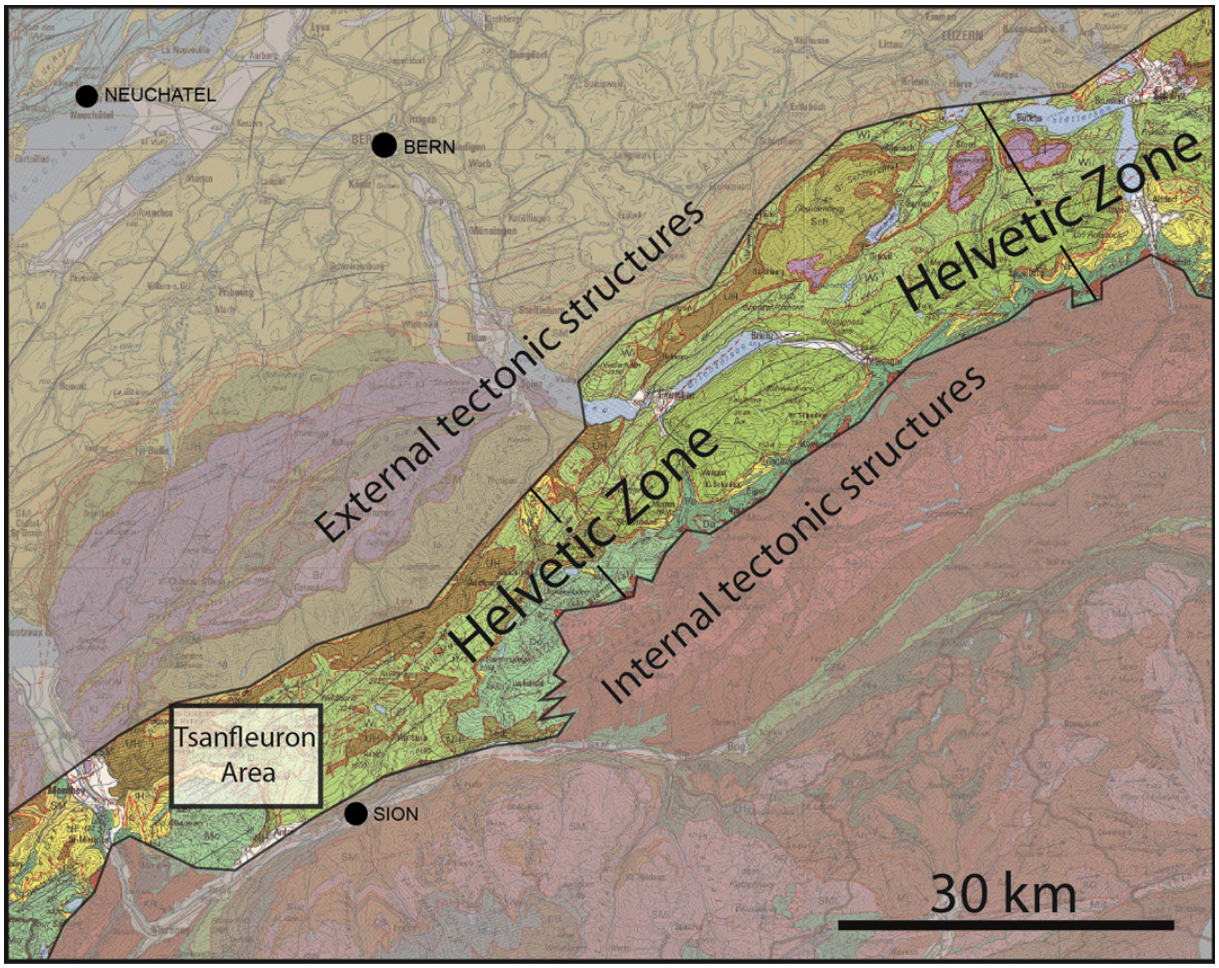

Figure B.1: General tectonic map of western swiss Alps. The Tsanfleuron area belongs to the Helevetic zone that connects the French and austrian Alps (Spicher, 1980).

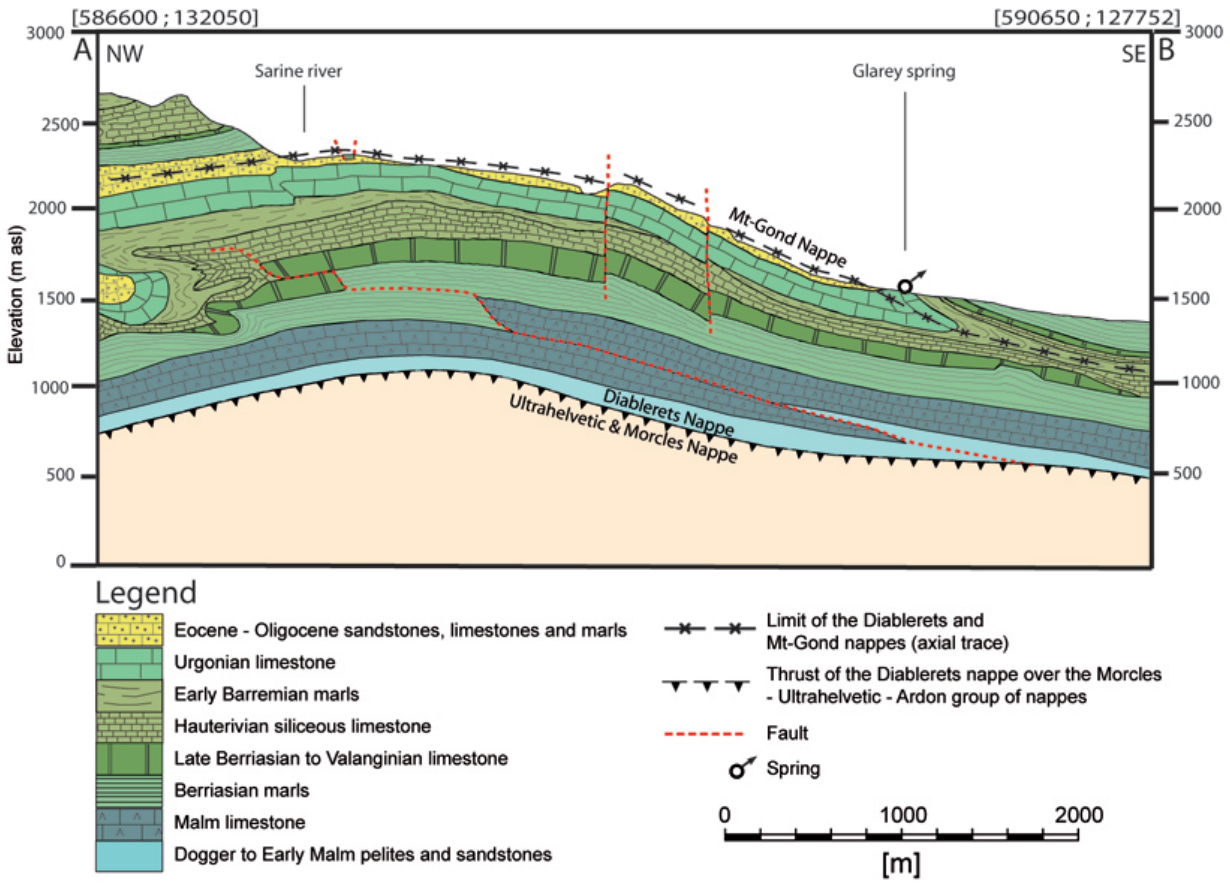

Figure B.2: Cross-section of the test site area towards the Glarey spring, where the isoclinal syncline connecting the Diablerets nappe and the Mt. Gond nappe is clearly visible. Note that the Cretaceous stratigraphy is more detailed than in the geological map (Fig. 3.1), which also shows the cross-section trace (modified from literature (Gremaud and Nessi, 2006)).

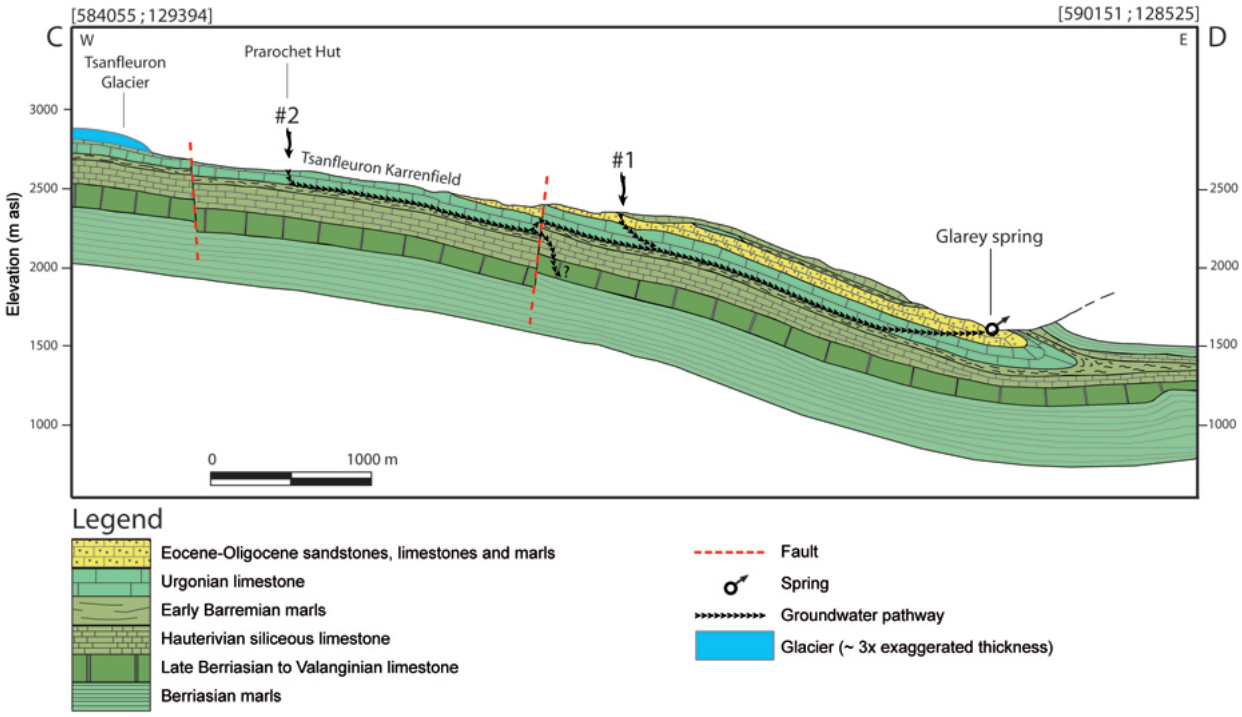

Figure B.3: Conceptual model of karst drainage from the Tsanfleuron glacier and karrenfield towards the Glarey spring, confirmed by tracer tests (injection points #1 and #2 are shown, also see Fig. 3.5). Water flow occurs near the base of the Urgonian-Eocene karst aquifer on top of the underlying Barremian marl towards the isoclinal syncline that collects all water and conveys it to the spring. Infiltration into deeper aquifers along faults is assumed (section line see Fig. 3.1). Figure modified from literature (Gremaud and Nessi, 2006)

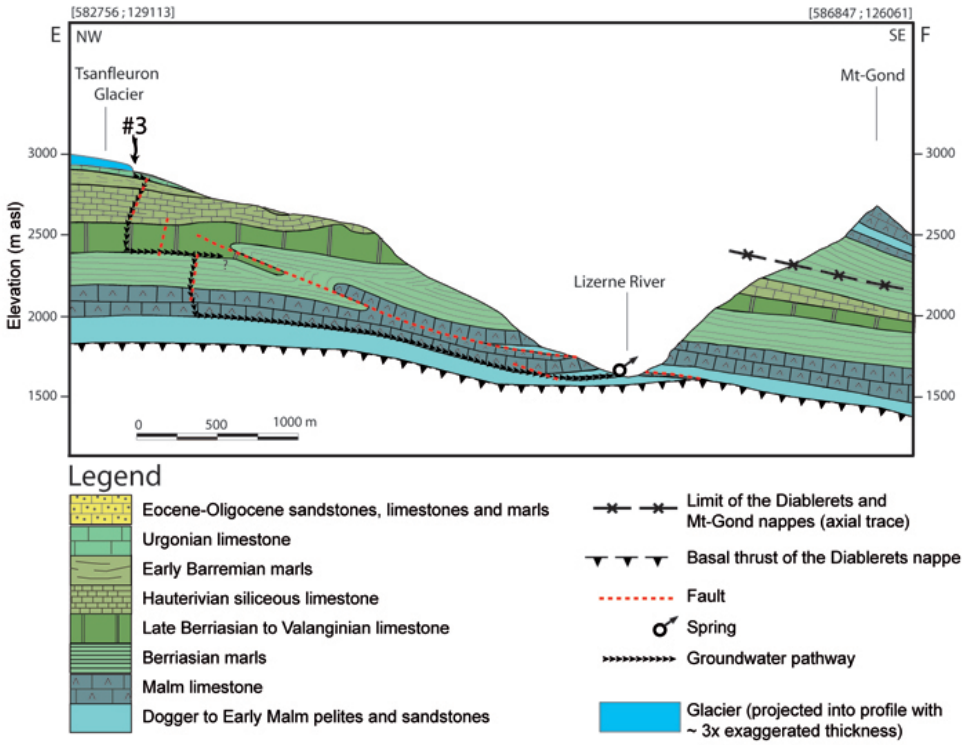

Figure B.4: Conceptual model of flow from the upper part of the Tsanfleuron glacier and karrenfield towards the Tschoetre spring, confirmed by tracer tests (injection point #3 is shown; see also Fig. 3.5). The tracer crossed the entire stratigraphic sequence, including several marl formations, in less than two days along deep fractures that opened due to the steep topography (glacier projected into section, see Fig. 3.1). Figure modified from literature (Gremaud and Nessi, 2006)

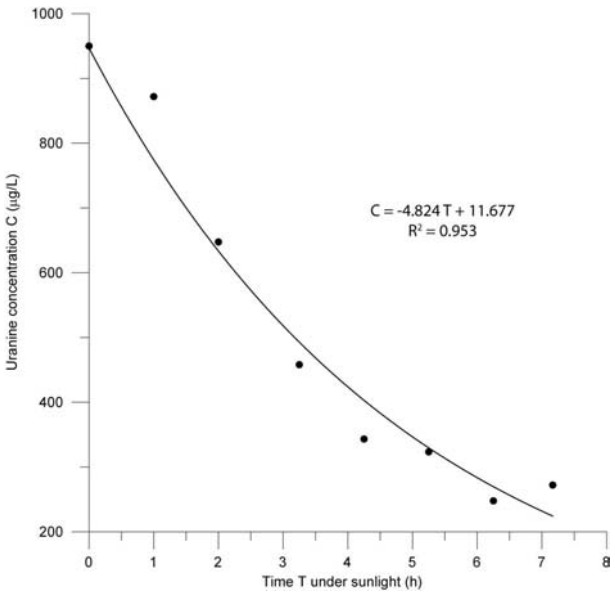

Figure B.5: Experimental degradation of uranine under sun light at 2300 meters.

Figure B.6: Photography of injection points on the karrenfield with the corresponding number.

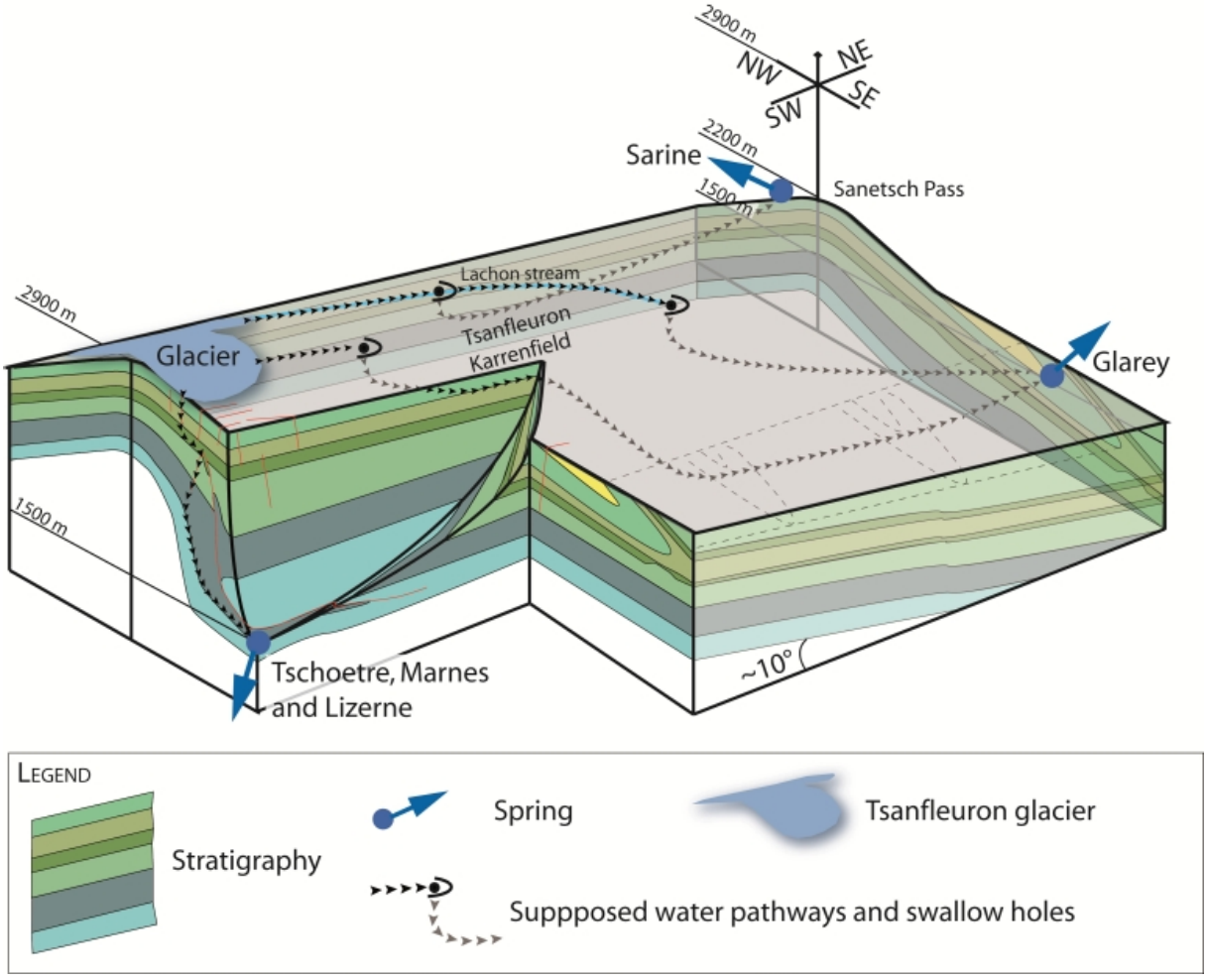

Figure B.7: Three dimensional conceptual model of flow from the Tsanfleuron glacier and karrenfield towards the Glarey, Sarine and Tschoetre springs.

Appendix C

Appendix from chapter 4

C.1 Glacier retreat since 1850, based on historical maps
C.2 Glacier thickness and coordinates of each RMT measurement point, part 1
C.3 Glacier thickness and coordinates of each RMT measurement point, part 2

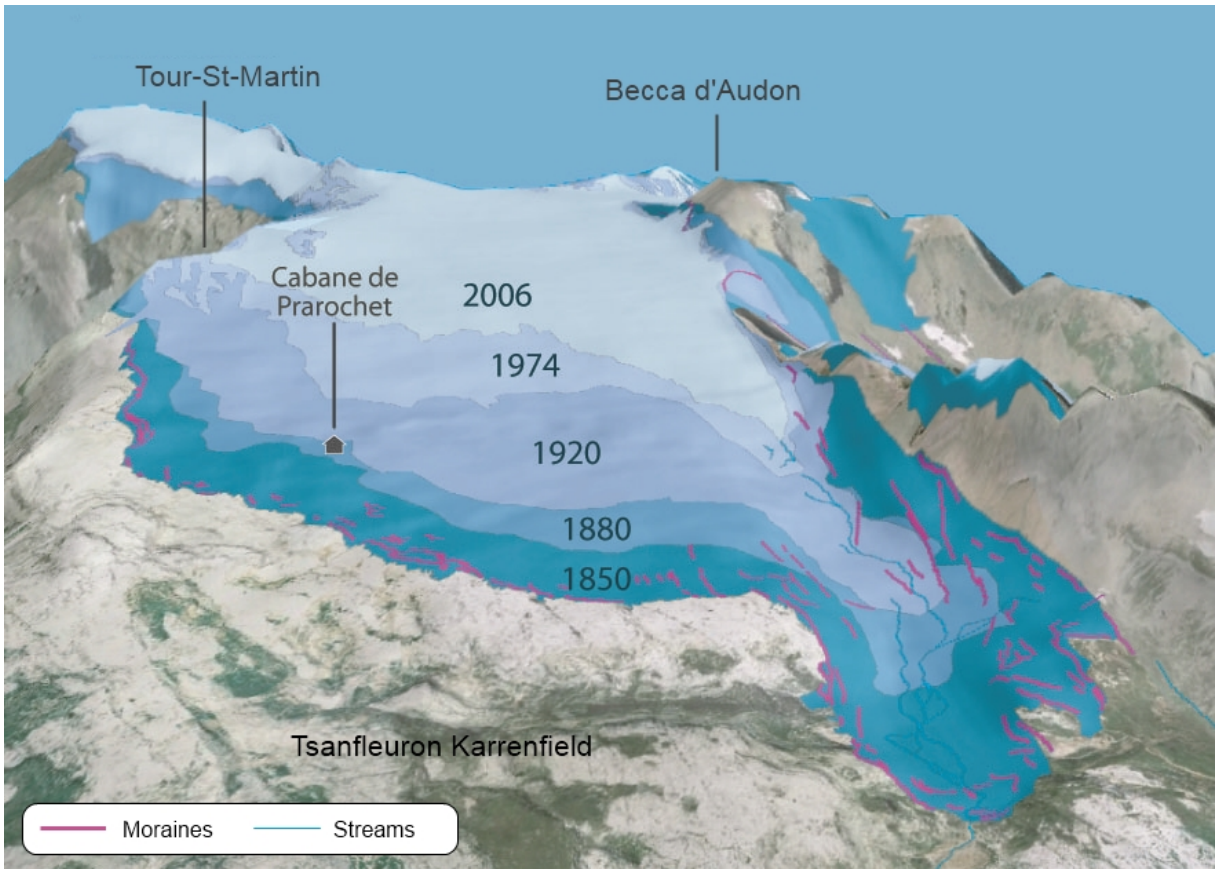

Figure C.1: Glacier retreat steps since 1850, based on historical maps (modified from Martin, S (2008), University of Lausanne, Switzerland).

Figure C.2: Thickness established by inverting RMT apparent resistivity and phases.

	X	Y	Z	Thickness		X	Y	Z	Thickness
1	583284	128977	2838	12.8	47	584078	129613	2707	4.6
2	583282	129025	2847	4.8	48	584093	129788	2711	12.5
3	583265	129079	2854	8.6	49	584096	129874	2711	13.9
4	583147	129349	2843	16.1	50	584094	129969	2706	20
5	583094	129543	2836	18	51	584102	130055	2707	23.9
6	583077	129612	2834	18.6	52	584100	130129	2708	17.5
7	583051	129698	2836	25.3	53	584090	130228	2705	24.7
8	583031	129781	2827	26.2	54	584035	130346	2708	26.6
9	583014	129844	2826	13.2	55	584075	130421	2711	12.3
10	582962	129975	2825	26.6	56	584079	130514	2718	36.8
11	582865	130053	2826	9.2	57	584013	130542	2718	49.6
12	582765	130103	2829	14.8	58	583918	130551	2731	23.9
13	582702	130147	2825	20.4	59	583703	130321	2749	22
14	582628	130206	2826	26.1	60	583711	130120	2767	32.6
15	582576	130335	2816	39.8	61	583713	130120	2751	25.4
16	582591	130442	2822	53.7	62	583718	130049	2752	23.3
17	582592	130505	2817	105.3	63	583079	129970	2752	23
18	582583	130595	2808	28.1	64	583690	129901	2752	28.2
19	582634	130604	2819	32.1	65	583682	129798	2752	25.2
20	582689	130606	2815	43.5	66	583655	129709	2757	35.4
21	582689	130639	2806	27.4	67	583632	129605	2749	27.6
22	582635	130639	2812	37.4	68	583626	129523	2754	8.9
23	582550	130634	2807	31.2	69	583627	129444	2759	20.3
24	582475	130639	2811	28.4	70	583629	129335	2766	4.9
25	582460	130569	2813	36.3	71	583555	129306	2786	2.4
26	582405	130518	2814	12.6	72	583474	129349	2799	8.5
27	582441	130449	2823	16.4	73	583448	129445	2791	6.6
28	582492	130364	2831	13.8	74	583452	129532	2790	12.6
29	582532	130305	2829	15.4	75	583464	129643	2787	26.8
30	582642	130339	2831	12.1	76	583455	129732	2794	14.9
31	582693	130338	2829	16.5	77	583398	129830	2797	27.5
32	582753	130340	2822	24.9	78	583373	129915	2797	22.2
33	582796	130325	2817	21.4	79	583342	130043	2795	20.7
34	582850	130273	2816	10.6	80	583303	130263	2792	16.4
35	582909	130198	2809	17.3	81	583304	130344	2790	13.5
36	582981	130119	2807	16	82	583324	130432	2799	16.4
37	583042	130061	2813	8.6	83	583206	130426	2798	8.4
38	583103	129978	2808	8.1	84	583206	130323	2799	23.5
39	583175	129891	2802	14.6	85	583207	130220	2800	13.4
40	583259	129790	2802	26.1	86	584932	130448	2547	6.3
41	583316	129695	2794	22.7	87	584913	130436	2568	7.3
42	583377	129613	2803	18.6	88	584889	130429	2571	8.9
43	583434	129508	2798	14.3	89	584866	130434	2586	9.9
44	584074	129334	2681	10.4	90	584843	130428	2588	8.9
45	584065	129419	2690	11	91	584828	130425	2592	9.7
46	584060	129514	2699	19.5					

Figure C.3: Thickness established by inverting RMT apparent resistivity and phases.

	X	Y	Z	Thickness		X	Y	Z	Thickness
92	584801	130424	2596	10.5	138	583414	129584	2799	25.8
93	584776	130422	2600	9.1	139	583456	129655	2794	36.6
94	584752	130420	2604	10.3	140	583491	129727	2789	43.6
95	584727	130420	2607	13.6	141	583526	129799	2784	33.4
96	584699	130418	2610	13.3	142	583564	129873	2776	36.1
97	584676	130418	2615	14.6	143	583592	129903	2769	39.1
98	584651	130414	2618	13.1	144	583649	130019	2764	30.2
99	584628	130417	2622	29.3	145	583694	130093	2755	28.5
100	584607	130409	2629	18.7	146	583746	130175	2753	30.1
101	584578	130409	2630	26.6	147	583925	130480	2735	110.4
102	584553	130409	2634	87.6	148	583960	130539	2727	126
103	584534	130401	2643	28.5	149	584009	130438	2719	110.8
104	584493	130391	2649	100.3	150	583850	130345	2732	85.2
105	584449	130376	2659	96.3	151	583651	130159	2758	44.3
106	584408	130367	2664	66.6	152	583541	130105	2769	29.5
107	584356	130365	2669	80.5	153	583443	130064	2787	53.4
108	584329	130362	2680	96.6	154	583301	130013	2799	107.6
109	584285	130337	2687	92.1	155	583188	129969	2804	8
110	584247	130325	2693	76.3	156	582942	129735	2842	57.5
111	584190	130335	2698	39.8	157	582836	129607	2867	43.1
112	584157	130326	2706	12.8	158	582937	129497	2861	44
113	584119	130330	2709	13	159	583065	129461	2848	79.5
114	584079	130323	2716	17	160	583284	129434	2823	93
115	583995	130321	2727	19	161	583381	129494	2805	20.6
116	583955	130319	2732	12	162	583424	129595	2798	43.6
117	583925	130304	2735	7	163	583485	129724	2794	35.5
118	583863	130314	2743	27	164	583572	129885	2778	13.3
119	583814	130309	2745	60	165	583807	130064	2747	19.4
120	583764	130304	2746	88	166	584034	130098	2719	26.7
121	583714	130300	2751	24.8	167	584155	130110	2705	16.7
122	583674	130294	2759	9.3	168	584166	130000	2704	41.8
123	583618	130318	2762	5	169	584168	129913	2703	5.3
124	583571	130314	2768	12.8	170	584185	129865	2702	8.3
125	583518	130323	2772	4.7	171	584150	129731	2701	14.3
126	583470	130328	2778	7.7	172	584128	129649	2701	54.8
127	583407	130321	2784	30.9	173	584075	129579	2708	49.1
128	583238	130269	2795	12.8	174	584007	129519	2716	63.5
129	583007	130202	2812	29.7	175	583930	129464	2724	60.3
130	582872	130198	2820	20.4	176	583844	129395	2730	57.3
131	582728	130184	2830	15.4	177	583828	129317	2727	63.3
132	582622	130114	2840	13.5	178	584299	129753	2679	7.7
133	582764	129931	2848	5.9	179	584445	130088	2662	26.7
134	582890	129766	2850	71.9	180	584550	130154	2644	11.1
135	582938	129662	2847	67	181	584653	130236.5	2625.5	14.3
136	582992	129552	2849	25.2	182	584756	130319	2607	22.9
137	583316	129358	2825	9.3					

Appendix D

Appendix from chapter 5

D.1 Fractionation calculation between snow and its meltwater
D.2 Elevation zones for precipitation repartition of isotopic values

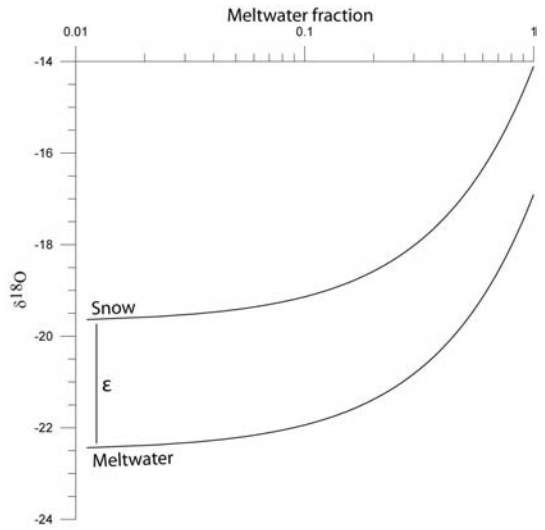

Figure D.1: Fractionation between snow and water during snow melt. By considering that snow volume equals 1, and removing percent by percent meltwater from this initial volume (using a fractionation factor α of 1.0028), two curves of isotopic variations for meltwater and snowpack are obtained.

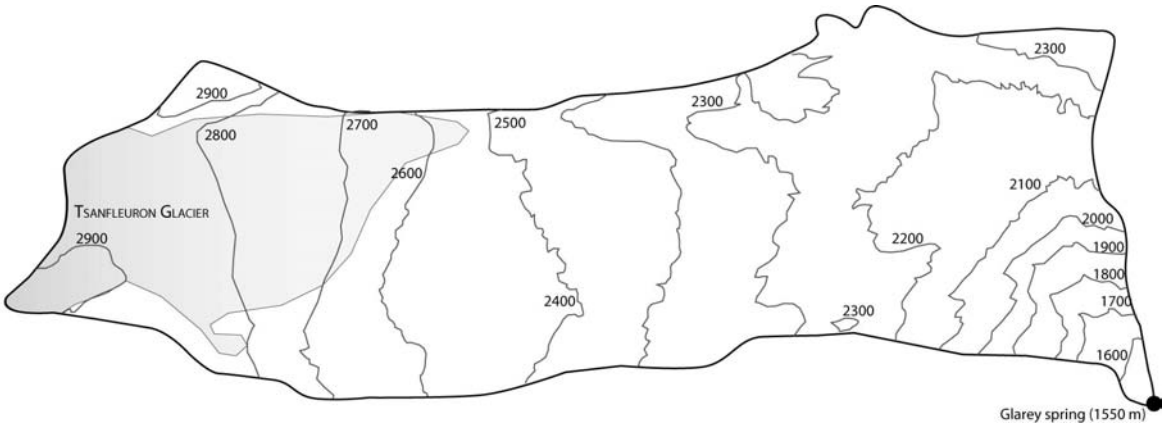

Figure D.2: Elevation zones for precipitation repartition of isotopic values. Each area was measured in order to have the isotopic weight for precipitation input

Appendix E

Appendix from chapter 6

E.1 Phase diagram of precipitation in relation with humidity and temperature
E.2 Annual variations of discharge, electrical conductivity and precipitations
E.3 Particle variations during a dry period in september 2009
E.4 Temperature and precipitation variations during the last century

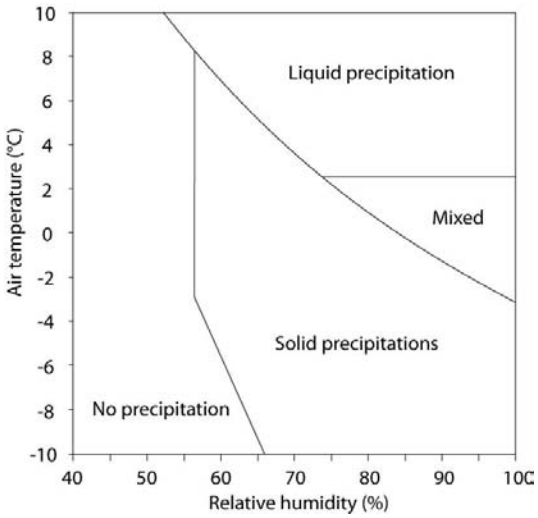

Figure E.1: Phase diagram of the precipitation in relation with air temperature and humidity (Rubel et al., 2000)

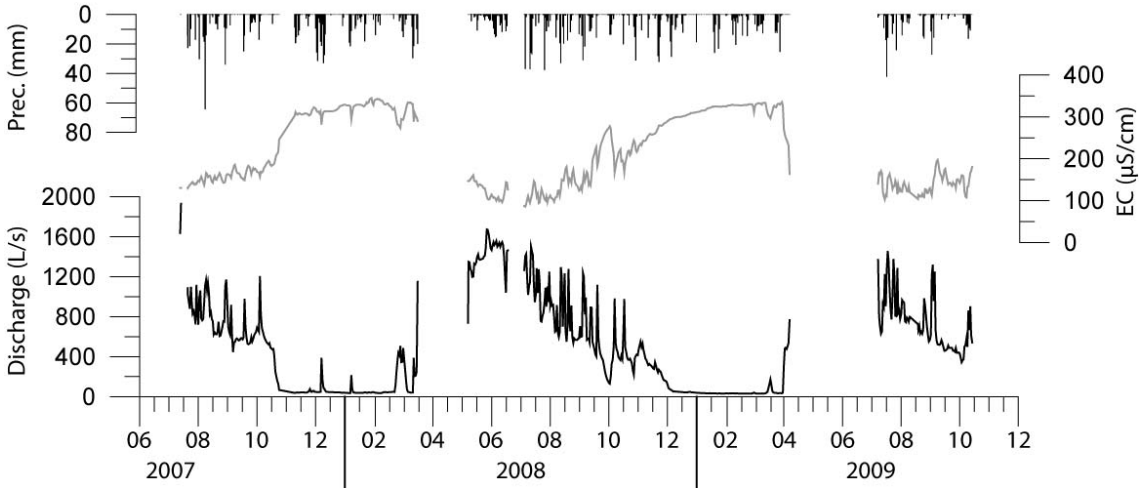

Figure E.2: Annual variations of discharge, electrical conductivity (EC) and precipitations (Prec).

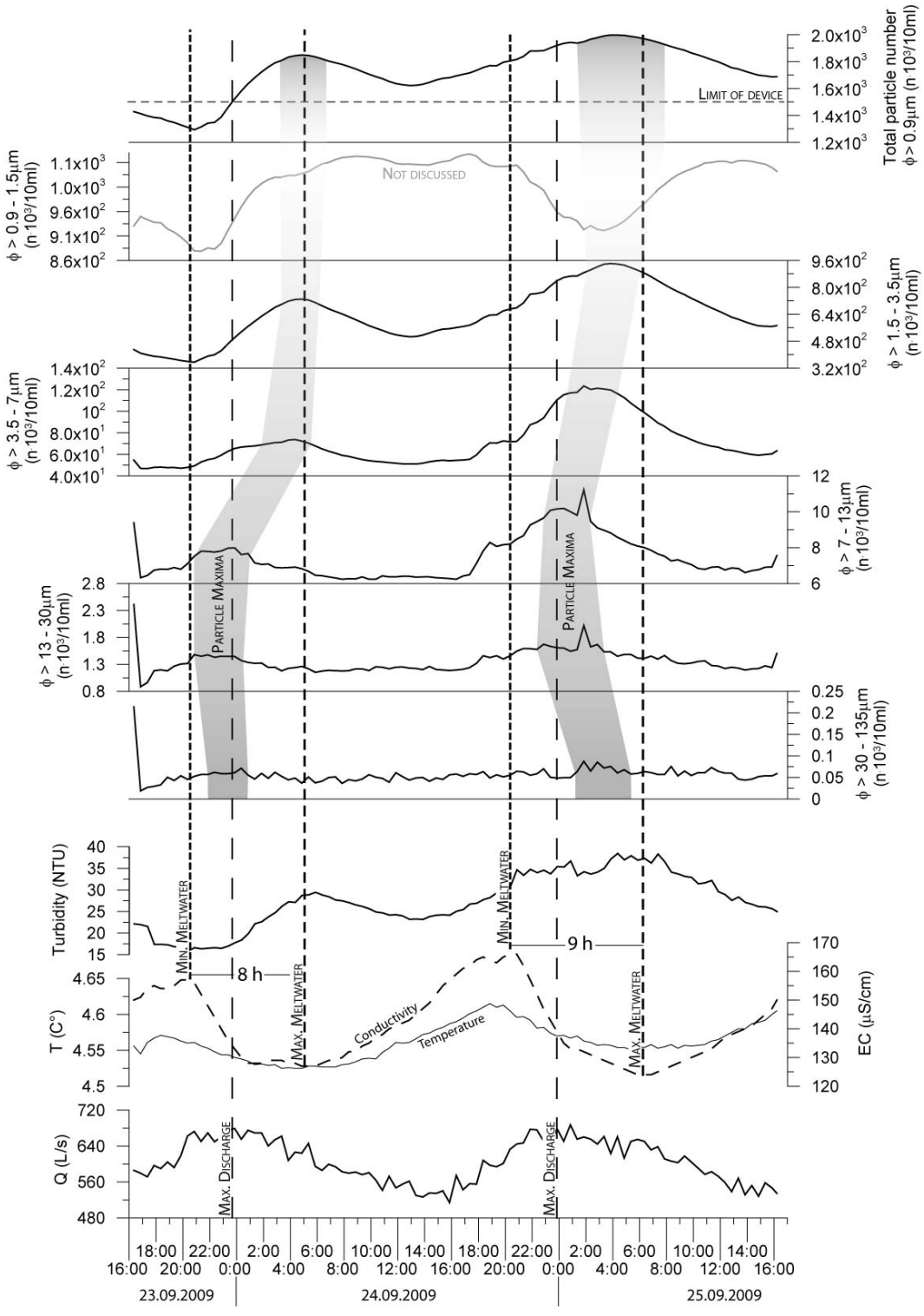

Figure E.3: Multi parameters diagram with time variations of chosen particles classes (ϕ>30 to 135, >13 to 30, >7 to 13, >3.5 to 7, >1.5 to 3.5 and >0.9 to 1.5 µm) during dry weather periods (Ramu, 2010). The smaller particle class is not discussed because it does not vary with turbidity or with total particles signal. Many uncertainties are present in these values because the device limit was often exceeded, creating coincidence cases. The particle maxima is time shifted with bigger particles mobilized during discharge pulses, before smaller particles that are transported by glacier meltwater (Low EC).

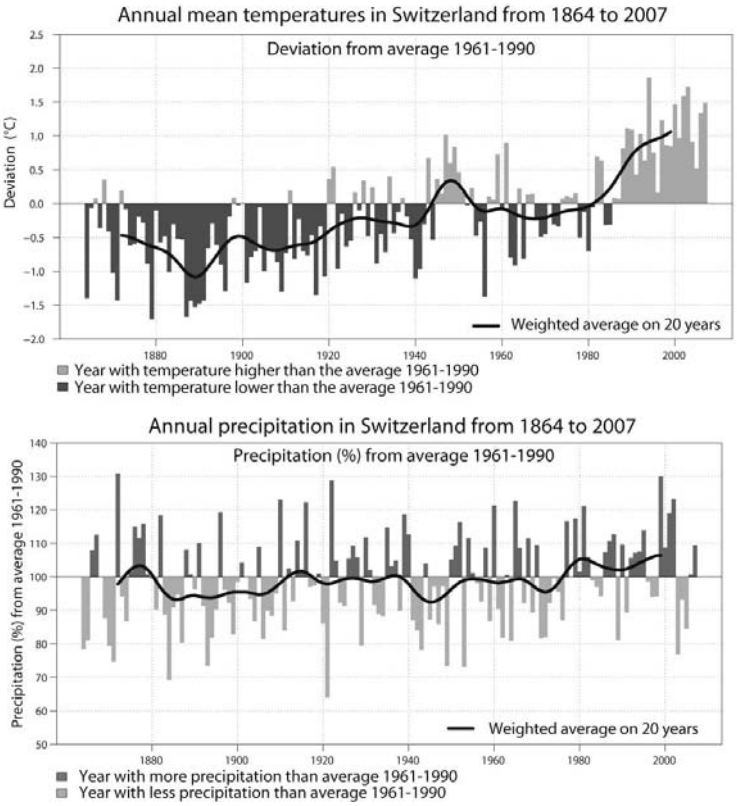

Figure E.4: Temperature and precipitation variations during the last century. Last decades show very high increase in temperature but no flagrant differences in precipitation volumes (OcCC, 2008).